DoKDoK 2013

doctoral students conference on optics

Proceedings

6th - 10th October, Ringberg Hotel Suhl, Germany

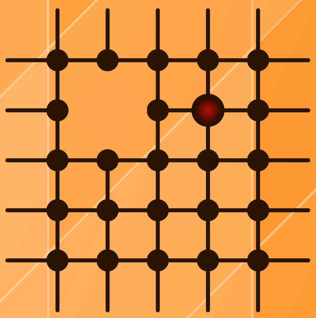

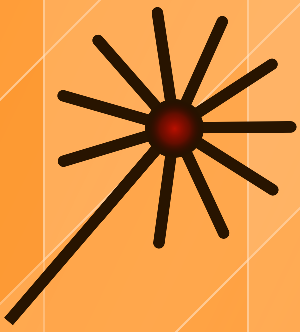

Abbe School of Photonics, Jena, Germany

DoKDoK 2013

06th – 10th October 2013, Ringberg Hotel, Suhl, Germany

PROCEEDINGS

Abbe School of Photonics, Jena, Germany

Imprint

DoKDoK 2013 – Proceedings

Editor-in-Chief & Conference Chair: Matthias Falkner (Matthias.Falkner@uni-jena.de)
Print: Friedrich-Schiller-Universität Jena – Druckzentrum
The DokDoK Logo was created by Jana Bierbach

Abbe School of Photonics
Friedrich-Schiller-Universität Jena
Physikalisch-Astronomische-Fakultät
Max-Wien-Platz 1
07743 Jena
Germany

Contents

Editorial Note

Die **DoK**DoK wird erwachsen. Bereits zum dritten Mal findet nun die "Doktorandenkonferenz zur Diskussion optischer Konzepte" statt. Das neu zusammengesetzte Organisationsteam konnte dabei die Erfahrungen seiner Vorgänger nutzen, um die Qualität der Konferenz weiter zu steigern. Vergleicht man die Entwicklung der **DoK**DoK mit der des Menschen, so ist sie nach Kindheit und Jugend nun in ihrer dritten Stufe erwachsen geworden und zu eigener Größe herangereift. Besonders deutlich wird diese Entwicklung durch die gewonnene Reputation, die sich in der hohen Anzahl der industriellen Sponsoren und internationalen sowie überregionalen Teilnehmer widerspiegelt. Zudem wird an die **DoK**DoK erstmals eine Herbstschule angeschlossen. Nicht weniger bedeutend ist es, dass wir erstmalig drei Keynote-Speaker für unsere Konferenz gewinnen konnten, die die auf der **DoK**DoK behandelte Bandbreite optischer Konzepte exzellent abbilden: Prof. Thomas Stöhlker vom GSI Darmstadt (Atomphysik in extremen Feldern), Prof. Markus Schmidt vom IPHT Jena (Optische Fasersensorik) und Prof. Markus Pollnau von der Universität Twente in den Niederlanden (Integrierte optische Mikrosysteme).

Die Leitgedanken der **DoK**DoK sind jedoch nach wie vor dieselben geblieben: Austausch und Networking. Bieten Facebook & Co. zahlreiche Möglichkeit zum informellen Chat im Internet, so fehlte es doch an einer Plattform zur fachlichen Diskussion der übergreifenden und speziellen Themen der eigenen Promotion. Aus diesem Grund wurde 2011 die **DoK**DoK ins Leben gerufen. Und aus diesem Grund stellen 51 Autoren in 37 Vorträgen und 16 Postern ihre aktuellen Forschungsergebnisse dar. Es ist eine Konferenz von Doktoranden für Doktoranden, die von Fragen sowie Diskussionen lebt und Verbindungen für die Zukunft knüpft.

Es ist mir eine Freude alle Teilnehmer willkommen zu heißen und allen anregende Diskussionen und eine erfolgreiche **DoK**DoK 2013 zu wünschen.

— —

DoKDoK has grown up. It's now the 3^{rd} edition of the "doctoral student's conference for the discussion of optical concepts" to take place. The new organizing team could build on the experience of their predecessors to further improve the quality of the conference. Comparing the evolution of **DoK**DoK to the human one, **DoK**DoK left behind childhood and juvenility and has matured to an institution of its own. This evolution is particularly evidenced by the acquired reputation, reflected in the high number of industrial partners as well as national and international participants. Furthermore, **DoK**DoK is completed by an autumn school for the first time. Most notably, three keynote speakers, who fairly well cover **DoK**DoK 's broad topical spectrum on optical concepts, have accepted the invitation to speak at **DoK**DoK : Prof. Thomas Stöhlker from the GSI Darmstadt (atomic physics in extreme fields), Prof. Markus Schmidt from the IPHT Jena (fiber sensors) and Prof. Markus Pollnau (integrated optical microsystems) from the University of Twente in the Netherlands.

Nevertheless, **DoK**DoK 's leitmotifs have still remained the same: scientific exchange and networking. While social networks like facebook offer numerous possibilities for noncommittal online chats, there was no platform for topical discussions of specific and general themes of the own doctorate. That's why **DoK**DoK was launched. And that's why 51 authors present their most current research results in 37 talks and 16 posters. **DoK**DoK is a conference for doctoral candidates organized by doctoral candidates that thrives on open research questions and establishes sustainable connections for the future.

It is my pleasure to welcome you as this year's participant and wish many fruitful discussions at a pleasant and successful **DoK**DoK 2013.

Matthias Falkner, General Conference Chair

Keynote Speakers

Prof. Markus Schmidt

Since November 2012 Markus A. Schmidt owns a full professorship for fiber optics at the Friedrich-Schiller University Jena (Germany) and is head of a newly established research group at the Institute for Photonic Technologies (IPHT). His main research topic is combining optical fiber technology with nanophotonic concepts for implementing devices with applications in areas such as biophotonics, plasmonics or nonlinear optics.

From 2006 to 2012 he was leader of the group ”nanowire” in the division of Philip Russel at the Max Planck Institute for the Science of Light in Erlangen (Germany). His main research topic was nanowires inside optical fiber with applications in areas such as nonlinear optics, plasmonics, opto-fluidics, material science, optical detectors, fiber polarizers, band gap structures and biophysics. Between April 2011 and March 2012 Markus Schmidt spend a twelve months research leave at the Centre of Plasmonics and Metamaterials at Imperial College London (UK), working on magnetoplasmonics and hybrid photonic-plasmonic systems. He finished his postdoctoral lecture degree (Habilitation) at the University Erlangen-Nuremberg in June 2012. He obtained his Dr.rer.nat. degree (2006) in nonlinear polymeric photonic crystals at the Technical University Hamburg-Harburg (Germany) and carried out his physics studies with the main focus on applied phyiscs at the University of Hamburg (Germany).

Keynote talk, Monday, 07.10., 09:00 - 10:20

Hybrid Photonic Crystal Fibers - fundamentals and applications

Hybrid photonic crystal fibers are fiber-type waveguides including multimaterial large-aspect ratio nano- and microstructures. Using the pressure-assisted melt-filling approach various hybrid waveguides have been fabricated inside photonic crystal fibers by filling the air holes with materials such as plasmonic metals, semiconductors, fluids or low-melting compound glasses.

In this talk I will review the latest results on fiber-based plasmonics, liquid sensing, high- contrast band gap guidance and mid-IR super continuum generation. I will also give an outlook about ongoing experiments and future developments of the entire field of in-fiber devices.

Prof. Thomas Stöhlker

Thomas Stöhlker received the M. Sc. and a PhD degree from the University of Gießen. After his habilitation at the University of Frankfurt, he became Professor at the Institute of Physics the University at the University of Heidelberg in 2007. At that time he also became head of the Atomic Physics Division of the Gesellschaft für Schwerionenforschung (GSI), Darmstadt. Since 2009, he leads the newly established Helmholtz Institute Jena that merges the extraordinary competences of the University of Jena in the field of optics and high intensity lasers with on-going scientific large scale projects and research facilities such as the European X-ray free-electron laser XFEL Hamburg or the Facility for Antiproton and Ion Research FAIR. In 2012, Thomas Stöhlker got professor at Institute for Optics and Quantum Electronics at the University of Jena. His scientific interest are broadly settled in the field of fundamental atomicphysics where he has contributed more than 330 publications. During his career, he received a number of honors and awards and is presently member of several advisory committees and review panels.

Keynote talk, Sunday, 06.10., 15:40 - 17:00

The International FAIR Project: New Frontiers for the Physics of Extreme Electromagnetic Fields

FAIR [1], the Facility for Antiproton and Ion Research, is the next generation accelerator complex for fundamental and applied research with antiproton and ion beams. It will provide worldwide unique facilities, allowing for a large variety of unprecedented fore-front research in physics covering topics such as quark-gluon dynamics, the symmetry between matter and antimatter, and the limits of stability for exotic nuclei. Key features of FAIR are intense beams of antiprotons and ions up to the heaviest and even exotic nuclei in virtually all charge states, covering an energy range from rest up to 30 GeV/u. FAIR is an international project with 16 partner countries and more than 2500 scientists and engineers are involved in the planning and construction of the accelerators and associated experiments which will be realized in a stepwise approach.

For atomic physics, FAIR will open novel challenging opportunities in the realm of strong and extreme electromagnetic fields [2]. The unique combination of the accelerator facilities at FAIR will make it possible to accelerate, store, and cool heavy ion beams at their highest charge state. These ion species can be exploited for a stringent test of *Quantum Electrodynamics* in the strong and critical field limit. Highly-charged ions also provide a unique access for the determination of fundamental atomic and nuclear properties. In this overview, the wide range of research opportunities will be discussed based on an overview of the present status of experiments aiming on the precise determination of the 1s Lambshift, the Hyperfine Structure and the g-factor of hydrogen-like ions at high-Z. In addition special emphasis will be given to novel instrumentation as a further important aspect of FAIR (e.g. detectors, laser, and ion traps). As an example, combining intense laser pulses with stored and trapped ions will allow for precision investigations of the properties of stable and exotic nuclei. It may also open up new possibilities for the study of parity violating effects in atomic systems, at unprecedented sensitivity.

[1] https://www.gsi.de/forschung_beschleuniger/fair.htm

[2] https://www.gsi.de/work/forschung/appa_pni_gesundheit/atomphysik/forschung/ap_und_fair/sparc.htm

Prof. Markus Pollnau

Markus Pollnau received the M.Sc. degree from the University of Hamburg, Germany, in 1992, and the Ph.D. degree for work performed at the University of Bern, Switzerland, in 1996, both in physics. After postdoctoral positions with the University of Southampton, UK and the University of Bern, he was a Project and Research Group Leader with the Swiss Federal Institute of Technology, Lausanne, Switzerland. In 2004, he became a Full Professor and Chair of the Integrated Optical MicroSystems Group, MESA+ Institute for Nanotechnology, University of Twente, Enschede, The Netherlands. He has contributed to more than 500 reviewed journal and international conference papers and ten book chapters in the fields of crystal and thin-film growth, rare-earth-ion spectroscopy, solid-state and fiber lasers, as well as waveguide fabrication, devices, and applications. He has presented 70 invited talks at international conferences and about 30 lectures at international summer schools.

Dr. Pollnau has held European, Swiss, and Dutch personal Fellowships and has obtained numerous National and European Research Grants. In 2013 he was awarded an ERC Advanced Grant from the European Research Council. He has been involved in the organization of major international conferences, e.g., as a Program and General Co-chair of the Conference on Lasers and Electro-Optics (2006/2008) and the Conference on Lasers and Electro-Optics Europe (2009/2011), as founding General Chair and Steering Committee Chair of the Europhoton Conference (2004/2008), and served as Topical Editor for the Journal of the Optical Society of America B(2007-2010) and on the Editorial Board of the journal Laser Physics Letters (2008-2011). In 2013 he was elected to the rank of Fellow by the Optical Society of America for ”for seminal contributions to rare-earth-ion spectroscopy and highly efficient dielectric waveguide amplifiers and lasers”.

Keynote talk, Wednesday, 09.10., 09:00 - 10:20

A fresh look at continuous-wave lasers: How they really work!

This lecture describes the operation principle of a continuous-wave (cw) laser. In order to keep the photon rate equation and its solution simple, usually the spontaneous-emission rate is neglected with the argument that it is so much smaller than the stimulated-emission rate. The direct consequence is that in a cw laser the gain would equal the losses. Yet, additional implications are that the light emitted by such a laser would be a pure sine wave with an infinite coherence length, its linewidth would become a delta function, its Q-factor would assume an infinite value, the coherent photon number would build up and coherence would manifest itself inside the resonator only when pumping above the laser threshold, and the threshold inversion would depend only on the total resonator losses. None of these implications holds true for any laser that mankind has ever created. Starting from vacuum fluctuations, we consider spontaneous emission directly in the photon rate equation, thereby a priori avoiding all these inconsistencies. It is then straight-forward to see that in a cw laser the gain is smaller than the losses, a cw laser does not only have a finite linewidth that can be derived in a very simple manner, but also a finite Q-factor, as well as two laser thresholds which are both different from the commonly assumed ”threshold inversion”. This work was performed in collaboration with Dr. Marc Eichhorn from the French-German Research Institute of St. Louis, France.

Pre-dinner talk, Wednesday, 09.10., 16:20 - 17:00

Want to become a professor? Turn left, then right, and through the forest, please!

Before asking yourself the question how to become a professor, as a potential candidate you should ask yourself the question whether it is desirable to become a professor. If the answer to this initial question is ”no”, let this pre-dinner talk convince you that your choice is right. If against all rational evidence the answer is ”yes”, your choice may nevertheless be right. You are welcome to participate in a lecture about the many Do’s and Don’t Do’s and what prey to look out for when hunting along the stony route towards academic independence and, moreover, what to expect when entering the academic ”paradise”.

Conference Schedule Overview

Time	Sunday		Monday		Tuesday		Wednesday		Thursday	
08:00 - 08:20			Breakfast		Breakfast		Breakfast		Breakfast	
08:20 - 08:40										
08:40 - 09:00										
09:00 - 09:20			**Keynote II** **Markus Schmidt**		**Session V** Beam Forming & Characterization	Brüning	**Keynote III** **Markus Pollnau**		**Session X** Modeling Systems Optically	Lopaeva
09:20 - 09:40						Becker				Stützer
09:40 - 10:00						Schulze				Eichelkraut
10:00 - 10:20						Vetter				Eilenberger
10:20 - 10:40			Coffee		Short Break		Coffee		Coffee	
10:40 - 11:00										
11:00 - 11:20	**Arrival & Registration**		**Session II** **Carl Zeiss Session on** **Biophotonics**	NN (Zeiss)	**Session VI** Communications	Emsia	**Session VII** Photonic Crystals & Fibers	Rutckaia	**Session XI** Optical Metrology	Zhong
11:20 - 11:40				Kopielski		Malekizandi		Spittel		Sojka
11:40 - 12:00				Jahn	Early Lunch			Schulze		Brüning
12:00 - 12:20				Zopf				Geiss		Fuchs
12:20 - 12:40	Lunch (less people)		Lunch		**LOT-QuantumDesign** **Social Day**		Lunch		**Departure**	
12:40 - 13:00										
13:00 - 13:20										
13:20 - 13:40										
13:40 - 14:00	**Opening Ceremony**		**Session III** Nanooptics I	Filter			**Session VIII** Fiber Lasers & Light Sources	Krämer		
14:00 - 14:20	**Session I** High Intensity Physics	Yeung		Fruhnert				von Grafenstein		
14:20 - 14:40		Wustelt		Kaiser				Chemnitz		
14:40 - 15:00		Würzler		Qi			Coffee			
15:00 - 15:20	Coffee		Coffee							
15:20 - 15:40							**Session IX** Nanooptics II	Falkner		
15:40 - 16:00	**Keynote I** **Thomas Stöhlker**		**Session IV** Optical Material Processing & Characterisation	Kämmer				Fasold		
16:00 - 16:20				Zimmermann				Walther		
16:20 - 16:40				Richter			**Pre-Dinner Talk** **Markus Pollnau**			
16:40 - 17:00			**Poster Presentation**							
17:00 - 17:20										
17:20 - 17:40										
17:40 - 18:00										
18:00 - 18:20	Dinner		Dinner				**Welcome of the new ASP doctoral students**			
18:20 - 18:40							**Conference Dinner**			
18:40 - 19:00										
19:00 - 19:20	**Active Fiber Systems** **Welcome Reception**		**LAYERTEC Poster Session**							
19:20 - 19:40										
19:40 - 20:00										

Conference Schedule

Sunday, 06th October 2013

11:00 Arrival & Registration

12:20 Lunch

13:40 **Opening ceremony**

01 – High Intensity Physics

Chair: Silvio Fuchs

14:00 MARK K. YEUNG

Helmholtz Institute Jena, Friedrich-Schiller-Universität, Jena, Germany

"Extreme Ultraviolet Surface High Order Harmonic Radiation from JETI-40 – Recent Experiments and Plans for the Future"

14:20 PHILIPP WUSTELT

Institute of Optics and Quantum Electronics, Friedrich-Schiller-Universität, Jena, Germany

"Ionization of atomic Ions under elliptical Polarization"

14:40 DANIEL WÜRZLER

Institute of Optics and Quantum Electronics, Friedrich-Schiller-Universität, Jena, Germany

"Velocity Map Imaging of Trajectory Controlled Above-Threshold Ionization Spectra of Xenon Using the Two-Color Field Technique"

15:00 Coffee Break

Keynote I

Chair: Daniel Richter

15:40 PROF. THOMAS STÖHLKER

GSI Helmholtzzentrum für Schwerionenforschung, Darmstadt, Germany

"The International FAIR Project: New Frontiers for the Physics of Extreme Electromagnetic Fields"

18:00 Dinner

19:00 **Active Fiber Systems Welcome Reception**

Possibility to chat with Prof. Thomas Stöhlker

Monday, 07th October 2013

Keynote II
Chair: Ria Krämer

9:00 Prof. Markus Schmidt
Institute of Photonic Technology, Jena, Germany
"Hybrid Photonic Crystal Fibers - fundamentals and applications"

10:20 Coffee Break

02 – Carl Zeiss Session on Biophotonics
Chair: Christian Vetter

11:00 Jean-Jean Johannes Kim
Carl Zeiss AG Corporate Human Resources, Oberkochen, Germany
"About Carl Zeiss"

11:20 Andreas Kopielski
Institute of Photonic Technology, Friedrich-Schiller-Universität, Jena, Germany
"One-pot annealing of DNA-nanoparticle structures"

11:40 Martin Jahn
Institute of Photonic Technology, Friedrich-Schiller-Universität, Jena, Germany
"Lipophilic sensor layers for detecting Sudan dyes using surface enhanced Raman scattering"

12:00 David Zopf
Institute of Photonic Technology, Friedrich-Schiller-Universität, Jena, Germany
"Spectral measurements on noble metal nanoparticles using imaging Fourier transform spectroscopy"

12:20 Lunch Break

03 – Nanooptics I
Chair: Stefan Fasold

13:40 Robert Filter
Institute of Condensed Matter Theory and Solid State Optics, Friedrich-Schiller-Universität, Jena, Germany
"Towards Strong Coupling of Nanoantennas and Quantum Systems"

14:00 MARTIN FRUHNERT
Institute of Condensed Matter Theory and Solid State Optics, Friedrich-Schiller-Universität, Jena, Germany
"Tunable magnetic dipole response of core-shell clusters"

14:20 THOMAS KAISER
Institute of Applied Physics, Friedrich-Schiller-Universität, Jena, Germany
"Effective photonic parameters from an eigenmode perspective"

14:40 JING QI
Institute of Condensed Matter Theory and Solid State Optics, Friedrich-Schiller-Universität, Jena, Germany
"Highly resonant and directional nanoantenna"

15:00 Coffee Break

04 – Optical Material Processing & Characterisation

Chair: Martin Jahn

15:40 HELENA KÄMMER
Institute of Applied Physics, Friedrich-Schiller-Universität, Jena, Germany
"Laser induced damage threshold (LIDT) with fs-laser pulses"

16:00 FELIX ZIMMERMANN
Institute of Applied Physics, Friedrich-Schiller-Universität, Jena, Germany
"On the evolution of primary constituents of ultrashort pulse-induced nanogratings"

16:20 DANIEL RICHTER
Institute of Applied Physics, Friedrich-Schiller-Universität, Jena, Germany
"Influence of Gouy phase on the spectral behaviour of a volume Bragg grating"

16:40 **Poster Presentation**

18:00 Dinner

19:00 **LAYERTEC Poster Session**

LAYERTEC Company Presentation

Tuesday 08th October 2013

05 – Beam Forming & Characterization

Chair: Jana Bierbach

09:00 Robert Brüning

Institute of Applied Optics, Friedrich-Schiller-Universität, Jena, Germany

"Numerical Mode Analysis of Laser Beams"

09:20 Nils Becker

Institute of Applied Physics, Friedrich-Schiller-Universität, Jena, Germany

"Airy pulses and pulses with arbitrary temporal trajectories"

09:40 Christian Schulze

Institute of Applied Optics, Friedrich-Schiller-Universität, Jena, Germany

"Beam quality measurements with a spatial light modulator"

10:00 Christian Vetter

Institute of Applied Physics, Friedrich-Schiller-Universität, Jena, Germany

"Generation of Optical Solenoid Beams for Particle Manipulation"

10:20 Short Break

06 – Communications

Chair: Daniel Richter

11:00 Ali Emsia

Institute of Microwave Engineering and Photonics, Technische Universität Darmstadt, Darmstadt, Germany

"DPSK-based reach extension for N$\times$Gbit/s NG-PON"

11:20 Mohammadreza Malekizandi

Institute of Microwave Engineering and Photonics, Technische Universität Darmstadt, Darmstadt, Germany

"Power budget extension for OFDM-TDM-WDM PON"

11:40 Lunch Break

LOT-QuantumDesign Social Day

13:00	(optional) city tour in Suhl: bus leaves at 12:30 from the hotel
14:30	Visit of the marine aquarium in Zella-Mehlis: the bus leaves at 13:45 from the hotel and at 14:00 from the Congress Centrum in Suhl (start- and endpoint of city tour)
16:30	Guided tour through the Viba factory in Schmalkalden: the bus leaves at 15:45 from the marine aquarium

In the evening we close this day with Dinner at the Viba factory (self pay)

Adresses:

Ringberghotel: Ringberg 10, 98527 Suhl
Congress Centrum Suhl: Friedrich-König-Straße 7, 98527 Suhl
Marine Aquarium Zella-Mehlis: Beethovenstraße 16, 98544 Zella-Mehlis
Viba Factory Schmalkalden: Nougat-Allee 1, 98574 Schmalkalden

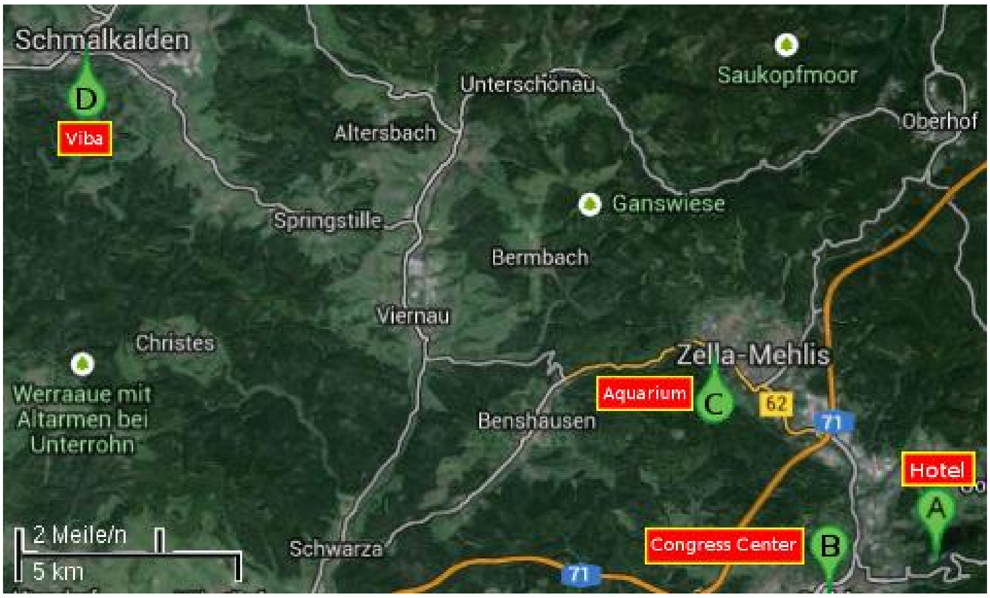

Wednesday, 9th October 2013

Keynote III

Chair: Matthias Falkner

9:00 Prof. Markus Pollnau
University of Twente, Enschede, The Netherlands
"A fresh look at continuous-wave lasers: How they really work!"

10:20 Coffee Break

07 – Photonic Crystals & Fibers

Chair: Ria Krämer

11:00 Viktoriia V. Rutckaia
Centre for Innovation Competence SiLi-nano, Martin-Luther-Universität, Halle, Germany
"Luminescence of Si/Ge-quantum dots resonators around 1550nm wavelength and enhancement with photonic crystal microcavities"

11:20 Ron Spittel
Institute of Photonic Technology, Friedrich-Schiller-Universität, Jena, Germany
"Band gap analysis of metal-filled photonic crystal fibers"

11:40 Christian Schulze
Institute of Applied Optics, Friedrich-Schiller-Universität, Jena, Germany
"Measuring the modal bend loss in multimode optical fibers"

12:00 Reinhard Geiss
Institute of Applied Physics, Friedrich-Schiller-Universität, Jena, Germany
"Fabrication of Freestanding Photonic Crystals in Lithium Niobate by Combining Focused Ion-Beam Writing and Ion-Beam Enhanced Etching"

12:20 Lunch Break

08 – Fiber Lasers & Light Sources

Chair: Felix Zimmermann

13:40 Ria G. Krämer
Institute of Applied Physics, Friedrich-Schiller-Universität, Jena, Germany
"High power 1.2 kW monolithic fiber laser with a femtosecond inscribed fiber Bragg grating"

14:00 Lorenz von Grafenstein

Institute of Applied Physics, Friedrich-Schiller-Universität, Jena, Germany

"Ultra-long enhancement cavities as a promising approach to raise femtosecond lasers to a new level of output parameters"

14:20 Mario Chemnitz

Department of Chemical Engineering and Biotechnology, University of Cambridge, Cambridge, United Kingdom

"Supercontinuum generation in an all-normal dispersion fiber for broadband MHz absorption spectroscopy"

14:40 Coffee Break

09 – Nanooptics II

Chair: Falk Eilenberger

15:20 Matthias Falkner

Institute of Applied Physics, Friedrich-Schiller-Universität, Jena, Germany

"Advanced experimental characterization techniques for plasmonic nanostructures"

15:40 Stefan Fasold

Institute of Applied Physics, Friedrich-Schiller-Universität, Jena, Germany

"Plasmonic Moire Magnifier"

16:00 Benny Walther

Institute of Applied Physics, Friedrich-Schiller-Universität, Jena, Germany

"Blessings and curse of silver in plasmonic nanostructures"

Pre-Dinner Talk

Chair: Matthias Falkner

16:20 Prof. Markus Pollnau

University of Twente, Enschede, The Netherlands

"Want to become a professor? Turn left, then right, and through the forest, please!"

18:00 **Conference Dinner** and **Official Welcome of the new ASP doctoral students**

Thursday 10th October 2013

10 – Modeling Systems Optically

Chair: Thomas Kaiser

09:00 ELIZAVETA D. LOPAEVA

Department of Applied Science and Technology, Politecnico di Torino, Torino, Italy

"Experimental realization of quantum illumination"

09:20 SIMON STÜTZER

Institute of Applied Physics, Friedrich-Schiller-Universität, Jena, Germany

"Hybrid Bloch-Anderson"

09:40 TONI EICHELKRAUT

Institute of Applied Physics, Friedrich-Schiller-Universität, Jena, Germany

"Diffusion and ballistic transport in non-Hermitian systems"

10:00 FALK EILENBERGER

Institute of Applied Physics, Friedrich-Schiller-Universität, Jena, Germany

"Black Holes and Revelations: on the Extraction of Optical Pulses from Cavities"

10:20 Coffee Break

11 – Optical Metrology

Chair: Matthias Falkner

11:00 MINYI ZHONG

Institute of Applied Physics, Friedrich-Schiller-Universität, Jena, Germany

"Design and Simulation of the Hyperchromatic Confocal System in Metrology"

11:20 FALKO SOJKA

Institute for Solid State Physics, Friedrich-Schiller-Universität, Jena, Germany

"Compensating geometric distortions, not only in CCD images, for enhanced quantitative analysis - shown by the example of LEED images"

11:40 ROBERT BRÜNING

Institute of Applied Optics, Friedrich-Schiller-Universität, Jena, Germany

"Vortex Beam Analysis Using Holographic Correlation Filters"

12:00 SILVIO FUCHS

Institute of Optics and Quantum Electronics, Friedrich-Schiller-Universität, Jena, Germany

"Towards extreme ultra violet coherence tomography with high harmonic generation light sources"

12:00 Official Closing of the Conference

Poster Contributions

1. ALAEE, RASOUL
   Institute of Condensed Matter Theory and Solid State Optics, Friedrich-Schiller-Universität, Jena, Germany

   ”Complete light absorption in deep-subwavelength graphene plasmonic structures”

2. DA SILVA, RICARDO E.
   Institute of Photonic Technology, Friedrich-Schiller-Universität, Jena, Germany

   ”Effect of the silica bridge thickness of suspended core fiber on the acousto-optic modulation of fiber Bragg gratings”

3. ECKNER, ERICH
   Institute of Optics and Quantum Electronics, Friedrich-Schiller-Universität, Jena, Germany

   ”Relativistic Frequency Synthesis of Light Fields”

4. HEISEL, CHRISTIAN
   Institute of Photonic Technology, Friedrich-Schiller-Universität, Jena, Germany

   ”Comparison of Electric Field Induced Second Harmonic (EFISH) in reflection and transmission from an oxidized silicon membrane”

5. HIDI, IZABELLA J.
   Institute of Physical Chemistry, Friedrich-Schiller-Universität, Jena, Germany

   ”Drug detection using LOC-SERS technology”

6. HOU, JIAMIN
   Institute of Condensed Matter Theory and Solid State Optics, Friedrich-Schiller-Universität, Jena, Germany

   ”Entanglement generation in the vicinity of nano-structure”

7. JOST, AURELIE
   Institute of Photonic Technology, Friedrich-Schiller-Universität, Jena, Germany

   ”Blind reconstruction of Structured Illumination Microscopy (SIM) data”

8. KNIPPER, RICHARD
   Institute of Photonic Technology, Friedrich-Schiller-Universität, Jena, Germany

   ”Field amplifying perfect absorber in the THz range”

9. LIU, WEICI

Institute of Condensed Matter Theory and Solid State Optics, Friedrich-Schiller-Universität, Jena, Germany

”High Power Dual-Wavelength Self-Similar Parabolic Pulse Yb3+ Doped Fiber Laser”

10. LORENZ, ADRIAN

Institute of Photonic Technology, Friedrich-Schiller-Universität, Jena, Germany

”Microstructured Optical Fibers from Preforms by Free Form Silica Laser Drilling”

11. MEYER, FRANK

Institute of Optics and Quantum Electronics, Friedrich-Schiller-Universität, Jena, Germany

”Generation of 2-Cycle Laser Pulses around 1.8μm for the Investigation of Strong Field Phenomena”

12. PAHLOW, SUSANNE

Institute of Physical Chemistry, Friedrich-Schiller-Universität, Jena, Germany

”Chip-based Isolation of Microorganisms with Subsequent Raman Spectroscopic ”

13. RADU, ANDREEA-IOANA

Institute of Physical Chemistry, Friedrich-Schiller-Universität, Jena, Germany

”Determination of vitamins by surface enhanced Raman spectroscopy (SERS)”

14. SHUKLA, SAPNA

Institute of Photonic Technology, Friedrich-Schiller-Universität, Jena, Germany

”Optical Sectioning in a Single Exposure Using Polarisation-Coded Structured Illumination Microscopy (picoSIM) and Nanogratings”

15. TALKENBERG, FLORIAN

Institute of Photonic Technology, Friedrich-Schiller-Universität, Jena, Germany

”Novel Hetero-Junction Solar Cell Concept based on Silicon Nanowires”

16. TIEGEL, MIRKO

Otto Schott Institute of Materials Research , Friedrich-Schiller-Universität, Jena, Germany

”Development of new laserglasses for high-energy systems – opportunities and challenges of alumino silicate glasses”

Abstracts

(first authors are in alphabetical order)

Complete light absorption in deep-subwavelength graphene plasmonic structures

Rasoul Alaee, Renwen Yu, Falk Lederer, and Carsten Rockstuhl

Institute of Condensed Matter Theory and Solid State Optics, Abbe Center of Photonics, Friedrich-Schiller-Universität Jena, D-07743 Jena, Germany

*Corresponding Author: *rasoul.alaee@uni-jena.de*

Abstract

Graphene plasmonics has sparked enormous research interest due to its tunability at terahertz and infrared frequecies. Here, we propose an analytical model to explain the physics of localized surface plasmon in graphene micro-ribbons. We also use a graphene micro-ribbon array separated from a metallic ground plate by a thick dielectric spacer as a building block to achieve a complete light absorber as an immediate application. The total absorption can be explained by means of a Fabry-Perot model and destructive interference. Our findings show the potential of using graphene to make tunable optical devices at terahertz and infrared domains.

INTRODUCTION

Graphene is a single-monolayer of carbon atoms, which has attracted a great deal of attention due to its unique electronic properties and tremendous potential for perspective applications. Recently, plasmons in graphene were studied experimentally. It was shown that the frequencies at which plasmons are excited can be tuned over a wide range of frequencies by means of chemical and electrostatic doping [1]. The discovery of tunable plasmons in graphene open up new avenues of research in tunable plasmonics, optoelectronics, and metamaterial devices [2]. Strong interaction of plasmons in graphene with light leads also to significantly high absorption at terahertz and infrared domains [1].

So far, graphene ribbon structures are widely used, since they are conveniently fabricated in plasmonic device [1]. Inspired by the ability of graphene micro-ribbons to support localized surface plasmon which can cause enhanced absorption, we study at first a generic resonance configuration that allows to excite plasmons in graphene micro-ribbons to elucidate the physics of the system. Specifically, the system consists of graphene micro-ribbons on a dielectric substrate. Moreover, we have developed a devoted homogenization strategy, so-called surface homogenization approach, to describe the effective properties of the structure on fully analytical grounds. This allows for the much simpler consideration of such materials in the design of functional applications.

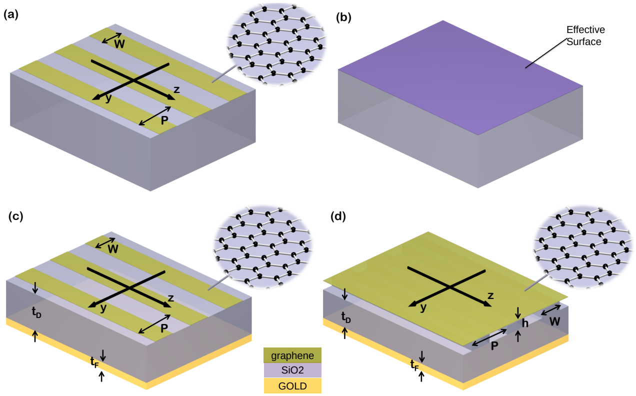

Figure 1: (a, b) Outline the first part of the contribution where a surface containing graphene micro-ribbons (a) is homogenized as a surface with an effective surface impedance (b). (c) Schematic of the absorber based on micro-ribbon. (d) Schematic of the absorber based on a single layer of graphene with dielectric grating. The geometrical parameters of the proposed structure are: $t_\mathrm{F} = 200$ nm, $t_\mathrm{D} = 1 - 35$ μm, $W = h = 1$ μm and $P = 2$ μm. The inset shows the honeycomb microscopic structure of the graphene.

A referential example for such an application is a Perfect absorber. Perfect absorbers can be used for the purpose of optical sensing and photovoltaics. Here, employing the idea of the proposed general resonance configuration, we use a graphene micro-ribbon array or a single layer of graphene on top of a dielectric grating as building blocks to achieve complete light absorption. We explain our findings by means of a Fabry-Perot model and destructive interference of light. Furthermore, we will show that the structure has total absorption for a wide range of angles of incidence and more importantly it is tunable via chemical and electrostatic doping of graphene.

NUMERICAL RESULTS

Figure 1 (a) presents a general resonance configuration based on graphene micro-ribbons. Here, the micro-ribbons are periodic in y direction and infinity extend in the other direction. They are deposited on a quartz substrate. Since graphene is a typical two-dimensional material, we may consider the so-called surface homogenization strategy [3] to homogenize the surface containing graphene micro-ribbons into one effective surface as shown in Fig. 1 (b). It has been verified that the effective surface homogenization strategy is qualified to model the actual configuration as shown in Fig. 2 (b). Furthermore, we point out that the resonance frequency of the effective surface is determined by the zero-crossing point of the reactance of the effective impedance [see Fig. 2 (a)], which can be employed to design graphene micro-ribbon based device, like perfect absorbers.

Using the knowledge of the general resonance configuration we can construct our absorbers. Figure 1 (c) and (d) show the structure of the absorbers under investigation. The absorbers consist of a graphene micro-ribbon array [see Fig. 1 (c)] or a single layer of graphene on top of a dielectric grating [see Fig. 1 (d)] separated from a metallic ground plate by a thick dielectric spacer. They are periodic in y direction and infinity extend in the other direction as well. The absorption of the graphene micro-ribbon based absorbers as a function of the thickness of the dielectric spacer (t_D) and the frequency of operation are depicted in Fig. 2 (c) and (d) for two cases. It shows that total absorption can be achieved at specific dielectric thickness which is repeating periodically close to resonance frequency. We will explain the mechanism of absorption by using a semi-analytical approach based on Airy's formula and compare these results. It will be verified that both approaches are in excellent agreement.

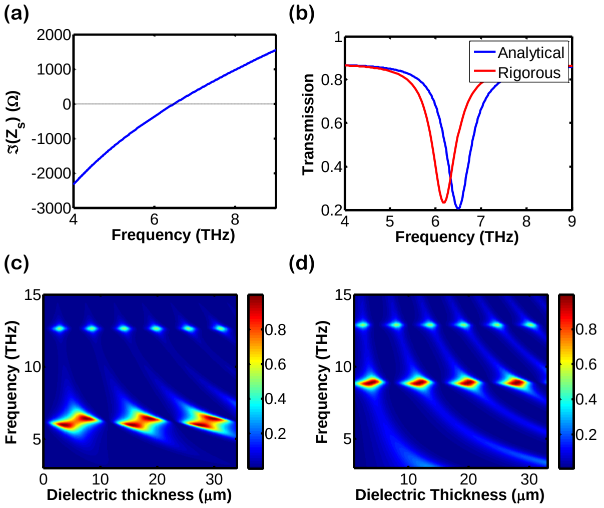

Figure 2: (a) Reactance of the effective surface impedance as a function of frequencies. (b) Transmission spectra given by rigorous calculation (red line) and analytical transfer matrix method (blue line). (c) and (d) Absorption as a function of frequency and dielectric thickness (t_D) for the absorbers with graphene micro-ribbon as well as a single layer graphene on top of dielectric grating, respectively. The electron-phonon relaxation time is assumed to be $\tau = 0.5$ps for chemical potential $\mu_c = 300\,$meV.

The underlying physics of total absorption can be understood by destructive interference of the of directly reflected light that experiences multiple reflection [4]. The resonance frequency of complete absorption could be easily tuned for a wide range of frequencies by doping graphene, i.e. changing its chemical potential. Furthermore, the angular dependency of the absorbers will be investigated as well and we will show that it is almost omnidirectional. Our study shows the potential of using graphene to make tunable optical devices at terahertz and infrared domains.

---

[1] Z. Fei, *et al.*, *Nature* **487**, 82 (2012).

[2] A. Grigorenko, M. Polini, K. Novoselov, *Nature Photonics* **6**, 749 (2012).

[3] O. Luukkonen, *et al.*, *Antennas and Propagation, IEEE Transactions on* **56**, 1624 (2008).

[4] R. Alaee, M. Farhat, C. Rockstuhl, F. Lederer, *Optics Express* **20**, 28017 (2012).

Airy pulses and pulses with arbitrary temporal trajectories

Nils Becker*[1], Falk Eilenberger[1], and Thomas Pertsch[1]

[1] *Institute of Applied Physics, Abbe Center of Photonics,*
Friedrich-Schiller-Universität, Jena

*Corresponding Author: *nils.becker@uni-jena.de*

Abstract

We investigate the propagation of Airy pulses, which are invariant under the influence of the propagation through dispersive media. We exploit a spectral-spatial modulation technique to generate Airy pulses and we use a crosscorrelation technique with an absolute timing reference to measure the longitudinal acceleration that is characteristic for Airy pulses.

INTRODUCTION

Airy pulses are optical pulses with the intensity profile of an Airy function. The Airy function is of interest, as it constitutes a linear, nonspreading solution to the Schrödinger equation [1]. It is therefore invariant under linear propagation, except for a parameter tunable level of self-acceleration. In recent years these results have been transfered to optics due to the similar structure of the underlying equations. However, Airy pulses are theoretical constructs as they carry infinite energy. Airy pulses with finite energy, called apodized Airy pulses, can be created by applying a cubic phase to a Gaussian pulse and up to some extent exhibit the same properties as theoretical Airy pulses. Analogous to Airy pulses are Airy beams which are diffraction-free and accelerate transversally [2].

The invariance of Airy pulses has been exploited to create linear light bullets in combination with Bessel beams [3] or Airy beams [4]. The acceleration of Airy beams has been used to create autofocusing waves [5] and bottle beams [6]. This kind of focal shaping has been proposed to be used in optical microparticle manipulation [7].

Airy beams and pulses also show the effect of self-reconstruction under propagation [8]. This has been exploited to counteract the effect of distortions i.e. due to nonlinear effects for example in supercontinuum generation [9].

Whereas Airy beams accelerate on a parabolic trajectory it has also been shown that quite similar non-spreading beams can be designed that follow arbitrary convex trajectories [10]. It has also been proposed that in dynamic linear index potentials Airy beams with arbitrary trajectories can be designed [11].

EXPERIMENTAL SETUP

The experimental setup is shown in Fig. 1. We use 50 fs pulses which we shape temporally with a spatial light modulator (SLM). In a first step a multiphoton intrapulse interference phase scan [12] is used to retrieve the phase of the input pulse which is then compensated by the SLM.

On this transform limited Gaussian pulse one can now apply arbitrary phase functions via the SLM. We use this setup to shape the input pulse into one delayed Gaussian pulse and one Airy pulse where the Gaussian pulse serves as a probe to measure relative delay. These two pulses are then propagated through a tunable dispersion stage.

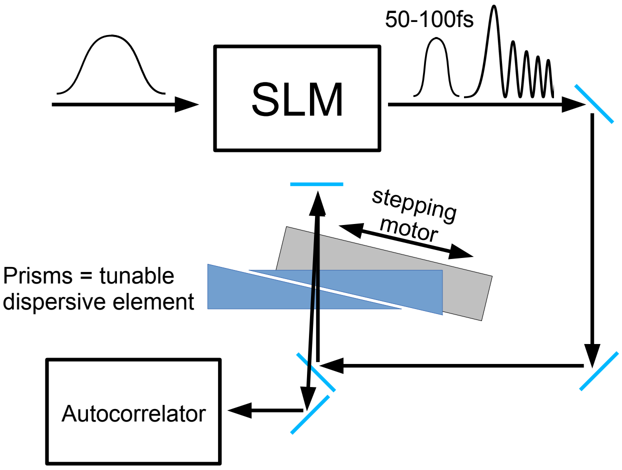

Figure 1: A schematic of the experimental setup.

This stage is composed out of two prisms (BK7), which can be moved against each other to change the dispersion of the beam path. The resulting pulses are then coupled into an autocorrelator, where we retrieve the crosscorrelation of the Airy and the Gaussian pulse from the outer lobes of the autocorrelation function. To achieve the best resolution in the crosscorrelation the Gaussian pulse is precompensated in the SLM so that it is transform limited at the end of the beamline.

This setup can be used to investigate the temporal position and shape of the Airy pulse in relation to the Gaussian pulse. Especially interesting is the position of the front lobe of the Airy pulse and hence of the crosscorrelation from which we can extract the temporal trajectory of the Airy pulse.

PARAMETER DEPENDENCE

The shape of the Airy pulse and its acceleration depend on three parameters: the cubic chirp γ that is applied to the initial Gaussian pulse, its temporal duration τ_0 and the accumulated chirp during propagation $\beta_2 z$ which is proportional to z for fixed group velocity dispersion β_2 of the prisms. The temporal trajectory of the pulse is proportional to

$$t(z) \propto \frac{1}{\gamma}\frac{(\beta_2 z)^2}{12}\,. \tag{1}$$

The first parameter γ is limited by the setup of the SLM. With our system we can shape within a range of $\gamma = \pm 30.000\,\mathrm{fs}^3$. The second parameter τ_0 describes the width of the pulses spectrum and sets a lower boundary on γ. To shape a narrow Gaussian spectrum into an Airy pulse the applied cubic chirp has to be sufficiently large to produce a clean Airy pulse. On the other hand we want to choose γ as small as possible to have a greater acceleration of the Airy pulse as can be seen from Eq. (1). Here we have to make a tradeoff.

As the temporal displacement is quadratically dependent on accumulated chirp of the pulse it can be advantageous to prechirp the pulses via the SLM. This way the absolute delay after propagation through the prisms is higher.

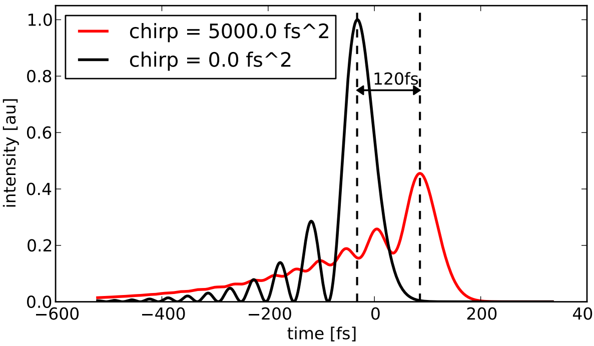

Figure 2: Simulation of the propagation of an Airy pulse for realistic parameters: $\tau_0 = 50\,\mathrm{fs}$, $\gamma = 10.000\,\mathrm{fs}^3$

For our system's parameters ($\tau_0 \approx 50\,\mathrm{fs}$, $\beta_2 z < 5000\mathrm{fs}^2$) simulations show that with $\gamma \approx 10.000\,\mathrm{fs}^3$ the absolute delay due to pulse acceleration is 120fs which is easily visible in the crosscorrelation (see Fig. 2).

OUTLOOK

With the current experimental setup and suitably chosen parameters it should be possible to generate Airy pulses, measure their acceleration and evaluate their stability under propagation. With the SLM it is also possible to apply almost arbitrary temporal phase profiles and thus it should be possible to generate pulses with almost arbitrary temporal trajectories.

---

[1] M. Berry, N. Balazs, *American Journal of Physics* **47**, 264 (1979).
[2] G. Siviloglou, J. Broky, A. Dogariu, D. Christodoulides, *Physical review letters* **99** (2007).
[3] A. Chong, W. H. Renninger, D. N. Christodoulides, F. W. Wise, *Nature photonics* **4**, 103 (2010).
[4] D. Abdollahpour, S. Suntsov, D. G. Papazoglou, S. Tzortzakis, *Physical review letters* **105**, 253901 (2010).
[5] D. G. Papazoglou, N. K. Efremidis, D. N. Christodoulides, S. Tzortzakis, *Optics letters* **36**, 1842 (2011).
[6] I. Chremmos, *et al.*, *Optics letters* **36**, 3675 (2011).
[7] P. Zhang, *et al.*, *Optics letters* **36**, 2883 (2011).
[8] J. Broky, G. A. Siviloglou, A. Dogariu, D. N. Christodoulides, *Optics express* **16**, 12880 (2008).
[9] C. Ament, P. Polynkin, J. V. Moloney, *Phys. Rev. Lett* **107**, 243901 (2011).
[10] E. Greenfield, M. Segev, W. Walasik, O. Raz, *Physical Review Letters* **106**, 213902 (2011).
[11] N. K. Efremidis, *Optics letters* **36**, 3006 (2011).
[12] V. V. Lozovoy, I. Pastirk, M. Dantus, *Optics letters* **29**, 775 (2004).

Numerical Mode Analysis of Laser Beams

Robert Brüning*[1], Philipp Gelszinnis[1], Christian Schulze[1], Daniel Flamm[1] and Michael Duparré[1]

[1] *Institute of Applied Optics, Abbe Center of Photonics, Friedrich Schiller University Jena, Fröbelstieg 1, D-07743 Jena, Germany*

*Corresponding Author: *robert.bruening@uni-jena.de*

Abstract

We present a comparitive study of four numerical methods to detect the mode content of a laser beam from at most two intensity images. The techniques are compared regarding temporal effort, stability, and accuracy, on the example of three multimode optical fibers, which differ in the number of supported modes.

INTRODUCTION

Techniques to decompose laser radiation into spatial modes have become indispensable tools in a broad range of research areas, such as optical signal transmission and communication, to depict valuable diagnostic tools for laser beam characterization and are particularly useful for the design and development of novel high-power lasers, especially of fiber laser systems. Hence, a variety of modal decomposition techniques were proposed, e.g., the S^2 imaging [1], the C^2 imaging [2], the correlation filter method [3], the usage of ring resonators [4] and numerical algorithms [5]. The advantages of numerical algorithms are the simple experimental realization, since only intensity measurements of the beam profile are required, and their flexibility, since they are applicable for different mode sets, such as free space or optical fibers beams. Owing to their simplicity, numerical methods are widely used [5–9].

We present a detailed experimental comparison of four numerical mode analysis techniques. The first method provides the modal decomposition by minimizing the squared error between the measured and reconstructed intensity distribution in the near- and far-field (Residual), the second method maximizes the correlation between the intensity distributions in the near- and far-field (Corr NF+FF), the third method maximizes the correlation only in the near-field (Corr NF) and finally the fourth method uses an iterative algorithm for the phase reconstruction with a subsequent modal decomposition, based on a Gerchberg-Saxton algorithm (GS) [?]. These techniques are applied to beams emerging from different multi mode optical fibers with increasing number of modes. The capability of the algorithms are compared regarding accuracy, repeatability, temporal effort and uniqueness of the retrieved solution and the influence of the initial values and the alignment process on the retrieved mode coefficients are discussed.

EXPERIMENTAL SETUP

The measurement setup is depicted in Fig. 1. A single frequency Nd:YAG laser (λ=1064nm) seeded a single-mode fiber (SMF), which was used as light source for the multi-mode fibers (MMF) under test. By variation of the transverse coupling position between SMF and MMF different higher-order mode contents were excitable in the MMF.

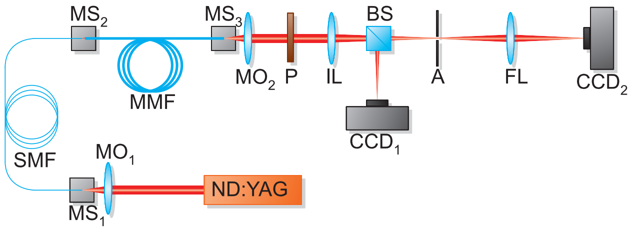

Figure 1: Scheme of the experimental setup. SMF - single-mode fiber, MMF - multi-mode fiber MO_1, MO_2 - microscope objectives, MS - micro mechanical shifter, P - polarizer, IL - imaging lens, BS - beam splitter, A - aperture, FL - Fourier-lens, CCD - camera.

A simple telescopic setup consisting of a microscopic objective and an imaging lens 4f-imaged the near-field of the fiber end face to the plane of the camera CCD_1. Separated by a beam splitter, a Fourier-lens was placed in a 2f-configuration to form the far-field image in the plane of the second camera CCD_2. A polarizer selected one vector component of the emerging beam to satisfy the scalar approximation of the LP modes. To generate higher-order modes we used a SMF with a smaller mode field diameter, which was transversally misaligned. An aperture was used to block the cladding light in the near-field plane, hence acting as a Fourier filter to the far-field image. By this very simple experimental setup the near- and far-field intensity distributions were simultaneously measurable.

RESULTS

To test the different methods, they were applied on the same intensity measurements taken from three different MMFs to control the number of involved modes. The reconstruction results for the fiber supporting three modes are depicted in Fig. 2. The comparison of the different techniques shows the best results for the correlation Corr NF method, whose applicability is limited to <6 modes due to ambiguity issues. For all other methods working in the near- and far-field no ambiguity was observed. The fastest algorithm was the Residual method, which enables real-time mode analyses. It was shown that the biggest influence of the reconstruction occurs by the alignment process of the optical axis and that the influence of the initial values was negligible.
Concerning the different fibers, guiding 3, 6 or 10 modes, a decrease of reconstruction accuracy with a simultaneous increase of the temporal effort was observed for an increasing number of modes.

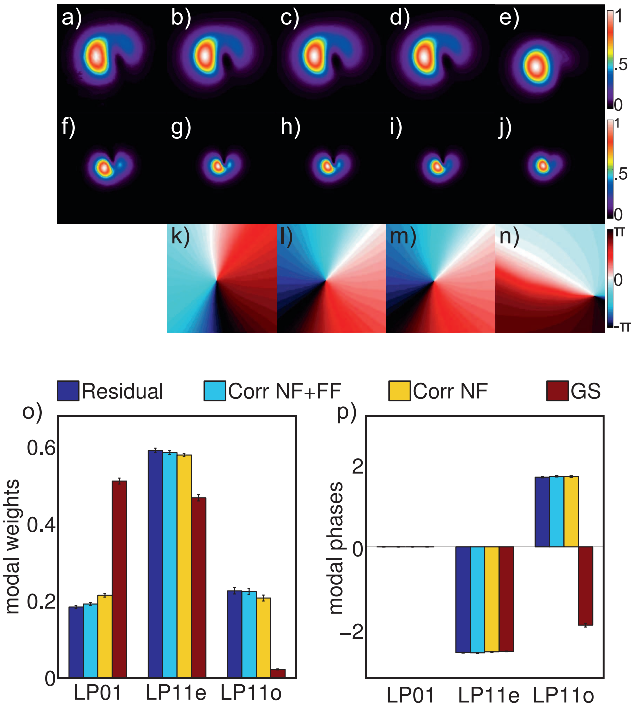

Figure 2: Example fiber A; a)-e) near-field intensities, f)-j) far-field intensities, k)-n) near-field phases from right to left: measured, Residual method, Corr NF+FF method, Corr NF method, GS method; o) relative power spectrum p) modal phases.

---

[1] J. W. Nicholson, A. D. Yablon, S. Ramachandran, S. Ghalmi, *Opt. Express* **16**, 7233 (2008).

[2] D. N. Schimpf, R. A. Barankov, S. Ramachandran, *Opt. Express* **19**, 13008 (2011).

[3] T. Kaiser, D. Flamm, S. Schröter, M. Duparré, *Opt. Express* **17**, 9347 (2009).

[4] N. Andermahr, T. Theeg, C. Fallnich, *Appl. Phys. B* **91**, 353 (2008).

[5] O. Shapira, A. F. Abouraddy, J. D. Joannopoulos, Y. Fink, *Phys. Rev. Let.* **94**, 143902 (2005).

[6] A. Cutolo, T. Isernia, I. Izzo, R. Pierri, L. Zeni, *Appl. Opt.* **34**, 7974 (1995).

[7] M. Skorobogatiy, *et al.*, *Opt. Express* **11**, 2838 (2003).

[8] F. Stutzki, *et al.*, *Opt. Lett.* **36**, 4572 (2011).

[9] H. Lü, P. Zhou, X. Wang, Z. Jiang, *Appl. Opt.* **52**, 2905 (2013).

Vortex Beam Analysis Using Holographic Correlation Filters

Robert Brüning*[1], Christian Schulze[1], Daniel Flamm[1] and Michael Duparré[1]

[1]*Institute of Applied Optics, Abbe Center of Photonics, Friedrich Schiller University Jena, Fröbelstieg 1, D-07743 Jena, Germany*

*Corresponding Author: *robert.bruening@uni-jena.de*

Abstract

We present a measurment techniques, which enables the characterization of vortex beams. In particular the correlation filter method yields access to the orbital angular momentum state spectrum and the orbital angular momentum density

INTRODUCTION

Vortex beams are a special class of optical beams, whose Poynting vector has an azimuthal component. This means the Poynting vector is non-parallel to the optical axis, but rather follows a spiral trajectory around it. Since the Poynting vector is always perpendicular to the phase front, this screw like trajectory arises from a helical phase front, which is also associated with the existence of an orbital angular momentum (OAM). In a two dimensional plane of such beams the phase distribution shows an azimuthal dependency and consequently points exists in which the phase is undefined, called phase singularities.

Since their discovery vortex beams found manifold applications [1], which requires suitable characterization techniques [2-5]. The basic concept of this work, the usage of holographic correlations filters, is successfully introduced in different areas of laser beam characterization [6]. The fundamental idea is to decompose the investigated beam in a complete and orthogonal set of eigenfunctions. Hence, the reconstruction of the complete field information becomes possible and different properties associated with vortex beams can be inferred. A valuable tool for modal decomposition is the correlation filter technique. Using suitable transmission functions, the determination of the modal coefficients resolved in modal weights and intramodal phases becomes possible. The detection of the whole modal spectrum is realizable by using a spatial multiplexing technique.

This work will show the capability of the detection of the underlying OAM states as well as determination of the OAM density distribution by applying the correlation filter (CF) method on vortex beams.

EXPERIMENTAL SETUP

The experimental setup for investigating vortex beams with holographic filters is depicted in Fig. 1. A single-frequency laser (Nd:YAG, 1064nm wavelength) was coupled into a single mode fiber to realize a pinhole for the generation of a plane wave after collimation with the microscope objective MO_2. This plane wave illuminates an SLM, which creates the vortex beams to be investigated in the first diffraction order. The other diffraction orders are blocked in the plane of an aperture, which was positioned in the Fourier plane of L_1. The telescopic setup consisting of L_1 and L_2 imaged the shaped vortex beam onto the correlation filter. After an optical Fourier-transformation of the diffracted beam the first diffraction order containing the correlation answers is recorded by camera CCD_2. Separated by the beam splitter, an image of the shaped beam is recorded with camera CCD_1.

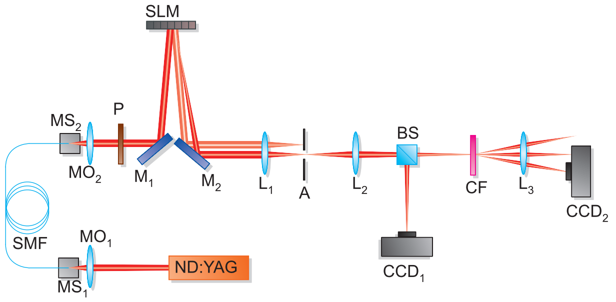

Figure 1: Setup for the investigation of vortex beams using holographic correlation filters; SMF - Single-mode fiber, $M_{1,2}$ - Mirrors, $MS_{1,2}$- Micro mechanical shifter, $MO_{1,2}$ - Microscopic objective, SLM - Spatial Light Modulator, P - Polarizer, $L_{1,2}$ - Lenses, A - Aperture, CF - Correlation filter, $CCD_{1,2}$ - Camera

RESULTS

At first a OAM sorter was realized to detect the existence of different OAM states in the investigated beam. To characterize the capability of the OAM sorter different Laguerre-Gaussian beams were shaped with the SLM to illuminate the CF. By illumination of pure vortex modes the purity of the detected signals was determined, which is shown in Fig. 2. It can be seen that the crosstalk is very low illustrating the proper orthogonality of the modes and filter functions. Secondly, the detection limit was investigated and determined to values of between 1% and 2% for the relative power of the corresponding vortex mode.

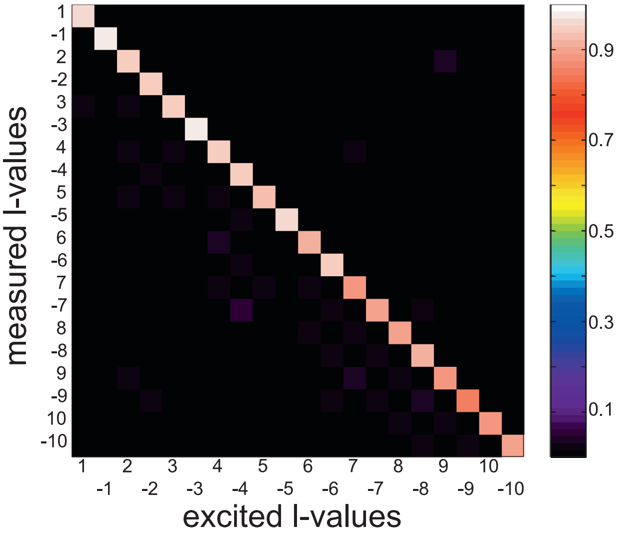

Figure 2: Crosstalk between detection channels of the OAM sorter.

Additionally, CFs were realized, which enables the decomposition of arbitrary beams in terms of vortex modes. Using these filters the reconstruction of the field was possible and enables the investigation of the singularity structure of the phase distribution and the determination of the OAM density. Figure 3 depicts one reconstruction example. Using the reconstructed phase distribution the position of the singularities can be detected easily..

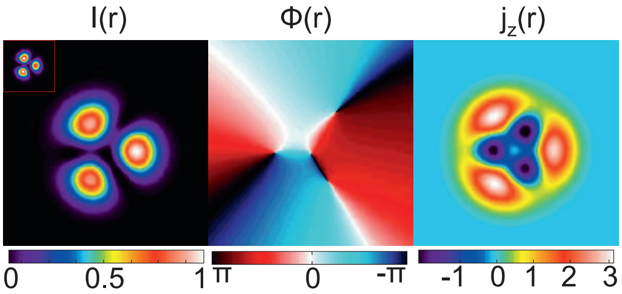

Figure 3: The reconstructed intensity, phase, and OAM density distribution. Inset depicts measured intensity.

[1] S. Franke-Arnold, L. Allen, M. Padgett, *Laser & Photon. Rev.* **2**, 299 (2008).

[2] N. R. Heckenberg, R. McDuff, C. P. Smith, A. G. White, *Opt. Lett.* **17**, 221 (1992).

[3] J. M. Hickmann, E. J. S. Fonseca, W. C. Soares, S. Chávez-Cerda, *Phys. Rev. Lett.* **105**, 053904 (2010).

[4] P. Genevet, J. Lin, M. A. Kats, F. Capasso, *Nat Commun* **3**, 1278 (2012).

[5] M. P. J. Lavery, *et al.*, *New Journal of Physics* **15**, 013024 (2013).

[6] T. Kaiser, D. Flamm, S. Schröter, M. Duparré, *Opt. Express* **17**, 9347 (2009).

Supercontinuum generation in an all-normal dispersion fiber for broadband MHz absorption spectroscopy

Mario Chemnitz*[1], Zhechao Qu[1], Sune Dupont[2], Søren R. Keiding[2], and Clemens F. Kaminski[1]

[1] *Department of Chemical Engineering and Biotechnology, New Museums Site, Pembroke Street, Cambridge, CB2 3RA, UK*

[2] *Department of Chemistry, Langelandsgade 140, 8000 Aarhus C, Denmark*

*Corresponding Author: *mario.chemnitz@gmail.com*

Abstract

We present a broadband single-shot spectroscope with an improved spectral noise characteristics. Improvements have been achieved by replacing a commercial supercontinuum fiber by a customised all-normal dispersion fiber. Pumped with 5ps pulses at 1064nm, this fiber shows a better pulse-to-pulse stability of its broadband output spectra. Numerical investigations of both fibers are used to substantiate experimental results.

INTRODUCTION

Absorption spectroscopy is the method of choice to monitor chemical processes due to its linear signal response. An absorption spectrum contains a variety of molecular information like substance concentration, system temperature, or pressure. For that reason this method is vastly employed e.g. in the field of combustion flame sensing and monitoring.

To monitor such processes optically is challenging on two sides. On the one hand, the absorption lines of combustion gases lie in the mid-infrared region, which can still be hardly addressed by lasers. Nevertheless, few overtone transitions and combinational modes e.g. of water vapour or methane allow read-outs in the near-infrared region as well which is more accessible up to date. On the other hand, combustion dynamics occur on the timescale of microseconds until milliseconds. To monitor these processes the spectral tuning rate of the detector should lie in the range of kilohertz or more.

For both reasons wavelength tuneable diode lasers are one of the most established light sources for fast combustion flame sensing. Unfortunately, these systems cannot provide broad bandwidth and kilohertz repetition rates simultaneously due to limited scan and pulse rates.

Novel white light (supercontinuum) fiber sources offer new possibilities to combine these features. New fiber types - so called photonic crystal fibers (PCF) - enable nonlinear spectral broadening of a pulsed pump source over several hundreds of nanometers. The flexible PCF design influences the chromatic fiber dispersion which gives access to a wide variety of nonlinear effects.

Supercontinuum fiber sources have been utilised in our group in the past years for single-shot absorption spectroscopy of two combustion gases simultaneously [1]. In these setups commercially available fibers have been used. Soliton driven supercontinua have been generated using a 5ps pump source at 1064nm. From this kind of nonlinearity we experienced a high spectral shot-to-shot noise. The recent advent of an all-normal dispersion fiber design from collaborators [2] gave evidence for improvements of the spectral noise characteristics of our technique. This work aims for an experimental and numerical investigation of this potential.

EXPERIMENTAL SETUP

The principal setup used for single-shot spectral analysis and absorption spectroscopy is shown in Fig.1. Pulses emitted from a fiber laser (5ps, 1064nm, 670kHz, >100kW peak power) are broadened spectrally in a photonic crystal fiber (supercontinuum generation). Then, the broadband pulses are stretched in time up to few hundreds of nanoseconds inside a kilometers-long dispersive fiber. The high chromatic dispersion leads to a temporal separation of the frequency components (massive chirp). This enables a pulse-wise spectral read-out by detecting the time trace with an ultrafast photo diode (InGaAs, 35ps re-

Figure 1: Scheme of the experimental setup of the single-shot spectrometer. A pulsed fiber laser pumps the supercontinuum generation in the PCF. The high dispersion in the next module leads to a separation of reddish and blueish wavelengths in time enabling broadband spectral measurements with ultrafast temporal sampling methods.

sponse time) and a 8GHz sampling scope. The measured time traces contain a spectrum-to-time mapping which has to be calibrated with an absorption spectrum of a known sample like water vapour in air.

The fibers under investigation are a commercial PCF which is operated in the anomalous dispersion regime and the customised all-normal dispersion PCF.

SIMULATION

In addition to the experimental single-shot spectral analysis, an efficient numerical model [3] was used to calculate supercontinuum spectra. It implements the nonlinear optical Schroedinger equation which describes the light propagation in optical fibers in an sufficient approximation. Linear and nonlinear parts of the equation were solved separately using a well-known split-step fourier method [4]. The model involves simple input phase noise and a realistic Raman model.

RESULTS AND DISCUSSION

Single-shot spectra have been measured for both types of PCF - the commercial one (Fig.2 right) and the customised one (Fig.2 left). Every single spectrum (blue) looks rather noisy. First after applying a smoothing window with a constant width of 500 sampling points to each individual spectrum reveals a significant message: the course spectral shape of the output of the all-normal dispersion PCF remains stable. These observations were proven with simulation results as well.

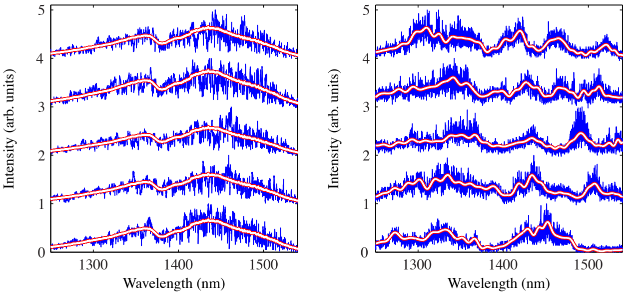

Figure 2: Original single-shot spectra (blue) and smoothened single-shot spectra (red) for both fiber types - left: normal dispersion PCF, right: anomalous dispersion PCF. Intensity in a.u., wavelength in nm.

Measurements and simulations identified the dominant nonlinear effect in the novel all-normal dispersion fiber as Raman scattering. This process is initiated by noise photons as well as soliton fission which is happening in the commercial fiber. Nevertheless, the well-defined Raman gain leads to a course spectrum which is more reproducible. This feature is highly beneficial for single-shot absorption spectra due to less necessary averages to reveal spectral features from background noise. This improves the spectral acquisition time by one order of magnitude demonstrably.

---

[1] C. Kaminski, R. Watt, A. Elder, J. Frank, J. Hult, *Applied Physics B* **92**, 367 (2008).

[2] L. Hooper, P. Mosley, A. Muir, *Optics Express* **19**, 4902 (2011).

[3] J. Hult, *Journal of Lightwave Technology* **25**, 3770 (2007).

[4] G. P. Agrawal, *Nonlinear fiber optics* (Academic Press, 2001).

Effect of the silica bridge thickness of suspended core fiber on the acousto-optic modulation of fiber Bragg gratings

Ricardo E. Silva[1,2], Alexander Hartung[1], Manfred Rothhardt[1], Alexandre A. P. Pohl[2] and Hartmut Bartelt[1]

[1]*Institute of Photonic Technology (IPHT),*
Albert-Einstein-Straße 9, 07745 Jena, Germany

[2]*Federal University of Technology-Paraná (UTFPR),*
Av. Sete de Setembro 3165, 80230901 Curitiba, Brazil

*Corresponding Author: *ricardoezq@yahoo.com.br*

Abstract

The acousto-optic modulation of Bragg gratings is investigated for suspended-core fibers. The bridge thickness is increased and the mechanical and the grating properties are simulated. An increase of the side lobe reflectivity is observed for larger bridge thickness.

INTRODUCTION

Modulation of fiber Bragg gratings (FBG) by longitudinal acoustic waves is of interest for tunable reflectors and modulators [1-3]. When an optical mode with effective index n_{eff} propagates in a non-perturbed grating of period Λ, it is reflected at the Bragg wavelength $\lambda_B = 2n_{\text{eff}}\Lambda$ (Fig. 1(a)). However, when a longitudinal wave is present along the fiber axis z, it produces a periodic strain profile, that modulates the index $n_{\text{eff}}(z)$ and the grating period $\Lambda(z)$, causing side lobes to appear on both sides of the Bragg wavelength (Fig. 1(b)). The side lobe separation $\Delta\lambda$ and reflectivity η, also known as efficiency, can be controlled by the frequency f and power P of the acoustic wave, respectively.

In single mode fibers (SMFs) the most acoustic power is located in the cladding, which reduces the overlap with the fiber core where the acousto-optic interaction occurs. To increase η, cladding etching and tapering techniques have been applied to reduce the fiber diameter [1]. However, the diameter reduction affects the mechanical stability and makes the optical properties more susceptible to surface contamination.

In this work, the acousto-optic effect is numerically investigated for a suspended core fiber (SCF) [4]. By investigating the modal and mechanical fiber properties, as well as the grating properties, we verified that the efficiency η can be increased compared to standard fibers by changing the fiber design and still keeping the cladding diameter.

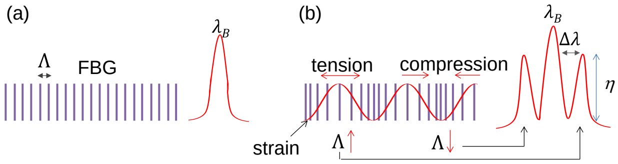

Figure 1: Behavior of fiber Bragg grating (a) without and (b) with longitudinal acousto-optic modulation.

METHODOLOGY

The investigated SCF fiber is composed of 3 air holes and geometric parameters described in [4]. For comparison, a SMF with same outer diameter of $D = 125$ µm and $d = 8.2$ µm core diameter is calculated. The fiber length and the FBG length is 25 mm in both cases.

The acoustical excitation is applied at the fiber end using a force of $F = 1.225\times10^{-4}$ N and a frequency $f = 1.091$ MHz. For the SCF, the force F is only applied on the incircle diameter area d. To study the effect of the bridge thickness on the efficiency η, SCF samples of bridge thickness $t = 180$ nm, 1080 nm and 1440 nm are designed. The incircle core and the air hole diameters are kept constant.

The finite element method (FEM) is used to calculate the effective index n_{eff} of the fundamental mode. The methodology to evaluate the strain induced by the acoustic wave is described in [2]. The FBG spectrum is simulated using the transfer matrix method [3] considering an initial grating of index modulation $\Delta n_{ac} = 10^{-4}$, reflectivity $R \sim 99\%$ and a Bragg wavelength centered at $\lambda_B = 1550$ nm.

RESULTS

Fig. 2(a)-(c) show the SCF cross sections with the fundamental mode intensity distribution for the investigated samples.

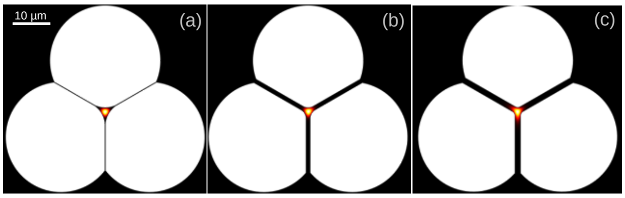

Figure 2: SCF cross section with the fundamental mode intensity distribution for the bridge thickness values of (a) t = 180 nm, (b) 1080 nm, (c) 1440 nm.

Fig. 3 compares the modulated FBG side lobe spectra of the SMF and the SCF for t = 180 nm and 1440 nm samples. The increase of efficiency η varies between 4.7% and 5.4%, respectively. Fig. 4(a) shows the efficiency variation. The efficiency increase is related to the increase of the effective index as shown in Fig. 4(f). For the 1440 nm bridge thickness, an increase of the confinement factor is also observed in Fig. 4(b). The strain decrease in Fig. 4(c) is due to the increase of the amount of silica in the cladding when the bridge thickness is increased (Fig. 4(d)). Although for thinner bridges the strain contributes to larger efficiency η, the optical effect is predominant on the mechanical effect for the investigated SCFs.

Fig. 3 shows that the SCF also produces a larger $\Delta\lambda$ than the SMF. The dependence of the wavelength shift is shown in Fig. 4(e). The decrease of $\Delta\lambda$ is due to the larger effective index when the bridge thickness is increased, as shown in Fig. 4(f).

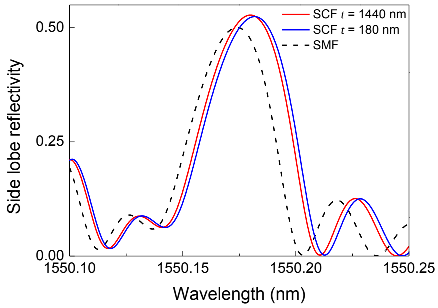

Figure 3: Modulated FBG side lobe spectra for t = 180 nm and 1440 nm samples compared to SMF.

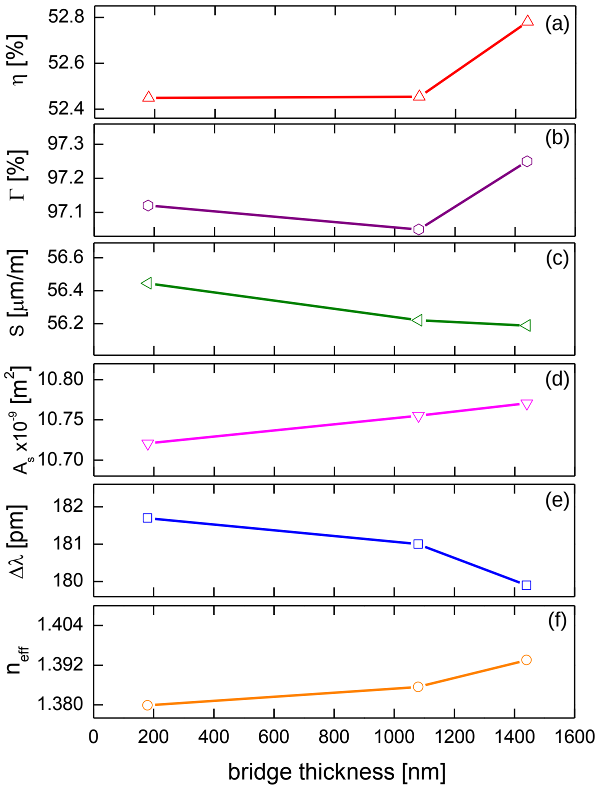

Figure 4: Variation of (a) side lobe efficiency η, (b) confinement factor Γ, (c) strain S, (d) fiber cross section silica area A_S, (e) Side lobe shift $\Delta\lambda$, and (f) effective index n_{eff} for the investigated geometries.

In summary, we have numerically investigated the optical and mechanical properties of FBGs in SCFs modulated by longitudinal acoustic waves. In particular, we studied the influence of the bridge thickness on the side lobe reflectivity and separation. As expected, the strain decreases with increasing bridge thickness. This effect is superimposed by an increased effective index of the guided mode with the Bragg grating. Compared to SMF the estimated increase of side lobe efficiency is 5.4%, which can be improved by increasing the air holes or by increasing the incircle core. Moreover, the SCF provides better mechanical stability compared to fiber taper techniques and protects the acoustic wave in the core, due to acoustical shielding by the cladding against external acoustic noise.

---

[1] W.F. Liu, P. S.-J. Russell, L. Dong, J. Light. Techn. **16**, 2006 (1998).
[2] R. E. Silva, M. A. R. Franco, P. T. Neves, H. Bartelt, and A. A. P. Pohl, Opt. Express. **21**, 6997 (2013).
[3] R.A. Oliveira, P. T. Neves Jr., J. T. Pereira, J. Canning, A. A. P. Pohl, Opt. Comm. **283**, 1296 (2010).
[4] A. Hartung, A. M. Heidt, and H. Bartelt, Opt. Express **19**, 12275 (2011).

Relativistic Frequency Synthesis of Light Fields

Erich Eckner[*1], Christian Rödel[1], Jana Bierbach[2], Matthew Zepf[2] and Gerhard Paulus[1]

[1] *Institut für Optik und Quantenelektronik, Max-Wien-Platz 1,*
07743 Jena, Germany

[2] *Helmholtz-Institut, Fröbelstieg 3, 07743 Jena, Germany*

[*] Corresponding Author: *erich.eckner@uni-jena.de*

Abstract

The conversion of an intense optical laser field into the XUV- and soft x-ray spectral range at solid density surface plasmas has attracted strong interest in the last decade. At relativistic interaction parameters, i. e. intensities $\gtrsim 10^{18}\,\mathrm{W\,cm^{-2}}$, high harmonic generation can be described by the model of the relativistic oscillating mirror (ROM). Recently, we have shown high conversion efficiencies in the order of $10^{-4} \ldots 10^{-6}$, which marks relativistic harmonic generation as one of the most promising routes towards attosecond pulse generation of unpreceded intensities. Here we report on relativistic frequency synthesis at plasma surfaces leading to the enhancement of particular harmonics with respect to their neighbours. Our experimental observations are substantiated by PIC simulations and a very intuitive analytic extension of the ROM model. We show that the enhancement is intrinsically connected to the relativistic nature of the surface motion, namely to the effect of retardation. This gives rise to a novel relativstic frequency synthesis in the XUV range utilizing relativistic nonlinearities.

INTRODUCTION

High harmonic generation by reflecting optical light from relativistic surface plasmas has been identified to be one of the most promising routes for the generation of intense attosecond pulses [1]. The generation of harmonics is described by the relativistic oscillating mirror (ROM) [2, 1] model as a reflection of the incident light at the oscillating plasma surface. So far, the ROM harmonic spectra observed in the experiments show a monotonic spectral decay as predicted by the ROM mechanism [3, 4] assuming a surface oscillation, for instance, with the laser frequency ω_L and $2\omega_\mathrm{L}$. We observed, however, a strong enhancement of particular harmonics at interaction parameter which are close to the ideal mirror case of a step-like density profile. An intuitive extension to the analytical trajectory in the ROM model can reproduce the spectral characteristics in the reflected field [5] which are corroborated by particle-in-cell (PIC) simulations.

EXPERIMENTAL OBSERVATION OF ENHANCED HARMONICS

In the experiments a frequency doubled[1] laser pulse (400 nm) is focussed onto a fused silica or plastic target up to relativstic intensities in the order of $10^{19}\,\mathrm{W\,cm^{-2}}$ under an incidence angle of 45° in p-polarization. At the rising slope of the pulse the solid surface is almost totally ionized. Hence, the laser pulse mainly interacts with an electron plasma with the initial electron density $n_\mathrm{e} \approx 100 n_\mathrm{c}$ in the case of fused silica or $n_\mathrm{e} \approx 50 n_\mathrm{c}$ in the case of plastic, respectively. Hereby, n_c denotes the critical electron density, at which plasma oscillations are in resonance with ω_L. Since light is propagating only in underdense plasmas ($n_\mathrm{e} < n_\mathrm{c}$), the laser gets reflected at the plasma surface.

The reflected light containing the high harmonic radiation is then measured by a flat-field or an imaging XUV spectrometer. Additional to the well known decay of the ROM harmonics we have observed an enhancement of particular harmonics at $2\omega_\mathrm{P}$ and $2\omega_\mathrm{P} \pm 2\omega_\mathrm{L}$. Here, $\omega_\mathrm{P} = \sqrt{\frac{n_\mathrm{e} e^2}{\varepsilon_0 m_\mathrm{e}}}$ is the natural frequency of a plasma oscillation at the electron density n_e.

---

[1] The frequency doubling guarantees low ASE- and prepulse intensities, such that the main pulse interacts with a steep plasma density profile.

RELATIVISTIC FREQUENCY SYNTHESIS

The oscillation of the electron plasma is driven by the forces of the electric and magnetic field of the laser. Thus, the surface oscillates periodically at frequencies $n\omega_{\mathrm{L}}$ with $n \in \mathbb{N}$. In PIC simulations matching our laser plasma parameters a strong surface oscillation at ω_{L} and ω_{P} is observed. For modelling the ROM harmonic spectrum we thus assume a surface trajectory consisting of only these two frequencies.

For a given surface trajectory

$$x(t) = \frac{a_{\omega_{\mathrm{L}}}}{\omega_{\mathrm{L}}}\sin(\omega_{\mathrm{L}} t + \varphi_{\omega_{\mathrm{L}}}) + \frac{a_{\omega_{\mathrm{P}}}}{\omega_{\mathrm{P}}}\sin(\omega_{\mathrm{P}} t + \varphi_{\omega_{\mathrm{P}}}) \quad (1)$$

the reflected field $E_{\mathrm{r}}(t)$ is connected to the incident field $E_{\mathrm{i}}(t)$ via

$$E_{\mathrm{r}}\left(t + \frac{x(t)}{c}\right) = E_{\mathrm{i}}\left(t - \frac{x(t)}{c}\right)\chi\left(\frac{\dot{x}(t)}{c}\right). \quad (2)$$

Here, the amplitude modulation $\chi(\beta) = \sqrt{\frac{1-\beta}{1+\beta}}$ takes photon number conservation into account. Due to the indirect and transcendent nature of the arguments of $E_{\mathrm{r/i}}$ the pure phase modulation is capable of generating harmonics from $x(t)$. This becomes clearer in the form

$$E_{\mathrm{r}}(t) = E_{\mathrm{i}}\left(t - 2\frac{x(t_{\mathrm{ret}}(t))}{c}\right)\chi\left(\frac{\dot{x}(t_{\mathrm{ret}}(t))}{c}\right), \quad (3)$$

where $$t = t_{\mathrm{ret}}(t) + \frac{x(t_{\mathrm{ret}}(t))}{c} \quad (4)$$

defines the retarded time $t_{\mathrm{ret}}(t)$.

The values of the oscillation amplitudes and phases in (1) can be obtained from the simulations. We show, that the ROM model including the oscillation at ω_{P} is able to reproduce the enhanced emission of harmonics at $2\omega_{\mathrm{P}}$ and $2\omega_{\mathrm{P}} \pm 2\omega_{\mathrm{L}}$. To investigate the origin of the enhanced harmonics, we analyze the influence of the retardation (4) on the harmonic spectrum. First, neglecting the retardation by using the approximation $t_{\mathrm{ret}}(t) = t$ in (3) leads to a steeper harmonic decay. Second, the enhanced harmonics appear at different frequencies, in contradiction to the experiment and simulation. Accordingly the effect of retardation is intrinsically connected to the appearance of the enhanced harmonics. This gives rise to a relativistic nonlinearity leading to a novel frequency synthesis in the XUV.

[1] G. D. Tsakiris, K. Eidmann, J. Meyer-ter-Vehn, F. Krausz, *New Journal of Physics* **8** (2006).

[2] R. Lichters, J. Meyer-ter-Vehn, A. Pukhov, *Physics of Plasmas* **3** (1996).

[3] J. Bierbach, *et al.*, *New Journal of Physics* **14**, 065005 (2012).

[4] C. Rödel, *et al.*, *Phys. Rev. Lett.* **109**, 125002 (2012).

[5] C. Rödel, *et al.*, *arXiv:1307.5635* (2013).

Diffusion and ballistic transport in non-Hermitian systems

T. Eichelkraut,[1] R. Heilmann,[1] S. Weimann,[1] S. Stützer,[1] S. Nolte,[1] A. Szameit[1]

[1]Institute of Applied Physics, Abbe Center of Photonics,
Friedrich-Schiller-Universität Jena, Max-Wien-Platz 1,
D-07743 Jena, Germany

*Corresponding Author: *Toni.Eichelkraut@uni-jena.de*

Abstract

We show that a rather sharp transition between ballistic and diffusive transport is present in *PT*-symmetric systems. This crossover depends solely on the gain-loss modulation. The theoretical predictions were experimentally verified utilizing an optical waveguide-array.

INTRODUCTION

Within the context of particle dynamics in low-dimensional systems, it is widely believed that the very structure of the system predetermines the transport regime, e.g. ballistic, diffusive, or localized. More specifically, it is assumed that the existence of randomness within the system is necessary in order to observe diffusive or even localized transport[1]. On the other hand, in the absence of randomness, the transport is always assumed to be ballistic[2]. On this account, our findings of observing a rather sharp transition between ballistic and diffusive transport in time-independent, ordered media is most surprising and counter-intuitive.

THEORY

In this work, we show theoretically and experimentally that in certain parity-time (*PT*) symmetric systems both transport regimes coexist, however on different time scales. The foundation for this paper was laid by the seminal work of El-Ganainy et al. in 2007[3], who introduced the concept of *PT*-symmetry within the context of optics, as well as the subsequent publication by Guo et al.[4], that elaborated on the equivalence between classical *PT*-symmetry and "quasi *PT*-symmetry". Our study was based on a *PT*-symmetric optical waveguide array exhibiting an alternating loss profile with homogeneous coupling between neighbouring waveguides, as indicated in Fig.1(a). Mathematically, the dynamics of such a structure can be described by an infinite set of coupled equations, which read

$$\begin{aligned} -i\partial_z a_n &= \delta_a a_n + \kappa b_{n-1} + \kappa b_n \\ -i\partial_z b_n &= \delta_b b_n + \kappa a_{n+1} + \kappa a_n . \end{aligned} \qquad (1)$$

Here, a_n and b_n represent the field amplitudes inside the lattice sites, κ is the coupling coefficient, and z is the longitudinal propagation direction. The waveguides exhibit alternating, complex propagation constants which are denoted by the respective values of δ_a and δ_b.

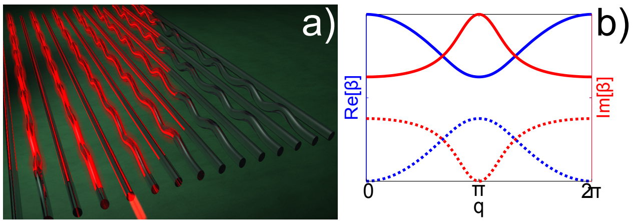

Figure 1: a) Schematic view of the waveguide array. Between every two straight waveguides there is one sinusoidally bend guide. b) Complex band structure of the array shown in (a). The upper band is depicted by solid lines, whereas for visualizing the lower band dotted lines were used.

The key-point of this study is that the coupling coefficients κ are equal between all waveguides, leading to so-called "broken" *PT*-symmetry[5] and, hence, a complex band structure, as indicated in Fig.1(b). To calculate the band structure, hence the relation between propagation constant β and transverse momentum q, the usual Ansatz $(a_n, b_n)^\top = \exp[i\beta z + inq](a_0, b_0)^\top$ was used. If one excites a single waveguide of such a structure, e.g., if $a_n(z=0) = \delta_{n0}$, $b_n(z=0) = 0$, initially all modes are excited and the evolution of the wavepacket is ballistic, as one would expect, which means that the variance increases quadratically with z. However, due to the imaginary part of the band structure the modes of the entire lower band decay. Additionally, also the modes in the upper band decay. Though, a small region around the mode whose eigenvalue possesses the smallest imaginary part decays slower, leading to a contraction of the wavepacket's spectrum. Due to this effect, for $z < 1/|\delta_a - \delta_b|$ the evolution is ballistic, whereas for $z > 1/|\delta_a - \delta_b|$ one can show that

$$a_n(z) \sim \exp[-n^2/(4wz)], \qquad (2)$$

where $w = \kappa^2/\Im\{\delta_a - \delta_b\}$. Consequently, the variance σ^2 of the wavepacket shows the diffusive spreading, which is essentially proportional to the first power of z, i.e., here we have $\sigma^2 = wz$. We emphasize that these dynamics cannot be achieved within any Hermitian system. In addition, even a more general PT-symmetric system is required to exhibit a non-trivial complex spectrum in order to show such a behaviour.

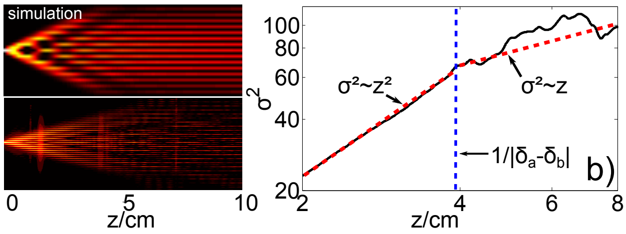

Figure 2: a) Comparison between simulation and experiment. b) Log-Log-plot of the dynamics of σ^2. The black curve visualizes the experimental data, whereas the dashed red line denotes the mean slope within both transport regimes. The transition point is depicted by the dashed blue line.

RESULTS & DISCUSSION

In order to probe the theoretical predictions experimentally, laser-written waveguide arrays inside fused silica were analysed. The deterministic losses within every second waveguide were introduced by sinusoidally bending these sites transverse to the lattice plane. In the experimental setup it was vigilantly ensured that the period of the sinusoidal bending was much smaller than the coupling length, in order to have an approximately homogeneous radiative loss along the propagation direction. As Fig.2(a) indicates, experimental results and theoretical predictions show an excellent agreement. The typical ballistic cone at small propagation distances as well as the subsequent "slower" diffusive spreading can be well observed via fluorescence measurements. A quantitative analysis of the evolution of σ^2 is presented in Fig.2(b). The double-logarithmic plot shows the two distinct regions with the respective slopes of $ln(\sigma^2) = 2ln(z)$ (ballistic) and $ln(\sigma^2) = ln(z)$ (diffusive). As mentioned above, the longitudinal transition "point" is approximately given by $z \approx 1/|\delta_a - \delta_b|$. Consequently, it can be solely tuned via the loss-detuning of the individual waveguides, i.e. the stronger the detuning is, the earlier the transition from the ballistic to the diffusive regime will be. In our experimental system, this was achieved by adjusting the period of the sinusoidal modulation and keeping the amplitude constant.

In conclusion, we present the experimental demonstration and theory of a rather sharp transition between ballistic and diffusive transport in PT-symmetric media. For our experiments, an optical waveguide array with modulated losses has been utilized. It is shown that the transition between both transport regimes depends solely on the gain-loss ratio.

References

[1] P.W. Anderson, "Absence of Diffusion in Certain Random Lattices," Phys. Rev. **109**, 1492 (1958).

[2] A. L. Jones, "Coupling of Optical Fibers and Scattering in Fibers," J. of Opt. Soc. of Am. **55**, 3 (1965).

[3] R. El-Ganainy et al., "Theory of coupled optical PT-symmetric structures," Opt. Lett. **32**, 17 (2007).

[4] A. Guo et al., "Observation of PT-Symmetry Breaking in Complex Optical Potentials," Phys. Rev. Lett. **103**, 093902 (2009).

[5] M. C. Zheng et al., "PToptical lattices and universality in beam dynamics," Phys. Rev. A **82**, 010103 (2010).

Black Holes and Revelations: on the Extraction of Optical Pulses from Cavities

Falk Eilenberger[1*], Irina Kabakova[2], Martijn de Sterke[2], Benjamin Eggleton[2], and Thomas Pertsch[1]

[1]Institute of Applied Physics, Abbe Center of Photonics, Friedrich-Schiller-Universität Jena, Max-Wien-Platz 1, 07743 Jena, Germany
[2]ARC Center for Ultrahigh-bandwidth Devices for Optical Systems (CUDOS), Institute of Photonics and Optical Sciences (IPOS), School of Physics, University of Sydney, New South Wales, 2006, Australia
[*]Corresponding Author: *falk.eilenberger@uni-jena.de*

Abstract

We present Cavity Optical Pulse Extraction (COPE) a novel scheme for the generation of ultrashort pulses from a CW excited Bragg cavity. The concept exploits a non-stationary perturbation of a resonantly enhanced harmonic field. We show COPE is based on a classical Event Horizon and derive a Hawking temperature.

INTRODUCTION

One of the most fundamental approximations of optics is stationarity; the notion that the environment of optical fields is static or changes slowly, if compared with time scales on which optical fields oscillate. This approximation leads to of one of the most powerful tools in optics: the harmonic field. Harmonic fields have a fixed wavelength and are eigensolutions of Maxwell's equations. They do not interact, as long as nonlinearity can be neglected.

The approximation is powerful because very few perturbations exist that can change the propagation environment of light fast enough, i.e. on the scale of femtoseconds, to go far beyond the adiabatic regime. Photonics itself, however, provides a mechanism to influence the propagation environment in a non-stationary manner: a strong, femtosecond trigger pulse (TP) acts like a non-stationary perturbation of the refractive index on a weak field [1].

In particular we show that the TP can efficiently extract photons stored in a Fiber-Bragg cavity, by a process which we call Cavity Optical Pulse Extraction [2] (COPE). The COPE mechanism can be exploited to generate ultrafast pulsed light sources in wavelength ranges that are otherwise inaccessible by broadband laser sources, such as the mid-IR. After discussion of properties of the COPE pulses and possible applications for this novel scheme of pulsed radiation, show that concepts developed for harmonic fields can be applied onto the non-stationary COPE field. This ansatz will lead us to an unexpected analogy: namely that the COPE process is analogous to the generation of electronic Hawking radiation [3] from primordial black holes, including hints on the assignment and measurement of a Hawking temperature in the COPE process.

FUNDAMENTALS

We conduct a numerical investigation of the propagation of light in a fiber Bragg grating, that is a Bragg cavity with a defect [4]:

$$\left[\pm i\partial_z + i\partial_t + \delta + 2\gamma P\left(z + v_g t\right)\right] A_\pm + \kappa\left(z\right) A_\mp = 0 \text{ ,(1)}$$

for $A_\pm(z,t)$, the COPE field amplitudes in forward (+) and backward $(-)$ direction. The frequency detuning $\delta = 2\pi(\lambda^{-1} - \lambda_\mathrm{B}^{-1})$ is the deviation of the inverse wavelength λ^{-1} from the Bragg resonance λ_B^{-1}, depending on the grating period Λ by $\lambda_\mathrm{B} = 2n\Lambda$. Here we assume resonant excitation ($\delta = 0$). The Bragg wavelength must match a CW laser source but is otherwise arbitrary. The grating itself is characterized by its coupling strength $\kappa(z) = \pi\Delta n(z)/\lambda_B$, proportional to the local, periodic refractive index modulation $\Delta n(z)$. The TP $P(z + v_g t)$ is counterpropagating through the COPE field and is a non-stationary refractive index perturbation mediated by cross phase modulation (XPM).

SOLUTIONS

Given a few technical assumptions we find analytic solutions to Eq. (1), describing the properties of the COPE field, extracted from the cavity by conversion of bound photons into propagating modes by XPM based side-band generation. The duration of the COPE field is almost equal to the duration of the TP and its power grows exponentially with cavity length and strength. It can be orders of magnitude larger than the CW excitation power. The dependence of the COPE power on the TP power is expressed by the clamping parameter $\alpha = L\kappa_0/\pi(P_0/\kappa_0)^2$. We find that for $\alpha < 1$ the COPE field has a near Gaussian shape and grows strongly with the applied TP power. For $\alpha > 1$ we, however, observe a constant output power and distinct pulse-splitting.

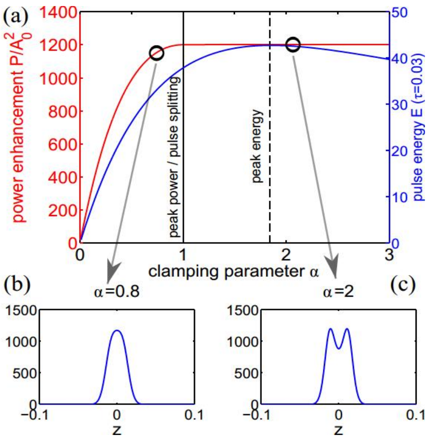

Figure 1: (a) Properties of COPE pulses vs. clamping parameter α (i.e. TP power P_0); (red) power enhancement and (blue) pulse energy. (b) Near-Gaussian shape of the COPE just before splitting point. (c) Double-peak shape of the COPE close above splitting at $\alpha = 1$.

STATIONARITY TRANSFORM

Being non-stationary, harmonic fields are not conserved in the COPE process, as is evident by the sidebands that make up the COPE pulse. In the frame of reference co-moving with the TP Eqs. (1) are, however, perfectly stationary, and harmonic fields are conserved. But the transformation mixes wavenumbers and frequencies and warps the dispersion relation of the system, as seen in Fig. 2.

In the co-moving frame cavity photons have the same frequency as unbound, propagating photons. The TP is a scattering potential, providing transverse momentum; scattering cavity photons into backwards moving photons. In the lab frame these have a new frequency.

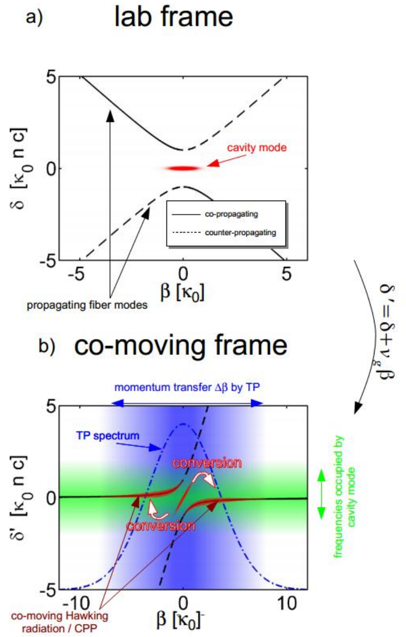

Figure 2: Dispersion relation of the COPE process in (a) the lab frame and (b) the co-moving frame. New wavenumbers due to scattering the stationary TP in (b) appear as new frequencies in (a).

EVENT HORIZON

We show that COPE is formally similar to the massive Regge-Wheeler process [5], describing the motion of particles in at a Black hole. Then we derive a Hawking temperature of

$$T = \frac{3.0 m_e c^2}{16\pi k_B \tau\kappa} = 3.6\cdot 10^{10}\,\mathrm{K}, \qquad (2)$$

for the COPE process, a finding which is backed up by the numerical measurement of COPE scattering rates, using coherent cavity modes [6].

---

[1] T. G. Philbin *et al.*, Science **319**, 1367 (2008).

[2] F. Eilenberger *et al.*, Scientific reports , [accepted] (2013).

[3] S. Hawking, Nature **248**, 30 (1974).

[4] H. Kogelnik and C. V. Shank, J. Appl. Phys. **43**, 2327 (1972).

[5] T. Regge and J. A. Wheeler, Phys. Rev. **108**, 1063 (1957).

[6] S. Weinfurtner *et al.*, Phys. Rev. Lett. **106**, 021302 (2011).

DPSK-based reach extension for $N\times$Gbit/s NG-PON

Ali Emsia*[1], Mohammadreza Malekizandi[1], Dieter Briggmann[1], Quang T. Le[1], and Franko Küppers[1]

[1] *Technische Universität Darmstadt, Institut für Mikrowellentechnik*
*und Photonik, Merckstarße,*64283 *Darmstadt, Germany*

*Corresponding Author: *emsia@imp.tu-darmstadt.de*

Abstract

In this paper we present a reach extension technique that can be used in th future Next Generation-Passive Optical network (NG-PON). We address to the high bandwidth demand, power budget enhancement, and the number of subscribers. Here, we consider Differential Phase Shfit Keying (DPSK). We demonstrate our experimental results for $12\lambda\times10$ Gbit/s/λ Wavelength Divsion Multiplexing (WDM) technology NG-PON. The reach extension techniqueis based on Semicondcutor Optical Aamplifier (SOA). We report 54 dB total optical power budget which enables different services for 512 users/λ.

INTRODUCTION

The increase in network traffic is anticipated to raise in the future [1]. The bandwidth demand of customers has evolved from ordinary telephone services to Internet, video, Web, online gaming applications, a few to be mentioned. To meet such a traffic demand is quite an effort, while reducing the cost of network deployments. The efforts with Next Generation Passive Optical Networks (NG-PON) are to increase the bit rate, the number of customers, the reach of the optical access networks, and to adapt it to the existing PON infrastructures. It is desirable to accommodate different services using a single platform in order to facilitate the network and reduce the related costs and Central Office (CO) footprint. This necessitates reach extension in PONs [2].

BUDGET EXTENSION CONFIGURATION

Fig. 1 illustrates the network architecture of hybrid TDM/WDM PON consisting of four main elements, 1) OLT, 2) Feeder line, 3) Power splitters and access lines and 4) ONUs. As depicted different wavelengths can be transmitted at the same time over a single optical fiber to various customers. Depending on the customers demand the connection could be either point-to-point or point-to-multipoint using power splitters (TDM trees).

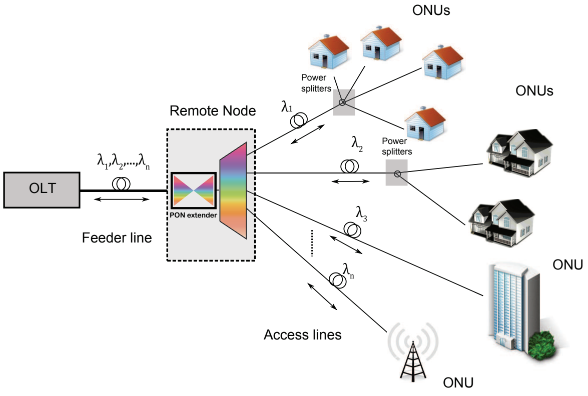

Figure 1: Hybrid TDM/WDM PON architecture.

In this paper, We demonstrate experimentally the optical power budget extension to 54 dB for downstream transmission. The SOA based SCA is comprised of Delay Line Interferometer (DLI) , two circulators, and a SOA. Fig. 2 shows the PON extender scheme which is placed in RN. The high input power at the input of SOA ensures that the amplifier operates in saturation regime. The outputs of circulators travel to the SOA from opposite sides, and experience the same gain. In this way, the low-level as well as high level signals get the same gain yielding an open eye.

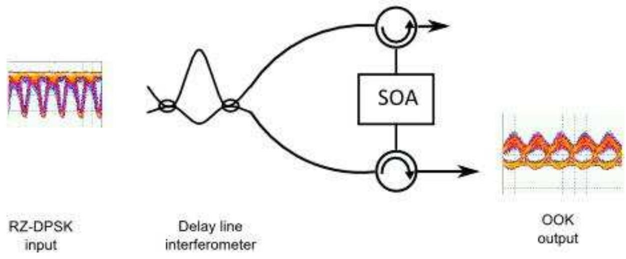

Figure 2: Saturated collision amplifier configuration.

EXPERIMENTAL SETUP

Fig. 3 exhibits the experimental setup. 2^{31}-1 PRBS is generated by PPG operated by Clk (Clock) at 10 GHz. .The remote node is the same as Fig. 4. The encoder converts the NRZ logic levels to RZ-DPSK. Twelve DFB lasers are at ITU grid wavelengths. The PCs are polarization controllers. The Mach Zehnder Modulator (MZM) are loaded from both sides to operate at push-pull, in order to increase the extinction ratio. The wavelengths are demultiplexed and multiplexed again to de-synchronize the data patterns on each wavelength. To reduce the pattern Mux and Demux (see Fig. 3) losses we used and EDFA after the multiplexer. Fig. 4 shows back-to-back BER measurements of 12 WDM channels. Assuming 10^{-3} (FEC limit), at 1550.89 nm the receiver sensitivity is -32 dBm. The optical power budget is 42 dB if the transmitter outputs 10 dBm.

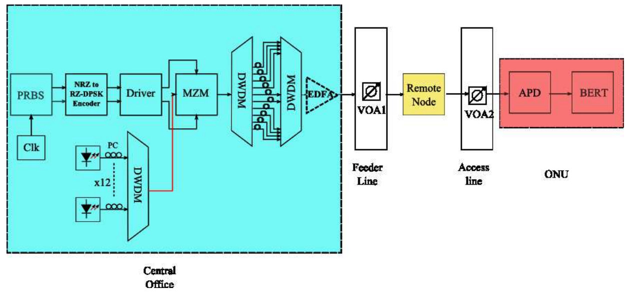

Figure 3: Saturated collision amplifier configuration.

In order to increase the power budget now the PON extender is considered into the setup. The SOA bias point was found to be optimum in terms of BER at 280 mA. Fig. 4 demonstrates the BER maps of the measured and results for downstream scenario back-to-back. The red dot shows access budget of 33 dB, 21 dBfeeder budgets.The measured BER map expresses 54 dB total optical power budget at 33 dB access budget and 21 dB feeder budget. this optical power budget enables transmission over feeder 70 km feeder line fiber ($\simeq$ 21 dB loss), 5 dB demultiplexer loss at the access line, 20 km access fiber (4 dB), and 256 customers (24 dB losses) . So, the configuration fits extensively well for XG-PON1 class N1 (29 dB), N2a (31 dB), N2b (31 dB), and E1 (33 dB). Furthermore, each channel support 512 users (assuming ouput of two circulators), we were able to transmit 12x10 Gbit/s , 12 channels simultaneously, which means 6144 clients having 10 Gbit/s data rate individually. thanks to the SCA configuration that remarkably increases the number customers in access networks.

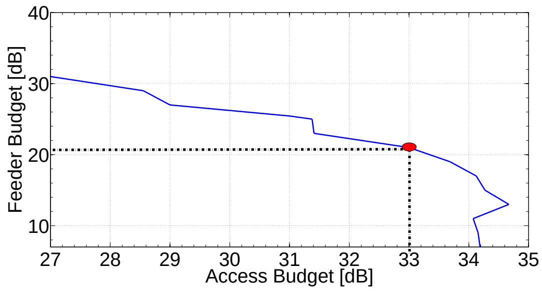

Figure 4: BER contours of measurement and simulation at 1556.55 nm.

CONCLUSIONS

We have presented a novel option for Nx10 Gbit/s WDM-PON power budget extension. We succeeded to boost the optical power budget 54 dB in DS back-to-back scenario. This optical power budget enables services to 6144 client in a WDM-PON. .We must mention that the power budget could be further extended using an extra SOA before DLI, while increasing the ASE noise.

---

[1] F. J. Effenberger, *The XG-PON System: Cost Effective 10 Gb/s Access*, JLT **29**, 403–409 (2011).

[2] A. Emsia, T. Q. Le, T. von Lerber, D. Briggmann, F. Küppers , *WDM-PON Upstream Budget Extension for 4x10 Gbit/s DPSK Directly Modulated Lasers*, Photonics Conference (IPC), IEEE , ME3 (2012).

Advanced experimental characterization techniques for plasmonic nanostructures

M. Falkner[1,*], E. Pshenay-Severin[1], C. Helgert[1], C. Menzel[2], C. Rockstuhl[2], F. Lederer[2], and T. Pertsch[1]

[1]Institute of Applied Physics and
[2]Institute of Condensed Matter Theory and Solid State Optics
Abbe Center of Photonics, Friedrich-Schiller-Universität Jena,
Max Wien Platz 1, 07743 Jena, Germany

[*]Corresponding Author: *Matthias.Falkner@uni-jena.de*

Abstract

We introduce a novel experimental scheme to characterize the transmission characteristics of optical metamaterials in amplitude and phase. The approach reveals all properties of the respective Jones matrix entirely on experimental grounds and was verified to be highly accurate. The presented Jones matrix formalism lifts issues associated with the assignment of effective properties to heterogeneous metamaterials and provides a straightforward, yet accurate description. Thus it is not required to resort on numerical simulations to disclose properties of metamaterials, for which the geometrical details of the considered structures or their material properties are often known with insufficient precision. We show how to discuss the pertinent properties of optical metamaterials once the Jones matrix is determined, and exemplarily present measurements of giant optical activity in a chiral metamaterial. The proposed experimental scheme enables the complex far-field characterization of a very broad class of generally dispersive and/or optically active media.

INTRODUCTION

The extraordinary optical behavior of artificial metamaterials is governed by the resonant nature of their constitutive elements. Recent developments in nanostructure technology enabled the fabrication of metamaterials composed of complex three-dimensional nanostructures [1]. This significant progress requires revising standard theoretical and experimental approaches for the characterization of optical properties of metamaterials. This holds particularly in the visible spectral domain where the mesoscopic size of the constituting nanostructures is not much smaller than the wavelength of light and the occurring strong spatial dispersion results in contradictive predictions when using the standard effective material parameters [2].

EXPERIMENTAL METHOD

Here we advance the experimental characterization of the far-field properties of optical metamaterials on the basis of an adapted Jones matrix formalism [3] which can disclose the transmission of light trough any optically active metamaterial by

$$\begin{pmatrix} E'_x \\ E'_y \end{pmatrix} = \begin{pmatrix} T_{xx} & T_{xy} \\ T_{yx} & T_{yy} \end{pmatrix} \begin{pmatrix} E_x \\ E_y \end{pmatrix}. \tag{1}$$

Since the four coefficients T_{ij} of the Jones matrix are in general complex-valued, interferometric measurements are necessary for their full experimental acquisition. For this purpose we developed a modified Jamin-Lebedeff-interferometer based on white-light Fourier-transform spectral interferometry in frequency domain (Fig. 1) which facilitates measurements of complex transmission and reflection coefficients for wavelengths from 600 nm to 1700 nm [4].

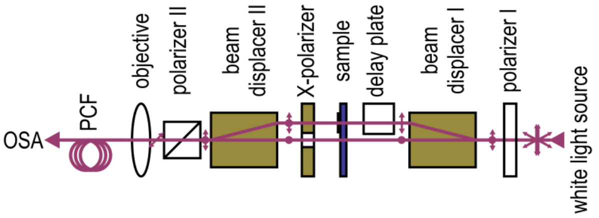

Figure 1: Sketch of the interferometric setup.

To measure the complex functions T_{ij}, a signal and a reference beam in the interferometer are cross-polarized, using birefringent crystals and polarization optics. The data acquisition comprises two measurements for each orthogonal polarization of the illuminating wave $[(E_x, 0)$ and $(0, E_y)]$ with the X-polarizer rotated to +45° or -45° with respect to the optical axis and relative to the incident polarization on the investigated sample and a known reference sample (Fig. 1). From this data, we can unambiguously access the absolute phase delay of each single coefficient of the Jones matrix. The accuracy of the method with respect to the optical phase delay was verified to be 20 mrad.

EXPERIMENTAL RESULTS

To demonstrate the strength of the approach, the method was applied to a chiral metamaterial composed of so-called loop-wire nanostructures [1] shown in Fig. 2a. The excellent agreement between the measured and simulated amplitudes and phases of T_{ij} is demonstrated in Fig. 2b-e.

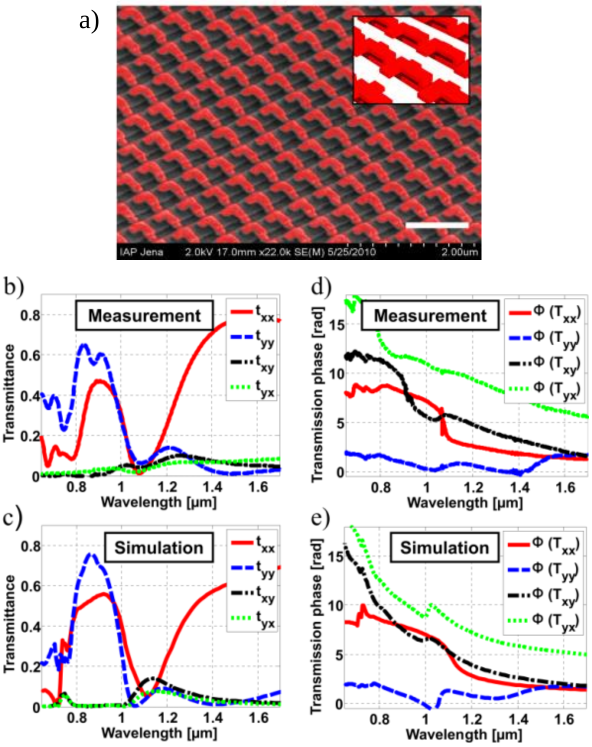

Figure 2: (a) False-colored, tilted view scanning electron microscopy image of the loop-wire metaatoms. The scale bar is 1 µm. The inset shows a corresponding sketch of the metaatoms without the supportive dielectric grating structure. (b) Measured and (c) simulated transmittances, (d) measured and (e) simulated transmission phase delays of the chiral nanostructured surface. The different colors indicate the four entries of the Jones matrix.

Thus, the developed experimental technique discloses for the first time the full complex transmission response for wavelengths from 600 nm to 1700 nm and allows for unambiguous quantification of, amongst others, circular dichroism, circular birefringence and polarization eigenstates of the chiral metamaterial across this broad spectral range. Specifically, the polarization output upon exciting the structure with an arbitrary input can be predicted immediately. It is shown that the fabricated loop-wire metamaterial exhibits giant optical activity for all wavelengths measured. Particularly, we found pure circular birefringence, i.e. a rotation of the polarization azimuth of linearly polarized light exceeding 50° at a wavelength around 1.08 µm. Normalized to the thickness of the metamaterial, this corresponds to a specific rotation of 3,3 • 10^5 °/mm which is, to the best of our knowledge, larger than that of any linear, passive and reciprocal medium reported to date.

CONCLUSION

In summary, we will present a novel interferometric scheme which allows for the direct measurement of the complex Jones matrix in the visible and near-infrared spectral domain, applicable not only to optical metamaterials, but rather to a very general class of dispersive media. The performance of the setup was demonstrated at a chiral metamaterial and reveals its giant optical activity.

[1] C. Helgert, E. Pshenay-Severin, M. Falkner, C. Menzel, C. Rockstuhl, E.-B. Kley, A. Tünnermann, F. Lederer, and T. Pertsch, Nano Letters **11**, 4400-4 (2011).

[2] C. R. Simovski, Optics and Spectroscopy **107**, 726-753 (2009).

[3] C. Menzel, C. Rockstuhl, and F. Lederer, Physical Review A **82**, 1-9 (2010).

[4] E. Pshenay-Severin, F. Setzpfandt, C. Helgert, U. Hübner, C. Menzel, A. Chipouline, C. Rockstuhl, A. Tünnermann, F. Lederer, and T. Pertsch, Journal of the Optical Society of America B **27**, 660 (2010).

Plasmonic Moiré Magnifier

Stefan Fasold*[1], Thomas Paul[2], Thomas Pertsch[1]

[1] Institute for Applied Physics, Abbe Center of Photonics,
Friedrich-Schiller-Universität, 07745 Jena

[2] Fraunhofer IOF, 07745 Jena

*Corresponding Author: *stefan.fasold@uni-jena.de*

Abstract

Moiré pattern are well known to be observable, e.g. in digital imaging, whenever two periodic structures do overlap each other. We will use this effect to magnify sub wavelength plasmonic structures and to make them visible in the optical domain.

Lord Rayleigh was the first person who described the Moiré pattern in 1874 [1] since this time a lot of groups exploited this topic. Especially in the 1960's and 1970's a lot of papers appeared ([1], [2]) and in the last years it was tried to use this approach to look at sub wavelength structures ([3], [4]).

In contrast to other imaging techniques like scanning near field microscopy, the application of Moiré patterns promises to process an entire sample in a single operation. No scanning is needed at all. Additionally the resolution of the Moiré pattern only depends on the accuracy of the production and measurement devices is not limited by the resolution limit.

However, the Moiré effect can only be exploited for periodically arranged structures, and the application to a single object is not possible.

PRINCIPLES OF MOIRÉ MAGNIFICATION

Moiré Effect. The Moiré effect is a special manifestation of the Alias effect and it appears whenever two periodic structures do overlap with each other. The first structure is usually referred to be the "structure grid" and the second one is called the "view grid".

Consider for example two one-dimensional transmission gratings with periods a_1 and a_2. When, in a simple picture, light consecutively propagates through both of these elements, then the transmitted light distribution will exhibit periodic features with a periodicity of:

$$a = \frac{a_1 a_2}{|a_1 - a_2|}$$

Thus, the difference between the periods a_1 and a_2 determines the magnification of the optical signal.

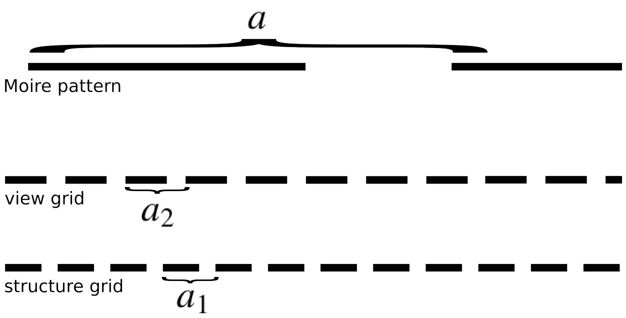

Figure 1: simplified picture of the Moiré effect; the system is illuminated from below and the Moiré pattern can be measured in the far field

Simulations Simulations were made by using the Fourier Modal Method for one dimensional gratings. Because of the big super period of the two gratings it is not possible to do simulations with two dimensional gratings in the same way.

First results are very promising and show Moiré pattern with an amplitude of 10% of the transmitted light over the complete visible spectrum.

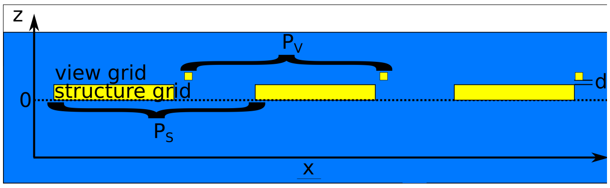

Figure 2: Simulation Setup, $P_S = 500nm$, $P_V = \frac{31}{30}P_S$, $d = 10nm$, $\lambda = 500 - 1000nm$

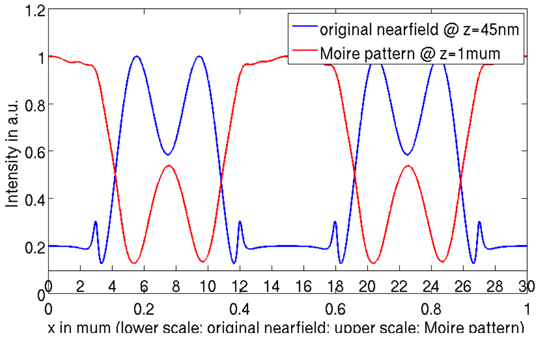

Figure 3: Near field of a single structure and the results from the Moiré simulation for a wavelength of 590nm. The Moiré pattern shows a magnification of 30 in comparison to the single structure.

The simulations and an easy theoretical model show that the possible resolution of this Moiré magnifier only depends on the size of a single structure of the view grid. By using more delta like structures in the view grid the resolution can theoretically be improved without limits. Unfortunately the amplitude of the Moiré pattern decreases when the view grid structure becomes smaller. In the simulations the chosen size for one view grid structure was 50nm. The results show near field features with approximately the same size. Additionally the near field is magnified by a factor of 30. By reducing the difference in the period arbitrary magnifications can be arrived.

Outlook The first structure of this kind is produced with electron beam lithography and some kind of Moiré pattern can be seen even with the bare eyes when a very small difference in the periods of structure and view grid is used. The next step is to characterize the optical properties and investigate whether the visible effects are actually the desired near fields of the structure and in which wavelength area the magnification device is working.
In conclusion the simulations show that the Moiré magnifier gives the possibility to directly observe the near field of any periodic structure and in a very broad wavelength area with classical optical elements and without the necessity to scan the sample.

---

[1] G. Oster, M. Wasserman, C. Zwerling, *Journal of the optical society of america* **54** (1964).

[2] R. McCurry, *Journal of Applied Physics* **37** (1966).

[3] Z. Liu, S. Durant, H. Lee, *OPTICS LETTERS* **32** (2007).

[4] D. Koller, U. Hohenester, A. Hohenau, *PRL* **104** (2010).

Towards Strong Coupling of Nanoantennas and Quantum Systems

Robert Filter, Karolina Słowik, Jakob Straubel, Carsten Rockstuhl, and Falk Lederer

Institute of Condensed Matter Theory and Solid State Optics, Abbe Center of Photonics Friedrich-Schiller-Universität Jena, Max-Wien-Platz 1, 07743 Germany

*Corresponding Author: *r.filter@gmx.de*

Abstract

The possibility to design optical near-fields using nanoantennas lead to incredible new possibilities to control light-matter-interactions, i.e. when coupled to quantum dots. In this contribution, the possibility to reach a strong coupling between nanoantennas and quantum dots will be discussed. We will futher outline the necessity to use a fully quantum description of the hybrid system obeying rich physical features. Our findings have direct consequences for next-generation quantum communication devices.

There is no doubt how nanoantenna-tailored light-matter interactions have influenced the physical sciences - groundbreaking applications have revealed the enormous potential of these devices. Nanoantennas are the tool of choice to mediate the interaction between light in the macroscopic and the nanoscopic world. In their usual setup, nanoantennas can be either operated as receivers or emitters; depending on the detailed properties of the nanoscale building block to which they are attached.

But the utilization of nanoantennas does not stop at this point. If for instance a quantum system is placed in the feed of a nanoantenna, the localization of modes can lead to a strong coupling of the quantum system to the nanoantenna as studied by Trügler and Hohenester [1] and Waks and Sridharan [2]. In such a setup, the nanoantenna acts as an active part of the system, not only as energy transmitter which enables fascinating new applications. Gonzales-Tudela et al. [3] i.e. discussed the use of nanostructures to weakly couple qubits and how this coupling changes the physical properties of the overall system.

Nevertheless, the surface of what is possible has just been scratched. Based on a recent study [4], we show how a carefully designed nanoantenna can be used to reach the strong coupling regime between two quantum systems. Our approach relies on a full description of the quantum and electrodynamic properties of the combined system. This self-consistent description is needed for the case of strong coupling. We suggest a particular nanoantenna design and show how to reach the strong coupling regime, see also Fig. 1.

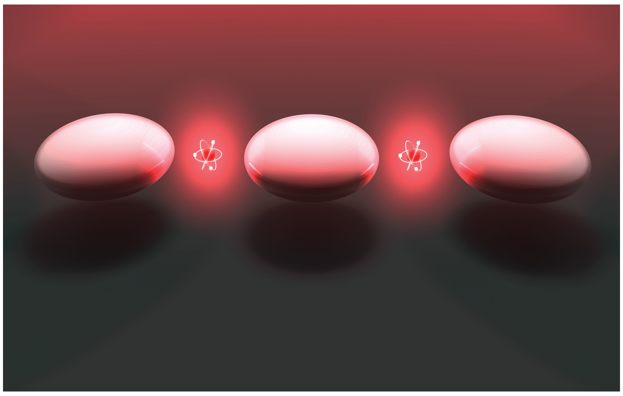

Figure 1: A general scheme of the considered hybrid system. A nanoantenna is strongly coupled to two atoms and excited by an external driving field.

The design is extremely powerful in several respects. First of all, due to the strong coupling, the energy states of the combined system are largely different to those of the bare quantum systems and can be engineered by the system's design. Second, the presence of the nanoantenna enables an efficient coupling to external fields. This enhanced coupling enables ultra-fast relaxation rates. Our work will thus help to engineer ultra-fast optical devices with tunable characteristics on the nanoscale.

We use the fully quantum description to predict changes in the experimentally observable spectra. Our contribution also renders the ambiguities obsolete on when to use a quantum or classical description: we derive a simple criterion to understand when a fully quantum approach is needed. We are also confident that the introduced thorough description of the electrodynamic and quantum mechanical properties of the combined system will hugely influence future developments of experimentally achievable quantum communication devices such as nonclassical light sources.

---

[1] A. Trügler, U. Hohenester, *Phys. Rev. B* **77**, 115403 (2008).

[2] E. Waks, D. Sridharan, *Phys. Rev. A* **82**, 043845 (2010).

[3] A. Gonzalez-Tudela, *et al.*, *Phys. Rev. Lett.* **106**, 020501 (2011).

[4] K. Słowik, R. Filter, J. Straubel, C. Rockstuhl, F. Lederer (2013).

Tunable magnetic dipole response of core-shell clusters

M. Fruhnert*, S. Mühlig, C. Rockstuhl, and F. Lederer

Institute of Condensed Matter Theory and Solid State Optics, Abbe
Center of Photonics, Friedrich-Schiller Universität Jena,
Max-Wien-Platz 1, 07743, Jena, Germany

*Corresponding Author: *martin.fruhnert@uni-jena.de*

Abstract

We investigate the magnetic response of meta-atoms amenable for a fabrication with bottom-up techniques. The meta-atoms consist of a dielectric core surrounded by a huge number of plasmonic nanoparticles. Contrary to the meta-atoms considered thus far, we study hollow plasmonic nanoparticles (shells) instead of solid spheres. With such building blocks we solve some of the most pertinent problems of self-assembled metamaterials, letting bulk negative index materials come in reach.

1 Introduction

A requirement for many applications from the field of metamaterials (MMs) and transformation optics is the availability of bulk materials that possess a strong response to the magnetic field in the visible and infrared (IR). Recently, it has been demonstrated that a magnetic response can be observed while relying on core-shell clusters [1]. These clusters consist of a dielectric core sphere covered by a huge number of plasmonic nanospheres forming a shell. At a particular frequency an effective current can be excited in the shell that oscillates around the core sphere, causing a scattered field that is identical to that of a magnetic dipole. The advantage of these core-shell clusters is their isotropic response when compared to ordinary meta-atoms such as split-rings or cut-plate pairs. Furthermore, these core-shell clusters can be fabricated by self-assembly techniques which allow to produce bulk materials at short time, large amounts, and low costs [2].

Here, we present a solution for the problem how to shift the magnetic dipole resonance of core-shell clusters to the near IR while maintaining their spatial dimensions. This is important to assure a smaller ratio of meta-atom size to operational wavelength which facilitates the homogenization of an eventual MM. To this end we exploit hollow metallic nanospheres in our novel meta-atoms. Our design reveals a magnetic response of a core-shell cluster with deep sub-wavelength dimensions. Moreover, the smaller radiation losses stipulated by the smaller size as well as the lower intrinsic absorption at near IR frequencies entail the opportunity to observe ultra strong resonances. This is a prerequisite to achieve a negative permeability of the MM. Although not shown here but shown at the DokDok conference, by extending the meta-atoms such that they sustain equally an electric resonance at the same frequency, we eventually achieve a negative index MM.

2 Core-Shell Clusters

It is well known that silver nanospheres posses a localized surface plasmon polariton (LSPP) at around 850 THz. This resonance can be shifted to smaller frequencies by considering silver nanoshells. They are characterized by an inner radius r_i and an outer radius r_a, as shown in Fig. 1a). The LSPP resonance frequency as a function of the shell thickness for a fixed outer radius r_a is shown in Fig. 1c). It can be clearly seen that the frequency down shift amounts to about 500 THz while increasing the inner shell radius from 0 nm to 14 nm. In the following we exploit such tunability to design deep sub-wavelength meta-atoms that posses a huge magnetic dipole response.

The referential design is a core-shell cluster with 60 nanospheres placed as sketched in Fig. 1b). The nanospheres have a distance of 77 nm from the center, a nearest neighbor distance of 4 nm, and a radius of 15 nm. They consist of silver, while the surrounding material is a dielectric with $\varepsilon = 1.7$. From Fig. 1d) it can be seen that the magnetic dipole response of these clusters is excited at 540 THz. The effective permeability was calculated with the Clausius-Mossotti equation

$$\mu_{eff} = \mu_s \frac{3 + \frac{2N\alpha}{V}}{3 - \frac{N\alpha}{V}}, \tag{1}$$

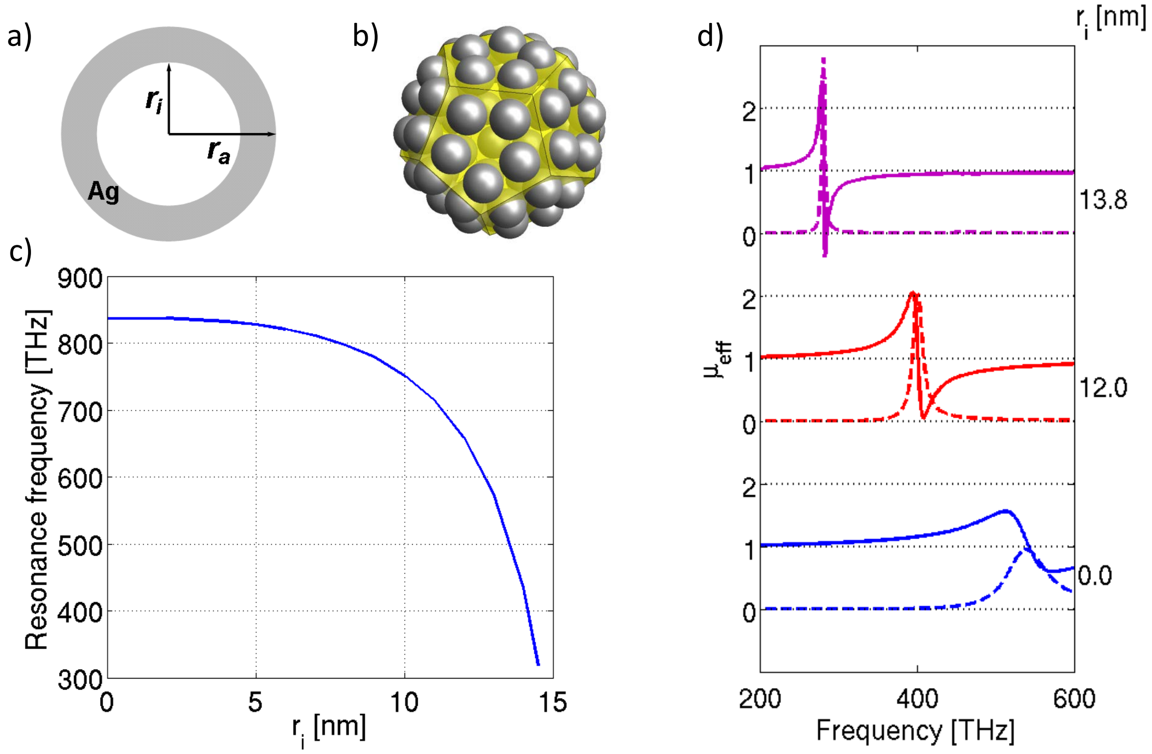

Figure 1: a) Sketch of a shell particle. b) Sketch of the core-shell structure. c) Resonance frequency vs. the inner shell radius r_i of a single silver shell with $r_a = 15$ nm. d) Effective permeability of core-shell structures with different inner radii r_i.

where $\mu_s = 1$ is the permeability of the environment, N is the filling fraction, V the volume of the unit cell, and α is the magnetic polarizability. The main idea now is to shift the resonance frequency of the polarizability to lower frequencies by using silver nanoshells instead of solid nanospheres to built the core-shell cluster. The magnetic response of shell particles with different inner radii is shown in Fig. 1d). Two effects are observed. First, the magnetic resonance shifts to lower frequencies into the IR. Second, the resonance features are sharpened if the resonance frequency is shifted to lower frequencies and eventually negative properties are observed.

We have shown that the magnetic response of core-shell clusters can be shifted to the IR regime by relying on silver nanoshells. The advantage is the reduced size of the cluster when compared to the resonance wavelength. In the best case this ratio is about 7 which can be considered as sufficient sub-wavelength.

3 Conclusion

A deep-subwavelength meta-atom that offers a strong magnetic dipole response has been designed. By starting from a core-shell cluster with a dodecahedron order for the shell nanospheres, this design has been further developed by considering nanoshells. It has been shown that the magnetic resonance can be tuned over a wide spectral domain while maintaining the spatial extent of the meta-atom. Although not shown here but shown at the conference, an extension of the meta-atom to let it to sustain an electric dipole response, allows to obtain a medium that supports backward waves, i.e. a negative index material.

---

[1] C. R. Simovski and S. A. Tretyakov, *Physical Review B* **79**, 045111 (2009).
[2] S. Mühlig *et al.*, *ACS Nano* **5**, 6586 (2011).
[3] C. Menzel *et al.*, *Optical Letters* **37**, 596 (2012).

Towards extreme ultra violet coherence tomography with high harmonic generation light sources

Silvio Fuchs*[1,2], Christian Rödel[1,2], Julius Biedermann[1], Martin Wünsche[1,2], Ulf Zastrau[1], Vinzenz Hilbert[1], Eckhart Förster[1,2], and Gerhard Paulus [1,2]

[1] *Institute of Optics and Quantum Electronics, Friedrich-Schiller University of Jena, Max-Wien-Platz 1, 07743 Jena, Germany*

[2] *Helmholtz Institute Jena, Helmholtzweg 4, 07743 Jena, Germany*

*Corresponding Author: *silvio.fuchs@uni-jena.de*

Abstract

We present a novel method for cross sectional imaging with nanometer resolution which is referred to as XUV coherence tomography (XCT). XCT uses extreme ultra violet light (XUV), e.g., from high harmonic generation (HHG). In XCT, the coherence length of few nanometers of broadband XUV sources is exploited. Thus, XCT extends optical coherence tomography (OCT) by improving the axial resolution from micrometers to nanometers. In a first step, we demonstrated XCT at synchrotron sources, successfully. Here, we present first results of an adaption of XCT using few-cycle laser driven HHG.

INTRODUCTION

Optical coherence tomography (OCT) is a well-established method to retrieve three-dimensional, cross-sectional images of biological samples in a non-invasive way using near-infrared radiation. The axial resolution of OCT is on the order of the coherence length $l_c \propto \lambda_0^2/\Delta\lambda_{\mathrm{FWHM}}$ which depends on the central wavelength λ_0 and the spectral width (FWHM) $\Delta\lambda_{\mathrm{FWHM}}$ of a light source. As a consequence, the axial resolution only depends on the spectrum rather than the geometrical properties of the radiation. OCT with broadband visible and near-infrared sources typically reaches axial (depth) resolutions in the order of a few micrometers [1].

However, in contrast, extreme ultra violet coherence tomography (XCT) takes advantage of the fact that the coherence length can be significantly reduced if broadband XUV and SXR radiation is used. XCT can display its full capabilities when used in the spectral transmission windows of the sample materials. For instance, the silicon transmission window (30-99 eV) corresponds to a coherence length of about 12 nm, thus suggesting applications for semiconductor inspection. In the water window at 280-530 eV, a coherence length as short as 3 nm can be achieved and highlights possible applications of XCT for life sciences.

XCT-SETUP

XCT utilizes a variant of a Fourier-domain OCT setup that completely avoids a beamsplitter [3, 4]. In the recent experimental setup broadband XUV light is focused on the surface of the sample. The reflected spectrum is measured either with a grating spectrometer, consisting of a gold transmission grating and a toroidal mirror (spectrometer-based OCT) [5], or with a photo diode (swept-source OCT) and a tunable source. The top layer reflection assumes the role of a reference beam. A Fourier transform including dispersion correction of the reflected spectrum needs to be computed for retrieving the structural information. A 3D image can be captured by scanning the focus over the sample.

XCT AT SYNCHROTRON SOURCES

Different samples containing silicon, gold, boron carbide, and platinum were successfully investigated with XCT at the synchrotron facilities DESY (Deutsches Elektronen-Synchrotron, Hamburg) and BESSY (Berliner Elektronenspeicherring-Gesellschaft für Synchrotronstrahlung) in the water and silicon transmission window. We found the expected values in resolution confirmed and we were able to record three dimensional images of buried nano-structures, see Fig 1.

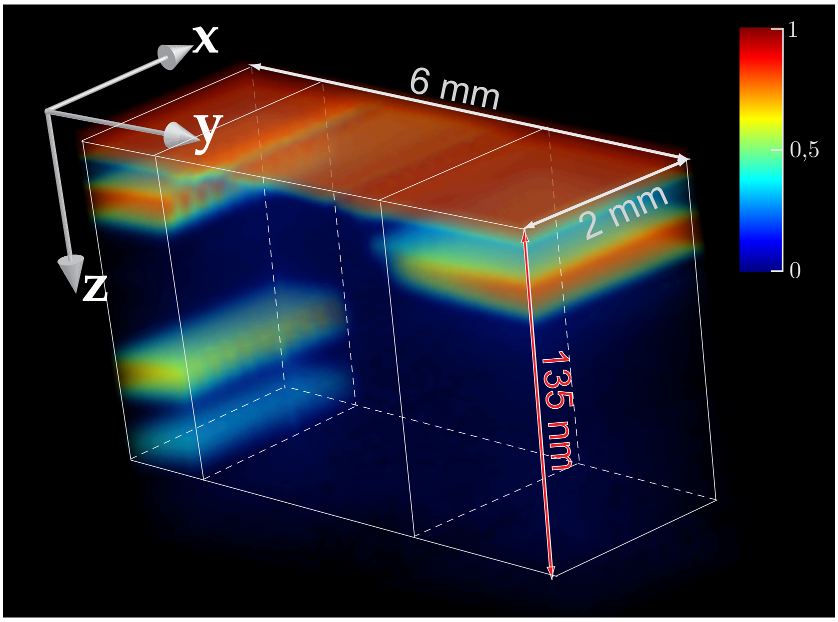

Figure 1: XCT scan of a volume that contains three different layer systems. The layer systems consist of thin gold layers buried and separated by silicon. The complete depth structure is reconstructed with an axial resolution of about 15 nm. The lateral resolution of this scan was limited by the spot size of the synchrotron focus to several hundred micrometers.

XCT WITH HHG SOURCES

Since XCT exploits the spectral broadness of the light source to achieve axial resolution it can be regarded as a perfect application for laser-driven HHG sources due to their intrinsic broad bandwidths. In fact, the bandwidth of HHG would have disadvantages for other imaging methods such as confocal microscopy or non diffractive imaging. In addition, HHG enables XCT to become a table top nanometer imaging technique. Here, we present first results of an adaption of XCT using few-cycle laser driven HHG.

In XCT, the depth information is contained in spectral modulations of the reflected light. Thus, the harmonic structure of HHG with multi-cycle laser pulses would superimpose and therefore weaken the modulations of the XCT signal. Hence, it is necessary to use few-cycle laser pulses to generate isolated attosecond XUV pulses with a broadband and smooth spectrum [6, 7]. First experiments to generate isolated attosecond pulses which fulfill the spectral requirements of XCT were performed.

---

[1] D.Huang et al., *Science* **254**, 1178-1181 (1991).

[2] W. Drexler and J. G. Fujimoto, *Optical Coherence Tomography* (Springer Verlag, Berlin, 2008).

[3] S. Fuchs et al., *Appl. Phys. B* **106**, 789-795 (2012).

[4] G. G. Paulus and C. Rödel, *Short-wavelength coherence tomography* (US Patent US 7,656,538 B2 2010)

[5] S. Fuchs et al., *Rev. Sci. Instrum.* **84**, 23101 (2013).

[6] G. Sansone et al., *Nature Photonics* **11**, 655-663 (2011).

[7] T. Popmintchev et al., *Nature Photonics* **4**, 822-832 (2010).

Fabrication of Freestanding Photonic Crystals in Lithium Niobate by Combining Focused Ion-Beam Writing and Ion-Beam Enhanced Etching

Reinhard Geiss*, Holger Hartung, Séverine Diziain, Michael Steinert, Frank Schrempel,
Ernst-Bernhard Kley, Thomas Pertsch, and Andreas Tünnermann

Institute of Applied Physics, Abbe Center of Photonics,
Friedrich-Schiller-Universität Jena, Max-Wien-Platz 1, 07743, Jena, Germany

*Corresponding Author: *geiss@iap.uni-jena.de*

Lithium niobate ($LiNbO_3$) is a material system widely used in nonlinear and integrated optics [1,2]. The growing interest in miniaturized optical systems, like photonic crystal (PhC) cavities, requires techniques to fabricate sub-micron structures in LiNbO3. Amongst others, ion-beam enhanced etching (IBEE) in combination with e-beam lithography has proven to provide high quality structuring of photonic micro and nano structures in $LiNbO_3$[3-7]. It relies on the reduced chemical stability of ion-beam irradiated $LiNbO_3$ that, as a result, becomes vulnerable to hydrofluoric (HF) acid [8-14].

For applications in fundamental research, on the other hand, the focus is on single devices and short processing times, which makes focussed ion-beam milling (FIB) an ideal tool. Now, the combination of both, IBEE and FIB, was successfully used to fabricate freestanding PhC structures as follows (Fig. 1): A piece of congruent, optical grade x-cut $LiNbO_3$ was irradiated with He ions with energies of 285 keV and a fluence of $5 \cdot 10^{16}\,\mathrm{cm}^{-2}$ at a temperature of 100 K. This irradiation leads to a buried damaged layer. At the last etching step this layer is selectively etched to form the air gap underneath the PhC membrane. After sputtering of a conductive Au layer, the $LiNbO_3$ was patterned by Ga-ion FIB milling. Subsequent wet etching with diluted HF acid (4%, 40°C for 5 min) now removed the buried damaged layer through the FIB milled holes, forming the final suspended PhC structure. In these structures, independent on feature size and shape, a systematic deviation of 20 nm from the original layout was found. It originates from the contamination of $LiNbO_3$ with Ga after FIB milling [15].

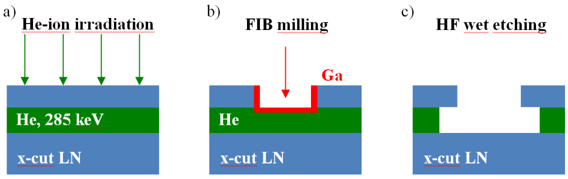

Figure 1: Schematic process flow of fabrication of photonic crystals by combining ion-beam enhanced etching and focused ion-beam (FIB) milling. a) Irradiation with helium ions of 285 keV energy. b) FIB milling with gallium contamination at the side walls. c) Wet etching in diluted hydrofluoric acid removes damaged material resulting in a freestanding patterned membrane.

During milling with 30 keV Ga ions, $LiNbO_3$ is sputtered and, at the same time, a layer of displaced atoms containing Ga forms at the surface. The thickness of this layer was calculated with the software SRIM [16] to be 17 nm, which is in good agreement with the observed deviations. The Ga has been detected with energy-dispersive X-ray spectroscopy (EDX) before the final HF etching. After the etching no residual Ga could be detected. It is therefore believed that the damage to the crystal structure induced by the Ga ions led to a reduced chemical stability, similar to the He ion irradiation, and to removal by wet etching. To ensure the required good crystalline, and consequently optical, quality of the $LiNbO_3$ after FIB patterning it is therefore essential to perform HF etching.

In conclusion, the combination of IBEE and FIB allows for PhC with hole diameters of down to 150 nm and membrane thicknesses of 300 nm. The optical characterization of such PhC cavities (Fig. 2) eventually showed resonances with Q-factors of several hundred according to the designed device performance.

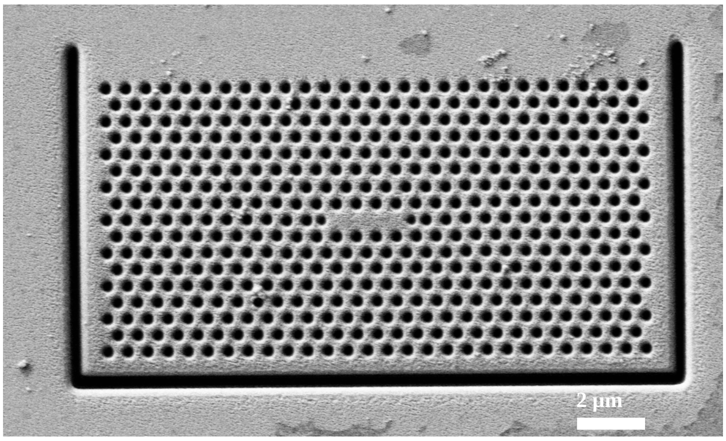

Figure 2: L3 photonic crystal cavity in a 400 nm thick $LiNbO_3$ membrane with conductive gold layer.

[1] L. Arizmendi, Physica Status Solidi A **201**, 253 (2004).

[2] F. Chen, Journal of Applied Physics 106, 081101 (2009).

[3] R. Geiss, S. Diziain, R. Iliew, C. Etrich, H. Hartung, N. Janunts, F. Schrempel, F. Lederer, T. Pertsch, and E.-B. Kley, Applied Physics Letters 97, 131109 (2010).

[4] H. Hartung, E.-B. Kley, A. Tünnermann, T. Gischkat, F. Schrempel, and W. Wesch, Optics Letters 33, 2320 (2008).

[5] H. Hartung, E.-B. Kley, T. Gischkat, F. Schrempel, W. Wesch, and A. Tünnermann, Optical Materials 33, 19 (2010).

[6] F. Schrempel, T. Gischkat, H. Hartung, T. Höche, E.-B. Kley, A. Tünnermann, and W. Wesch, Optics Letters 34, 1426 (2009).

[7] A. Sergeyev, R. Geiss, A. S. Solntsev, A. Steinbrück, F. Schrempel, E.-B. Kley, T. Pertsch, and R. Grange, Opt. Express 21, 19012 (2013).

[8] C. I. H. Ashby, G. W. Arnold, and P. J. Brannon, Journal of Applied Physics 65, 93 (1989).

[9] J. Reinisch, F. Schrempel, T. Gischkat, and W. Wesch, Journal of The Electrochemical Society 155, D298 (2008).

[10] F. Schrempel, T. Gischkat, H. Hartung, E.-B. Kley, and W. Wesch, Nuclear Instruments and Methods in Physics Research Section B 250, 164 (2006).

[11] T. Gischkat, F. Schrempel, T. Höche, and W. Wesch, Nuclear Instruments and Methods in Physics Research Section B: Beam Interactions with Materials and Atoms 267, 1492 (2009).

[12] T. Steinbach, F. Schrempel, T. Gischkat, and W. Wesch, Physical Review B 78, 184106 (2008).

[13] F. Schrempel, T. Steinbach, T. Gischkat, and W. Wesch, Nuclear Instruments and Methods in Physics Research Section B: Beam Interactions with Materials and Atoms 266, 2958 (2008).

[14] G. Götz and H. Karge, Nuclear Instruments and Methods in Physics Research 209-210, 1079 (1983).

[15] M. A. Draganski, E. Finkman, B. C. Gibson, B. A. Fairchild, K. Ganesan, N. Nabatova-Gabain, S. Tomljenovic-Hanic, A. D. Greentree, and S. Prawer, Diamond and Related Materials **35**, 47 (2013).

[16] J.F. Ziegler, J.P. Biersack, U. Littmark, The Stopping and Range of Ions in Solids, Pergamon, New York (1985)

Comparison of Electric Field Induced Second Harmonic (EFISH) in reflection and transmission from an oxidized silicon membrane

P.-C. Heisel*[1], G. P. Nyamuda[2], E. G. Rohwer[2], H. Stafast[1,2], and C. Steenkamp[2]

[1] *Institute of Photonic Technology (IPHT), Albert-Einstein-Str. 9,*
07745 Jena, Germany

[2] *Laser Research Institute (LRI), Department of Physics, University*
of Stellenbosch, Private Bag X1, Matieland 7602, South Africa

*Corresponding Author: *per-christian.heisel@ipht-jena.de*

Abstract

Comparative measurements of the electric field induced second harmonic (EFISH) from the Si/SiO$_2$ interfaces at the front (reflection) and the rear side (transmission) of thin silicon membranes are presented. EFISH in transmission shows a larger amplitude and faster kinetics than EFISH in reflection for the same fs laser irradiation of the sample. This contra-intuitive finding is rationalized by differences in the electron injection from Si into SiO$_2$ at both interfaces.

INTRODUCTION

Progressive miniaturization of semiconducting devices with silicon (Si) makes the characteristics of the oxidized surface increasingly important. They strongly depend on the charge carrier dynamics across the Si/SiO$_2$ interface. These are conveniently investigated by electric field dependent second harmonic (SH) generation as a contact-free tool [1].

During the past decades many studies on the second harmonic generation at the Si/SiO$_2$ interface have been performed in reflection [1]. In 2010 the first EFISH measurement in transmission of a thin Si membrane (about 10 μm) was presented by Nyamuda et al. [2].

EXPERIMENTAL SETUP

The presented measurements were performed with freestanding membranes of $4 \times 4\,\mathrm{mm}^2$ size and about 10 μm thickness produced by chemical etching of a slightly p-doped monocrystalline silicon wafer of $<100>$ orientation [2, 3]. After cleaning the sample using hydrofluoric acid, a natural oxide is grown within 48 hours to reach its equilibrium state.

The incident laser pulses originate from a commercial femtosecond laser system with pulse durations of (75 ± 5) fs and a repetition rate of 80 MHz at 800 nm wavelength. The light is focused on the sample to gain strong SH signals [3]. A scheme of the measurement geometry is shown in figure 1.

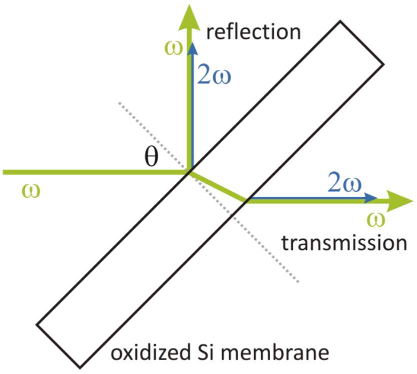

Figure 1: Scheme of EFISH measurements in reflection and transmission from a thin oxidized Si membrane

RESULTS AND DISCUSSION

Typical EFISH signals in transmission and reflection from a thin Si membrane and their temporal development are shown in figure 2 parts (a) and (b), respectively, for the same incident laser irradiation. Their temporal evolution reflects the changes of the quasi-static electric field E_{dc} across the Si/SiO$_2$ interface caused by laser induced electron injection. This field reaches equilibrium within about 20 minutes.

The incident fs laser light at 800 nm (1.55 eV) applied at high intensities allows electron excitation to the Si conduction band above the SiO$_2$ conduction band level via three photon absorption starting either from the Si valence band at the Γ-point or from the Si conduction band near the X-point (electrons from preceding laser pulse).

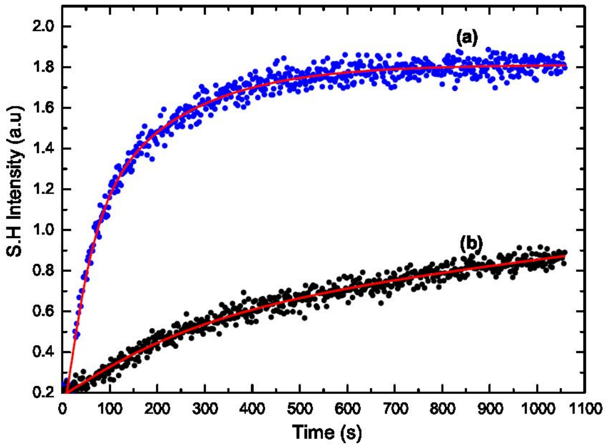

Figure 2: EFISH signal in transmission (a) and reflection (b) measured at a 10 µm silicon membrane with the same laser input power

The excited hot electrons in Si create ”image charges” in the SiO_2 at the opposite side of the interface (figure 3). For all charges an average distance d from the interface is assumed (vertical optical transitions). The resultant image force $F_{im} = \frac{Q^2}{16\pi\varepsilon_0\varepsilon_{eff}\cdot d^2}$ depends on the total charge Q of the electrons in the Si conduction band and the induced positive image charge which increase with the third power of the incident laser intensity. F_{im} furthermore depends on the effective permittivity ε_{eff} of the Si/SiO_2 system [4] and the average distance d. In a first approximation the Q values at both interfaces are equal as the estimated laser electric fields are nearly identical in this case. There are, however, differences in the effective d values: a displacement Δd is assumed by the momentum transfer from the absorbed photons onto the excited electrons. Due to different directions of the incoming laser beam with respect to the front and the rear interfaces of the Si/SiO_2 sample Δd affects d in opposite ways. This causes a larger force between the hot electrons and the image charges at the rear (r) side than at the front (f):

$$F_f = \frac{Q_f^2}{K\cdot(d+\Delta d)^2} < F_r = \frac{Q_r^2}{K\cdot(d-\Delta d)^2},$$

with $K = 16\pi\varepsilon_0\varepsilon_{eff}$. This equation shows, that hot electron injection from Si into SiO_2 becomes more efficient at the rear than at the front interface. Thus the quasi-static electric field E_{dc} across Si/SiO_2 builds up faster and larger at the rear side. Both effects are reflected in figure 2 by the EFISH signal development $I^{(2\omega)}(t) \approx \left|\chi^{(3)}\cdot E_{dc}(t)\right|^2 \cdot \left(I^{(\omega)}\right)^2$.

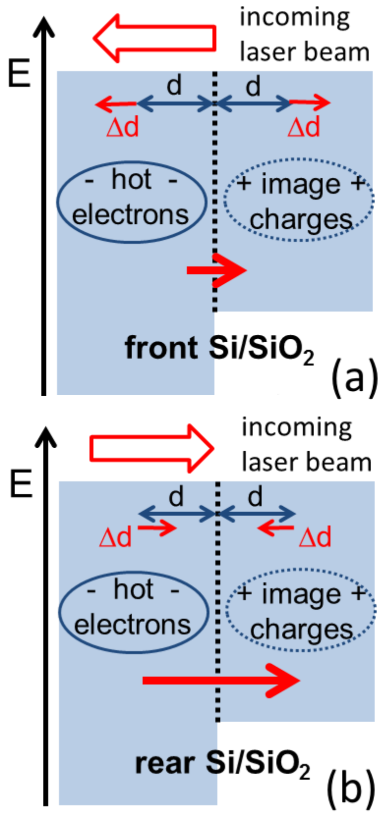

Figure 3: Schemes of the injection of hot electrons from Si into SiO_2 at the front (a) and rear Si/SiO_2 (b). The red arrows across the interface illustrate the image force F_{im}

---

[1] G. Lüpke, *Surface Science Reports* **35**, 75 (1999).

[2] G. P. Nyamuda, E. G. Rohwer, C. M. Steenkamp, H. Stafast, *Applied Physics B* **104**, 735 (2011).

[3] G. P. Nyamuda, *PhD thesis*, Physics Department, University of Stellenbosch, South Africa (2010).

[4] V. K. Adamchuk, V. V. Afanas’ev, *Progress in Surface Science* **41**, 111 (1992).

Drug detection using LOC-SERS technology

Izabella Hidi[1], Dana Cialla[1,2], Thomas Henkel[2], Karina Weber[1,2], and Jürgen Popp[*1,2]

[1]*Institute of Physical Chemistry and Abbe Center of Photonics,*
Friedrich-Schiller-University Jena,
Helmholtzweg 4, 07743 Jena, Germany

[2]*Institute of Photonic Technology (IPHT),*
Albert-Einstein-Strasse 9, 07745 Jena, Germany

[*]Corresponding Author: *juergen.popp@uni-jena.de*

Abstract

In the treatment of various diseases the determination of the effective and, at the same time, safe dosage of drugs still represents a challenge for the medical community [1]. Furthermore, drug interactions which imply the alteration of the effect of one drug by the presence of another concurrently administered can easily occur [2, 3]. In this contribution, we will present the determination of the limit of detection of epirubicin by means of Lab-on-a-Chip Surface Enhanced Raman Spectroscopy (LOC-SERS). Further studies will be carried out to detect the drug in body fluids.

INTRODUCTION

Epirubicin is an anti-cancer antibiotic administered alone or in combination therapy along with i.e. cisplatin and 5-fluorouracil [4]. During treatment, a high interpatient heterogeneity of drug plasma concentration was observed [5]. This, combined with the high number of on-going trials for optimizing the dosage for the achievement of the maximal therapeutic effect with minimal toxicity [6] requires the development of a fast and robust method for online monitoring of the drug concentration in body fluids.

Nowadays, the literature is overwhelmed by the optimization of various high performance liquid chromatography (HPLC) techniques [7] in order to detect biologically relevant molecules. One of the main disadvantages of this technique is that for every analyte a suitable eluent has to be found and an additional method has to be used for detection. To overcome all these drawbacks, in the last years, the LOC-SERS technology has gained the interest of the scientific community due to its molecular specificity and high sensitivity combined with a high throughput [8]. Usually, when it comes to SERS, the development of a reproducible substrate is of major interest. Even if the number of metallic substrates increases every year [8], the most cost effective is still the production of metallic nanoparticle colloidal solutions. By using these substrates in a droplet based microfluidic platform, the limitation of reproducibility of cuvette measurements is also overcomed [9].

METHOD AND RESULTS

The design of the microfluidic platform used during our measurements is presented in Fig. 1. The device offers the possibility to inject six different reagents. Among these, two ports are used for the SERS substrate and its activation agent . Through a third injector mineral oil is supplied. Therefore, a segmented flow is assured, resulting in a large number of independent and identical micro reactors. By using this microfluidic chip, reproducible dosing of analytes is provided by a computer controlled neMESYS Cetoni high performance syringe pump system. Furthermore, the efficient mixing is achieved by the two meandering channels. Accordingly, the same conditions are provided for every measurement. For detection, SERS is the method of choice. This technique was proven to offer high sensitivity and specificity for the detection of molecules of biological interest; being an important candidate for bioanalytical applications [8,10].

In conclusion, by combining the high sample throughput of the droplet based microfluidic platform with fast detection by means of SERS analysis, our method may be the technique of choice for future determination of drugs from biological fluids at therapeutic concentrations.

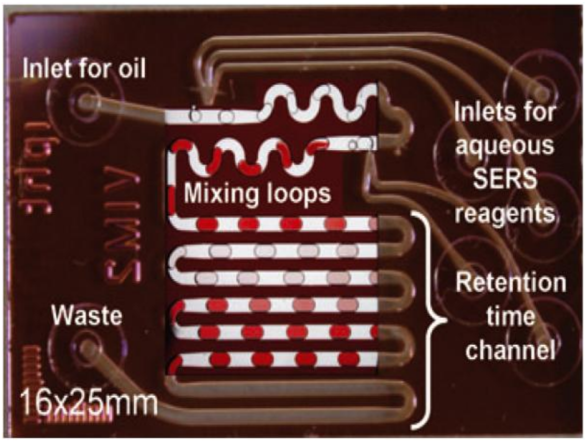

Fig. 1 Microfluidic chip with two phase liquid/liquid segmented flow profile.

ACKNOWLEDGEMENTS

For funding the PhD project of Izabella Hidi within the framework “Carl-Zeiss-Strukturmaßnahme” is gratefully acknowledged. The projects “QuantiSERS” and “Jenaer Biochip Initiative 2.0” within the framework “InnoProfile Transfer – Unternehmen Region“ are supported by the Federal Ministry of Education and Research, Germany (BMBF).

---

[1] H. Mu, R. Holm, A. Müllertz, International Journal of Pharmaceutics, 10.1016/j.ijpharm.2013.03.054.

[2] J. G. Bovill, Journal of Clinical Anesthesia **9**, 3S (1997).

[3] P. S. Kruger, N. M. Freir, B. Venkatesh, T. A. Robertson, M. S. Roberts, M. Jones, Intensive Care Medicine **35**, 717 (2009).

[4] J. M. Kirkwood, A. Tarhini, J. A. Sparano, P. Patel, J. H. Schiller, M. T. Vergo, A. B. Benson III, H. Tawbi, Cancer Treatment Review **39**, 27 (2013).

[5] F. Lachâtre, P. Marquet, S. Ragot, J. M. Gaulier, P. Cardot, J. L. Dupuy, Journal of Chromatography B: Biomedical Sciences and Applications **738**, 281 (2000).

[6] National Cancer Institute, ClinicalTrials.gov Identifier: NCT01624441.

[7] K. E. Maudens, C. P. Stove, W. E. Lambert, Journal of Chromatography B **879**, 2471 (2011).

[8] D. Cialla, A. März, R. Böhme, F. Theil, K. Weber, M. Schmitt, J. Popp, Analytical and Bioanalytical Chemistry **403**, 27 (2012).

[9] I. W. Sztainbuch, Journal of Chemical Physics **125** 124707 (2006).

[10] A. Walter, A. Mräz, W. Schumacher, P. Rösch, J. Popp, Lab on a Chip **11** 1013 (2011).

Entanglement generation in the vicinity of nano-structure

Jiamin Hou[*1], Karolina Slowik[1], Carsten Rockstuhl[1]

[1] *Institute of Condensed Matter Theory and Solid State Optics,*
Abbe Center of Photonics, Friedrich-Schiller-Universität Jena,
D-07743 Jena, Germany

[*] Corresponding Author: *jiamin.hou@uni-jena.de*

Abstract

It is interesting to explore the transfer of quantum states via light and matter interaction. Qubit-qubit interaction can be mediated via the field generated by the nano-structure and share a much stronger quantum correlation compared to the classical one. We show that maximally entangled qubit bipartite system can be obtained in the vicinity of nano-structure in our proposal.

INTRODUCTION

When the size of the metallic structures reduce down to the nano scale, they exhibit the ability to concentrate light into a very small volume, thus enhancing the interaction between its radiation field with quantum systems of size much smaller than the wavelength which are closely located around them.

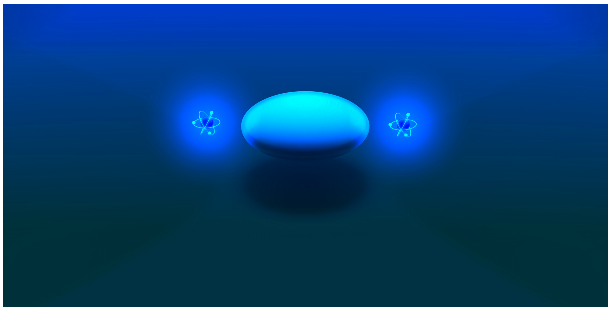

Figure 1: Qubit bipartite system in the vicinity of nano-particle.

For any composite system, entanglement arises when there exist pure states of the system in which the part of the system do not have pure states of their own[1]. Under the two-level approximation, these quantum systems are equivalent to the qubits used in the quantum information theory.

In the weak coupling regime, we are allowed to adiabatically eliminate the field generated by the nano-structure and the qubit bipartite system hybridizes to give a four level system (see Fig.2). Consequently, the two qubits start to get entanglement with each other. The dynamics of the reduced qubit system is governed by the Lindblad master equation, see Eq.(1).

$$\dot{\rho}_s = -i[\hat{H}_{\text{eff}}, \rho_s] + \hat{\mathscr{L}}_{\text{eff}}\rho_s. \tag{1}$$

$\hat{H}_{\text{eff}}$ is the effective Hamiltonian of the qubit bipartite system, while $\hat{\mathscr{L}}_{\text{eff}}$ is the effective Liouville operator. it consists of a modified free spontaneous decay rate γ of the qubit bipartite system and an interacting loss rate γ_{12}.

There are two different transition channels in the reduced bipartite system (see Fig.2): $|E\rangle \rightarrow |S\rangle \rightarrow |G\rangle$, decaying with an enhanced rate $\gamma + \gamma_{12}$ and $|E\rangle \rightarrow |A\rangle \rightarrow |G\rangle$ decaying with a reduced rate $\gamma - \gamma_{12}$. Two maximally entangled Bell states are formed: Symmetric state $|S\rangle = \frac{1}{\sqrt{2}}(|eg\rangle + |ge\rangle)$, and Antisymmetric state $|A\rangle = \frac{1}{\sqrt{2}}(|eg\rangle - |ge\rangle)$.

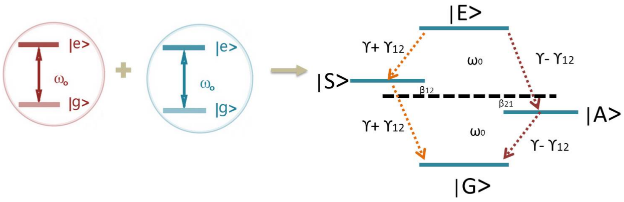

Figure 2: Hybridization of the system. Symmetric transition channel decays with an enhanced rate $\gamma + \gamma_{12}$ (super-radiant), antisymmetric transition channel) decays with a reduced rate $\gamma - \gamma_{12}$ (sub-radiant).

Concurrence is taken as the measure of degree of entanglement of the qubit bipartite system, defined as[1]:

$$C(\rho) = max\{0, \lambda_1 - \lambda_2 - \lambda_3 - \lambda_4\}, \tag{2}$$

with λ_i being the eigenvalues of $\sqrt{\rho_s \tilde{\rho}_s}$ in descending order.

NUMERICAL RESULTS

The specific geometry we consider here is a metallic nano particle (could be silver for example) of size $10nm \sim 1\mu m$, with loss rate Γ. Two qubits are located very close to it, with $|e\rangle$ being the excited state and $|g\rangle$ being the ground state, separated by transition frequency $\tilde{\omega}_0 = \frac{\omega_0}{\Gamma}$. They couple to the nano-structure with the normalized coupling strength $\tilde{g} = \frac{g}{\Gamma}$. An additional external driving field is given as $\tilde{\Omega} = \frac{\Omega}{\Gamma}$.

- **Two cases of entanglement generation**:

Two identical qubits :

When the two qubits are identical with each other, the antisymmetric state $|A\rangle = \frac{1}{\sqrt{2}}(|eg\rangle - |ge\rangle)$ is decoupled from the other three states. We start with the initial condition as one of the qubits being its excited state, and the other one being its ground state[2], then the probability antisymmetric state stays always a constant $P(|A\rangle) = 0.5$, as a result the concurrence can also reach as high as 0.5 as is shown in Fig.3.

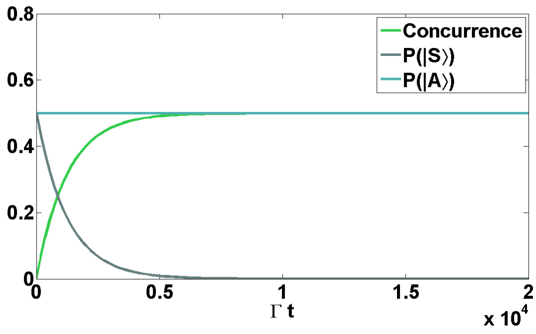

Figure 3: Entanglement generation, with initial condition $|e\rangle \otimes |g\rangle \otimes |0\rangle$. Coupling constant $\tilde{g}_1 = \tilde{g}_2 = 10^{-3}$, $\tilde{\Omega} = 0$. In this case, the antisymmetric state $|A\rangle$ is decoupled from the other three states and contributes to the concurrence.

Two non-identical qubits $\omega_1 \neq \omega_2$:

A more promising case is when we detune the transition frequency of the two qubits. As a result, the occupation probability of antisymmetric state $|A\rangle$ can be affected by the external drive through the coherence of the reduced system. Noticeably, the entanglement is accessible by the external driving field, furthermore, this concurrence generated in this scenario does not suffer from free space spontaneous decay.

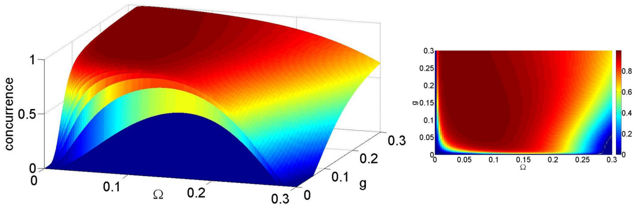

Figure 4: Maximal entanglement generation. Concurrence in the steady state as a function of coupling constant and the external driving field. Detuned qubits frequency: $\Delta\tilde{\omega}_1 = -\Delta\tilde{\omega}_2 = 10^{-3}$.

- **Observation and Detection of entanglement**:

We can analyse the state of the qubit bipartite system by plotting the wigner function of the field generated by the nano-structure. We observe that when the two qubits are maximally entangled, the field can be approximated as a coherent state $|\alpha\rangle$.

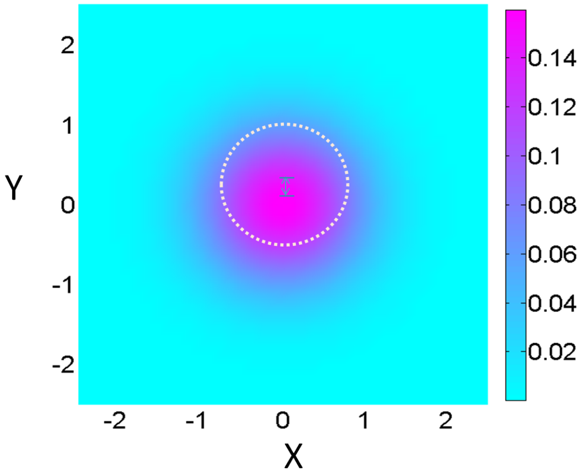

Figure 5: Detection of the entanglement. Wigner function of the photon state.

---

[1] W. K.Wooters, *Quantum Information and Computation* **1**, 27 (2001).

[2] Martín-Cano, *Physical Review B* **84**, 235306 (2011).

Lipophilic sensor layers for detecting Sudan dyes using surface enhanced Raman scattering

Martin Jahn[1], Dana Cialla[1,2], Karina Weber[1,2], and Jürgen Popp[*1,2]

[1]*Institute of Physical Chemistry and Abbe Center of Photonics,*
Friedrich-Schiller-University Jena,
Helmholtzweg 4, 07743 Jena, Germany

[2]*Institute of Photonic Technology (IPHT),*
Albert-Einstein-Strasse 9, 07745 Jena, Germany

[*]Corresponding Author: *juergen.popp@uni-jena.de*

Abstract

The fast and reliable detection of illegal food additives is a topic of great interest in life sciences. Here we present an approach for detection of the carcinogenic azo dye Sudan III based on surface enhanced Raman spectroscopy (SERS). As SERS substrate enzymatic generated silver nanoparticles with a lipophilic sensor layer are employed. The function of the lipophilic layer is to repel water-soluble substances from the surface. Thus, the remaining water-insoluble molecules can be separated and separately investigated by means of SERS.

INTRODUCTION

Sudan dyes belong to the group of azo dyes and are widely used for staining in industrial and scientific applications [1]. Due to their indirect carcinogenicity there use in food products is prohibited in the European Union. Nevertheless, due to the fact that in some countries these substances are still allowed as pigment in the food industry, there is a need for a fast and reliable testing method. The nowadays standard detection method consists of high-performance liquid chromatography (HLPC) combined with UV/VIS- or mass spectroscopy. The main drawback of this extremely sensitive technique is its high time expenditure.

Our aim is to develop a fast testing procedure for Sudan dyes and other water-insoluble substances based on surface enhanced Raman spectroscopy (SERS) [2,3]. SERS is our method of choice because it combines the high specificity of Raman spectroscopy with the signal enhancement induced by metallic nanoparticles.

Within this contribution, we present an approach using enzymatically generated silver nanoparticles (EGNPs) with a so called lipophilic sensor layer (LSL) for the detection of Sudan molecules by SERS. This layer is applied to prevent the agglomeration of water-soluble competitors originating from the sample matrix onto the surface.

SILVER NANOPARTICLES WITH A LIPOPHILIC SENSOR LAYER

A variety of top down and bottom up approaches was developed by many research groups to produce metallic nanostructures for SERS applications. By using electron beam lithography (EBL) almost every desired planar structure is realizable. However, the high technical effort which is associated with this method is disadvantageous for the planned low cost application. Thus, we are using enzymatically generated silver nanoparticles prepared by a fast and cost-efficient fabrication protocol for the Sudan detection. The EGNP fabrication is based on the

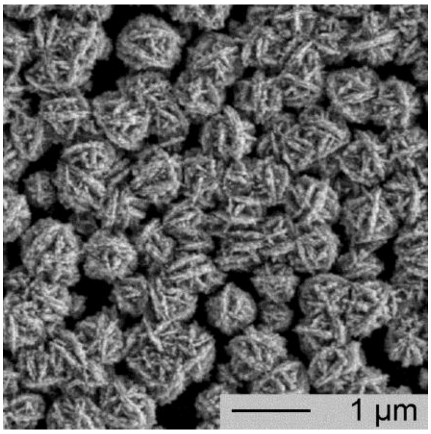

Fig. 1 SEM image of desert rose like enzymatically generate silver nanoparticles on a glass substrate.

enzyme mediated deposition of silver ions from a silver containing solution [4]. To immobilize the enzymes onto the substrates surface, biotin labeled oligonucleotides are used. Biotin molecules form a strong non-covalent bonding to the protein streptavidin which is connected to the enzyme. After enzyme immobilization, the silver deposition takes place which results in desert rose like silver particles (see Fig. 1).

For the extraction of Sudan dyes from real food samples often methanol or acetonitrile is used. To get rid of competing water-soluble substances, which are as well parts of the sample matrix, a so called lipophilic sensor layer is applied. This layer consists of hydrophobic hydrocarbons with a thiol group for creating bonds to the silver particles. By self-assembling processes a monolayer of these molecules is formed. Due to this layer, water-insoluble substances get repelled from the surface whereas water-insoluble molecules remain on it and are detectable via SERS.

DETECTION OF SUDAN III

In proof of principle experiments single substance solutions, containing Riboflavin or Sudan III, were used to demonstrate the operability of this system. Thereby, a remarkable decrease of the Riboflavin modes signal intensity was observed while applying the LSL. In contrast, the influence of the LSL on the Sudan III signal is much less.

In Fig. 2 reference SERS spectra of the pure substances are compared to spectra of a methanol based mixture of Sudan III and Riboflavin. For the reference spectra (black and grey lines) pure EGNPs without LSL were employed. The SERS spectra of the mixture are depending strongly on the kind of substrate which was used. On pure EGNPs typical Riboflavin modes are visible almost exclusively whereas the detection of Sudan III is impossible. In contrast, the spectra employing EGNPs with lipopophilic layers display Riboflavin as well as Sudan III modes. This proofs the usability of LSLs on SERS substrates for discriminating water-soluble and –insoluble molecules.

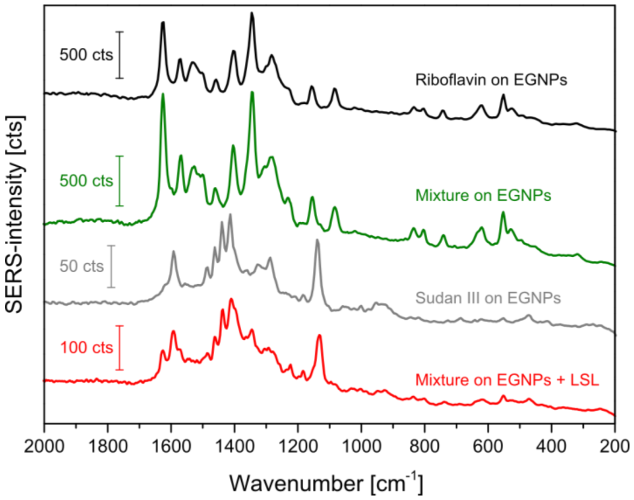

Fig. 2 SERS spectra of Riboflavin (black), Sudan III (grey) and the mixture of both substances (green) on pure EGNPs. The red line shows the SERS spectra of the analyte mixture on EGNPs with LSL for comparison.

The focus of our ongoing work is the application of the presented testing scheme for the detection of Sudan III in dye spiked food samples. Furthermore, different extraction techniques to get rid of unwanted water-insoluble substances from the food matrix need to be tested.

ACKNOLEDGEMENTS

Funding the research projects ‘QuantiSERS’ and ‘Jenaer Biochip Initiative 2.0’ within the framework ‘Unternehmen Region – InnoProfile Transfer’ by the Federal Ministry of Education and Research, Germany (BMBF) is gratefully acknowledged.

---

[1] R. Rebane, I. Leito, S. Yurchenko, und K. Herodes, Journal of Chromatography A **1217**(17), 2747 (2010).

[2] D. Cialla, A. März, R. Böhme, F. Theil, K. Weber, M. Schmitt, and J. Popp, Anal. Bioanal. Chem. **403**, 27 (2012).

[3] S. Pahlow, A. März, B. Seise, K. Hartmann, I. Freitag, E. Kämmer, R. Böhme, V. Deckert, K. Weber, D. Cialla, und J. Popp, Engineering in Life Sciences **12,** 131 (2012).

[4] K.K. Strelau, T. Schüler, R. Möller, W. Fritsche, and J. Popp, ChemPhysChem **11**, 394 (2010).

Blind reconstruction of Structured Illumination Microscopy (SIM) data

Aurélie Jost*[1,2], Anne Sentenac[3], and Rainer Heintzmann[1,2,4]

[1]*Institute of Physical Chemistry, Abbe Center of Photonics, Friedrich-Schiller University Jena, Germany*

[2]*Institute of Photonic Technology, Jena, Germany*

[3] *Fresnel Institute, Marseille, France*

[4] *King's College London, Randall division, United Kingdom*

*Corresponding Author: *aurelie.jost@ipht-jena.de*

Abstract

Structured illumination microscopy is a powerful biological imaging technique which necessitates elaborated processing. Here, we present a novel reconstruction algorithm which is robust against experimental imprecisions. We show super-resolution optically sectioned images of fluorescent labeled cells.

INTRODUCTION

Fluorescence microscopy is a valuable tool for biological research. Methods that enable nm-scale imaging are sought for. The resolution of a microscope is fundamentally limited by diffraction. It is convenient to describe the information content of an image in Fourier space. A microscope objective transmits the sample frequencies up to a given cut-off $\nu_{cut-off} = 2NA/\lambda$ with NA the numerical aperture of the objective and λ the wavelength. Higher frequencies (*i.e.* smaller details of the initial object) are lost.

Illuminating the sample with a fine pattern of light down-modulates high frequencies, making them accessible for detection. The structured illumination microscopy (SIM) method exploits this effect and achieves up to a two-fold resolution enhancement [1, 2].

IMAGING AND RECONSTRUCTION PROCESSES

In SIM, the measured image can be written as

$$I_{det} = (\rho \cdot I_{illu}) \otimes h \, , \qquad (1)$$

where ρ is the fluorophore density, I_{illu} the illumination pattern, $\otimes$ the convolution operation, and h the point spread function (PSF). In Fourier space, eq. (1) becomes

$$\tilde{I}_{det} = \left(\tilde{\rho} \otimes \tilde{I}_{illu}\right) \cdot \tilde{h} \, , \qquad (2)$$

where $\tilde{}$ represents the FT. The resolution improvement that follows from this principle is illustrated in Fig. 1(a). I_{illu} is typically a sinusoidal grating, so that $\tilde{I}_{illu}$ exhibits three peaks in Fourier space: the 0 and $\pm 1^{st}$ orders. In order to have as many measurements as there are unknowns, three raw images are acquired for three different lateral positions of the grating. The procedure is then repeated for two new orientations of the grating. The l-th grating is $I_{illu,l}$ for l=1..9 here.

The crucial role of the processing algorithm is therefore to reconstruct a super-resolution image out of this series of raw images. The classical approach consists of separating, shifting and recombining the orders in Fourier space (see Fig. 1b)). It requires knowledge of the grating positions and period. However, these experimental parameters are not always easily determined (aberrations, misalignments...), hence a potential for artefacts [3].

Recently, a novel reconstruction method (Blind-SIM) was introduced [4] which does not require prior knowledge of the grating parameters. The illumination pattern is therefore not limited to harmonic functions.

Both ρ and I_{illu} are estimated by minimizing

$$F(\rho, I_{illu}) = \sum_{l=1}^{L} || [\rho \cdot I_{illu,l}] \otimes h - I_{det,l} ||^2 . \qquad (3)$$

This cost functional is minimized alternately with respect to ρ and I_{illu}. Several constraints can be introduced to improve the performance of the algorithm.

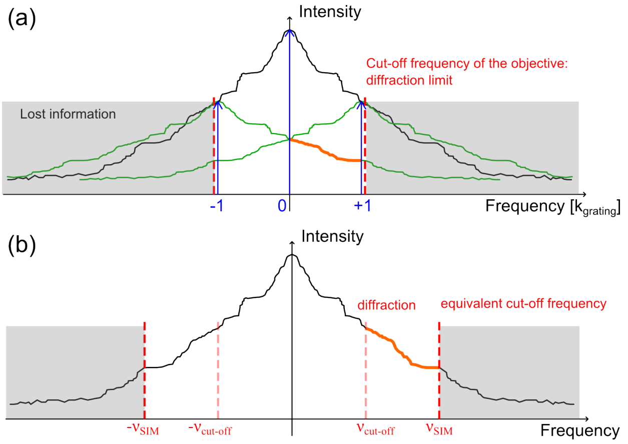

Figure 1: Resolution enhancement in structured illumination microscopy (SIM). (a) The convolution of $\tilde{\rho}$ (black) with $\tilde{I}_{illu}$ (blue) leads to new components (green). They are shifted so that new information is transmitted (orange). (b) After reconstruction (shift of the orange part), the equivalent pass-band is two times larger.

BLIND-SIM RECONSTRUCTIONS

Thin samples. To assess the performance of blind-SIM, we first reconstructed 2D simulated objects. The resolution of the results corresponded to theory, which validates the blind-SIM method. We also obtained successful reconstructions of samples illuminated by strongly distorted fringes. Blind-SIM also successfully reconstructed experimental data, *e.g.* from ultra-thin paxillin-labeled cells and samples illuminated in total internal reflection.

However, a requirement was that the sample should be very thin. If some light was coming from other planes than the focal one, as it is the case in thicker samples, the algorithm failed to reconstruct the high frequencies. This induced sophisticated (and not always biologically-relevant) sample preparation and reduced the field of application of the method.

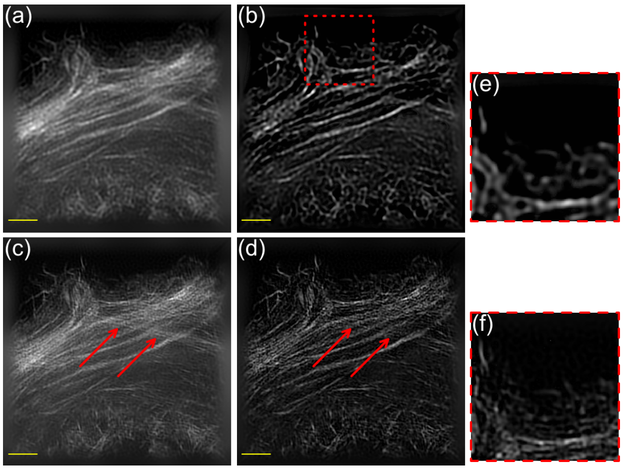

Figure 2: Experimental results using: (a) 2D Wide-field (WF) deconvolution, (b) 3D WF deconvolution, (c) 2D blind-SIM, and (d) *thick slice* blind-SIM. (b,d) The out-of-focus information (*e.g.* red arrows) is rejected. (e) Close-up of the dashed box in (b). (f) Close-up of the same region but in (d). Scale bar: 2 μm

Thick samples. We modified the blind-SIM algorithm so that it can reject the out-of-focus light in single-slice images of thick samples. For this, we performed the same deconvolution as described above, but using the 3D PSF and an extended stack of data. More precisely, the 2D data were placed in the center position of a stack where all other planes were empty. Due to the axial extent of the PSF, some information was added there during the deconvolution process.

Reconstructions of both simulated and experimental samples demonstrate that the *thick slice* blind-SIM algorithm achieves, as wanted, an optical sectioning effect as well as the expected super-resolution (Fig. 2). Data acquired on a commercial SIM microscope were reconstructed using both 2D and *thick slice* blind-SIM. The comparison between Fig. 2 (e) and Fig. 2 (f) provides an example of achieving super-resolution. The improvement of the *thick slice* implementation with respect to 2D-blind SIM is visible on the out-of-focus filaments indicated by the red arrows.

---

[1] R. Heintzmann, C. Cremer, *SPIE* 185 (1998).

[2] M. G. L. Gustafsson, *Journal of Microscopy* **198(2)**, 82 (2000).

[3] K. Wicker et. al., *Opt. Express* **21(2)**, 2032 (2013).

[4] E. Mudry et al., *Nature Photonics* **6(5)**, 312 (2012).

Effective photonic parameters from an eigenmode perspective

Thomas Kaiser*[1], Carsten Rockstuhl[2], and Thomas Pertsch[1]

[1] *Institute of Applied Physics, Abbe Center of Photonics, Friedrich-Schiller-Universität Jena, Germany*

[2] *Institute of Condensed Matter Theory and Solid State Optics, Abbe Center of Photonics, Friedrich-Schiller-Universität Jena, Germany*

*Corresponding Author: *thomas.kaiser.1@uni-jena.de*

Abstract

The concept of introducing effective parameters such as the 'effective index' to photonic structures will be reviewed. Examples include waveguides, fibers, gratings, holograms, metamaterials and other structures. An analysis based on electromagnetic eigenmode expansion uncovers the limits of such an approach and clarifies the range where such parameters can be considered as meaningful. In addition to the effective index, a parameter originating from electrical engineering is discussed which gains more and more importance in photonics – the impedance.

The 'index of refraction' of a certain material is the parameter of utmost importance in optics. As photonic structures became more and more complex, it became necessary to introduce an 'effective' index which describes the behavior of an entire device or structure rather than just a constituting material. Examples where such approaches are well known include waveguides, optical fibers, gratings, holograms, photonic crystals, and metamaterials. However, especially for the last mentioned class of photonic structures, the task of finding meaningful effective parameters has been proven to be subtle.

This leads to the question what is actually meant by an 'effective' index, what behavior of the structure should be predicted by it and how is it calculated?

Originally, the concept of an effective index allows a structure to be treated as if the optical properties of the structure were those of a material having exactly this index of refraction. If one knows for example the effective index of a single mode fiber, it is easy to choose the most efficient coupling lens by matching the numerical apertures. Neither the knowledge about the specific geometric details of the fiber (step-index, parabolic, PCF, …) nor the involved materials with their 'generic' indices of refraction are required for that task. The reason for this great simplification lies in the singlemode property of the fiber. The effective index appears in this context just as the propagation constant, renormalized by the free-space wavenumber, i.e., a property of the mode propagating in the fiber.

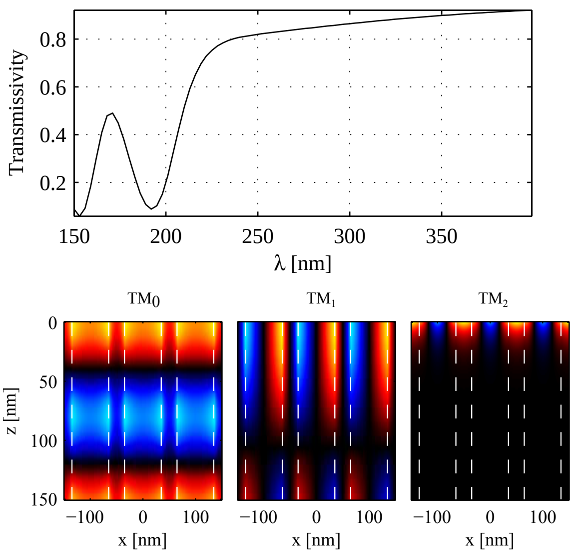

Figure 1: Upper: Transmission of an Al grating used as UV polarizer. Lower: Mode profiles of the grating modes at $\lambda = 193\,\text{nm}$.

What happens if the structure has more than one mode? In principle, every photonic structure has an infinite number of modes, but only few are usually of interest (in the above example only the guided fundamental mode). In a modal expansion,

$$\mathbf{E}(\mathbf{r},\omega) = \sum_l c_l\,\mathbf{E}_l(\mathbf{r},\omega)\exp\left[ik_0\, n_{\text{eff}}^{(l)} z\right], \qquad (1)$$

the effective indices may now gain imaginary parts if absorptive or radiative loss is present or the mode is

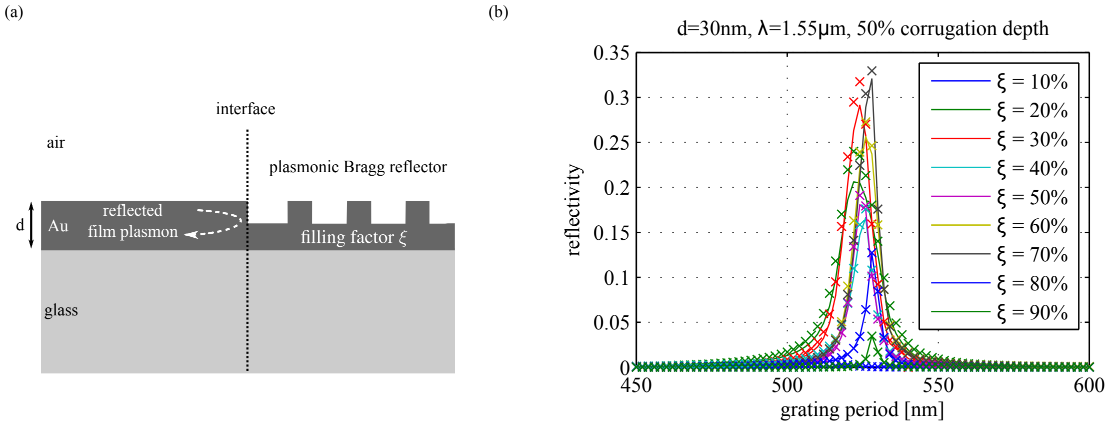

Figure 2: (a) plasmonic IMI waveguide terminated by a Bragg reflector. (b) reflection of the guided plasmon calculated rigorously (lines) and with the impedance concept (crosses).

evanescent, they might be folded into a band structure (if the structure possesses periodicity and $\mathbf{E}_l(\mathbf{r})$ has an explicit z-dependence) or they may have unusual signs (if metal nanostructures are involved as in so-called metamaterials). Additionally, if more than one mode plays a role, an effective medium description of the structure is not possible anymore.

Hence, two things are important for the decision if an effective medium description is possible: the 'nature' of the modes, and their excitation. Fig. 1 shows the transmission spectrum of an Al grating. Down to $\lambda \approx 220\,\mathrm{nm}$, the grating acts as polarizer and is well describable with effective medium theories. However, it can be seen that for wavelengths smaller than 220 nm, the transmission shows more complex features which do not fit into simple theories. The reason for this is can be found with a modal analysis, which reveals that this wavelength is the cut-off for the second order grating mode. It can propagate for lower wavelength whereas higher order modes cannot reach the bottom of the grating, shown also in Fig. 1. It is evident that the properties of the modes (especially their loss given as $\mathrm{Im}[n_{\mathrm{eff}}]$) is a key fact that determines if a mode needs to be considered or not. The second issue concerns the c_l and is if a mode is excited in a structure or not, which has to be determined analytically and also experimentally [1].

Apart from the effective index, electrical engineers use a second quantity to describe systems – the impedance. Its purpose is to characterize the coupling *between* two structures with a simple parameter in the same way the effective index describes the propagation *in* it. The surface Fresnel reflection for example can be expressed using impedances by

$$r = \frac{Z - Z_0}{Z + Z_0}. \tag{2}$$

If effective medium theories apply, the impedance is not really necessary in optics since $Z \sim 1/n$ and everything can be expressed using the (effective) refractive index. However, as structures become more and more sophisticated and effective medium theories start to fail, there is a desire to keep the concept and applicability of well-known relations as (2). The question is just how to generalize the impedance, which is simply the ratio E_0/H_0 for a simple plain wave, to hold for complex modes of sophisticated structures?

It was recently shown that this is possible based on an eigenmode expansion using unconjugated reciprocity [2]. Fig. 2 shows the results of this framework for the reflection of a Bragg reflector in an IMI plasmonic waveguide, which was conceptual impossible to describe before. The definition also reproduces former findings for specific structures (as free space, hollow core waveguides, photonic crystals or metamaterials) and applies to a very wide range of new plasmonic structures [3].

---

[1] T. Kaiser, D. Flamm, S. Schröter, M. Duparré, *Optics Express* **17**, 9347 (2009).
[2] T. Kaiser, S. B. Hasan, T. Paul, T. Pertsch, C. Rockstuhl, *Physical Review B* **88**, 035117 (2013).
[3] T. Kaiser, S. Diziain, C. Helgert, C. Rockstuhl, T. Pertsch, *CLEO: 2013* (2013), p. QW3N.3.

Laser induced damage threshold (LIDT) with fs-laser pulses

Helena Kämmer*[1], Felix Dreisow[1], and Stefan Nolte[1]

[1] *Institute of Applied Physics, Abbe Center of Photonics,*
Friedrich-Schiller University, Albert-Einstein-Straße 15, 07745
Jena, Germany

*Corresponding Author: *helena.kaemmer@uni-jena.de*

Abstract

The laser induced damage threshold was measured for Si wafer with ultrashort laser pulses. We examin the dependency of the threshold fluence on the pulse repetition rate.

INTRODUCTION

The improvement of existing and the development of new laser systems is always limited by properties of the optical components used. Therefore it is necessary to characterise these elements. One of the most important parameter is the so-called laser induced damage threshold (LIDT) which defines the threshold when damage starts to occure.

Commonly the measured data were collected with pulse length in the ns regime. In a large range of pulse durations one can scale the measured LIDT to the real LIDT by $\sqrt{\tau/\tau_M}$, where τ is the target pulse duration and τ_M the pulse duration where the measurement was performed. However, this law does not hold for ultra short laser pulses due to appearance of non-equilibrium effects and non-linear absorption.

In addition, one can expect a dependence of the LIDT on the laser repetition rate as observed e.g. for drilling experiments [1]. This has, however, not been investigated in detail so far. In order to investigate this dependence we have realised an automated setup according to ISO 21254 [2].

MEASUREMENT METHODS

LIDT is a statistical method where, depending on the choosen method, a selected number of spots N are illuminated with a specific number of pulses by keeping the pulse energy constant. For each energy one can calculate the propability of destruction P with the following equation:

$$P_i(K) = \frac{N_{idK}}{N_{iK}} \tag{1}$$

Therefore, one needs the number of spots N_{iK} which were illuminated with the same pulse energy, represented by the energy index i, and the same number of pulses K. N_{idK} accounts for the number of spots which were destroyed at these energies.

The ISO International Standard includes two different measurement methods to ensure the comparability and uniformity of the threshold values [2].

With the so-called 1-on-1 method one laser pulse is shot on one spot on the sample and one evaluates if this point is damaged. The measurement is done for several points with the same energy and followed by a stepwise increase or decrease of the pulse energy. It is required to scan energies from no damage to damage at every spot. According to [2] the minimum number of spots for one energy to have a reliable statistic is ten.

The second method, S-on-1, is an enhancement of the 1-on-1 method with an online detection of the destruction and a pulse counter. Instead of illuminating one sample spot with only one pulse it is illuminated with at maximum S pulses. That means it is detected after how many laser pulses each spot on the sample is destroyed till the upper limit of pulses S is reached. As soon as the spot is damaged or S is attained the measurement is stopped and one continues with the next spot. Finally one knows after how many pulses damage occured or if the sample is intact. Typically S=10,000 is used.

DETECTION METHOD

There are different methods to detect if the sample is damaged. An offline methode is to inspect the sample with a microscope after the measurement and to count the destroyed spots. Another method is the detection of scattered laser light. If the sample is damaged the surface roughness and thus the intensity of the scatterd light increases compared to an intact surface. Comparison with reference signal allows for detection of changes at the sample surface.

Irrespective of the measurement method or detection method it is necessary to proof the damage with differential interference contrast microscopy, also known as Nomarski microscopy [2]. Damaged parts are visible due to differences of the refractive index between the intact and damaged parts of the sample.

EXPERIMENTAL SETUP

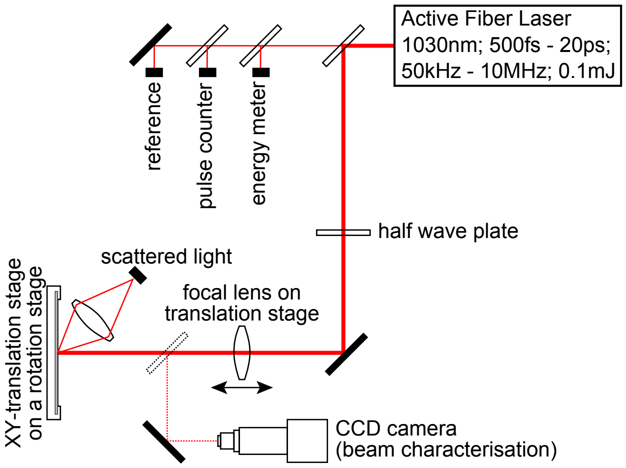

Figure 1: Schematic drawing of the LIDT measurement setup

Fig. 1 shows the experimental setup. The fiber laser used as source enables measuring S-on-1 LIDT at a wavelength of 1030nm, with a pulse duration between 500fs and 20ps, pulse repetition rate from 50kHz to 10MHz and an output energy up to 100μJ.

To ensure reproducibility and comparability the experimental conditions like spatial and temporal beam profile, output energy and number of pulses have to be monitored during the measurement. For this purpose a CCD camera, pulse counter, energy meter (Fig. 1) and an autocorrelator (not shown) are included in the setup.

The sample is mounted on a translation stage to enable movement in the plane perpendicular to the beam direction. A focusing lens (f=250mm) is used to achieve a small spot size (d=50μm) and therefore high laser fluences. It is mounted on a translation stage to adjust the longitudinal focus position to the sample. By rotating the sample measurements can be performes at a defined angle.

RESULTS

We examine the damage threshold of a Si wafer for different pulse repetition rates. The results are shown in Fig. 2 for a pulse duration of 500fs.

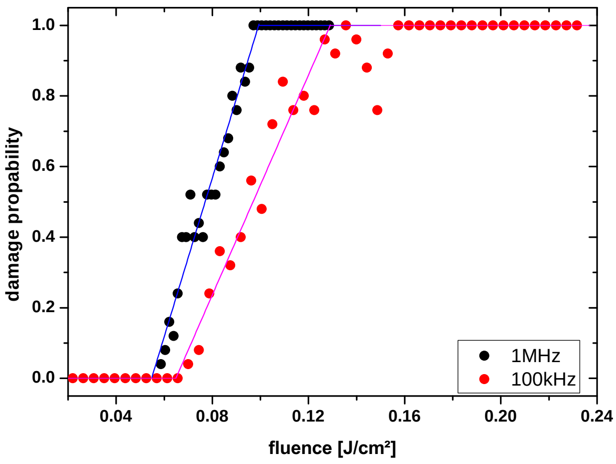

Figure 2: 10000-on-1 LIDT of a Si wafer for 100kHz and 1MHz pulse repetition rate

It is clearly visible that the zero propability threshold decreases from 0.0649J/cm^2 to 0.0549J/cm^2 for increasing repetition rate from 100kHz to 1MHz respectively. One explanation is the occurence of heat accumulation since pulses hit the sample in shorter intervalls and corresponding to that the damage threshold decreases. Another reason could be the existence of defect states with a lifetime in μs regime. Further measurements for different laser repetition rates and materials are planned to clearify the behaviour of the LIDT.

We acknowledge financial support from BMBF in the frame work of the project ScanLine.

---

[1] A. Ancona, F. Röser, K. Rademaker, J. Limpert, S. Nolte, A. Tünnermann, *Optics Express* **16**, 12 (2008).

[2] *Lasers and laser-related equipment - test methods for laser-induced damage threshold - Part 1 - Part 4*, DIN EN ISO 21254-1/2/3/4 (2011).

Field amplifying perfect absorber in the THz range

Richard Knipper [a,b], Uwe Hübner [b] ,Thomas Mayerhöfer [b], Torsten May [b], Hans-Georg Meyer [b],
Dana Cialla [a,b], Karina Weber [a,b], Jürgen Popp [a,b]

a Institut für Physikalische Chemie und Abbe Center of Photonics,
Friedrich-Schiller-Universität Jena,
Helmholtzweg 4, 07743 Jena, Deutschland
b Institut für Photonische Technologien (IPHT),
Albert-Einstein-Straße 9, 07745 Jena, Deutschland

*Corresponding Author: *jürgen.popp@ipht-jena.de*

Abstract

To enable a new access route to molecular and intermolecular resonances and provide solutions to important problems like the detection of DNA hybridization, the adaption of the concept of a perfect absorber and its use for the enhancement of resonance signals in the THz range is introduced. Within this contribution, the complete technological chain – simulations, fabrication and optical measurement of the fabricated perfect absorber – will be shown and discussed. Furthermore, first investigations on biological samples will be presented.

INTRODUCTION

Perfect absorbers [1] combine resonant absorption and local field enhancement and can thus be valuable substrates for spectroscopic investigations. Based on the perfect (or total) absorber concept introduced for use in the IR region [2], a perfect absorber for the range around 1.5THz was designed. The use of this substrate for reflectance spectroscopy can supplement other spectroscopic techniques like THz time domain spectroscopy (TDS), THz attenuated total reflection (ATR) [3] and THz absorption spectroscopy. It is based on resonant absorption in a thin dielectric layer enclosed between a nanostructured metallic thin film and a closed metallic back-reflector.

The application of such a perfect absorber as a field-enhancing substrate allows distinguishing analytes on the basis of variations in the spectral profile of the perfect absorber due to specific THz resonances of the analyte. Thus, the perfect absorber enhances the sensitivity for example, for the torsional modes in DNA. Intermolecular resonances can also be enhanced in the spectral area accessible by this setup[4].

RESULTS

In order to realize a perfect absorber for THz frequencies, simulations with Lumerical FDTD Solutions 2012 were carried out, showing promising results [Fig.1] Due to the dependency of the resonance on the thickness of the dielectric layer, the resonance frequency can be adjusted to fit a wavelength range relevant for specific biomedical and life-science applications. Matching the absorber to a specific analyte absorption frequency leads to an analyte signal superimposing with the reflection curve.

The simulation yielded a suitable template with dimensions in the range of tens of nanometers. In order to achieve the required sub µm resolution, electron beam lithography (EBL [5]) was used to fabricate feature sizes as low as 35nm, which were needed to achieve a high field enhancement. The theoretical simulations showed that a 45µm long and 100nm wide strip of gold features a strong absorption in the desired range when organized with a 50nm gap in axis and ca. 200nm off axis [Fig. 2].

The EBL was done on a Vistec SB350 EBL with a single resist layer (SML 300 from EM Resist Ltd.). The simulations have shown that the resonance frequency of the absorber is highly sensitive to material properties and structural dimensions. Especially the predicted theoretical field enhancement in the gap region in the order of 10^3 for the electromagnetic field promises a capable and sensitive analytical tool.

The fabrication was successfully performed with very good conformity and feature sizes as were demanded [Fig.3]. First potential applications will be discussed and supported by first reflection measurements.

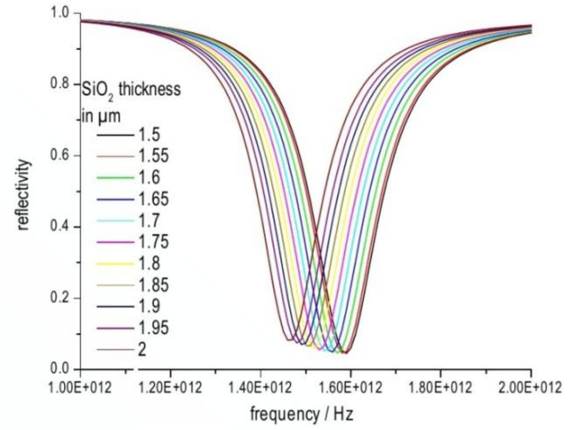

Figure 1 Theoretical dependency of the resonance on the dielectric layer´s thickness based on simulations by Lumerical FDTD Solutions.

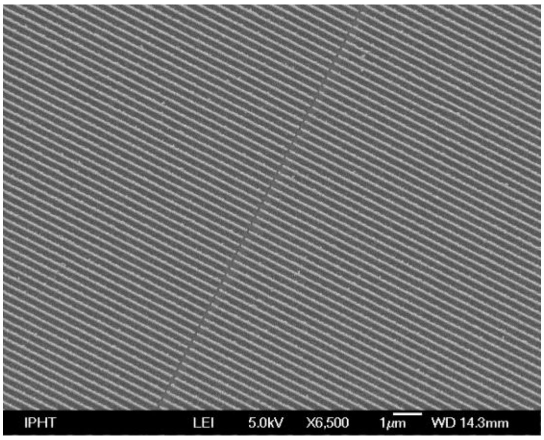

Figure 2 Overview of the perfect absorber structure resonant at 1.5 THz.

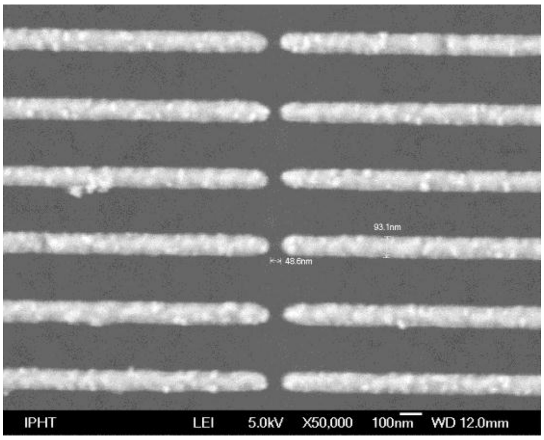

Figure 3 Close-up of the gap region. The gap is approx. 48nm wide; the bars are 93 nm wide, which is close to the 50nm gap size and 80nm bar width of the simulated design.

EXPERIMENTAL SETUP

EBL was performed using a VisTec SB350 E-Beam. The needed resist system (SML 300) was prepared by standard spin-on coating and tempering. The gold layer was prepared by thermal evaporation; the dielectric layer of SiO_2 was deposited by plasma-enhanced chemical vapor deposition (PECVD) in a reactor from Sentech.

For analytical tasks, a Bruker Vertex 80v FTIR spectrometer with a superconducting bolometer as detector was used. A Jeol 6700F scanning electron microscope was used for images shown in Figures 2 and 3.

---

[1] K. Chen,R. Adato, and H. Altug,” Dual-Band Perfect Absorber for
Multispectral Plasmon-Enhanced Infrared Spectroscopy” in ASC Nano, Vol. 6 No. 9 pp. 7998-8006(2012)

[2] N. Liu, M. Mesch, T. Weiss, M. Hentschel, and H. Giessen, „Infrared Perfect Absorber and Its Application As Plasmonic Sensor” in Nano Lett.2010,10, 2342–2348

[3] D. A. Newnham and P. F. Taday, “Real-world applications of terahertz pulsed technology” in Applied Spectroscopy, Vol. 62, Issue 4, pp. 394-398 (2008)

[4] M. Walther, B. M. Fischer, P. U. Jepsen „Noncovalent intermolecular forces in polycrystalline and amorphous saccharides in the far infrared” in Chemical Physics Vol. 288 pp. 261–268 (2003)

[5] C. Vieu F. Carcenac1, A. Pépin, Y. Chen, M. Mejias, A. Lebib, L. Manin-Ferlazzo, L. Couraud, H. Launois,” Electron beam lithography: resolution limits and applications” in Applied Surface Science, Vol. 164 Issue 1-4, pp. 111-114 (2000)

One-pot annealing of DNA-nanoparticle structures

Andreas Kopielski*, Anne Schneider, Andrea Csáki and Wolfgang Fritzsche

[1]*Institute of Photonic Technology (IPHT),*
Albert-Einstein-Straße 9, 07745 Jena, Germany

*Corresponding Author: andreas.kopielski@*ipht-jena.de*

Abstract

DNA-Origami technique allows the precise positioning of single molecule like proteins, flourophore dyes and plasmonic nanoparticles on the nanoscale. Here we present a one-pot solution for the preparation of defined DNA-nanoparticle structures by self- assembly.

INTRODUCTION

Since the first idea to use DNA as a material for nanostructures in 1982 [1], DNA nanotechnology becomes an important field in nanotechnology. Today it is possible to produce nearly any desired DNA shape in 2D or 3D in high yield. These nanostructures can also be combined to nano-arrays [3]. Small DNA strands can be synthesized chemically and can be modified with chemical groups or fluorophores. So the DNA-shapes can serve as a nano-breadboard for a wide range of materials and allow for a nano scaled patterning.

Fig. 1: AFM image of 4 specific combined DNA–Origamis each labeled with DNA hairpins forming one letter.

DNA-NANOPARTICLES STRUCTURES

In principle, in DNA-Origami a long single strand of DNA (scaffold) get folded by many different small DNA strands (staple strands) [2]. Gold nanoparticles were covered with thiol-modified staple strands. That's why these strands are directly part of the DNA structure. This method encourage an one-pot solution for DNA-nanoparticle shapes and pattern by skipping the downstream hybridization step on sticky ends as often reports in literature [4].

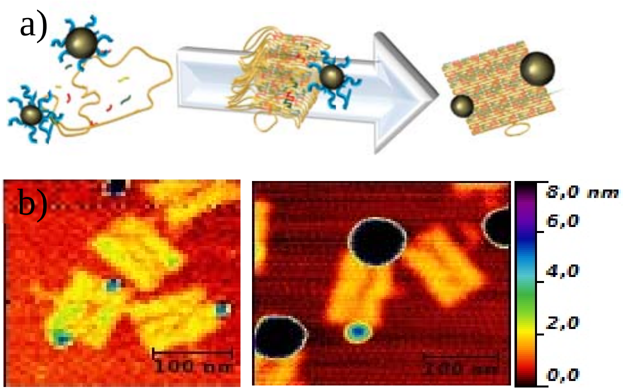

Fig 2: Sketch of self- assembled DNA-nanoparticle-Structure (a) and AFM images of specifically bonded gold nanoparticles 2x 5 nm (left) / 5 and 15 nm (right) on a DNA rectangle (b).

CONCLUSIONS

DNA-Origami is a powerful tool for the precise patterning of nanoparticles. An one-pot self-assembly would not only promote the automatization of the production of these constructs but also increase the stability of these structures because the DNA strands which cover the nanoparticles are an integrated part of the DNA-Origami.

---

[1] N.C. Seeman, *J. Theor.Biol.* 99,1982, 237-247.

[2] P. Rothemund , Nature 440 (7082) , 2006, 297–302.

[3] S.Woo et al., Nature Chemistry (VOL 3); 2011,:620-627

[4] Baoquan Ding et al., J. Am. Chem. Soc., 2010, 3248–3249

High power 1.2 kW monolithic fiber laser with a femtosecond inscribed fiber Bragg grating

Ria G. Krämer[1], Andreas Liem[2], Eric Freier[2], Christian Voigtländer[1], Jens U. Thomas[1], Daniel Richter[1], Thomas Schreiber[2], Andreas Tünnermann[1,2] and Stefan Nolte[1,2]

[1]*Institute of Applied Physics, Abbe Center of Photonics, Friedrich-Schiller-Universität Jena,*
Max-Wien-Platz 1, D-07743 Jena, Germany

[2]*Fraunhofer Insitute of Applied Optics and Precision Engineering,*
Albert-Einstein-Str. 7, D-07745 Jena, Germany

[*]Corresponding Author: *ria.kraemer@uni-jena.de*

Abstract

We report on a monolithic high power cw fiber laser realized via a fiber Bragg grating inscribed directly into the active core by ultrashort laser pulses with an output power of more than 1 kW in an Yb-doped large mode area fiber at 1080 nm.

INTRODUCTION

Fiber Bragg gratings (FBGs) have a growing importance for the development of highly robust and compact high power fiber laser systems. As narrow band reflectors they offer the possibility of the realization of integrated fiber lasers. Additionally, the evolution of femtosecond inscription of FBGs paved the way for the design of monolithic systems [1,2]. Here, we report on a monolithic continuous wave fiber laser at 1080 nm in an Yb-doped large mode area (LMA) fiber realized via a femtosecond inscribed FBG with an output power of 1.2 kW, limited only by the pump power.

INSCRIPTION OF FBG

In order to inscribe the FBG into the active fiber, the phase mask scanning technique [3] was used. Here, the femtosecond laser pulses (800 nm, 120 fs, 1 kHz) are focused through a cylindrical lens into the fiber along the fiber axis (see figure 1). A phase mask placed above the fiber generates a two-beam interference pattern which is then imprinted as a grating pattern into the fiber core. The fiber we used was an Yb-doped Nufern 20/400 fiber. The resulting grating had a reflection wavelength of 1077.8 nm with a strength of 98% and a FWHM bandwidth of 0.4 nm.

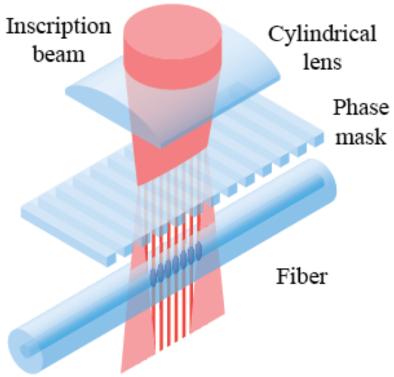

Figure 1: Schematic of the phase mask inscription.

EXPERIMENTAL SETUP

The schematic of the experimental setup for the fiber laser is shown in figure 2. The FBG acted as the highly reflecting (HR) mirror, whereas the Fresnel reflection of the cleaved end face of the fiber acted as the output coupler. The fiber was pumped at 976 nm and the pump light was not launched through the HR FBG, but through the other side.

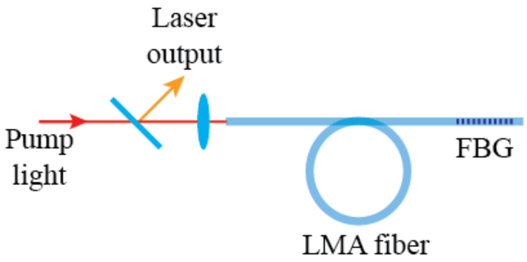

Figure 2: Schematic of laser setup.

EXPERIMENTAL RESULTS

The resulting high power laser had a slope efficiency of 82% with a maximum output power of 1.18 kW. The center wavelength was at 1079.8 nm and the FWHM was 0.6 nm. The beam quality measurement results in an M^2 of 1.07, verifying a single fundamental mode operation.

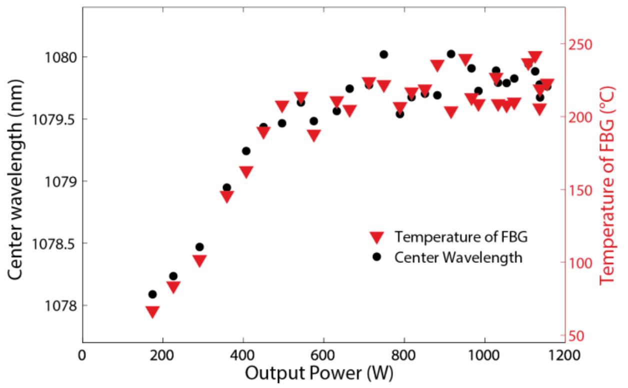

Figure 4: Center wavelength and temperature of FBG in dependency of the output power.

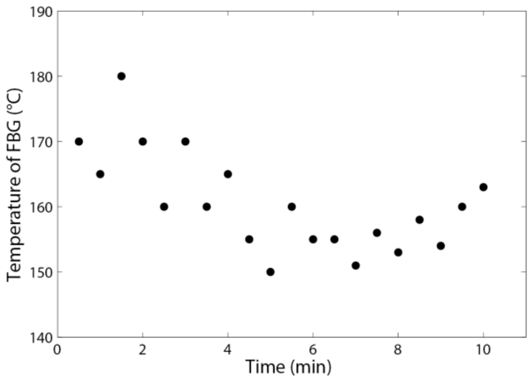

Figure 3: Measurement of temperature of FBG at 500 W output power over 10 minutes.

During the experiments we observed a heating of the FBG. In order to minimize this, we applied an air cooling fan close to the FBG. Figure 3 shows the center wavelength and temperature of the FBG measured with an infrared camera in dependency of the output power. First, a steady increase of the temperature is observed, until it reaches approximately 200°C at about 500 W output. At this point we logged the output power as well as the temperature for 10 minutes (see figure 4). The output power was stable, however the temperature slightly decreased. We assume an annealing of defects introduced due to the femtosecond inscription of the FBG, which led to a heating of the fiber. Due to this process the temperature of the grating stayed rather stable at about 200°C even though the output power was increased up to almost 1.2 kW.

CONCLUSION

We showed for the first time (to the best of our knowledge) a high power monolithic fiber laser with only a femtosecond inscribed HR FBG with an output power of 1.18 kW, only limited by the pump power. We observed a heating of the FBG, most probably caused by defects resulting from the inscription process. These defects could be partially annealed, resulting in a stabilization of the grating temperature.

---

[1] E. Wikszak, J. Thomas, J. Burghoff, B. Ortac, J. Limpert, S. Nolte, U. Fuchs and A. Tünnermann, Optics Letters **31,** 16 (2006).

[2] N. Jovanovic, M. Aslund, A. Fuerbach, S. D. Jackson, G. D. Marshall and M. J. Withford, Optics Letters **32**, 19 (2007).

[3] J. Thomas, E. Wikszak, T. Clausnitzer, U. Fuchs, U. Zeitner, S. Nolte. and A. Tünnermann, Applied Physics A: Material Science Process **86**, 2 (2007).

High Power Dual-Wavelength Self-Similar Parabolic Pulse Yb3+ Doped Fiber Laser

Weici LIU

Friedrich Schiller University,
Institute of Condensed Matter Theory and Optics,
D-07743 Jena, Germany

*Corresponding Author:weici.liu@*uni-jena.de*

Abstract

A simple and switchable high power dual-wavelength self-similar parabolic pulse Yb3+-doped fiber laser scheme is proposed, which is based on normal dispersion single-mode fiber, Yb3+ doped gain fiber and multimode fiber Bragg grating.

INTRODUCTION

High power multi-wavelength ultra-short pulse source is significant in laser weapon technology, remote sensing, space optical communication and so on. Rare-earth-doped fiber laser has attracted much attention for generating compact, stable, multi-wavelength ultra-short pulse source.

However, the pulse power is limited due to the modulation instability inside a fiber laser resonator. Self-similar (SS) parabolic pulse, which self similarly evolves and propagates in optical fibers with normal group velocity dispersion(GVD) and gain, will not break at high power level and can be de-chirped to obtain a femtosecond pulse from which thousands of watts peak power has been realized.[1,2] Thus it has a bright prospect for high power ultra-short pulse fiber lasers.

This paper introduces the design of simple, switchable, high power dual-wavelength SS parabolic pulseYb3+ doped fiber lasers based on multimode fiber Bragg grating (MMFBG) .

SCHEME AND RESULTS

Fig.1 shows the proposed configuration of the high power dual-wavelength SS parabolic pulseYb3+ doped fiber laser.

The scheme is discussed in detail as follows. The pump source is 980/1060 nm laser through a WDM coupler. The normal dispersion single-mode fiber(SMF) is 5 meters with β2>6.0×10-3ps2m-1,γ ≤3×10-3 W-1m-1. The active medium Yb3+ doped fiber(YDF) is of length 3 meters with the absorption coefficient 23 dB/m. The SS parabolic pulse generates in YDF and SMF. The stable lasing wavelength can be obtained by PC that adjust the polarization states of different modes, and balance the gain and loss between the peak reflections of the MMFBG. The wavelength selection depends on MMFBG which has multiple reflection peaks and has been successfully applied to obtain multi-wavelength oscillation in fiber laser with the polarization dependence characteristic. The optical circulator (OC) connects the MMFBG to the laser cavity, and ensures the pulses propagating in a single direction. The isolator is favorable for stabilizing multi-wavelength lasing because of preventing reverse propagating light. Dispersive delay line (DDL) (β2≤—3.0×10-2s2m-1) is for compressing the pulse. The laser output emerges from the 80% port of the 20:80 optical coupler, which makes the most use of power. The isolator is favorable for stabilizing dual-wavelength lasing because of preventing reverse propagating light. Therefore, high power dual-wavelength ultrashort SS parabolic pulse can be obtained.

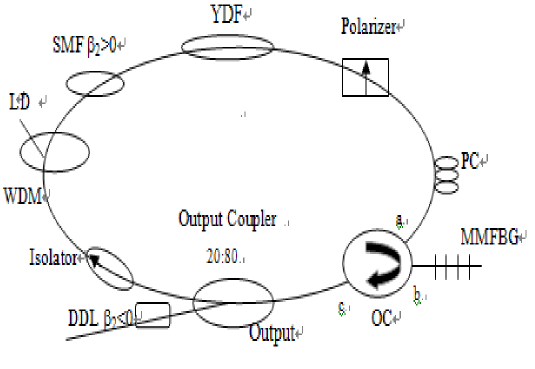

Fig.1. Schematic of the setup for dual-wavelength SS parabolic pulse Yb3+-doped fiber laser MMFBG-based.

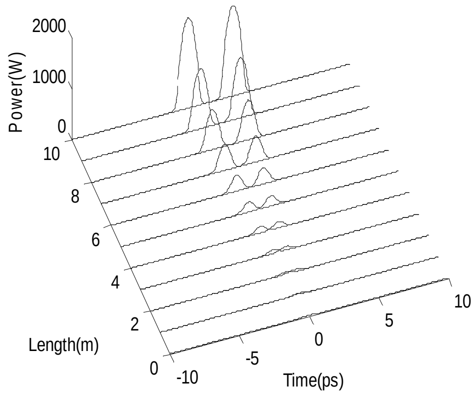

(a)

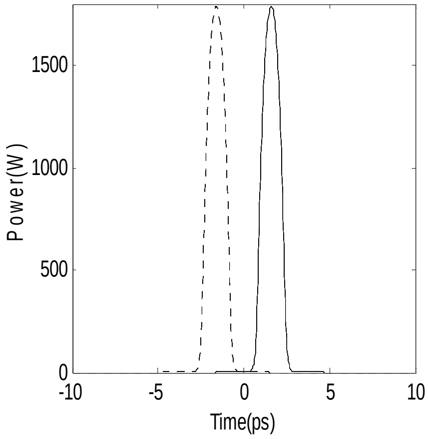

(b)

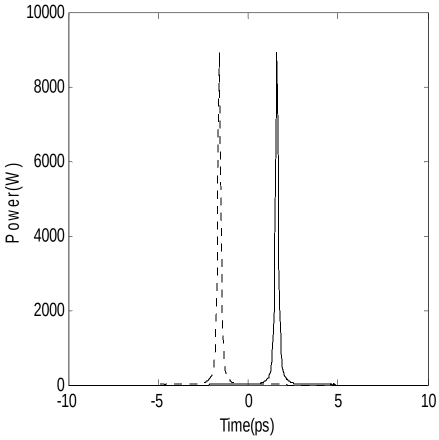

(c)

Fig.2.(a) . The evolution of dual-wavelength parabolic SS pulse; (b). before compressing (c) after compressing

Fig.2.a. shows the SS parabolic evolution of high power dual-wavelength pulses. For the input field a Gaussian pulse with λ0=1550nm; T_0 =0.5ps which is the half-width; E_{pulse} =30pj, β_2 = 4.0×10－2ps2/m, γ = 2.3×10－3 W-1m-1, g = 0.5 m-1,the fiber length is 9m. The pulses evolve asymptotically. It indicates the fact that allows us to achieve high energy dual-wavelength SS parabolic pulses.

Compared fig.2.b with fig.2.c, we can learn that higher power and more ultrashort pulse is gained by compressing the pulse. It indicates the fact that allows us to achieve high power dual-wavelength ultrashort SS parabolic pulse.

CONCLUSION

In conclusion, we have proposed a kind of high power dual-wavelength SS parabolic pulse Yb3+-doped fiber laser which is MMFBG based ,simple configuration, low cost. The simple scheme and fabrication of a dual-wavelength selection and flexile control laser is fascinating.

---

[1] J M. Dudley, C Finot, D J. Richardson and G Millot. Self-similarity in ultrafast nonlinear optics[J]. Nature physics 2007, 3(9): 597-603.

[2] Nie Bai, Pestov Dmitry, Wise Frank W, Dantus Marcos. Generation of 42-fs and 10-nJ pulses from a fiber laser with self-similar evolution in the gain segment [J]. Opt. Express, 2011,19(13):12074-12080.

Experimental realization of quantum illumination

E. D. Lopaeva*[1,2], I. Ruo Berchera[1], I. P. Degiovanni[1], S. Olivares[3,4,5], G. Brida[1], and M. Genovese[1]

[1]INRIM, Strada delle Cacce 91, Torino I-10126, Italy
[2]DISAT, Politecnico di Torino, Torino I-10129, Italy
[3]Dipartimento di Fisica, Universita degli Studi di Milano, Milano I-20133, Italy
[4]Dipartimento di Fisica, Universita degli Studi di Trieste, Trieste I-34151, Italy
[5]CNISM UdR Milano Statale, Milano I-20133, Italy

*Corresponding Author: *elizaveta.lopaeva@gmail.com*

Abstract

In both classical and quantum measurements noisy and lossy environment influences the results a lot and may cover them up completely. But there are protocols in which quantum correlations are not so easy to mask, therefore they may be utilized to strongly improve the accuracy of the experimental data even in presence of large amount of noise and losses. We have experimentally realized the quantum illumination protocol and demonstrated the advantages of the quantum correlation measurements in presence of the intensive multimode thermal bath.

INTRODUCTION

In quantum optical measurements using the quantum states of light allows to improve the sensitivity and/or resolution of the measurements. But the benefits of the noise suppression below classical noise limit can vanish in case of noisy and lossy measurements. A protocol exploiting quantum light preserving a strong advantage over the classical counterparts even in presence of large amount of noise and losses can encourage the developments of quantum technologies in real world allowing unprecedented results in quantum information, metrology, imaging and sensing.

Quantum illumination (QI) was theoretically introduced [1-4] as a technique which allows to determine absence or presence of a partially reflecting object in a noisy thermal bath by illuminating it with one of two quantum correlated beams.

The concept of the quantum illumination was formulated for the photon pairs. This work proposes a photon counting based realization of quantum illumination protocol in a mesoscopic regime (some thousand of photons per pulse) in cases of twin-beams presenting multimode spatial quantum correlations.

More in detail, at the input of one detector there is a beam that serves as a reference, while a second detector collects a combination of a background noise (for instance the thermal bath) and the reflected part of the second correlated beam that has interacted with the object (Figure 1).

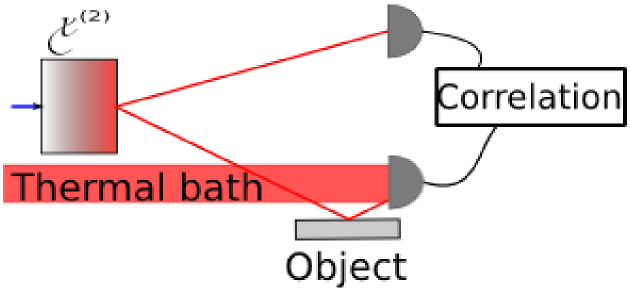

Figure 1: The principal scheme of the quantum illumination protocol. There are two correlated beams (for example from the parametric down-conversion process in a nonlinear crystal). If there is no object, the second correlated beam does not reach the detector.

EXPERIMENTAL SETUP

We realized the QI protocol by correlations of twin beams generated by parametric down-conversion (PDC) in a BBO crystal and detected by the pixels of a CCD camera. A non zero value of the covariance between correlated pixels can reveal the presence the object despite the background. If the object is absent, the second beam is not reflected by the object to the CCD, and no correlation is revealed.

We compared the performance of twin beams (TW) with the one of a classically correlated thermal beams (TH) which turns out to be more efficient classical strategy in this photon counting framework. In TH case the beam with the thermal statistics is just separated on the beamsplitter into two classically correlated beams. In that case it is impossible to distinguish the presence or absence of the object in the thermal bath.

Conclusions

It was experimentally proved that an advantage of orders of magnitude (in terms of error probability – Figure 2) can be preserved in presence of large losses and dominant background. This achievement provides a significant example of ancilla assisted quantum enhanced imaging/sensing protocol, besides the few previous realizations (e.g. in [5]), with the benefit of working in a noisy and lossy environment.

That way real application of quantum technologies is going to be possible in spite of the common believe that they are limited by their fragility to noise and losses.

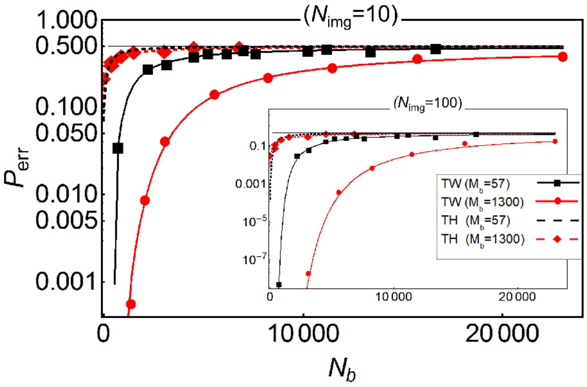

Figure 2: Error probability of the target detection versus the total number of photons of the thermal background. TW and TH are for twin beams and thermal split beams respectively, while M_b is the number of independent modes of the thermal background. The curves are the corresponding theoretical predictions.

[1] S. Lloyd, Science **321**, 1463 (2008).

[2] S. Tan et al., Phys. Rev. Lett. **101**, 253601 (2008).

[3] J. H. Shapiro and S. Lloyd, New Journ. of Phys. **11**, 063045 (2009).

[4] S. Guha and B. I. Erkmen, Phys. Rev. A **80**, 052310 (2009).

[5] G. Brida, M. Genovese and I. Ruo Berchera, Nat. Phot. **4**, 227 - 230 (2010); G.Brida et al., Phys. Rev. A **83**, 063807 (2011); N. Treps et al., Science **301**, 940 (2003).

Microstructured Optical Fibers from Preforms by Free Form Silica Laser Drilling

Adrian Lorenz*[1], Martin Becker[1], Marcel Werner[2], Oliver Fitzau[2], Dominik Esser[2], Jens Kobelke[1],
Anka Schwuchow[1], Manfred Rothardt[1], Kay Schuster[1], Dieter Hoffmann[2], Hartmut Bartelt[1]

[1]*Institute of Photonic Technology IPHT,*
Albert-Einstein-Straße 9, 07745 Jena, Germany

[2]*Fraunhofer Institute for Laser Technology ILT,*
Steinbachstr. 15, 52074 Aachen, Germany

*Corresponding Author: *adrian.lorenz@ipht-jena.de*

Abstract

We describe a laser drilling technology suitable for the creation of preforms for microstructured optical fibers from solid silica rods. This technology enables the realization of fiber designs that can not be addressed easily by common stack-and-draw technology.

INTRODUCTION

In the last years many complex fiber designs for special applications were proposed. These mostly microstructured solutions are often very hard to bring to a real preform for fiber drawing. The state of the art stack-and-draw technology uses a mostly triangular packaging of rods made e.g. of silica or chalcogenide glass surrounded by a tubing. Furthermore, special designs like Archimedean lattice and butterfly structures are accessible. Beyond this, a wide range of techniques exists for soft glasses and polymers such as extrusion, mechanical drilling and casting. For fused silica ultrasonic drilling of preforms for polarization maintaining or suspended core fibers with large holes is also applicable. But most of this common preform fabrication technologies are not able to produce designs with irregular hole structure or arrangement such as the golden spiral PCF or a rectangular lattice in silica fibers. The presented technique [1] is promises to overcome this disadvantage.

PREFORM DRILLING

For the drilling process the beam of a Q-switched laser system (InnoSlab design, 532 nm / 16 ns / 230 µJ) is passed through a vertically aligned glass rod and focused on its bottom side. In the next step the designed cross section pattern is scanned point by point to ablate material at the requested areas. After this layer is completely scanned the focus is moved up in the glass rod and the next layer is ablated using the same pattern. Repeating this procedure layer by layer until the top end face is reached will result in a preform with the desired hole structure. With this technique any symmetrical or non-symmetrical arrangement of holes is possible. The diameters of the holes have to be in the range of 600 µm to 8 mm over a total processable preform length of 80 mm in silica glass. The typical processing time is 8 h. Optimized laser parameters and longitudinal layer spacing (~20 µm) ensure the complete removal of ablated material and small surface roughness (average roughness <3 µm). The conicity of the holes could be approximated to be less than 0.01° (from Table 1).

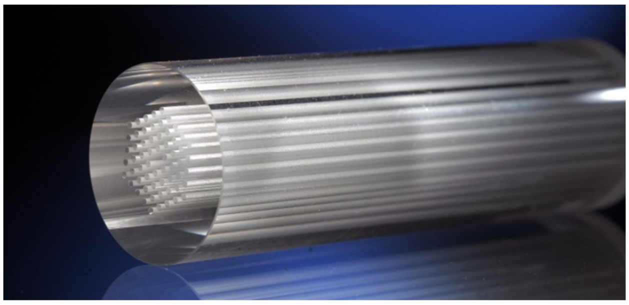
Figure 1: Laser drilled preform.

FIBER DRAWING AND COMPARISON

For comparison to stack-and-draw technology a preform with a four ring hexagonal air hole structure was produced at the ILT (Figure 1). For the drawing process at the IPHT an overpressure of about 350 Pa was applied to reduce collapsing of the holes due to surface tension. However, in a first drawing experiment this pressure was not able to overcome collapsing and therefor the ratio d/Λ (d: diameter of holes, Λ: distance between hole centers) changes from preform (0.51) to fiber (0.2). The technological difficulties in setting up the right parameters for temperature and pressure for this new type of preform are to be eliminated in the next experiments.

	Preform	fiber	relation
D_{outer}	28 mm	200 µm	0.71 %
d	0.784 mm (top) 0.772 mm (bottom)	0.9..1.1 µm	0.25 %
Λ	1.53 mm	10.2 µm	0.66 %
d/Λ	0.51	0.2	39 %

Table 1: Preform and fiber values related to laser drilling technique.

	Preform	fiber	relation
D_{outer}	14.65 mm	126.5 µm	0.86 %
d	0.428 mm	3.6 µm	0.84 %
Λ	1.000 mm	8.4 µm	0.84 %
d/Λ	0.428	0.43	101 %

Table 2: Preform and fiber values related to stack-and-draw technology.

In the fiber from the laser drilled preform the decreased ratio d/Λ results in weak confinement and with this larger leakage loss and a high sensitivity to bending occurs. Compared to these losses the influence of the roughness inside the holes and material absorption on the light guiding was too small to be evaluated. The effective numerical aperture is approximated from the fundamental space filling mode to be NA=0.06 at 1500 nm decreasing to 0.04 at 1000 nm. The comparison to a fiber from stack-and-draw technology with nearly the same initial d/Λ (Table 2) could only be geometrical, because in PCFs the light guiding probabilities are very sensitive to the geometrical dimensions (d/Λ and λ/Λ). As can be seen in Figure 2 the fiber from laser drilling has very homogeneous distribution of the holes, but the diameter of the holes is decreasing outwardly which could be explained by a temperature gradient inside the preform during the drawing process. However the fiber from stack-and-draw shows a good homogeneity only in the center region but larger deviations in the outer rings regarding hole position as well as diameter.

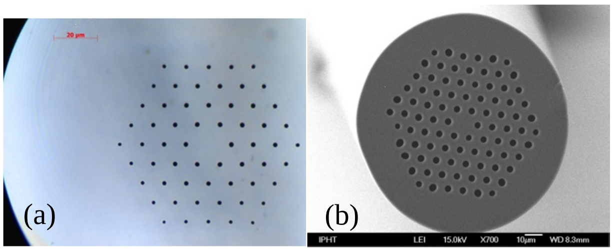

Figure 2: Fiber cross sections (a) fiber from laser drilled preform, (b) fiber made with stack- and-draw.

PERSPECTIVE: GOLDEN SPIRAL PCF

The recently proposed [2] golden spiral fiber (Figure 3(a)) is a good example for an irregular arrangement of holes which is up to now not accessible with common preform fabrication techniques in silica. The holes (diameter d) are arranged with $r = r_0\sqrt{m}$ (r_0: scaling parameter) and $\phi = m \cdot 137.5°$ for $m \in \mathbb{N}$, the angle is due to the golden ratio. Our calculations show that the announced high birefringence is mainly based on the high structural asymmetry of the core region. This effect is larger for higher d/r_0 and λ/r_0 (Figure 3(b)). From a technological point of view for higher d/r_0 drilling might not be a problem but fiber drawing from this preforms seems to be challenging.

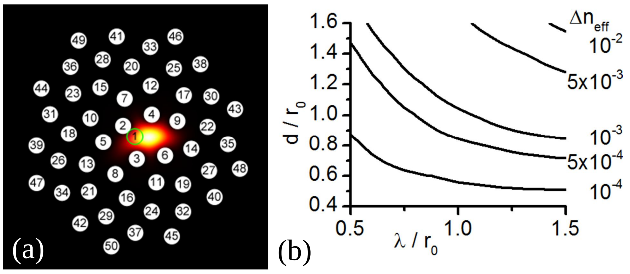

Figure 3: (a) Geometry and fundamental mode of the Golden spiral PCF for d/r_0=1 and λ/r_0=1.5, the central hole (number 1) is missing.
(b) Birefringence Δn_{eff} for the fundamental mode.

---

[1] M. Becker et al., “Laser drilled Free-Form Silica Fiber Preforms for Microstructured Optical Fibers”, Optical Fiber Technology (2013), in press, http://dx.doi.org/10.1016/j.yofte.2013.06.001

[2] A. Agrawal et al., “Golden spiral photonic crystal fiber: polarization and dispersion properties”, Optics Letters **33**, 22 (2008).

Power budget extension for OFDM-TDM-WDM PON

Mohammadreza Malekizandi*[1], Ali Emsia[1], Dieter Briggmann[1], Quang Trung Le[1], Ivan Djordjevic[2], and Franko Küppers[1]

[1] *TU Darmstadt, Merckstrasse 25, Darmstadt, Germany;*

[2] *University of Arizona, 1401 E University Blvd, Tucson, USA;*

*Corresponding Author: *mrzandi85@gmail.com*

Abstract

In this paper we are going to transmit the Orthogonal Frequency Division Multiplexing (OFDM) modulated signal in a hybrid of Time Division Multiplexing (TDM) and Wavelength Division Multiplexing (WDM) for Passive Optical Network (PON) system to have the most efficient use of bandwidth. Furthermore in order to decrease the number of Central Offices (COs) and also increase the number of Optical Network Users (ONUs) we try to find a suitable power budget extension method.

INTRODUCTION

Due to progressive bandwidth demand for newfangled bandwidth intensive applications, spectrum efficiency in PONs will be an issue very soon. From the other side network operators are always interested to decrease the deployment costs and at the same time cover more users. Therefore, we propose to use the OFDM which is one of the most bandwidth efficient candidates for high data rate transmission and also power budget extension, which helps to decrease the number of COs and increase the reach of the optical links [1].

OFDM TRANSCEIVER

To generate the Optical OFDM (OOFDM), in the transmitter (Fig. 1), digital bits are generated and mapped to a higher order modulation format (for example DQPSK), and then passed through an OFDM modulator. After that, the baseband signal will be up converted to the intermediate frequency by IQ mixer and finally to the optical frequency with the use of a Mach Zender Modulator (MZM) and a laser. Conventional OOFDM consists of an optical carrier and two sidebands. Because of fiber dispersion and nonlinearity of optical devices, these sidebands would be moved into a different phase which causes self-cancellation and signal degradation. Single Side Band (SSB) can treat this problem and combat the power [2]. Therefore we use an optical bandpass filter (OBPF) after MZM to filter out one of the sidebands and build SSB-OOFDM.

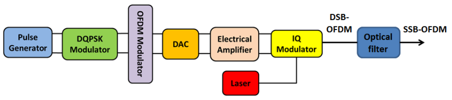

Figure 1: OFDM treansmitter [3]

To receive the OFDM, as it is depicted in Fig. 2, OOFDM signal is received and down converted from optical frequency to intermediate frequency, by an avalanche photo diode (APD) and then to the base band frequency, by an IQ mixer. After demodulating OFDM signal, DSP implementation is needed to estimate the effect of channel and correct the phase of data before demapping and measuring the Bit Error Rate (BER).

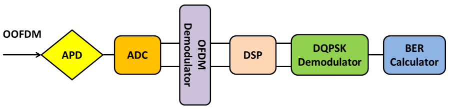

Figure 2: OFDM receiver [3]

POWER BUDGET EXTENSION CONFIGURATIONS

As we mentioned we implement a WDM-TDM PON to use the advantages of both of WDM and TDM. Hybrid PON attempts to combine the large aggregated capacity of WDM-PON with the efficient utilization of resources of TDM-PON. Hybrid PON also adopts multiple channels, as in WDM-PON, while allowing channel sharing among multiple ONUs, as in TDM-PON. As it is depicted in Fig. 3 our WDM setup consists of four 10 Gbit/s OFDM channels with the 50 GHz channel spacing according to ITU-Grid. Channels are multiplexed and launched to the transmission line via an Arrayed Waveguide Grating (AWG) multiplexer. In the feeder line, we have 40 km SMF and a variable optical attenuator (VOA) to see how long the feeder line can be prolonged. In the RN, optical signal will be amplified by SOA or EDFA. Then the channels will be separated via AWG demux and each wavelength can serve many ONUs separately. At the end, in the access line there is 10 km fiber and a VOA to see how many ONUs can be served by splitting data into different paths. The data can be split into different paths by a 1:M splitter.

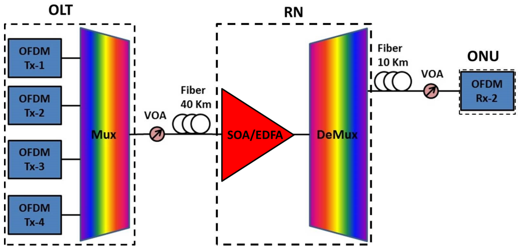

Figure 3: OFDM-WDM Power budget extension [3]

Simulation results are depicted in Fig. 4 & 5 in case of without and with fiber, respectively. The illustrated curves are called isoBER. In this paper we assume forward error correction FEC standard, therefore we consider bit error rate of 10^{-3}. As you can see from Fig. 5 in feeder line there is 13 dB power budget penalty, which means extending the feeder line up to 65 km is possible. In the access line in case of SOA we can use 18 dB power budget to split between 16 ONUs in each channel (1:16 splitters),which means 64 users in total and the remaining power is 6 dB for loss compensation, which can be used for RN demultiplexer and downstream/upstream circulators. But in case of EDFA in the access line we can use 27 dB power budget to split between 64 ONUs in each channel (1:64 splitters),which means 256 users in total and the remaining power is 9 dB for loss compensation.

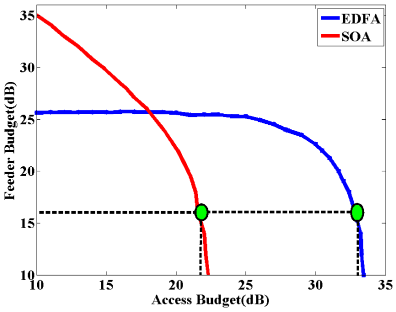

Figure 4: Comparison of EDFA and SOA for OFDM WDM, without fiber [3]

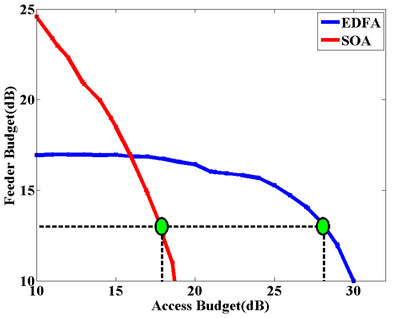

Figure 5: Comparison of EDFA and SOA for OFDM WDM, 40 km feederline & 10 km access line [3]

CONCLUSION

In this paper we used OFDM to improve the bandwidth efficiency in hybrid of TDM and WDM-PON and also tried to find a suitable power budget extension method in order to decrease the number of COs and increase the number of ONUs. We saw, although SOA is much cheaper than EDFA, but since EDFA has better performance and the number of severed users is almost four times more than SOA case, additional costs would be covered easily.

---

[1] A. Emsia, *et al.*, *IPC* (2013).

[2] C. Wang, *et al.*, *Photonics Technology Letters, IEEE* **22**, 820 (2010).

[3] M. Malekizandi, Higher Order Modulation Formats for PON, Master's thesis, TU Darmstadt (2013).

Generation of 2-Cycle Laser Pulses around 1.8 μm for the Investigation of Strong Field Phenomena

Frank Meyer*[1], Max Möller[1,2], Thomas Weber[1,2], A. Max Sayler and Gerhard G. Paulus[1,2]

[1] *Institut für Optik und Quantenelektronik, Max-Wien-Platz 1, 07743 Jena, Germany*

[2] *Helmholtz Institut Jena, Max-Wien-Platz 1, 07743 Jena, Germany*

*Corresponding Author: *frank.meyer@uni-jena.de*

Abstract

We realize a simple approach for the generation of intense $0.75\,$mJ $12\,$fs laser pulses at $1.8\,\mu$m. The idler of an optical parametric amplifier, pumped by a conventional Ti:Sa laser, is spectrally broadened by nonlinear propagation in a hollow core fiber. Nearly transform limited pulses are obtained by exploiting the linear propagation in fused silica in the anomalous dispersion regime. These pulses are beneficial for studying strong-field phenomena with high ponderomotive energies.

INTRODUCTION

Today, state of the art Titanium Saphire based Chirped Pulse Amplification (CPA) laser systems combined with a hollow core fiber (HCF) compressors or broadband Optical Parametric Chirped Pulse Amplification (OPCPA) systems are capable of producing intense ultrashort pulses which contain less than two optical cycles. When focused, intensities in the range of $10^{14}\,\mathrm{W/cm^2}$ and higher can be reached easily, giving rise to strong field effects like High Harmonic Generation (HHG), Nonsequential Double Ionisation (NSDI) or Above Threshold Ionisation (ATI).

Due to the steep intensity profile of few-cycle pulses, saturation effects in the leading edge of a pulse are greatly suppressed. Also, effects due to the carrier envelope phase (CEP) become relevant in strong fields.

A characteristic scaling parameter [1] in strong-field physics is the ponderomotive pontential $U_p \propto I\lambda^2$, defined as the cycle-averaged kinetic energy of a free electron in a laser field with intensity I and wavelength λ. Upscaling of U_p leads to e.g. higher ATI electron energies and also larger photon energies in HHG experiments, which opens the door for the generation of even shorter attosecond pulses up to keV photon energies.

However, with conventional sources for few-cycle pulses one is limited to wavelengths around $0.8\,\mu$m.

Here we realize a simple setup [2, 3] that adopts the well known HCF compression scheme to the mid infrared [4]. The output of a Ti:Sa based CPA system is converted to a wavelength of $1.8\,\mu$m in a commercial optical parametric amplifier (OPA). The output is spectrally broadened in a HCF and subsequently compressed close to its fourier limit by propagation in fused silica (FS), without the need for specially designed chirped mirrors.

We measure a FWHM pulse duration of $12\,$fs, which corresponds to two optical cycles at pulse energies of $0.75\,$mJ.

EXPERIMENTAL SETUP

The setup is shown in Fig. 1. A table-top Ti:Sa CPA system produces $9\,$mJ $35\,$fs pulses at a repition rate of $1\,$kHz.

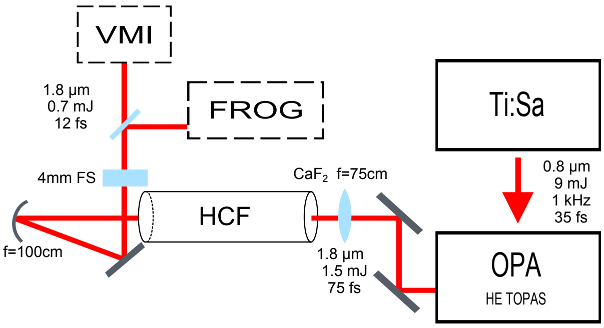

Figure 1: Experimental Setup. For details see experimental section.

It pumps a commercial white light seeded OPA consisting of three OPA-stages. Both the idler beam at $1.8\,\mu$m with a pulse energy of $1.4\,$mJ and the signal at

$1.4\,\mu$m and $1.8\,$mJ in energy can be used at the output with an overall conversion efficiency of about 35%. The idler is chosen with a dichroic beam splitter and then focused into a 1 m long HCF with a plano convex lens of $f = 75\,$cm. The fiber has a diameter of $400\,\mu$m and is filled with Argon at a pressure of 1 bar.

The spectral broadening takes place during nonlinear propagation, mainly due to self-phase modulation (SPM) and self steepening [5]. Argon was chosen as a trade off between a high nonlinear coefficient for effective broadening and high ionisation potential to avoid plasma formation. The gas is injected at the back end of the fiber, while the front end is permanently evacuated by a membrane pump. This differential pumping causes a pressure gradient in the fiber which suppresses plasma induced defocusing at the entrance.

After collimation with a concarve, $f = 100\,$cm silver mirror the pulse is compressed with 4 mm of FS. The spectral phase accumulated during propagation in the fiber is compensated by the anomalous dispersion exhibited by FS at this wavelength. It not only balances the group delay dispersion (GDD) but also the third-order dispersion (TOD).

Pulse characterization is carried out with a conventional home built SHG-FROG, which has been shown to be reliable down to the few-cycle regime [6]. To avoid additional dispersion, beam seperation is achieved by geometrical beam splitters and a convex silver mirror is used to focus both optical arms into a $50\,\mu$m thick BBO, cut for Type 1 phase matching at 21°. The broad phase matching bandwidth needed here is guaranteed by the flat dispersion curves of BBO in this spectral region.

The two arms are overlapped at small angle of 2° to seperate the background and SHG signal of the two individual beams from the SHG signal caused by the overlapping beams. The FROG spectrogram is then measured with a commercial Avaspec spectrometer.

Pulse durations of about 12 fs can be achieved reliably by fine tuning the gas pressure in the fiber for effective broadening without simultaneous plasma formation and the amount of glas placed in the beam path after the fiber. Also, the grating seperation of the Ti:Sa compressor must be tuned to adjust the pulse duration of the pump pulse.

With such pulses available, angularly resolved ATI spectra can be obtained with a velocity map imaging (VMI) spectrometer, especially desgined for high energy electrons up to 80 eV with a relative energy resolution below 2%.

RESULTS AND DISCUSSION

Fig. 2 shows the FROG trace of a 12.5 fs (FWHM) pulse along with its intensity autocorrelation, which is obtained by integrating all spectral components. The symmetry of the trace indicates proper alignment of the FROG apparatus, while minor distortions are due to power fluctuations after the fiber. No major satellite pulses are visible in the FROG trace or the autocorrelation, corresponding to a flat spectral phase in good agreement with results obtained with a retrieval algorithm not shown here.

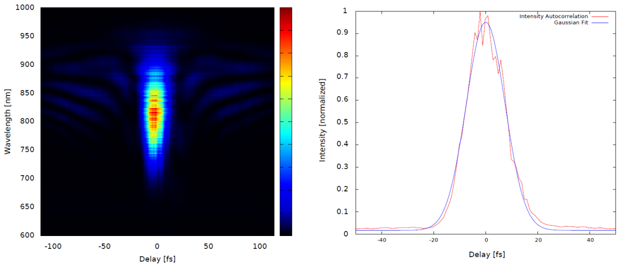

Figure 2: FROG trace (left) and autocorrelation with a gaussian fit (right).

First data from ATI measurements with a VMI spectrometer show the expected scaling of the electron energy with U_p. Similar features unique to long wavelength spectra, like the absence of a plateau caused by rescattered electrons can be observed.

CONCLUSION AND OUTLOOK

In conclusion we realized a reliable source for generating intense 2-cycle pulses at $1.8\,\mu$m. First ATI experiments show that these pulses can be used to study strong-field effects. In a next step control over the CEP will be realized to investigate the resulting effects on ATI spectra.

[1] G. G. Paulus, H. Walther, *Above-threshold ionization: from classical features to quantum effects*, vol. 48 (2002).

[2] B. E. Schmidt, *et al.*, *Applied Physics Letters* **96**, 121109 (2010).

[3] B. E. Schmidt, *et al.*, *Optics express* **19**, 6858 (2011).

[4] E. Granados, L.-J. Chen, C.-J. Lai, K.-H. Hong, F. X. Kärtner, *Optics express* **20**, 9099 (2012).

[5] P. Béjot, B. Schmidt, J. Kasparian, J.-P. Wolf, F. Legaré, *Physical Review A* **81**, 063828 (2010).

[6] A. Baltuska, . . . , *IEEE Journal of* **35**, 459 (1999).

Chip-based Isolation of Microorganisms with Subsequent Raman Spectroscopic Identification

Susanne Pahlow[1,2], Sandra Kloß[1], Konstantin Kirsch[2], Uwe Hübner[2],

Dana Cialla[1,2], Karina Weber[1,2], Petra Rösch[1] and Jürgen Popp*[1,2]

[1] *Institute of Physical Chemistry and Abbe Center of Photonics, Friedrich-Schiller-University Jena*
Helmholtzweg 4, 07743 Jena, Germany

[2] *Institute of Photonic Technology,*
Albert-Einstein-Str. 9, 07745 Jena, Germany

*Corresponding Author: *juergen.popp@ipht-jena.de*

Abstract

We have developed a Raman compatible chip for isolating microorganisms from complex media. The isolation of the bacteria is achieved by using antibodies as capture molecules. Due to the very specific interaction with their targets, this approach is promising for isolation of bacteria even from complex mixtures like body fluids. Our choice of capture molecules also enables the investigation of samples with an unknown content of bacteria, since the antibodies can capture a broad range of bacteria based on their analogue cell wall surface structures. The capability of our system is demonstrated for a broad range of different Gram positive and Gram negative germs.

INTRODUCTION

Fast and reliable detection of pathogens is an important issue in various fields of application. For example, in medical diagnostics a rapid diagnosis of sepsis can dramatically improve the odds of survival for the patient [1]. The earlier the pathogen responsible for the infection can be identified, the faster an appropriate antibiotic therapy can be initiated. Currently, the recommended method for diagnosing sepsis is still based on blood cultures [2]. This approach is not only time consuming, but also bears the risk of false negative results, since the pathogens do not necessarily have to be present in the patients' blood [3]. Promising methods for pathogen detection include polymerase chain reaction (PCR) and Raman microspectroscopy. Both approaches offer a high sensitivity and specificity. However, Raman microspectroscopy could be an even more attractive tool for label free detection of bacteria on species level, since the bacteria merely have to be isolated from their surrounding matrix and no further sample preparation steps, as for instance DNA extraction, are required. Raman microspectroscopy allows fast identification of bacteria due to the characteristic Raman spectrum of each species.[4-6]

Within this contribution a Raman compatible chip for isolation of microorganisms from various samples [7] is introduced. The chip was designed to be integrated into a microfluidic chamber for future automatization of the system. The isolation of the bacteria is achieved by using antibodies as capture molecules. Due to the very specific interaction with their targets, this approach is promising for isolating bacteria even from complex mixtures like body fluids. The current chip layout offers eight measuring fields. Each of them can be modified with a different type of antibody, in case it is desired to screen the sample for different bacteria. For investigation of samples with an unknown content of bacteria, we modified the chip with antibodies that capture a broad range of bacteria based on their analogue cell wall surface structures.

RESULTS & DISCUSSION

In order to investigate the capability of our system we performed isolation experiments with different Gram-positive (i.e. *S. epidermidis, S. cohnii, B. subtilis*) and Gram-negative bacteria (i.e. *E. coli, P. putida, P. stutzeri*). Each examined species could be successfully isolated with the chip based system.

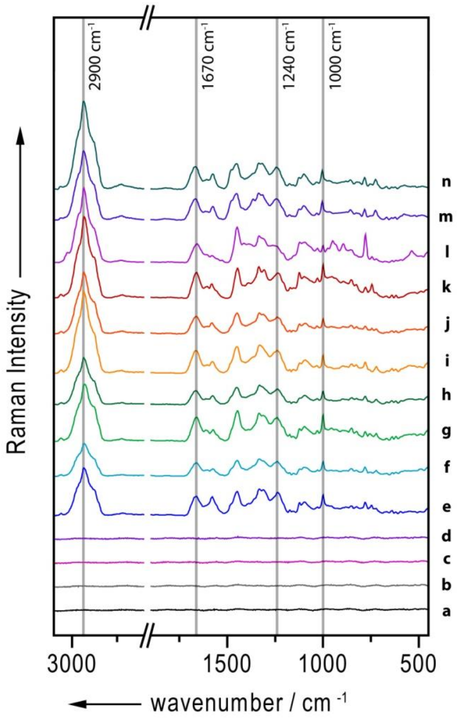

Figure 1: Background spectra of the aluminium substrate (**a** untreated, **b** silanized, **c** with anti-Gram-positive and **d** anti-Gram negative antibody) and background corrected mean spectra calculated from at least 20 single cell spectra of the investigated species (**e** *P. aeruginosa*, **f** *K. pneumoniae*, **g** *E. coli*, **h** *E. faecalis*, **i** *E. faecium*, **j** *S. aureus*, **k** *S. epidermidis*, **l** *S. cohnii*, **m** *P. stutzeri*, **n** *P. putida*). For clarity the spectra were shifted vertically.

Furthermore Raman spectra of the isolated bacteria cells were recorded (see **Figure 1**). All the content of the bacteria cells like proteins, lipids, DNA, RNA etc. contribute to the spectra. For example each species investigated exhibits a broad band centered at 2900 cm^{-1}, which results from CH stretching vibrations of CH_2 and CH_3 groups, that are found in proteins, lipids, nucleic acids and carbohydrates. Two other common features in the spectra resulting from the presence of proteins in the cells are the amide I and amide III bands at 1670 and 1240 cm^{-1}, respectively. Also the very sharp band at 1000 cm^{-1}, which can be ascribed to phenylalanine, is a characteristic band present in all bacteria spectra.

ACKNOWLEDGEMENT

Funding of the research projects ‘FastDiagnosis’ (13N11350) and ’JBCI 2.0’ (03IPT513Y – Unternehmen Region, InnoProfile Transfer) by the Federal Ministry of Education and Research (BMBF), Germany, is gratefully acknowledged. We would like to thank Carolin Steinbrücker for many helpful discussions. Further we would like to thank Dr. Jan Dellith for acquiring the SEM images and Christa Schmidt for recording the AFM images.

---

[1] A. Kumar, D. Roberts, K. E. Wood, B. Light, J. E. Parrillo, S. Sharma, R. Suppes, D. Feinstein, S. Zanotti, L. Taiberg, D. Gurka, A. Kumar, M. Cheang, Critical Care Medicine **34**, 1589 (2006).

[2] R. P. Dellinger, M. M. Levy, J. M. Carlet, Critical Care Medicine **36**, 1394 (2008).

[3] A. C. Heffner, J. M. Horton, M. R. Marchick, A. E. Jones, Clinical Infectious Diseases 2010, 50, 814. S. Meisel, S. Stöckel, M. Elschner, P. Rösch, J. Popp, Analyst **136**, 4997 (2011).

[4] S. Stöckel, S. Meisel, M. Elschner, P. Rösch, J. Popp, Angew. Chem., Int. Ed. **51**, 5339 (2012).

[5] S. Meisel, S. Stöckel, M. Elschner, F. Melzer, P. Rösch, J. Popp, Appl. Environ. Microbiol. **78**, 5575 (2012).

[6] M. Knauer, N. P. Ivleva, R. Niessner, C. Haisch, Analytical and Bioanalytical Chemistry **402**, 2663 (2012).

[7] S. Pahlow, S. Kloß, V. Blättel, K. Kirsch, U. Hübner, D. Cialla, P. Rösch, K. Weber, J. Popp ChemPhysChem, accepted DOI: 10.1002/cphc.201300543.

Highly resonant and directional nanoantenna

Jing Qi*[1], Thomas Kaiser[2], Thomas Pertsch[2], and Carsten Rockstuhl[1]

[1] *Institute of Condensed Matter Theory and Solid State Optics,*
Abbe Center of Photonics, Friedrich-Schiller-Universität Jena,
Max-Wien-Platz 1, 07743 Jena, Germany

[2] *Institute of Applied Physics, Abbe Center of Photonics,*
Friedrich-Schiller-Universität Jena, Max-Wien-Platz 1, 07743
Jena, Germany

*Corresponding Author: *jing.qi@uni-jena.de*

Abstract

Plasmonic nanoantennas permit many functional components for future generations of nanoscale optical devices. They have been intensively studied and means were devised to engineer their optical response. However, a frequently encountered limitation consists in their low quality factor. Here, we lift this issue for an electric dipolar nanoantenna by suggesting to combine it with plasmonic Bragg gratings as a supporting structure. Besides significantly enhancing the directional emissivity, this nanoantenna supports extraordinarily sharp resonances. This specific design promises to achieve many novel applications, e.g. in the field of cavity quantum electrodynamics where the strong coupling regime for light and matter comes in reach.

INTRODUCTION

With the purpose to stretch the functionality of antennas at radio frequencies to the visible spectrum, optical nanoantennas are used to localize external illuminations at the nanoscale by exploiting surface plasmon polaritons (SPPs), or to improve the radiative properties of emitters as e.g. localized light sources[1, 2, 3].

In general, two key parameters are considered to assess the performance of an optical nanoantenna: the field enhancement[4, 5] and the radiation pattern[6, 7]. However, a limitation frequently encountered is the small quality factor of optical nanoantennas. To lift this issue, we propose a novel nanoantenna that has a significantly enhanced quality factor.

ANTENNA DESIGN

In our novel design the nanoantenna is endowed with plasmonic gratings. If the Bragg condition is met, the reflection coefficient gets significantly enhanced and the radiative losses are strongly reduced. This is the key to achieve the high quality factor. Meanwhile grating structure also functions as a plasmonic coupler, compensating the momentum mismatch between SPPs and incident light wave[8]. The extended gratings automatically assist the antenna to collect energy and guide it towards the central antenna. As an additional benefit this engineered nanoantenna exhibits a highly directive radiation pattern.

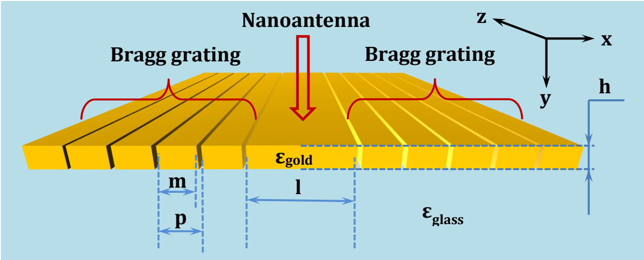

Figure 1: Schematic illustration of the investigated nanoantenna terminated with Bragg gratings.

Figure 1 shows the schematic of the investigated nanoantenna. It is assumed to be invariant in z direction. The central component is a gold nanoantenna with length l. Gratings are attached to both sides of the central nanoantenna. After a few preliminary optimization steps, the grating can be characterized by a period p and a filling factor m/p, with m being the width of the metallic part. The nanoantenna resonance is excited by a plane wave propagating in y direction and its electric field is polarized along x direction. The excited SPPs bounce back and forth in the central nanoantenna and eventually cause a resonance.

ANTENNA PROPERTY

Figure 2 compares the two major properties of nanoantennas: the spectrally dispersive characteristics of the nanoantenna and the radiation patterns at the resonance which express how the nanoantenna scatters its radiation into the far field.

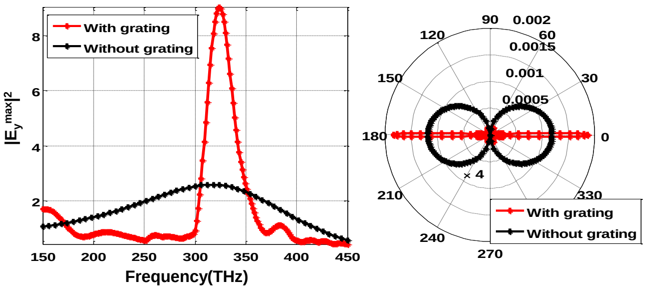

(a) (b)

Figure 2: (a) Enhancement of the intensity of the normal field component $|E_y^{\max}|^2$ above the nanoantenna with (red curve) and without optimized gratings (black curve) (b) Radiation patterns of the nanoantenna with (red curve) and without optimized gratings (black curve).

As shown in Fig. 2(a), the field is strongly enhanced at the resonance and the line width is largely reduced when the gratings are attached to the bare nanoantenna. With optimized grating terminations, the quality factor amounts almost to Q = 11, much higher than for the bare nanoantenna (Q = 1.4). Clearly, the incorporation of suitable antenna terminations increases the quality factor at least by a factor of 7.

In addition, the ordinary electric dipolar radiation pattern is compressed into a very narrow angle cone [see Fig. 2(b)]. Similar to the modification of transmitted light of a subwavelength aperture, the supporting gratings reshape the radiation pattern of a solid nanoantenna. Without the gratings, the directivity of a dipole antenna is only 1.4 dB. However, when the carefully tailored gratings are attached on both sides, its directivity raises up dramatically to 12 dB, approximately an order of magnitude in enhancement.

In conclusion, we propose a novel design for nanoantennas. We show that carefully tuned plasmonic gratings that endow the antenna can efficiently collect energy from the environment and confine it inside the antenna. Therefore, our nanoantenna can support extraordinarily sharp resonances and possess much larger quality factors when compared to bare dipolar antenna. Moreover, our antenna also exhibits a highly directional emissivity.

[1] L. Novotny and N. van Hulst, Nature Photon. **5**, 83 (2011).

[2] P. Bharadwaj, B. Deutsch and L. Novotny, Adv. Opt. Photon. **1**, 438 (2009).

[3] J. Dorfmüller, R. Vogelgesang, W. Khunsin, C. Rockstuhl, C. Etrich and K. Kern, Nano Lett. **10**, 3596 (2010).

[4] J. Zhang , W. Zhang, X. Zhu, J. Yang, J. Xu and D. Yu, Appl. Phys. Lett. **100**, 241115 (2012).

[5] R. Filter, J. Qi, C. Rockstuhl and F. Lederer, Phys. Rev. B **85**, 125429 (2012).

[6] G. Grzela, R. Paniagua-Domínguez, T. Barten, Y. Fontana, J.A. Sánchez-Gil and J. Gómez Rivas, Nano Lett. **12**, 5481 (2012).

[7] L. Novotny and B. Hecht, *Principles of Nano-Optics*, (Cambridge University Press, 2006)

[8] S. Maier, *Plasmonics: Fundamentals and Applications*, (Springer, 2007).

Determination of vitamins by surface enhanced Raman spectroscopy (SERS)

Andreea Radu[1], Dana Cialla[1,2], Karina Weber[1,2], and Jürgen Popp[*1,2]

[1] *Institute of Physical Chemistry and Abbe Center of Photonics,*
Friedrich-Schiller-University Jena,
Helmholtzweg 4, 07743 Jena, Germany

[2] *Institute of Photonic Technology (IPHT),*
Albert-Einstein-Strasse 9, 07745 Jena, Germany

[*] Corresponding Author: *juergen.popp@uni-jena.de*

Abstract

Despite the intensive progress made in the fields of diagnostics and treatment of diseases, preventing instead of treating remains the better solution. In order to do that, one should seriously consider the dietary regime. Therefore, when deciding on individual diets, information related to food quality, food composition and vitamin content is essential. We propose a method of detecting vitamins by using surface enhanced Raman spectroscopy (SERS) and enzymatically generated silver nanoparticles (EGNP).

INTRODUCTION

As compared with our method of detection, the most used one for this type of measurements is, nowadays, high performance liquid chromatography (HPLC) [1] combined with various other detection techniques such as UV/Vis spectroscopy, mass-spectroscopy or diode array detection. HPLC is a reliable, sensitive and reproducible technique. However, it also has some major drawbacks such as being time consuming and having difficulties detecting co-elution. Spectroscopic techniques have the advantage of being faster and easier to perform. Moreover, they have been lately used to analyze carotenoids in food products, such as tomato fruits and oranges [2, 3]. Also, they are adaptable to analyze more sensitive vitamins such as retinol [4] or α-tocopherol [5].

METHOD AND RESULTS

Among the different spectroscopic techniques, SERS provides a large enhancement of the specific Raman fingerprint signal of the studied analyte using a wide range of SERS available substrates [6]. The main advantages of the method are the low quantities of sample volume, little sample preparation and the fact that the analysis is performed rapidly as compared with other techniques. All these make SERS a good candidate for carotenoids analysis. Furthermore, in previous work [7] it was proved that trace amounts of vitamins (i.e. riboflavin) can be easily detected by using silver nanoparticles prepared by enzyme-induced reduction. The approach is using EGNPs, which are developed by a bottom-up protocol. The whole production concept is based on the enzymatic activity of horseradish peroxidase (HRP), which is immobilized on the surface of glass slides and is able to reduce silver ions from a solution, leading to their accumulation around the enzyme and, finally, to the formation of a particularly rough nanostructure [8].

We are currently using these substrates to characterize a wider range of vitamins, such as retinol (vitamin A), α-tocopherol (E), cholecalciferol (D3), riboflavin (B2), β-carotene and lycopene. These are all required for different biological functions of the human body [1,4,5]. Nevertheless, the human organism does not produce them. Instead, they are either digested from food or ingested as dietary supplements [1]. Accordingly, in a second step of the experiments, the named vitamins are detected from complex matrices consisting of mixtures of those substances extracted directly from food.

ACKNOWLEDGEMENTS

Funding of research projects “QuantiSERS” and “Jenaer Biochip Initiative 2.0” within the framework “InnoProfile Transfer – Unternehmen Region“ the Federal Ministry of Education and Research, Germany (BMBF) is gratefully acknowledged.

---

[1] J. Płonka, A.Toczek, V. Tomczyk, Food Analytical Methods **5**(5), 1167 (2012).

[2] J. Qin, K. Chao, M. S. Kim, Postharvest Biology and Technology **71**, 21 (2012).

[3] J. F. Li, Y. F. Huang, Y. Ding, S. B. Li, Z. L. Yang, X. S. Zhou, F. R. Fan, W. Zhang, Z. Y. Zhou, D. Y. Wu, B. Ren, Z. L. Wang and Z. Q. Tian, Nature, 464, 392–395 (2010).

[4] N. Failloux, I. Bonnet, M. H. Baron, E. Perrier, Applied Spectroscopy **57**(9), 1117 (2003).

[5] J. R. Beattie, C. Maguire, S. Gilchrist, L. J. Barrett, C. E. Cross, F.Possmayer, M. Ennis, J. S. Elborn, W. J. Curry, J. J. McGarvey and B. C. Schock, The FASEB Journal **21**(3), 766 (2007).

[6] D. Cialla, A. März, R. Böhme, F. Theil, K. Weber, M. Schmitt and J. Popp, Analytical and Bioanalytical Chemistry **403**(1), 27 (2012).

[7] H. Schneidewind, T. Schüler, K. K. Strelau, K. Weber, D. Cialla, M. Diege, R. Mattheis, A. Berger, R. Möller and J. Popp, Beilstein Journal of Nanotechnology **3**, 404 (2012).

[8] K. K. Strelau, T. Schüler, R. Möller, W. Fritzsche, J. Popp, ChemPhysChem **11**(2), 394 (2010).

Influence of Gouy phase on the spectral behaviour of a volume Bragg grating

Daniel Richter*[1], Christian Voigtländer[1], Ria G. Krämer[1], Jens U. Thomas[1], Andreas Tünnermann[1,2], and Stefan Nolte[1,2]

[1] *Institute of Applied Physics, Friedrich Schiller University Jena,*
Albert-Einstein-Straße 15, 07745 Jena, Germany

[2] *Fraunhofer Institute for Applied Optics and Precision*
Engineering, Albert-Einstein-Straße 7, 07745 Jena, Germany

*Corresponding Author: *daniel.richter.1@uni-jena.de*

Abstract

Within the Rayleigh length of an Gaussian beam the phase front of the propagating light experiences a delay with respect to a plane wave due to its divergent expansion. This so called Gouy phase shift can be investigated directly or indirectly by different methods. Here, we present the first to our knowledge direct observation of the spectral Gouy shift when probing a VBG with a fiber. While varying the distance between fiber and grating the central wavelength of the reflection signal shifts which can be attributed to the influence of the mentioned phase shift and fits well to our simulations.

INTRODUCTION

Volume Bragg gratings (VBGs) are optical divices exhibiting a periodic refractive index structure typically inside bulk glass. Due to their characteristics they can be employed for a wide range of applications such as beam combiners for e.g. fiber or solid state lasers, frequency stabilizers of semiconductor lasers or pulse compressors in case of chirped VBGs. Here we report on the measurement of the spectral Gouy shift by the help of a femtosecond written VBG. In the theory on Gaussian beams an additional phase term occurs which pays tribute to the propagation behavior of a Gaussian beam with respect to a plane wave. Thereby the beam adapts a longitudinal phase delay within the Rayleigh length. This phase shift better known as the Gouy phase can experimentally be measured when using a passive fiber and characterizing the reflection behavior of the VBG by adopting the fiber end facet to the grating. Measuring the reflected signal by the help of a circulator while changing the distance between fiber and grating end facet one is able to observe a spectral shift of the central wavelength of the reflected signal which can be attributed to the Gouy phase. To prove this assertion we carried out numerical/theoretical calculations which fit very well with our measurements.

EXPERIMENTS

For our experiments we used a femtosecond laser pulse written VBG inside fused silica generated by using the phase-mask-scanning technique([1, 2]). After generating the grating we polished the relevant side surface down to the grating to make sure not to lose too much energy of the probing beam. Additionally we used immersion oil between the fiber and grating end facet to reduce losses and background noise.

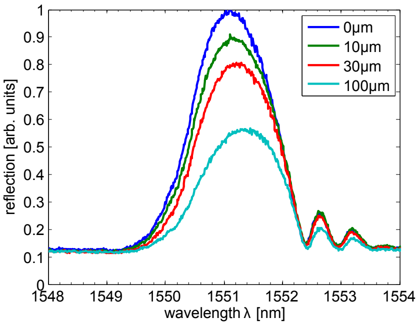

Figure 1: Normalised, measured reflection signals for different distances between fiber and grating. An increase of the distance implies an increase of the central wavelength.

We employed a standard SMF-28 fiber with a mode-field-diameter of 10μm at 1550nm. This leads to a RAYLEIGH length in air/fused silica of $50/73\mu$m.

The RAYLEIGH length defines the main distance interval in which a significant shift of the central wavelength can be observed. In our case we could measure a shift of 200pm at a distance of 100μm in immersion oil. This approach for shifting the central wavelength of the reflection of the grating might be very useful e.g. for fine-tuning the emission signal of laser diodes. Furthermore this effect can be enhanced by using a smaller mode-field-diameter.

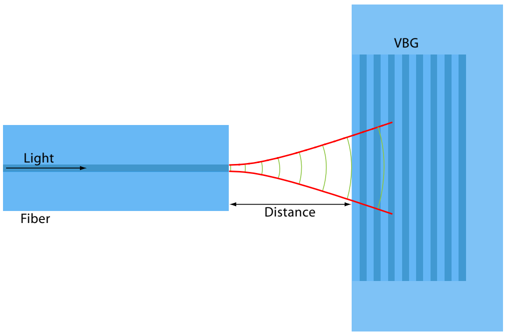

Figure 2: Sketch of the measurement setup. The distance between fiber and polished VBG sample can be varied.

---

[1] J. Thomas et al., *Applied Physics A: Materials Science & Processing* **86**, 153 (2007).

[2] C. Voigtlaender et al., *Applied Physics A: Materials Science & Processing* pp. 1–4 (2010).

Luminescence of Si/Ge-quantum dots resonators around 1550nm wavelength and enhancement with photonic crystal microcavities.

Viktoriia Rutckaia*[1], Vadim Talalaev[2], Frank Heyroth[3], Benjamin Koehler[3], and Joerg Schilling[1]

[1]*ZIK SiLi-nano, Karl-Freiherr-von-Fritsch-Straße 3,*
D-06120, Halle(Saale), Germany

[2]*Max-Planck-Institut für Mikrostrukturphysik*
Weinberg 2, D-06120 Halle, Germany

[3]*Martin-Luther-Universität Halle-Wittenberg*
Interdisziplinäres Zentrum für Materialwissenschaften / Nanotechnikum
Heinrich-Damerow-Str. 4, D-06120 Halle(Saale), Germany

*Corresponding Author: *viktoriia.rutckaia@physik.uni-halle.de*

Abstract

The defects in two dimensional photonic crystal slabs are microcavities with small mode volume and can exhibit large Q-factors. This leads to large enhancement of spontaneous emission rate causing an overall enhancement of radiative recombination efficiency [1]. The aim of this work is to show how the Q-factor of particular defect modes can be altered by adjusting the geometry of the pores neighboring to the cavity. This involves changing of their diameter and variation of their position. We present defect resonance calculation using COMSOL multyphysics. The mode volume is determined from the field distribution and theoretical values of Purcell factor are obtained. Experimental studies of the luminescence enhancement in the microcavities involve microphotoluminescence measurements on Ge quantum dots embedded in Si. Defect resonances were observed experimentally and their Q-factors were obtained from the luminescence spectra.

INTRODUCTION

Photonic crystals are structures with periodic dielectric permittivity and due to the Bragg reflections can have a forbidden light propagation for certain directions and frequencies, i.e. photonic band gap. Photonic band gap allows one using such structures for light manipulation, for instance as low-loss waveguides and different types of reflective coating films.

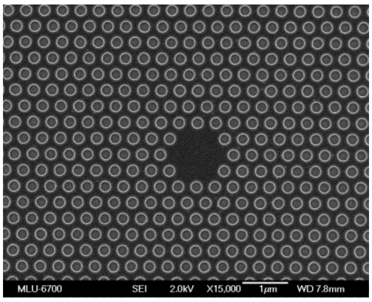

Fig.1. H2 defect in 2-dimensional photonic crystal.

Figure 1 presents 2D photonic crystal made of triangular lattice of air holes in silicon slab. Introducing a defect into a photonic crystal localized states appear in the band gap. Light with a certain frequency can be trapped inside the microcavity.

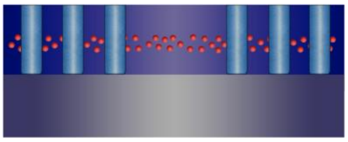

Fig.2. Side view of photonic crystal with defect introduced to silicon slab embedded with Ge-quantum dots. Grey area is silica substrate.

This effect can be used for the luminescence enhancement of low efficient Si/Ge QD that is actual for telecomm applications. Figure 2 shows the realization principle of photonic crystal for light enhancement applications. Changing the geometry of the microcavity surroundings one can provide larger Q-factor and lower mode volume and, hence, higher radiative emission rate.

MODELING

Ge quantum dots luminescence is suppressed by the holes interface, thus the microcavity should have space away from interfaces. On the other hand, the smaller cavity is the smaller will be the mode volume. Therefore the smallest of “big” cavities is considered in this work (Fig.1.) – so-called H2 defect.

Two dimensional photonic crystal shown on Fig.1. was modeled in COMSOL multiphysics package through numerical solving of Maxwell equations. Silicon slab with holes is surrounded by air. Thickness of the slab was fixed as 220 nm that is equal to half wavelength. Pores diameter and periodicity were chosen as 240 nm and 400 nm respectively. These values showed the highest Q-factor for the considered cavity modes.

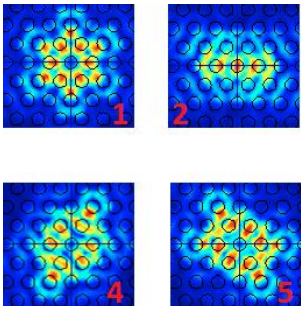

Fig.3. H2 cavity modes considered in this work.

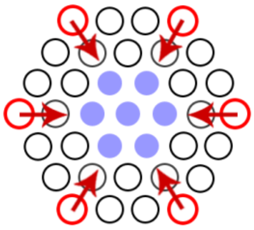

Fig.4. Shifting of two second adjacent to cavity pores in modeling.

Geometry change that includes shift of six second nearest to defect pores (Fig.4.) and change of their diameter shows that for certain existing modes (Fig.3.) Purcell factor is strongly affected with cavity surrounding (Fig.5.).

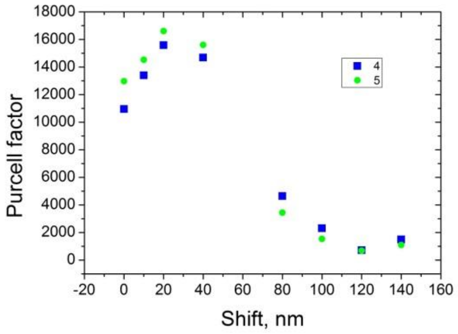

Fig.5. Dependence of Purcell factor on holes shift shown on Fig.4. for cavity modes 4 and 5.

EXPERIMENT

Ge quantum dots were grown with molecular beam epitaxy. Photonic crystal was fabricated with e-beam lithography and further reactive ion etching.

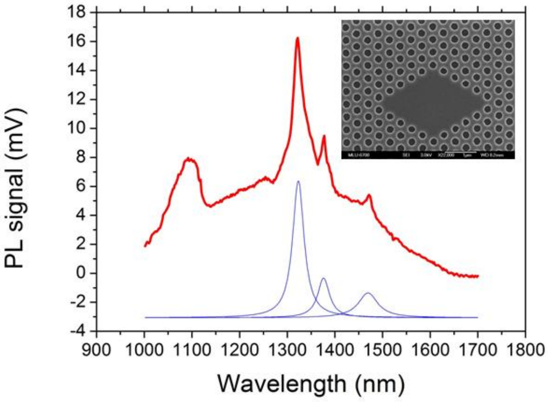

Fig.6. The luminescence spectra of structure shown in the inset. Three peaks correspond to localized modes were fitted with Lorentzians.

Luminescence was measured at room temperature with micro-photoluminescence setup. Fig.6. shows an example of luminescence enhancement with low Q-factor due to the losses into the substrate. That can be improved with underetching of the sacrificial layer.

---

[1] J.S.Xia,Y.Ikegami, and Y.Shiraki, Appl.Phys.Let.89,201102(2006)

Beam quality measurements with a spatial light modulator

Christian Schulze*[1], Daniel Flamm[1], Andrew Forbes[2], Michael Duparré[1]

[1] *Institute of Applied Optics, Abbe Center of Photonics, Friedrich Schiller University, Jena, Germany*

[2] *Council for Scientific and Industrial Research, National Laser Centre, Pretoria, South Africa*

*Corresponding Author: *christian.schulze@uni-jena.de*

Abstract

We present a simple and easy to use technique to determine the beam propagation ratio M^2 based on digital holograms allowing a fast M^2 measurement without any moving components.

INTRODUCTION

Laser beam quality is an important parameter in many application fields, such as laser material processing, microscopy, and telecommunication. Because of its simplicity the beam propagation ratio M^2 is commonly known and widely used to quantify laser beam quality. It compares the beam parameter product (product of waist radius and divergence half-angle) of the beam under test to that of a fundamental Gaussian beam [1]. The definition of the M^2 value and its instruction for measurement are detailed in the ISO standard [2]. Accordingly, the M^2 value is determined from measuring the beam cross sections at various planes along the propagation direction and subsequent fit of the beam's second order moments. Since this procedure is very time-consuming several alternative but still ISO-conform techniques were developed, such as the measurement of the beam intensity at a fixed plane and behind several rotating lens combinations [3], multiplane imaging using diffraction gratings [4], multiple reflections from an etalon [5], direct measurement of the beam moments by specifically designed transmission filters [6], and field reconstruction by modal decomposition [7], respectively. In principle, all approaches to determine the beam propagation ratio require several measurements of either varying beam sizes and/or varying beam curvatures. This has traditionally been achieved by letting the beam propagate in free space, i.e., nature provides the variation in the beam parameters through diffraction. However, this propagation can be achieved all-digitally using a spatial light modulator as shown recently [8], which will be reviewed here. Accordingly, the spatial light modulator can be used, first, as a lens with tunable focal length (method A), and second, to manipulate the angular frequency spectrum of the beam yielding its digital propagation (method B).

EXPERIMENTAL SETUP

Figure 1 depicts the experimental setup for method A and B. In both cases the beam illuminates an SLM, which displays a phase pattern $\Psi_f = \frac{\pi}{\lambda f}(x^2 + y^2)$, which is the phase function of a spherical lens with f the focal length, λ the wavelength, and x, y the transverse coordinates (variable lens method A), or $\Psi_{k_z} = k_z z$ (angular spectrum modification, method B), where z is the propagation direction, and k_z the z-component of the wave vector [8]. The last mentioned approach hence depicts the optical representation of the angular spectrum method [9]. In A, a camera is placed behind the SLM at any distance, whereas in B, the camera is placed behind a $2f$-setup with an additional lens. In both cases the camera is placed at a fixed position behind the SLM on which the phase patterns are changed consecutively and no moving components are required [8].

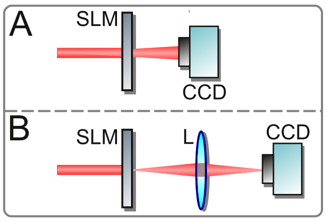

Figure 1: Schematic experimental setup for method A and B. SLM - spatial light modulator (actually working in reflectance), L - lens, CCD - camera.

From the camera images the beam diameter as a function of z and f was inferred from measuring the second order moments [2]. By fitting the beam diameter as a function of z or f with the theoretical expectations, the M^2 value is obtained [8].

RESULTS

To test the two methods, different Laguerre-Gaussian modes LG$_{pl}$ were generated, since their M^2 value and beam diameter is known to scale with the mode indices p and l. For convenience, only one SLM was used simultaneously for the generation of the sample beams as well as to depict the phase patterns Ψ for analysis (instead of using two SLMs, one for beam generation and one for analysis). The sample beams were generated by displaying the respective LG mode patterns using complex amplitude modulation [10], and were superimposed with the lens function Ψ_f (method A) or the propagation factor Ψ_{k_z} (method B) for analysis [8]. The results for an LG$_{21}$ beam are depicted in Fig. 2, for method A [Fig. 2(a)] yielding an M$^2 = 6.22$, and for method B [Fig. 2(b)] yielding an M$^2 = 6.04$, both from fitting the measured data. In general, we found for the investigated LG beams a maximum deviation of the M^2 parameter of 5% from the theoretical value, which demonstrates the high fidelity of measurement.

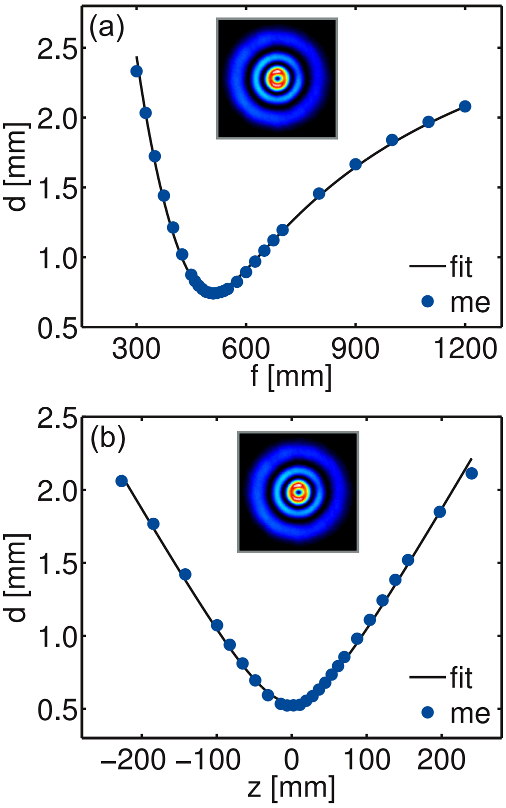

Figure 2: Measured beam diameter as a function of the variable focal length f fitted with the theoretically expected curve [(a), method A], and as a function of the propagation distance z fitted hyperbolically [(b), method B]. Insets depict measured beam intensity [8].

---

[1] A. E. Siegman, *DPSS (Diode Pumped Solid State) Lasers: Applications and Issues* (Optical Society of America, 1998), p. MQ1.

[2] ISO, ISO 11146-1:2005 Test methods for laser beam widths, divergence angles and beam propagation ratios — part 1: Stigmatic and simple astigmatic beams (2005).

[3] G. Nemes, A. E. Siegman, *J. Opt. Soc. Am. A* **11**, 2257 (1994).

[4] R. Cortés, R. Villagómez, V. Coello, R. López, *Rev. mex. Fis.* **54**, 279 (2008).

[5] M. Scaggs, G. Haas (Proc. SPIE, 2012), vol. 8236, pp. 82360H–1.

[6] A. Letsch, Charakterisierung allgemein astigmatischer laserstrahlung mit der methode der zweiten momente, Ph.D. thesis, Universität Stuttgart (2009).

[7] D. Flamm, *et al.*, *Appl. Opt.* **51**, 987 (2012).

[8] C. Schulze, D. Flamm, M. Duparré, A. Forbes, *Opt. Lett.* **37**, 4687 (2012).

[9] J. W. Goodman, *Introduction to Fourier Optics* (McGraw-Hill Publishing Company, 1968).

[10] V. Arrizón, U. Ruiz, R. Carrada, L. A. González, *J. Opt. Soc. Am. A* **24**, 3500 (2007).

Measuring the modal bend loss in multimode optical fibers

Christian Schulze*[1], Adrian Lorenz[2], Daniel Flamm[1], Alexander Hartung[2], Siegmund Schröter[2],
Michael Duparré[1]

[1] *Institute of Applied Optics, Abbe Center of Photonics, Friedrich Schiller University, Jena, Germany*

[2] *Institute of Photonic Technology, Jena, Germany*

*Corresponding Author: *christian.schulze@uni-jena.de*

Abstract

We present the measurement of mode resolved bend loss in a multimode fiber. Using correlation filters the power of each mode is measured for various bending diameters of the fiber from which the bend loss is inferred. The experimental results are compared to those of rigorous bend simulations and to analytic formulas known from the literature.

INTRODUCTION

Today optical fibers are used in manifold applications, including telecommunication, novel sensors, and generation and transportation of high optical powers [1]. In practice, nearly every fiber is bent to a certain degree to enable compact systems, which makes bending one of the most widespread effects wherever fibers are used. In multimode fibers, bending impacts differently on the individual modes since they differ, e.g., in effective refractive index, intensity and phase distribution. Accordingly, the bend-induced losses differ from mode to mode. This behavior can be employed to advantage in fiber lasers to suppress higher-order modes, and to achieve effective single mode operation of multimode fibers [2]. On the other hand, the bend loss becomes critical when the transmission of several modes is required, such as in modern telecommunication, where mode multiplexing techniques are expected to enhance the capacity of today's information transmission [3].

In the literature the theoretical treatment of bent fibers, especially of step-index fibers having a cylindrical core of homogeneous refractive index, is well-known. Various bending models and simulations exist, dealing with the influence of bending, even in the multimode regime of fibers [4,5]. Bend loss measurements however were limited a long time to the single mode regime [6], or to a quasi-single-mode regime [7]. Only recently it was shown that correlation filters provide easy access to the bend loss of each mode [8], an approach, which will be reviewed in the following, since it depicts a valueable measurement tool for the characterization and design of fibers and fiber lasers, especially to prove the reliability of several proposed bend-resistent fiber designs [9], and for investigating the transmission properties of fibers in mode-multiplexed telecommunication.

EXPERIMENTAL SETUP

Figure 1 depicts the experimental setup for measuring modal bend loss using correlation filters. A single-frequency Nd:YAG laser at 1064 nm wavelength was used to seed a multimode optical fiber, which was coiled with different bending diameters. The fiber output was relay imaged onto the correlation filter and a camera (CCD_1). The correlation filter in combination with a subsequent 2f-setup and a second camera CCD_2 enabled to measure the power of each mode as a function of the bending diameter. The fiber under test was a step-index fiber, which supports three modes, a fundamental mode called LP_{01}, and two higher-order modes called $\mathrm{LP}_{11\mathrm{e}}$ and $\mathrm{LP}_{11\mathrm{o}}$.

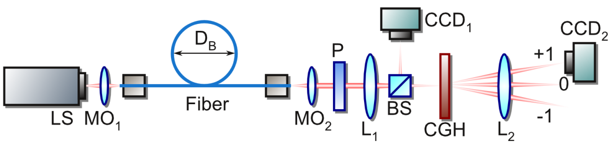

Figure 1: Experimental setup. (a) LS - laser source, $\mathrm{MO}_{1,2}$ - microscope objectives, D_B - bending diameter, P - polarizer, $\mathrm{L}_{1,2}$ - lenses, BS - beam splitter, CGH - computer-generated hologram, $\mathrm{CCD}_{1,2}$ - cameras [8].

RESULTS

From measuring the mode power for each bending diameter the bending loss per mode can be inferred. The corresponding results are depicted in Fig. 2(a) for the LP$_{01}$ and in Fig. 2(b) for the LP$_{11e}$ and LP$_{11o}$ modes. All measurements are compared to rigorous loss simulations using COMSOL Multiphysics®, and to analytical loss formulas [5]. Regarding the fundamental mode LP$_{01}$ [Fig. 2(a)], the measured loss values are in good agreement with the rigorous simulations, whereas the results using the analytical loss formula are one order of magnitude too low. This deviance can be explained by the fact that the analytical approach does not consider mode field deformation during bending, which the rigorous simulations do and accordingly yield a better agreement. Concerning the higher-order LP$_{11}$ modes as depicted in Fig. 2(b), it can be seen that the mode LP$_{11e}$ exhibits a clearly higher loss than the LP$_{11o}$ mode. This is reasonable, since the intensity distribution of the mode LP$_{11e}$ was oriented in the bending plane (mode LP$_{11o}$ oriented perpendicularly), and hence experiences higher losses (cf. orientation of the modes in Fig. 2). The comparison to the analytical results reveals good agreement, but no differentiation between the modes LP$_{11e}$ and LP$_{11o}$ is possible [5]. Regarding the rigorous simulation the LP$_{11e}$ and LP$_{11o}$ modes are separated in the same order as measured, but the simulated separation is larger than the measured one. This might be caused by the fact that an idealized step-index profile was used to describe the refractive index distribution of the optical fiber.

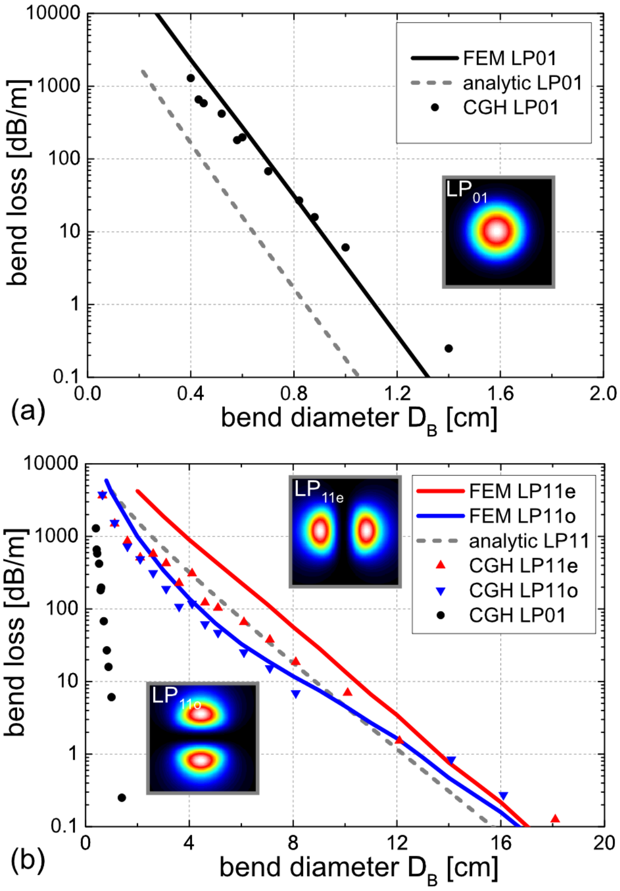

Figure 2: Modal bend loss as a function of bending diameter D_B for (a) the fundamental mode LP$_{01}$ and (b) the higher-order modes LP$_{11e}$ and LP$_{11o}$. (CGH) measurements, (FEM) rigorous loss simulations, (ana) analytical loss formula. Insets depict mode intensity patterns [8].

[1] F. Mitschke, *Glasfasern - Physik und Technologie* (Spektrum Akademischer Verlag, 2005).

[2] J. P. Koplow, D. A. V. Kliner, L. Goldberg, *Opt. Lett.* **25**, 442 (2000).

[3] Z. Wang, N. Zhang, X.-C. Yuan, *Opt. Express* **19**, 482 (2011).

[4] D. Marcuse, *J. Opt. Soc. Am.* **66**, 216 (1976).

[5] R. Schermer, J. Cole, *Quantum Electronics, IEEE Journal of* **43**, 899 (2007).

[6] L. Faustini, G. Martini, *Lightwave Technology, Journal of* **15**, 671 (1997).

[7] N. Shibata, M. Ohashi, K. ichi Kitayama, S. Seikai, *Opt. Lett.* **10**, 154 (1985).

[8] C. Schulze, *et al.*, *Opt. Express* **21**, 3170 (2013).

[9] J. M. Fini, S. Ramachandran, *Opt. Lett.* **32**, 748 (2007).

Optical Sectioning in a Single Exposure Using Polarisation-Coded Structured Illumination Microscopy (picoSIM) and Nanogratings

Sapna Shukla*[1,2], Rainer Heintzmann[1,2,3], and Kai Wicker[1,2]

[1]*Institute of Physical Chemistry,*
Friedrich Schiller University, Jena, Germany

[2]*Institute of Photonic Technology, Jena, Germany*

[3]*King's College London, Randall Division, United Kingdom*

*Corresponding Author: *sapna.shukla@ipht-jena.de*

Abstract

Wide-field microscopy is severely limited for thick samples. By using a modified structured illumination technique called picoSIM, optical sectioning in a single exposure is performed, resulting in high temporal and spatial resolution. The polarization-coded pattern is produced by a nanograting, which also enables the use of incoherent light. Results from material and biological samples demonstrate the optical sectioning ability of the technique.

INTRODUCTION

Conventional wide-field microscopy, though a great tool in biological as well as material imaging, is significantly restricted in performance when dealing with thick samples. Sample features in the focal plane are illuminated uniformly along with out-of-focus features. This leads to contributions from these non-focal planes to the image, causing a blurring effect and lower signal to noise ratio.

Optical sectioning methods like structured illumination microscopy (SIM) aim to eliminate these out-of-focus contributions and exclusively retain the focal plane information. SIM is a wide-field technique that is significantly faster than most point-scanning methods like confocal microscopy and additionally provides resolution enhancement in all directions [1]. However, the need to acquire at least three images for each sample slice proves to be a limiting factor in terms of speed.

Polarization-coded structured illumination microscopy (picoSIM) is a modified version of SIM that performs optical sectioning in a single exposure, yielding high temporal and spatial resolution. The use of a specialized grating to produce polarization-encoded grating lines furthers the use of this technique for reflection microscopy.

THEORY

Principle. In the polarization-coded illumination pattern, the orientation of the polarization vector for each grating line changes periodically, producing a uniform intensity distribution with linearly varying polarization [Fig. 1].

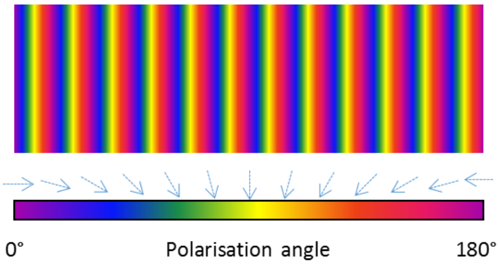

Fig. 1: Polarization distribution ín a picoSIM illumination pattern. Orientation of the polarization vector varies linearly from 0º to 180º degrees within a period.

The light from the sample retains the polarization to at least a certain degree, owing to polarization anisotropy. This light is then separated into different SIM images with shifted grating positions by an analyzer in different orientation. The polarized grating pattern is only present in the focal plane and the grating contrast vanishes in the out-of-focus region. Therefor there is only a selective modulation of intensity in the focal plane while the out-of-focus regions remain unmodulated. By reconstructing the acquired 'SIM' images, the unmodulated or out-of-focus information can be eliminated, yielding an optically sectioned image with suppressed out-of-focus blur.

Nanograting. The above mentioned polarized pattern is non-trivial to generate and needs an elaborate optical setup containing a diffraction grating [2]. However, with the efforts of our collaborators [3], a specialized grating has been fabricated where nano-cavities (30 x 300 x 200 nm^3) are etched into a fused-silica glass substrate with a fs-laser. These nano-cavities are arranged in such a fashion that the polarization vector of the cavities rotates by a certain angle periodically, acting like quarter wave plates with varying orientation, thus resulting in a variable polarization distribution in the grating as described above.

Not only does this significantly reduce the complexity of the setup, but it also enables the use of incoherent illumination which is otherwise difficult to achieve with the diffraction-grating approach. With the use of incoherent illumination, the application of picoSIM can be extended from fluorescent samples to reflective samples like metallic surfaces which would otherwise exhibit speckles in the detected images.

EXPERIMENTAL SETUP

The setup consists of an illumination and a detection sub-unit. In the illumination sub-unit, an incoherent light source is used and the beam path is aligned in the Köhler arrangement to produce a uniform field of illumination at the grating plane. There are two apertures – field aperture and incoherence aperture to select the diameter and the numerical aperture of the illuminating field. The grating is imaged onto the sample using an objective and tube lens combination housed in a Zeiss inverted microscope body. To guide the light from the tube lens to the objective, a 50:50 non-polarizing beam splitter plate is used for material samples, while a high quality dichroic filter set is used for biological (fluorescent) samples.

The detection sub-unit has two arms at 45° to each other. The light from the samples is divided into two halves and filters into two orthogonal polarization components in each arm using a polarizing beamsplitter and mirror combination. Hence we get four SIM images with grating position corresponding to 0°, 45°, 90° and 135° as required for the reconstruction.

RESULTS & DISCUSSION

The method has been verified to work for material as well as biological samples. When compared to the wide-field image [Fig. 2(a)], the reconstructed material sample [Fig. 2(b)] has suppressed out-of-focus blur and improved resolution. The darker region on the left of the reconstructed image shows out-of-focus features that contribute to a lot of blur in the wide-field image. Similar results are seen in a fluorescene-stained adult rat cardiomyocyte sample [Fig. 2(c) and (d)].

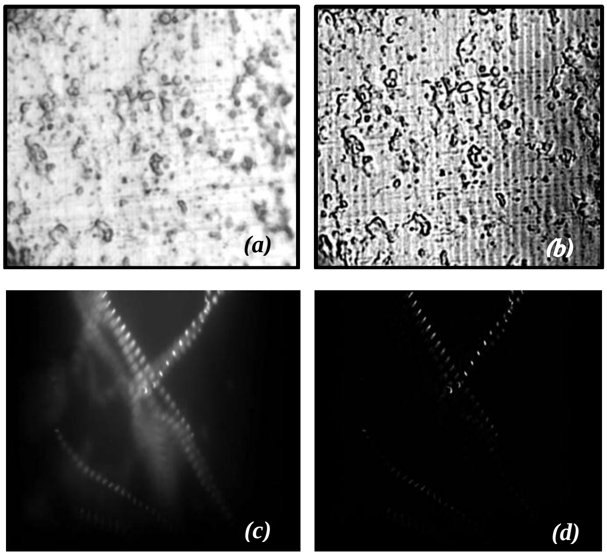

Fig. 2: (a) and (b) are wide-field and reconstructed images of an aluminium foil sample. (c) and (d) are wide-field and reconstructed images of a fluorescene stained adult rat cardiomyocyte sample [*image courtesy of Mr. Daniel Appelt*].

Some crucial challenges include distortion of the polarization by the dichroic coating of the fluorescence filter and the beamsplitter. Residual gratings formed are also a problem. These challenges can be overcome by experimental modifications like inclusion of a compensating filter pair and blocking higher diffraction orders or can be corrected for using sophisticated reconstruction algorithms.

---

[1] M. A. A. Neil, R. Juskaitis, and T. Wilson, Optics Letters 22: 1905-1907 (1997)
[2] K. Wicker, R. Heintzmann, Journal of Optics 12, 084010 (2010)
[3] AG Stefan Nolte, Institute for Applied Optics, Friedrich-Schiller Univeristy, Jena, Germany.

Compensating geometric distortions, not only in CCD images, for enhanced quantitative analysis - shown by the example of LEED images

Falko Sojka*, Roman Forker, and Torsten Fritz

Friedrich Schiller University Jena, Institute of Solid State Physics,
Helmholtzweg 5, 07743 Jena, Germany

*Corresponding Author: *falko.sojka@uni-jena.de*

Abstract

We developed and implemented an algorithm to determine and correct systematic distortions in LEED-images. The procedure is independent of the design of the device and will also take into account distortions which are not caused by the CCD but by the experimental setup. For this purpose, only a calibration image with a well-known structure is required. The algorithm provides a correction rule which can be used to rectify all further measurements generated with the same device. In detail, we distinguish between a radial and an asymmetric distortion. As an application example we use low energy electron diffraction images.

INTRODUCTION

Low energy electron diffraction (LEED) on epitaxial layers is a competitive method to examine long-range ordering at the surface. However, due to limitations like distortion of the LEED images, often additional efforts have to be made in order to derive precise epitaxial relations. [1, 2] Regardless of the actual research method, many authors do not exploit the full potential of their experiments by discussing the uncorrected, distorted data.

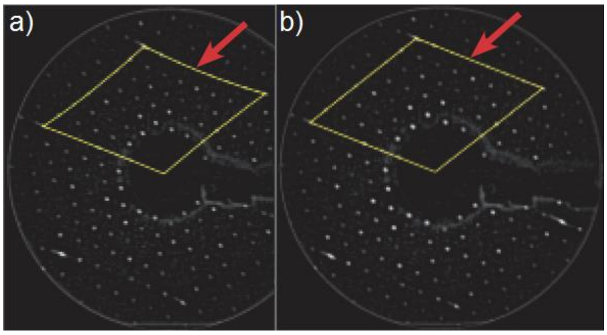

Figure 1: MCP-LEED images of Si(111) 7x7 taken at 75.2eV before a) and after b) correction. [3]

Chung *et al.* developed a method which is in principle capable of accounting for any type of deviation from the ideal image. [4] Yet, their method is meant to rectify distortions due to the imaging device only, because the calibration was made with a known external real-space reference consisting of a plate with regularly distributed holes placed on the detector and illuminated with nearly parallel radiation. Stimulated by the analysis of micro-channel plate and spot-profile analysis low-energy electron diffraction (MCP-LEED and SPA-LEED, respectively) patterns we strive for a correction method that considers distortions stemming from the apparatus itself and from the imaging conditions. Therefore, we utilize an internal reciprocal-space reference which enables us to determine distortions of diffraction patterns even where no 2D recording device (i.e., a CCD, an image plate, etc.) is employed, as in the case of a SPA-LEED. [5]

METHOD

The algorithm we developed and implemented to correct systematic distortions in LEED-images is independent of the design of the device. For our case, diffraction images of LEED-patterns, the used reference points are bright diffraction spots in the image. A sample of a Si(111) surface with a 7x7 reconstruction provides images with a well-known structure and a suitably high number of diffraction spots. But the algorithm also works with other samples as well as you can describe the ideal structure geometrically.

After the determination of the experimental spot positions, the program fits numerically the ideal structure to the experimental one. In the course of this, nine different parameters are optimized including a radial distortion (4 parameters). Figure 2 shows the measured radial symmetric distortion for three different LEED devices.

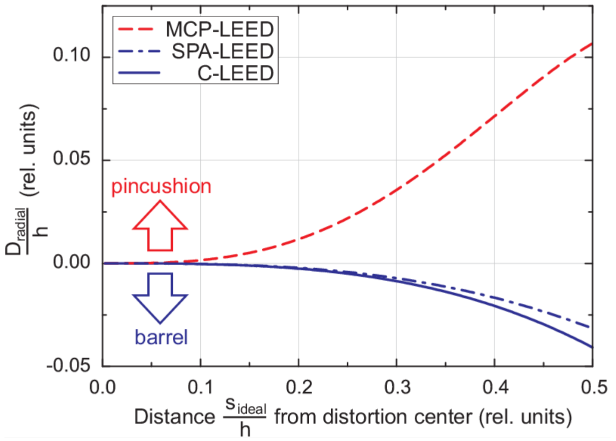

Figure 2: Determined radial symmetric distortions for three different LEED devices.

The deviations between the fitted spot positions and the real ones indicate the discrete asymmetric distortions in the image. By an approximation of a vector field to these discrete reference points we obtain the whole asymmetric distortion. Figure 3 shows the measured asymmetric distortion for the different devices.

The last step is the reconstruction of the ideal undistorted image. Here, we use the results of the radial and asymmetric distortion to fill an empty pixel map with the correct grey values gathered from the original image, see Figure 4.

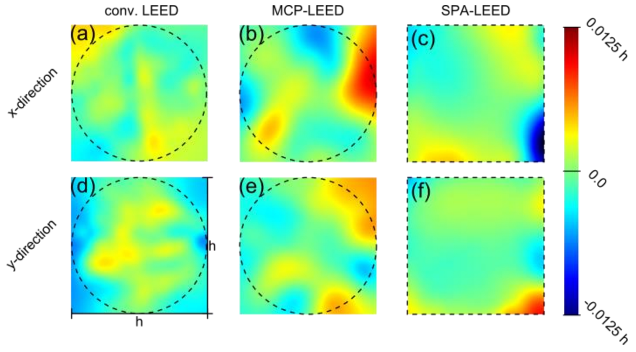

Figure 3: Determined asymmetric distortions for three different LEED devices.

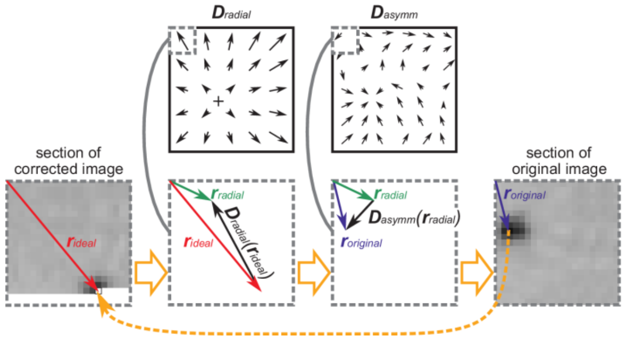

Figure 4: Scheme of creating the corrected images using the original LEED image and the results of the determination of the distortions.

Our algorithm was created to correct LEED images but the concept should be beneficial for other types of imaging devices as well.

---

[1] F. Sojka, M. Meissner, C. Zwick, R. Forker, and T. Fritz, Rev. Sci. Instrum. **84**, 015111 (2013).

[2] F. Sojka, M. Meissner, C. Zwick, R. Forker, M. Vyshnepolsky, C. Klein, M. Horn-von Hoegen, and T. Fritz, Ultramicroscopy **133**, 35 (2013).

[3] The Omicron NanoTechnology, Newsletter **16**, 12 (2012).

[4] J.-S. Chung, H. S. Youn, and H.-D. Joo, J. Korean Phys. Soc. **44**, 256 (2004).

[5] M. Horn-von Hoegen, Z. Kristallogr. **214**, 591 (1999).

Band gap analysis of metal-filled photonic crystal fibers

Ron Spittel, Markus A. Schmidt, Hartmut Bartelt

*Institute of Photonic Technology, Albert-Einstein-Str. 9, 07745
Jena, Germany*

*Corresponding Author: *ron.spittel@ipht-jena.de*

Abstract

A cladding mode analysis of a gold-filled photonic crystal fiber is presented by means of the density of states of the hexagonal unit cell. In addition, we propose a simplified full-vectorial analytical model based on a circular unit cell.

INTRODUCTION

All-silica photonic crystal fibers (PCFs) can be utilized to introduce liquid metals inside their holes in order to form cylindrical wires after cooling, exhibiting diameters in the range of a few hundred nanometers [1]. Due to the negative dielectric function of most metals in the VIS and IR, surface plasmon polaritons (SPPs) can exist at the metal-silica interface and propagate along the wires [2]. In contrast to SPPs on planar interfaces the effective refractive index of some of these surface plasmon modes can cross the silica line which enables an excitation of the SPPs via the core mode of the PCF [3]. The theoretical description of the SPPs on a single wire is analogous to that of a step-index fiber [4], while the treatment of a system of multiple wires needs a complex coupled mode theory and is applicable only for a finite number of wires. The formation of a band structure in an infinite periodic lattice of silver wires was studied earlier and the existence of photonic band gaps (PBGs) in such kind of fibers has been confirmed theoretically [5]. Here we present a simplified model for the estimation of the band edges.

BAND DIAGRAM

In order to obtain the band diagram it is possible to calculate density of states (DOS) of the hexagonal array of wires. Therefore, a finite element method (FEM) was used. Using periodic boundary conditions the propagation constants for a mesh of Bloch-wave vectors in the reciprocal space of the irreducible Brillouin zone was calculated for a large range of wavelengths. Subsequently, the density of states for every wavelength was calculated [6]. Figure 1 shows the DOS plot of a unit cell with a lattice constant (pitch) of $\Lambda = 1250\,\mathrm{nm}$ and a gold wire radius $a = 250\,\mathrm{nm}$. At small wavelengths the SPPs are well confined on the wire and do not penetrate far into the silica matrix, resulting in a dispersion not very different from a single wire. For increasing wavelengths the SPPs extend more and more into the silica and begin to interact with their neighbors which leads to a distinct splitting of the eigenvalues and to the formation of bands.

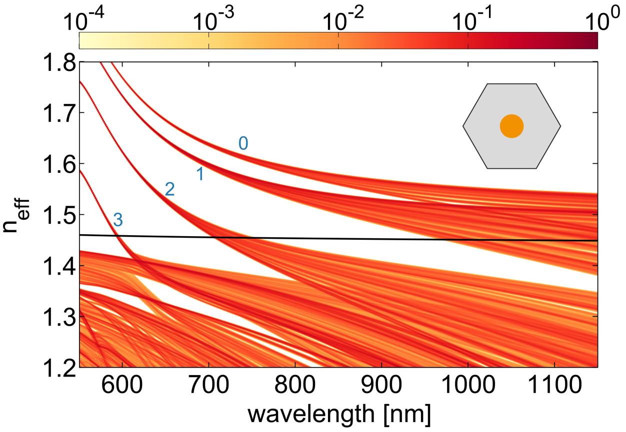

Figure 1: DOS plot of a gold-filled PCF. SPP mode orders are labeled blue. The black line represents the refractive index of silica $n_2 = \sqrt{\varepsilon_2}$.

ESTIMATION OF BAND EDGES

Although very helpful, the rigorous calculation of the DOS is extremely time consuming. For practical purposes it is sufficient to know the position of only the edges of each band in order to be able to distinguish between a bands and a band gap of the cladding of the PCF. In an earlier work, Birks et al. utilized the scalar wave equation in combination with mode symmetry properties in order to approximate the band edges of a all solid band gap fiber [7]. Unfortunately, this approach fails for the description of surface modes and

	bottom: $\vec{E}_r(R)=0, \vec{H}_\theta(R)=0$	top: $\partial\vec{E}_r/\partial r\big\|_R=0, \partial\vec{H}_r/\partial r\big\|_R=0$
C	$K'_m(\alpha)$	$m^2\hat{K}_m(\alpha)\hat{K}_m(\alpha)-\alpha^4\frac{n_{\text{eff}}^2}{\varepsilon_2}K''_m(\alpha)K''_m(\alpha)$
D	$-I'_m(\alpha)$	$-m^2\hat{I}_m(\alpha)\hat{K}_m(\alpha)-\frac{n_{\text{eff}}}{\varepsilon_2}\sqrt{\frac{\mu_0}{\varepsilon_0}}m\left[m^2+\alpha^2-1\right]+\alpha^4\frac{n_{\text{eff}}^2}{\varepsilon_2}I''_m(\alpha)K''_m(\alpha)$
E	$K_m(\alpha)$	$m^2\hat{K}_m(\alpha)\hat{K}_m(\alpha)-\alpha^4\frac{n_{\text{eff}}^2}{\varepsilon_2}K''_m(\alpha)K''_m(\alpha)$
F	$-I_m(\alpha)$	$-m^2\hat{I}_m(\alpha)\hat{K}_m(\alpha)-n_{\text{eff}}\sqrt{\frac{\varepsilon_0}{\mu_0}}m\left[m^2+\alpha^2-1\right]+\alpha^4\frac{n_{\text{eff}}^2}{\varepsilon_2}I''_m(\alpha)K''_m(\alpha)$

Table 1: Boundary condition parameters for the bottom and top band edges.

thus, has to be extended to a full-vectorial model. It is based on a circular approximation of the hexagonal unit cell, introducing the equivalent unit cell radius $R=(\sqrt{3}/2\pi)^{1/2}\Lambda$. From Maxwell's equations one can derive the dispersion relation of a metal wire (ε_1) in the circular unit cell (ε_2)

$$[\varepsilon_1\Psi_1-\varepsilon_2\Psi_2][\Psi_1-\Psi_3]=m^2. \tag{1}$$

The parameter m corresponds to the azimuthal mode order and the functions Ψ_1, Ψ_2 and Ψ_3 are given by

$$\Psi_1=\frac{b_2}{n_{\text{eff}}}\left[m+q_1\frac{I_{m+1}(q_1)}{I_m(q_1)}\right] \tag{2}$$

$$\Psi_2=\frac{b_1}{n_{\text{eff}}}\left[m+q_2\frac{C\cdot I_{m+1}(q_2)-D\cdot K_{m+1}(q_2)}{C\cdot I_m(q_2)+D\cdot K_m(q_2)}\right] \tag{3}$$

$$\Psi_3=\frac{b_1}{n_{\text{eff}}}\left[m+q_2\frac{E\cdot I_{m+1}(q_2)-F\cdot K_{m+1}(q_2)}{E\cdot I_m(q_2)+F\cdot K_m(q_2)}\right], \tag{4}$$

where $q_j=k_0a\sqrt{n_{\text{eff}}^2-\varepsilon_j}$ and $b_j=(n_{\text{eff}}^2-\varepsilon_j)/(\varepsilon_1-\varepsilon_2)$. The parameters C, D, E and F depend on the boundary conditions at the $r=R$ and are given in table 1, using the substitutions $\alpha=k_0R\sqrt{n_{\text{eff}}^2-\varepsilon_2}$, $\hat{I}_m(\alpha)=I_m-\alpha I'_m(\alpha)$ and $\hat{K}_m(\alpha)=K_m-\alpha K'_m(\alpha)$. Figure 2 shows the approximated band diagram of the same fiber as in figure 1 using equation (1). A comparison of both results shows a good agreement. Some of the bands below the silica line correspond to volume modes that are not localized at the wire surface and have not been taken into account for our calculations. We believe that this model is a very fast and promising method for the estimation of the band structure of SPPs and can be utilized as a starting point for a rigorous calculation using numerical methods.

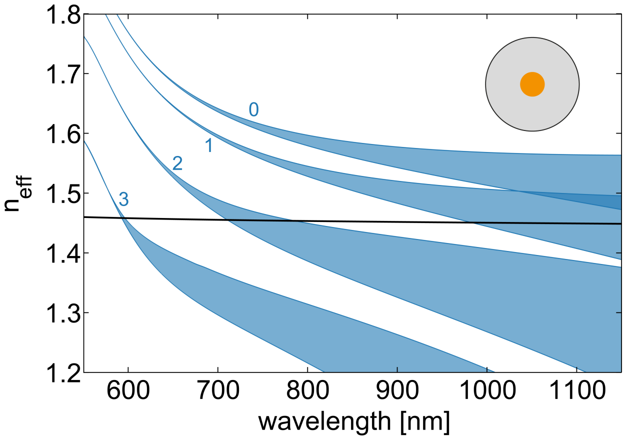

Figure 2: Approximated band diagram of the SPPs. The black line represents the refractive index of silica.

---

[1] H. W. Lee, *et al.*, *Optics Express* **19**, 12180 (2011).

[2] L. Novotny, C. Hafner, *Physical Review E* **50**, 4094 (1994).

[3] H. W. Lee, M. A. Schmidt, H. K. Tyagi, L. P. Sempere, P. S. J. Russell, *Appl. Phys. Lett.* **93**, 111102 (2008).

[4] M. A. Schmidt, P. S. J. Russell, *Optics Express* **16**, 13617 (2008).

[5] C. G. Poulton, M. A. Schmidt, G. J. Pearce, G. Kakarantzas, P. S. J. Russell, *Optics Letters* **32**, 1647 (2007).

[6] J. M. Pottage, *et al.*, *Optics Express* **11**, 2854 (2003).

[7] T. A. Birks, G. J. Pearce, D. M. Bird, *Optics Express* **14**, 9483 (2006).

A new transport regime: Hybrid Bloch-Anderson localization of light

S. Stützer*[1], Y.V. Kartashov[2,3], V.A. Vysloukh[4], A. Tünnermann[1], V.V. Konotop[5] S. Nolte[1], L. Torner[2] and A. Szameit[1]

[1] *Institute of Applied Physics, Abbe Center of Photonics, Friedrich-Schiller-Universität Jena, Max-Wien-Platz 1, 07743 Jena, Germany*

[2] *ICFO-Institut de Ciencies Fotoniques, and UniversitatPolitecnica de Catalunya, 08860 Castelldefels (Barcelona), Spain*

[3] *Institute of Spectroscopy, Russian Academy of Sciences, Troitsk, Moscow Region, 142190, Russia*

[4] *Departamento de Fisica y Matematicas, Universidad de las Americas—Puebla, 72820 Puebla, Mexico*

[5] *Centro de Física Teórica e Computacional and Departamento de Física, Faculdade de Ciencias Universidade de Lisboa, Lisboa 1649-003, Avenida Professor Gama Pinto 2, 1649-003 Lisboa, Portugal*

*Corresponding Author: *simon.stuetzer@uni-jena.de*

Abstract

We investigate the interplay of two qualitatively different localization mechanisms: Bloch oscillations and Anderson localization in a system of weakly-coupled optical waveguides.

Time-independent potentials, which frustrate transport and lead to localization of an evolving wave packet, are under investigation in many areas of physics. Probably the most prominent phenomena that tend to suppress wave transport are Bloch oscillations and Anderson localization. Both effects rely on the transformation of the infinitely extended wave packet into a spatially localized (either oscillating or stationary) mode but the underlying mechanisms are completely different. Whereas Bloch oscillation – that is an electron undergoes localized oscillations in a periodic lattice – arise in the presence of an external constant electric field [1]; Anderson localization appear in disordered potentials [2]. Beside many fields like solid-state physics, acoustics or physics of microwaves, Bloch oscillation and Anderson localization are observed in optics where in particular optical waveguide arrays are used in order to analyze the transport properties of a propagating wave packet [3, 4].

In our work, we address the interplay between these two qualitatively very different localization scenarios. Therefore we utilize arrays of evanescently coupled waveguides. We emphasize that the effect of disorder on Bloch oscillations was never analyzed before for the discrete light diffraction scenario. In contrast to recent works [5, 6] we present the first direct observation on the destruction of Bloch oscillations and gradual transition to Anderson localization. In order to describe Bloch-Anderson transition we consider light propagation in a waveguide array with a linear refractive index gradient and randomized refractive indices of individual guides. This system is adequately modeled by a Schrödinger equation for the field amplitude ψ,

$$i\frac{\partial\psi}{\partial z} = -\frac{1}{2}\frac{\partial^2\psi}{\partial x^2} - R(x)\psi - \alpha x\psi. \qquad (1)$$

Here, x and z are the (dimensionless) transverse and longitudinal coordinates, normalized to the characteristic width and diffraction length, respectively. The super-Gaussian refractive index profile of the array is described by $R(x) = \sum_j n_j \exp[-(x - jd)^6/w^2]$ with waveguides widths w, separation d and individual refractive index of each guide n_j. The refractive index gradient is described by α and a on-disorder disorder results from a random fluctuation of the refractive index, $n_j \in [n_0 - n_d, n_0 + n_d]$, where n_0 is the averaged refractive index and n_d determines the degree of so-called diagonal disorder. In order to characterize the output light distribution, we calculate the statistically averaged intensity distribution $I_{av} = \frac{1}{N}\sum_{l=1}^{N} |\psi_l(x,z)|^2$, the integral beam center, the variance and the inverse form-factor (characterizing the width of the wave packet). We run numerical simulations for several amounts of n_d and different values of α to investigate the dependencies of the quantities σ_{av} and x_{av} on those parameters.

In our experiments, we employ curved waveguide arrays in order to realize a transverse linear refractive index gradient [3]. These arrays were fabricated in fused silica using the direct laser-writing technology. The disorder was introduced by applying a random writing velocity during the writing process, $v \in [v_0 - v_d, v_0 + v_d]$, with $v_0 = 100\,\text{mm/min}$ as the mean value and v_d as an experimentally control parameter for the disorder level. The light evolution in samples was monitored by a fluorescence microscopy technique [7]. This approach opens a direct view on the wave packet evolution in our Bloch-Anderson potentials. With respect to the statistical nature of Anderson localization, we averaged intensity distributions over an ensemble of 20 random samples written with the fixed disorder level v_d.

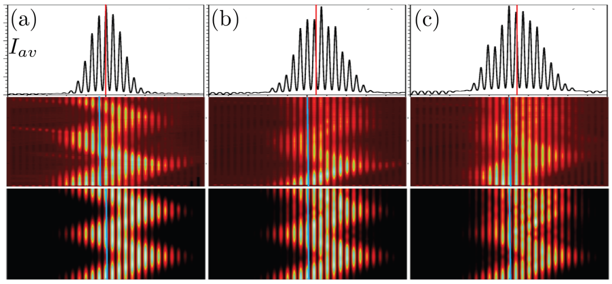

Figure 1: Experimentally observed (middle row) and calculated (bottom row) averaged intensity distributions showing hybrid Anderson-Bloch localization for broad input beam in a 100 mm long sample. The top row shows a cross section of the intensity distribution I_{av}. Panels (a) correspond to the ordered array, in (b) the fluctuations of the writing velocity are defined by $v = 14$ mm/min, while in (c) the fluctuations were $v = 28$mm/min. The blue lines indicate the center of the input beam.

A showcase of the light dynamics for a broad excitation in our sample with length $L = 100\,\text{mm}$ is depicted in Fig.1. The curvature radius $R = 1120\,\text{mm}$, yielding a Bloch period of $z_B = 38\,\text{mm}$. Note, that in the ordered system ($v_d = 0\,\text{mm/min}$) conventional Bloch oscillations occur and the output intensity distribution at the end facet of the sample is always symmetric, but shifted due to the oscillations - see Fig.1(a). // When increasing the disorder ($v_d = 14\,\text{mm/min}$), the Bloch oscillations are partially washed out and the dynamic intensity distribution approaches a static distribution, as in the case with a narrow excitation. However, now the profile is shifted and, moreover, asymmetric, which is the signature of hybrid Bloch-Anderson localization. This is clearly visible in Fig.1(b). For stronger disorder $v_d = 28\,\text{mm/min}$ the output pattern is still asymmetric, and the Anderson localization starts dominating the Bloch oscillation - see Fig.1(c). Note that the transition of the averaged intensity distribution from an asymmetric distribution (Bloch regime) to an exponentially localized wave packet for growing disorder strength that is a significant fingerprint of the hybrid Bloch-Anderson transport - see Fig.2.

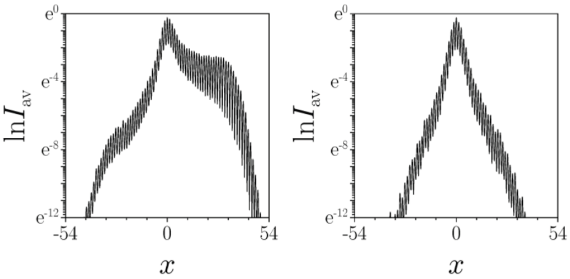

Figure 2: Averaged output intensity distributions from numerical calculations of Eq.(1) at $z = 200$, $\alpha = 0.04$ for $n_d = 0.5$ (left) and $n_d = 1.5$ (right).

In conclusion, we observed the gradual transition between two qualitatively different localization scenarios - Bloch oscillations and Anderson localization. We identified a new localization regime for broad excitations, where disorder results in the formation of asymmetric averaged intensity distributions. For our experiments we use an optical system. However, our findings are general, as clearly evident by the analogy between the quantum Schrödinger equation and the paraxial wave equation.

[1] C. Zener, Proc. R. Soc. A 145, 523 (1934); F. Bloch, Z. Phys. **52**, 555 (1928).

[2] P.W. Anderson, Phys. Rev. **109**,1492(1958).

[3] U. Peschel et al. Opt. Lett. **23**, 1701 (1998); G. Lenz et al. Phys. Rev. Lett. **83**, 963 (1999).

[4] T. Schwartz et al., Nature **446**, 525 (2007); Y. Lahini et al., Phys. Rev. Lett. **100**, 013906 (2008).

[5] E. Diez et al., Microelectronic Engineering **43-44** 117 (1998); A. R. Kolovsky, Phys. Rev. Lett. **101**, 190602 (2008).

[6] T. Schulte et al., Phys. Rev. A **77**, 023610 (2008); S. Drenkelforth et al., New J. Phys. **10**, 045027 (2008).

[7] A. Szameit et al., J. Phys. B **43**, 163001 (2010).

Novel Hetero-Junction Solar Cell Concept based on Silicon Nanowires

Florian Talkenberg*[1], Ricardo Beck[1], Daniel Jacobs[1], Stefan Illhardt[1], Andreas Dittrich[1] Arne Bochmann[12], Steffen Teichert[2] and Vladimir Sivakov[1]

[1] *Institute of Photonic Technology,*
Albert-Einstein-Straße 9, D-07745 Jena, Germany

[2] *University of Applied Sciences,*
Carl-Zeiss-Promenade 2, D-07745 Jena, Germany

*Corresponding Author: *florian.talkenberg@ipht-jena.de*

Abstract

Semiconductor-insulator-semiconductor (SIS) hetero-junction solar cell architecture based on silicon nanowires (SNW) has been realized using top-down and atomic layer deposition approaches. Influence of processing parameter of wet chemical etching and atomic layer deposition for the nanowires and hetero transition formation to optical and electrical properties of realized cells will be presented and discussed in details.

INTRODUCTION

In the foreseeable future recourses of fossil fuels will end. Apart from nuclear energy, wind and solar energy generation becomes more important. Especially the photovoltaic energy production has a high potential for improvement because of current efficiency of 18-20% of commercial cell modules. Therefore in the past several different concepts are developed. From the view of current modules as 1st generation using pn-junction, thin film solar cells represent the 2nd generation. In 3rd generation the surface of solar cells is equipped with nanostructures to improve absorption properties and increase surface. Aside this, development of multi-junction cells reaches a current efficiency of up to 40%.

Different methods can be applied for the realization of nanostructured surfaces for solar cell applications. Next to reactive ion etching (RIE), possibilities to create nanowires on a silicon surface are the vapor-liquid-solid (VLS) also called bottom-up and wet chemical etching (WCE) also called top-down methods. Benefits of WCE method [1] are the high scalability as well as easy and simple realization and a highly light absorbing surface over 90% in visible range of light.

Semiconductor-Insulator-Semiconductor (SIS) hetero-junction solar cells have been investigated since 1970s [2, 3]. The charge carrier separation is not based on a p-n-junction as usually used in solar cells, but on a quantum mechanical tunnelling process of the minority carriers through the tunnel barrier.

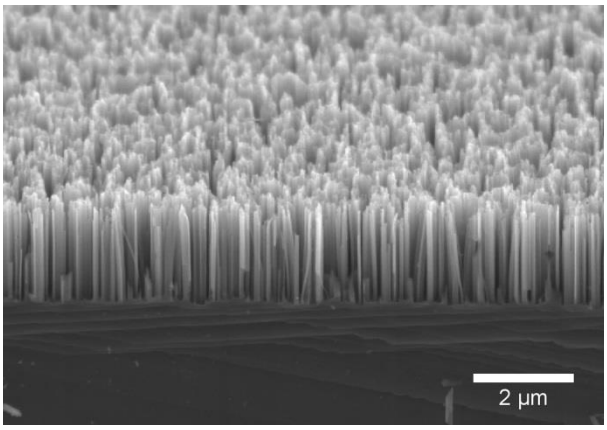

Figure 1. Scanning electron microscope (SEM) micrograph of wet chemical etched silicon nanowires in Si(100) wafer.

In previously published works by Shewchun et al. silica (SiO_2) was favoured as a tunnelling oxide which was formed unintentionally or by thermal oxidation of the silicon substrate [2, 3]. A new applied deposition technique such like atomic layer deposition (ALD) allows us to realize very homogeneous thin films at the angstrom-scale that offer the possibility to grow a new barrier materials for SIS concept.

The most used material in many electronic devices as transparent conductive oxide (TCO) and transparent front contact is Indium Tin Oxide (ITO).

One of the promising TCO alternatives is Aluminium Doped Zinc Oxide (AZO) which can reach a specific electric resistivity of ~10^{-3} Ω*cm and a transmission over 90% in visible range, and can be deposited by ALD technique as well.

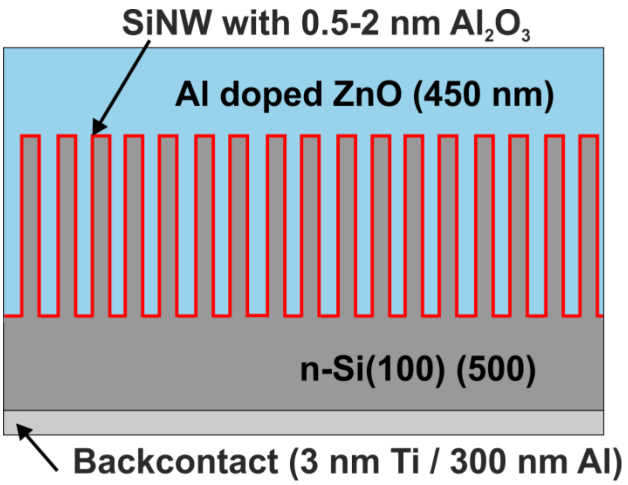

Figure 2. Schematic representation of semiconductor-insulator-semiconductor solar cell architecture based on silicon nanowires.

EXPERIMENTAL SETUP

Lowly phosphorous doped ($N_d \approx 5x10^{15}$ cm^{-3}) 4 inch Si(100) and Si(111) wafers with a 300 nm Ti/Al back contact were used as substrates for the SIS solar cells formation. SiNWs (Fig. 1) are created by a two-step wet chemical etching (WCE) process [1]. Further, samples were transferred to an atomic layer deposition reactor (OpAL, Oxford Inst.) chamber. The self-limiting ALD process enables perfect uniformity control over the deposited film thickness, so we were able to form a 5 – 20 Å thin tunnel barrier of alumina, hafnium oxide with an accuracy of 1 Å uniformly around the complex shaped nanowires. Subsequently, 450 nm thick aluminium doped zinc oxide (AZO) front contact was in situ deposited using a thermal ALD option. I-V-curves under illumination of the SiNW based solar cell are measured using a sun simulator (AM1.5, 1000 W/m², SS-80 PET).

RESULTS

Formation of semiconductor-insulator-semiconductor solar cell on wet chemical etched silicon nanowires covered with Al_2O_3 and HfO_2 tunnelling barriers by atomic layer deposition technique was realized. Basic cell parameters could be identified as well as charge carrier separation mechanism. A reproducible conversions efficiency of near 4% can be reached. Advanced investigations of produced parameters and material composition promise continuing improvement of efficiency and potential for low cost solar cells with such design.

OUTLOOK

We strongly suppose that 600-700 mV open circuit voltages and power conversation efficiency of 15% are realistic values for such type of solar cell. The most promising and important factor is the improvement of the open circuit voltage which can be tuned by the surface structure.

---

[1] V. Sivakov, F. Voigt, B. Hoffmann, V. Gerliz, S. Christiansen, INTECH; "Nanowires - Fundamental Research", ISBN 978-953-307-327-9; ed. Abbass Hashim; Chapter 3; 45-80, 2011.

[2] J. Shewchun, J. Dubow, A. Myszkowski und R. Singh, *J. Appl. Phys.* 49(2), 855-864, 1978.

[3] J. Shewchun, J. Dubow, C. W. Wilmsen, R. Singh, D. Burk und J. F. Wager, *J. Appl. Phys.* 50(4), 2832-2839, 1979.

Development of new laserglasses for high-energy systems – opportunities and challenges of alumino silicate glasses

Mirko Tiegel*[1], Andreas Herrmann[1], Christian Rüssel[1], Jörg Körner[2], Diethard Klöpfel[2], Joachim Hein[2] and Malte C. Kaluza[2]

[1]*Otto-Schott-Institut,*
Fraunhoferstraße 3, 07743 Jena, Germany

[2]*Institute of Optics and Quantum Electronics,*
Max-Wien-Platz 1,07743 Jena, Germany

*Corresponding Author: *mirko.tiegel@uni-jena.de*

Abstract

Ytterbium doped alumino silicate glasses with different network former (Li, Mg and Zn) are investigated as potential new amplifying material for high-power laser systems. These glasses show better thermo-mechanical properties than established laser glasses as e.g. lower thermal expansion coefficients and lower thermal stresses. In general they have broader emission spectra but lower fluorescence lifetimes. Interestingly fluorescence lifetimes increase with decreasing average atomic weight of the glasses.

INTRODUCTION

Nowadays, for high power glass-based laser systems the glass composition of choice are phosphate glasses due to their high solubility of rare earth ions, their relatively long fluorescence lifetimes of doped ions and their advantageous spectroscopic properties. [1]

Generally, the predominant disadvantages of these glasses are their thermo-mechanical limitations. [2] Their application in high average power laser systems results in substantial thermal loading. This is especially true if high repetition rates are necessary, producing high mechanical stresses within the glass. At ultrahigh power amplification stages, the thermally induced stress may result in the formation of micro-cracks and finally in the destruction of the lasing material. Here the application of glasses with higher thermal shock resistance is required. Therefore the biggest challenge for the development of ultrahigh power glass-based laser systems is the design and development of glasses with much improved thermo-mechanical properties, while good lasing characteristics have to be maintained.

Alumino silicate (AS) glasses are a well studied glass system with a very good glass forming ability and low crystallization tendency in a broad compositional range. [3] Furthermore these glasses possess very good mechanical and thermo-mechanical properties such as high fracture strength, a high Young's modulus and a low coefficient of thermal expansion. [4]

In addition, alumino silicate glasses have a high chemical durability, a low OH^- and platinum solubility [5] and a high solubility for rare earth compounds. Furthermore, the good glass forming ability of the alumino silicate system allows high compositional variation and therefore permits the tailoring of most physical properties. The thermal expansion coefficient, for example, has to be minimized to achieve a high thermal shock resistance. Thus AS glasses seem to be a very promising laser host material with respect to high power applications.

EXPERIMENTAL PROCEDURES

Glasses were melted from raw materials of especially high purity (Fe <10 ppm, other metals <0.5 ppm) in batches of 200 to 400 g in a covered platinum crucible at 1550 to 1620 °C. The batch compositions, calculated average atomic weights and thermal stress values are summarized in Table 1. The glasses were doped with Yb_2O_3 at a doping concentration of 1×10^{20} Yb^{3+} cm^{-3} (0.2 mol%).

Table 1: Compositions and average atomic weights Ā of the studied glasses

Sample	Composition [mol%]			Ā [u]	σ_T [MPa/K]
	Al_2O_3	SiO_2	M_2O, MO		
LiAS	20	60	20	18.4	0.71
LiMgAS	20	60	20	19.2	0.55
MgAS	20	60	20	20.2	0.55
LiZnAS	20	60	20	20.5	0.43
MgZnAS	20	60	20	21.4	0.53
ZnAS	20	60	20	22.7	0.46

Thermal stress values are calculated by:

$$\sigma_T = \frac{E\alpha}{1-\nu} \tag{1}$$

where the Young’s moduli E and the Poisson’s ratio ν are measured by ultrasonic method and the thermal expansion α is measured with dilatometry.

The fluorescence lifetimes of Yb-doped glasses are determined with pulsed excitation (970 nm) of a very small sample volume.

RESULTS

All alumino silicate glasses show small thermal stress values with less than 0.71 MPa/K. As expected magnesium and zinc alumino silicate glasses have the lowest thermal stress values.

Figure 1 shows the fluorescence lifetimes of Yb-doped alumino silicate glasses. Moderate lifetimes of 1050 to 750 µs are measured. Addition of lithium to zinc and magnesium alumino silicate increases the fluorescence lifetime up to 10 %. In general a lifetime increase with decreasing average atomic weight has been found.

In figure 2 the thermal stress values versus fluorescence lifetimes of the alumino silicate samples (blue) are compared with established phosphate laser glasses such as FP15 and P100. The figure clearly shows that AS glasses in general have low thermal stress values while fluorescence lifetimes in the range of pure phosphate glasses can be achieved. Fluoride phosphate glasses on the other hand show very high fluorescence lifetimes but poor thermo-mechanical properties.

Furthermore these alumino silicate samples show broader emission spectra than phosphate and fluoride phosphate glasses (not shown) facilitating chirped pulse amplification. Hence a lithium containing magnesium or zinc alumino silicate glass could be a promising laser material especially with respect to ultrahigh power systems or applications with high repetition rates.

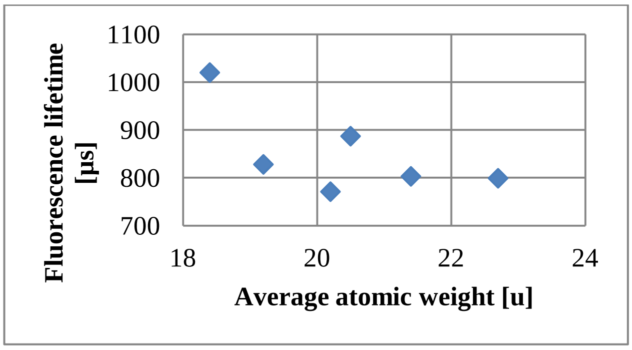

Figure 1: Fluorescence lifetime of alumino silicate glass samples versus average atomic weight.

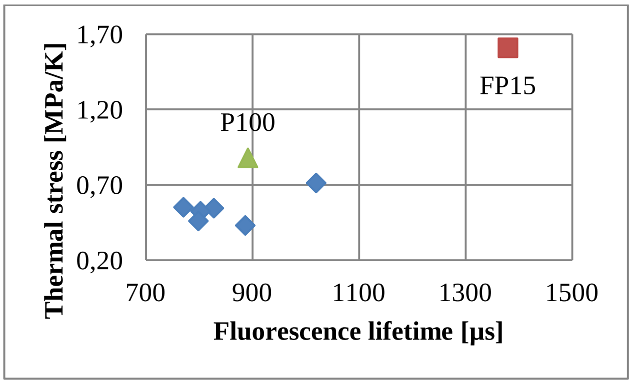

Figure 2: Thermal stress values versus fluorescence lifetime of aluminosilicate glasses, a phosphate glass (P100) and a fluoride phosphate glass (FP20) doped with 1 × 10^{20} $Yb^{3}+$ cm^{-3}.

---

[1] J. H. Campbell, J. S. Hayden and A. Marker, Int. J. Appl. Glass Sci., **2**, 3–29 (2011).

[2] J. H. Campbell and T. I. Suratwala, J. Non-Cryst. Solids, **263–264**, 318–341 (2000).

[3] S. M. Logvinkov, G. D. Semchenko and D. A. Kobyzeva, Refractories, **37**, 378–381 (1996).

[4] P. Wange, T. Höche, C. Rüssel and J. Dieter Schnapp, J. Non-Cryst. Solids, **298**, 137–145 (2002).

[5] T. Izumitani, M. Matsukawa and H. Miyade, NIST Spec. Publ., **756**, 29–34 (1988).

Generation of Optical Solenoid Beams for Particle Manipulation

Christian Vetter*[1], Toni Eichelkraut[1], and Alexander Szameit[1]

[1]*Institute of Applied Physics, Abbe Center of Photonics,*
Friedrich-Schiller-Universität Jena, Max-Wien-Platz 1,
D-07743 Jena, Germany

*Corresponding Author: *Christian.Vetter@uni-jena.de*

Abstract

We demonstrate the experimental realization of solenoid optical beams that are rotating in space and time. Those beams are of particular interest in optical micro-manipulation and are achieved by means of interfering higher-order Bessel beams.

INTRODUCTION

The remote manipulation of micro- and nanosize particles is crucial in modern generation nano-technology. Beyond that, the ability of pushing and dragging living cells at will would be a priceless tool in biology and other life science. While conventional beams are only capable of displacing particles along the beam propagation direction, solenoid beams might offer continuous bidirectional transport of large amounts of particles [1]. Here, we present theory on solenoid intensity profiles, propose a flexible, experimental way to achieve them, and discuss the ability to control the beams in temporally.

THEORY

Bessel beams of n^{th} order exhibit a helical phase front with n rotations over one oscillation period. When interfering two Bessel beams of different order, the helicity leads to a constructive interference along a spiraling path [2, 3]. This can be understood by considering the electric field distribution of a Bessel beam, that is given by

$$E(r,z,t) = \mathcal{J}_{\mathrm{n}}(k_{\mathrm{r}} r)\, \mathrm{e}^{\mathrm{i}n\varphi}\, \mathrm{e}^{\mathrm{i}(k_z z - \omega t)} \tag{1}$$

with $\mathcal{J}_{\mathrm{n}}$ the Bessel function of the first kind, $k = \sqrt{k_{\mathrm{r}} + k_z}$ the wavenumber, $\mathrm{e}^{in\varphi}$ the azimuthal (helical) phase term and z as the propagation direction. Substituting this definition in the equation for two beam interference and assuming $I(r,t) \sim |E(r,t)|^2$ leads to

$$\begin{aligned} I(r) = {} & \mathcal{J}_{\mathrm{n}}^2(k_{\mathrm{r1}} r) + \mathcal{J}_{\mathrm{m}}^2(k_{\mathrm{r2}} r) + 2\, \mathcal{J}_{\mathrm{n}}(k_{\mathrm{r1}} r) \mathcal{J}_{\mathrm{m}}(k_{\mathrm{r2}} r) \\ & \times \cos((n-m)\varphi + (k_{\mathrm{z1}} - k_{\mathrm{z2}})z)\,. \end{aligned} \tag{2}$$

The last term on the right hand side describes a rotation in space as long as $\Delta k_{\mathrm{z}} = k_{\mathrm{z1}} - k_{\mathrm{z2}} \neq 0$. Figure 1 shows some examples for intensity profiles at a fixed position $z = 0$. Please note that the accelerating behavior is by no means in conflict with fundamental physical law since the center of energy still propagates along a straight line.

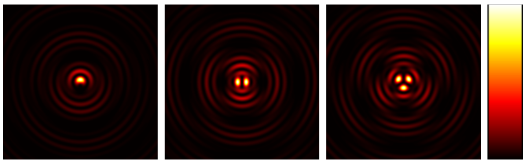

$n = 0$, $m = -1$ $n = +1$, $m = -1$ $n = +1$, $m = -2$

Figure 1: Exemplary intensity distributions for different order Bessel beams. The quantities n and m represent the order of the involved Bessel functions.

SETUP

For the generation of interfering higher-order Bessel beams, we exploit the fact, that Bessel beams are a conical superposition of plane waves. Hence, the Fourier spectrum of a Bessel beam exhibits a sharp ring. Within a Mach-Zehnder setup, two axicon lenses are used to generate different zero order Bessel beams. They are Fourier transformed by means of a lens and the resulting rings are imaged onto a Spatial Light Modulator (SLM). The SLM allows to add different phase helicities to both rings which are subsequently transformed back using a second lens. As both rings produce Bessel beams of different order at the same lateral position, the interference corresponds to the previously shown theory. In order to rotate the resulting solenoid beam temporally, a continuous phase offset can be added to one of the Bessel beams. Figure 2 illustrates the above described setup.

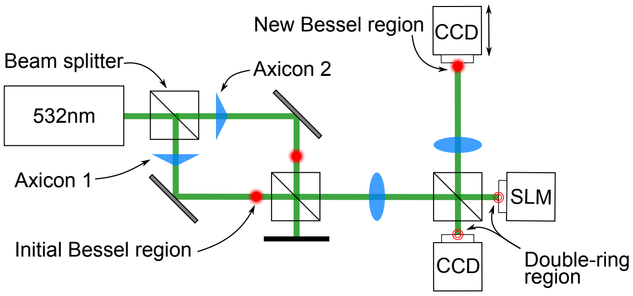

Figure 2: Experimental setup for spiral generation.

Results & Discussion

As part of our experiments, axicons with base angles of 1° and 2° were used in combination with a lens of focal length $f = 200\,\mathrm{mm}$ which results in ring diameters of 1.8 mm and 2.7 mm, respectively. The back transformation was performed by a lens exhibiting the same focal length f. With these values, simulations based on Equation 2 as well as various experiments have been performed. Figure 3 presents exemplary results. The beam has been rotated temporally by continuously adding a phase offset to one of the rings on the SLM. Consequently, each picture in Figure 3 is rotating in time. The speed and direction of the rotation are controlled by the SLM. For a smooth rotation, the angular velocity should not exceed the frame rate of the SLM.

It has been demonstrated experimentally as well as in theory that interfering Bessel beams of different order result in various intensity profiles that exhibit a solenoid behavior. We proposed an experimental setup which provides control over ring diameter and imaging properties. Furthermore, the setup offers an easy access to the angular orientation of the beam and thus enables a temporal rotation. We believe that our findings will find use particularly in the manipulation of complex fluids and nano-particles [4].

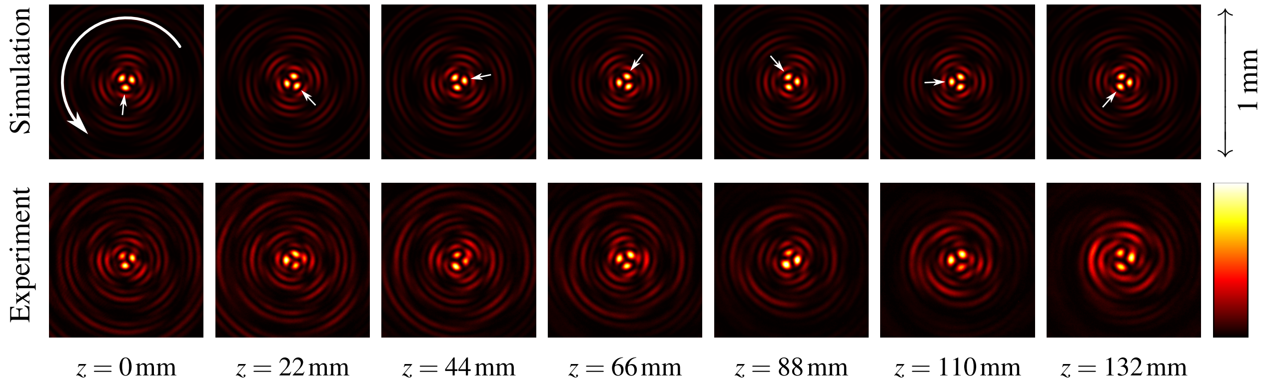

Figure 3: Spatial intensity rotation resulting from interfering Bessel beams exhibiting the orders $n = 1$ and $m = -2$. The resulting solenoid is rotatable by adding a phase offset to one of the Bessel beams.

References

[1] S. Lee, Y. Roichman and D. G. Grier, in *Optics Express* Vol. **18**, No. 7, Mar 2010

[2] R. Vasilyeu, A. Dudley, N. Khilo, and A. Forbes, in *Optics Express*, Vol. **17**, No. 26, Dec 2009

[3] R. Rop, A. Dudley, C. López-Mariscal, and A. Forbes, in *Journal of Modern Optics*, Vol. **59**, No. 3, Feb 2012

[4] C. Rotschild *et al.*, in *Frontiers in Optics*, OSA Technical Digest (CD), paper FME2, 2008

Ultra-long enhancement cavities as a promising approach to raise femtosecond lasers to a new level of output parameters

L. von Grafenstein,*[1] S. Breitkopf,[1] T. Eidam,[1,2] I. Pupeza,[4] H. Carstens,[4] S. Holzberger,[4] E. Fill,[4]
A. Klenke,[1,2] J. Limpert[1,2,3] and A. Tünnermann[1,2,3]

[1]*Institute of Applied Physics, Abbe Center of Photonics, Friedrich-Schiller-Universität Jena,*
Albert-Einstein-Str. 15, 07745 Jena, Germany

[2]*Helmholtz-Institute Jena,*
Max-Wien-Platz 1, 07743 Jena, Germany

[3]*Fraunhofer Institute for Applied Optics and Precision Engineering,*
Albert-Einstein-Str. 7, 07745 Jena

[4]*Max-Planck-Institute for Quantum Optics,*
Hans-Kopfermann-Str. 1, 85748 Garching

*Corresponding Author: *lorenz.von-grafenstein@uni-jena.de*

Abstract

We propose a concept to scale up the pulse energy of state-of-the-art femtosecond-fiber-amplifiers by coherent temporal combination. As a combining element for the temporally 100 ns separated pulses (10 MHz repetition rate) we suggest a non-steady-state enhancement cavity using a fast switching-element to dump the enhanced pulses at 15 kHz.

INTRODUCTION

Enhancement cavities are passive optical resonators with very high finesse. The circulating power inside these resonators can be several orders of magnitude larger than the in-coupled power. Nowadays, such cavities are commonly used for the generation of high-order harmonics at high repetition rates. With fs-pulses an enhancement factor of 1800 has been shown [1]. The pulses from a mode-locked laser are continuously coupled in and overlap in the cavity. Due to constructive interference they will form one, very intense pulse which is circulating inside the resonator. The henceforth followed approach is to dump the high energetic pulse repeatedly after 666 pulses are stacked. In this way the 10 MHz repetition rate of a front-end femtosecond-fiber-CPA system is transformed to high pulse energies without significant loss of average power. A schematic setup is depicted in Fig. 1. In a first stage, the created pulses will achieve energies at the multi-mJ-level at a repetition rate of 15 kHz. This is already way above the state of the art of any known laser concept. Future systems could have even higher output parameters and be used to drive the next generation of particle accelerators [2].

CONCEPT

The dumping of pulses enhanced within a cavity has been shown multiple times during the past decades [3-5]. The free spectral range of the cavities in these experiments is typically around 100 MHz. Therefore, a very fast switch with a rise time of around 10 ns is necessary to couple out a single pulse. All of these approaches used a fast acousto-optical modulator (AOM) as switching

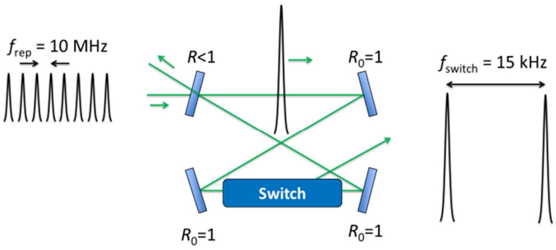

Figure 1: Schematic setup of an enhancement-cavity based amplification. The high initial repetition frequency f_{rep} is transformed to high pulse energies at a lowered repetition rate f_{switch}.

element. The transmissive nature of these elements limits the pulses in average and peak power due to introduced dispersion, losses and possibly destruction. Since even losses of less than 0.1 % hamper an effective enhancement of 666 pulses significantly, only a reflective switch is suitable for out-coupling at higher pulse energies. Several switching elements are under investigation at the moment. The most promising one is a fast rotating chopper wheel with mirrors attached to its rim. During the build-up, no mirror interacts with the circulating field. When the 666th pulse circulates, a mirror enters the beam path and couples the pulse out. To reach a technologically feasible switching time of about 100 ns, the duration between two successive pulses - and, therefore, the cavity length - has to be as long as possible. Using a lower repetition rate at the same average power allows additionally higher initial pulse energies. This results in a lower number of pulses that are necessary to reach a high energy of the enhanced pulse. On the downside, the adjustment and stabilization gets more challenging with increasing cavity length. Therefore, a cavity length of 30 m has been found to be the most suitable solution.

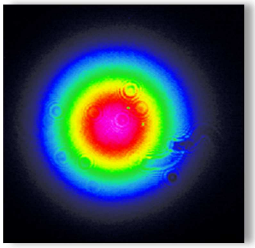

Figure 2: Intensity profile of the enhanced beam.

EXPERIMENTAL SETUP & PRELIMINARY RESULTS

The chosen cavity length of 30 m equals 10 MHz repetition rate. It is formed by 15 ultra-low-loss mirrors and one in-coupling mirror which are arranged in a bow-tie ring geometry. The challenging stabilization of such a long cavity is done using the Pound-Drever-Hall method. First experiments have been carried out with a continuous-wave oscillator at 1064 nm as seed. So far, enhancement factors of up to 500 have been achieved, which is to our knowledge the highest enhancement that has been shown in such a long cavity. The enhancement was also successfully stabilized for several minutes with an excellent spatial mode quality (See Fig. 2).

OUTLOOK

In the next development stage an oscillator delivering fs-pulses will be used as a seed for the cavity before a state-of-the-art front-end fiber-CPA-system will be employed. The stretched pulses will be enhanced to confirm the high power capability of this concept.

---

[1] I. Pupeza, T. Eidam, J. Rauschenberger, B. Bernhardt, et al., Optics letters **35**, 2052–2054 (2010).

[2] G. Mourou, B. Brocklesby, T. Tajima, and J. Limpert, Nature Photonics **7**, (2013).

[3] T. Heupel, M. Weitz, and T. W. Hänsch, Optics letters **22**, 1719–21 (1997).

[4] E. O. Potma, C. Evans, X. S. Xie, R. J. Jones, and J. Ye, Optics letters 28, 1835–7 (2003).

[5] R. J. Jones and J. Ye, Optics letters **29**, 2812–4 (2004).

[6] R. W. P. Drever, J. L. Hall, F. V. Kowalski, J. Hough, G. M. Ford, a. J. Munley, and H. Ward, Applied Physics B Photophysics and Laser Chemistry **31**, 97–105 (1983).

Blessings and curse of silver in plasmonic nanostructures

Benny Walther[1], Stefan Fasold[1], Matthias Falkner[1], Bernd Schröter[2], and Thomas Pertsch[1]

Friedrich-Schiller-Universität Jena
[1]Institut für Angewandte Physik
Albert-Einstein-Straße 15, 07745 Jena, Germany

[2]Institut für Festkörperhysik
Helmholtzweg 5, 07743 Jena, Germany

[*]Corresponding Author: *benny.walther@uni-jena.de*

Abstract

With its unparalleled plasmonic properties silver is a favorable material for nanostructures to operate at visible light. We investigate origin and consequences of the chemical degradation process such silver structures are subject to and find ways to prevent the sample aging.

INTRODUCTION

Metallic nanostructures continue to be a very active field of research. By supporting surface-plasmon polariton resonances these structures interact quite strongly with light and therefore promise novel applications in optics and life sciences. New devices for light shaping, imaging, sensing and microscopy are just some among them.

While size, shape and arrangement of the nanostructures are crucial tuning parameters to obtain the intended functional response, the other critical ingredient is the material the structures are made of. Noble metals have favorable optical properties and provide strong resonances at visible and near-infrared frequencies. Silver, though, is the only choice among them when distinct and narrow resonances at the bluish end of the visible spectrum are asked for. With its high plasma frequency and low propagation losses silver would be an ideal material e.g. for the design of advanced multi-color metamaterial holograms [1]. Other metals, like gold, whose resonances are restricted to the red and infrared regardless of size and shape of the nanostructures, cannot fulfill the same task.

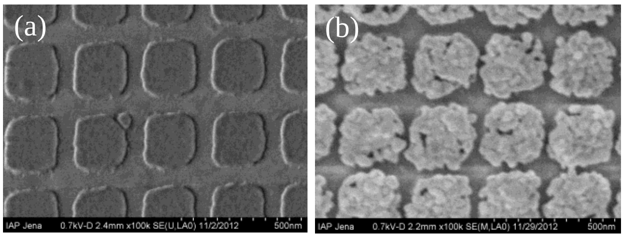

Figure 1: Silver nanoplates with a period of 300 nm (a) right after fabrication, (b) four weeks later.

However, unlike gold, silver has a tendency to be chemically unstable. The known process of corrosion, where silver tarnishes by exposure to air, has tremendous effects on the optical performance of silver-based nanomaterials. This constitutes a problem either for samples which cannot be sealed with an appropriate protection layer (applied as spin-on coating or by ALD) or for samples which are scheduled to obtain such a layer but whose fabrication process extends over a longer time due to delays and waiting periods. Since both cases are an issue at our institute, especially regarding the goal of designing and fabricating metamaterial holograms for visible wavelengths, the process of silver degradation has been investigated. In the talk the interesting and somewhat contradicting results are presented.

SOLVING THE MYSTERY

The literature comes up with different explanations on what is happening when silver nanoparticles degrade. Some scientists attribute the degradation to a reaction of silver with oxygen [2]. More commonly expressed is the opinion that reactions with ambient sulfur (H_2S, OCS) lead to the formation of Ag_2S [3, 4]. These reactions also require the presence of oxygen, though,

$$4\ Ag + O_2 + 2\ H_2S \rightarrow 2\ Ag_2S + 2\ H_2O,$$

and are enhanced by humidity and the presence of NO_2. Figure 1 shows scanning-electron microscopy (SEM) images of silver nanoplates fabricated at our institute. While in the fresh sample the 30 nm thick silver layer is smooth, Figure 1a, four weeks of storage in laboratory air leave the surface appear ragged an covered with crystallites, Figure 1b. However, the initial assumption that in fact Ag_2S-nanocrystallites had formed, needed yet to be confirmed.

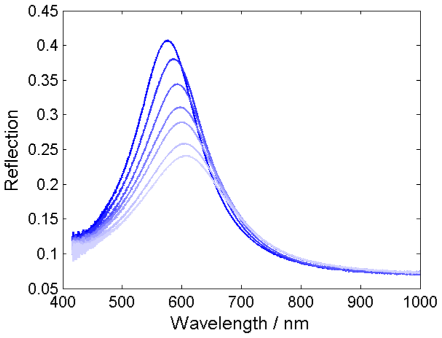

Figure 2: Reflection spectra of aging silver structure.

Meanwhile the aging process had also changed the optical properties of the nanostructures. The resonance supported by the periodically arranged, rectangular plates redshifted by around 30 nm during that time. Also, the resonance had weakened and broadened as seen in the reflectivity spectra shown in Figure 2. These measurements were performed during the four-week silver-aging process with a Bruker FTIR Hyperion 2000 spectrometer. Monitoring the spectra continuously, a sensitive relationship to temperature and humidity could not be established. Instead it seems that turbulence in the room air on weekdays (air conditioning, people traffic), supplying fresh reactants to the surface, increased the rate of degradation.

The spectral measurements involved a significant amount of irradiation of the sample. The known reshaping process of silver particles due to UV-light exposure [5] can confidently be excluded here, as prior and later non-irradiated samples showed similar aging. Nevertheless, lighting conditions as well as atmospheric conditions needed to be controlled to draw further conclusions. Therefore, samples with continuous silver films on SiO_2 and/or Si substrates were stored under various atmospheres (vacuum, N_2-atmosphere, H_2S-enriched atmosphere, laboratory air, office air) and at the same time under various lighting conditions (no light/shadowed, normal office light, strong halogen lamp with/without filters for VIS and NIR). The samples were characterized by SEM images before and after storage. Also, analyses of the chemical composition (elements) were carried out by means of energy-dispersive x-ray analysis (EDX) and by Auger-electron-spectroscopy.

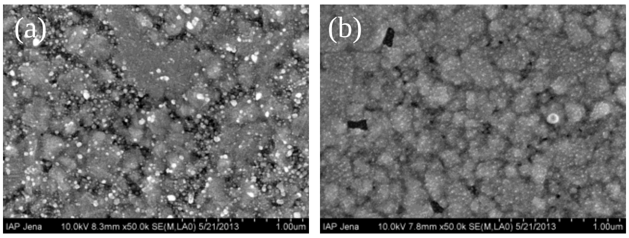

Figure 3: Silver film after storing (a) in light and (b) in shadow.

CONCLUSION

The evaluation of the data indicates, as expected, that vacuum and nitrogen atmosphere provide nearly perfect protection to the sample. In the other cases small crystallites had formed at a quantity depending on atmosphere and lighting, Figure 3. Further, the chemical analyses decline the theory that oxygen is involved as an end product of the silver degradation reaction. Instead, the presence of sulfur seems to correlate with the visually perceived (via SEM) crystallites. However, in some cases strong degradation did not coincide with high levels of sulfur. The presence of other elements such as Na and Cl, which were both detected (not necessarily both at the same time), might play a major role.

As part of the study's outcome a sample storage box was constructed which allows for keeping silver samples in N_2 atmosphere and/or at low pressure (~0.2 bar abs.) for several days or even up to weeks.

[1] B. Walther, C. Helgert, C. Rockstuhl, F. Setzpfandt, F. Eilenberger et al., Adv. Mat. **24,** 6300 (2012).

[2] M. Losurdo, I. Bergmair, M. M. Giangregorio, B. Dastmalchi et al., J. Phys. Chem. C **116**, 23004 (2012).

[3] M. D. Mcmahon, R. Lopez, H. M. Meyer III, L. C. Feldman et al., Appl. Phys. B **80**, 915 (2005).

[4] W. Cao, H. E. Elsayed-Ali, Materials Letters **63**, 2263 (2009).

[5] Q. Zhang, J. Ge Dr., T. Pham, J. Goebl, Y. Hu et al., Angew. Chem. **121**, 3568 (2009).

Velocity Map Imaging of Trajectory Controlled Above-Threshold Ionization Spectra of Xenon Using the Two-Color Field Technique

Daniel Würzler*[1], Max Möller[1,2], Frank Meyer[1], A. Max Sayler[1,2], Gerhard G. Paulus [1,2]

[1] *Institut für Optik und Quantenelektronik, FSU Jena*
Max-Wien-Platz 1, 07743 Jena, Germany

[2] *Helmholtz Institut Jena*
Max-Wien-Platz 1, 07743 Jena, Germany

*Corresponding Author: *daniel.wuerzler@uni-jena.de*

Abstract

Recent researches show that adding a weak second harmonic field perpendicular to a strong fundamental beam provides the ability to control high harmonic generation by suppressing recombination of certain electron trajectories. In this study, a collinear interferometer is built in order to combine an ultrashort laser pulse with its second harmonic field in the target area. Subsequently, control over electron trajectories of Xenon in above-threshold ionization is demonstrated.

INTRODUCTION

Many strong-field phenomena like high harmonic generation, non-sequential double ionization and above-threshold ionization (ATI) depend on the trajectory of freed electrons in the oscillating laser field. Therefore, the ability to govern the trajectories provides a general tool to investigate the ultrafast dynamics with sub-cycle resolution.

It has been shown that adding a weak second harmonic field perpendicular to a strong fundamental beam is suitable for controlling the classical electron trajectories, as the energy, the time of flight and the spatial symmetry of the trajectories is sensitive to any additional field [1]. In addition, adding a second or third harmonic field parallel to the fundamental field is capable to change the probability of the different trajectories [2].

In this study, the perpendicular two-color technique is applied to control electron trajectories in ATI of Xenon. First a collinear two-color interferometer is realized and second the angular dependent ATI spectra are observed by using a velocity map imaging spectrometer (VMI).

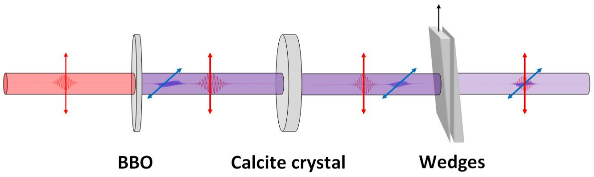

Figure 1: Schematic of the two-color setup

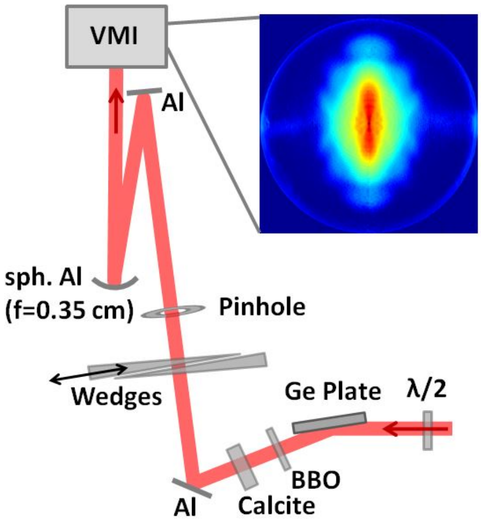

Figure 2: Schematic of the experimental setup

TWO-COLOR FIELD

For the mathematical description of the two-color field, the waveform of both components is considered to be the combination of a Gaussian envelope, where the full-width at half of the maximum duration is given by τ, with a linear oscillation with carrier frequency ω, the relative Phase φ_{rel} and the peak intensity E_0 [3]. One writes $E_{red}(t) = E_{r_0} e^{-2\ln 2\left(\frac{t}{\tau}\right)^2} \cos(\omega t)$ for the fundamental field and $E_{blue}(t) = E_{b_0} \cdot e^{-2\ln 2\left(\frac{t+\Delta t}{\tau}\right)^2} \cdot \cos(2\omega t + \varphi_{rel})$ for the second harmonic field. If both pulses propagate through optical media, different group velocities cause a delay between the red and blue part of the field. The displacement is given by $\Delta t = \frac{L}{v_{g_{red}}} - \frac{L}{v_{g_{blue}}}$, where L is the thickness of the optical medium and v_g the group velocity of the field component.

EXPERIMENTAL SETUP

The collinear interferometer (Fig. 1) consists of a 200 μm BBO, a 3000 μm birefringent calcite crystal and two fused silica wedges on a translation stage. The collimated beam of the used Ti:Sapphire chirped-pulse laser system (800 nm / 35 fs pulses) propagates through the BBO, whereby up to 15 % of second harmonic light is generated. The different group velocities of the fundamental and the SHG pulse in air and the BBO need to be compensated to achieve a pulse overlap in the target area. Hence, the propagation velocity of 400 nm light in BBO, air and fused silica is slower then the propagation velocity of 800 nm light, the group velocity dispersion is being precompensated by the calcite. Therefore the calcite crystal is arranged so that the blue light propagates over the fast axis. The wedges are used to overlap the beam in the target as well as to control the relative phase. To find the pulse overlap the brightness of the VMI pictures has to be maximized. Fig. 2 shows the whole setup with an example of a VMI picture of Xenon acquired with assumed intensity of 10^{14} W/cm^2 with a ratio E_{b_0}/E_{r_0} of ∼0.35. The intensity is controlled with a half-wave plate and a germanium plate which is set up in Brewster reflection.

RESULTS

Fig. 3 shows the first measured results off Xenon for changes of the wedge position, which corresponds to a change of $\sim 4\pi$ in the relative phase. The results show a clear modulation of the plateaus according to changes in the relative phase, but also a asymmetry between both plateaus, which is modulated with the half periodicity. This asymmetry shows a great similarity to the results for two-color measurements with parallel field components [4]. This could be caused by a discrepancy between the BBO angle and the phase matching angle, so the BBO creates a small SHG component parallel to the fundamental field.

In conclusion, the results show the capability to overlap the pulses and control the electron trajectories by the relative phase between the two fields. Further measurements will focus on an improvement of the alignment and using a smaller E_{b_0}/E_{r_0} ratio.

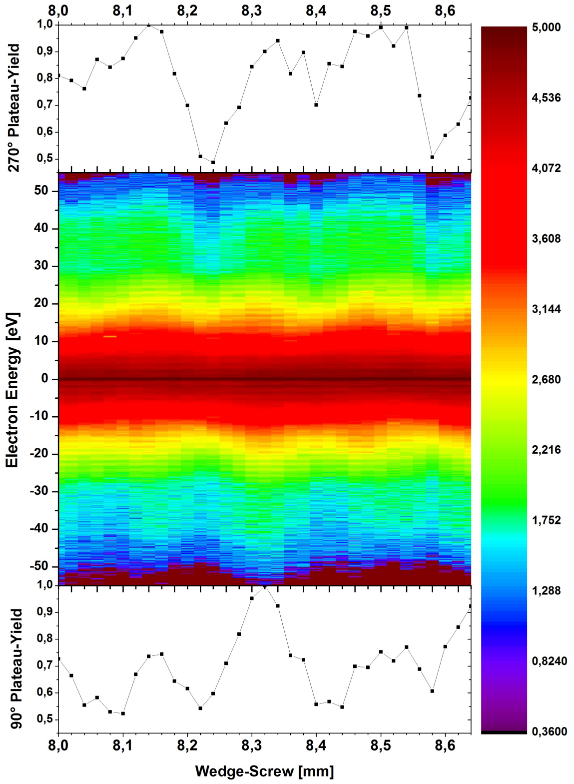

Figure 3: ATI-spectra of Xe in direction of the polarization of the fundamental laser field, with comparison of the total plateau yields (between 30 eV - 50 eV) as function of the position of the wedges

---

[1] D. Shafir et al., *Nature* **485**, 7398 (2012).

[2] T. Zuo et al., *Physical Review A* **51**, 3991-3998 (1995).

[3] Z. Chang, *Fundamentals of Attosecond Optics*, (CRC Press / Taylor & Francis, Boca Raton, 2011).

[4] H. Li et al., *Physical Review A* **84**, 043429 (2011).

Ionization of atomic Ions under elliptical Polarization

P. Wustelt*[1,2], M. Möller[1,2], T. Rathje[1,2], A. M. Sayler[1,2] and G. G. Paulus[1,2]

[1] *Institut für Optik und Quantenelektronik, Max-Wien-Platz 1,*
07743 Jena, Germany

[2] *Helmholtz Institut Jena, Max-Wien-Platz 1,*
07743 Jena, Germany

*Corresponding Author: *philipp.wustelt@uni-jena.de*

Abstract

We study the sequential multiple ionization of noble gas ions in intense, femtosecond laser pulses. We measure the ion momentum distribution after single-, double, triple- and quadruple-ionization. Using elliptically polarized laser pulses provides additional information about the ionization times. An analysis of the ion momentum distributions gives the electron kinematics of each ionization step.

INTRODUCTION

Tunneling ionization of atoms and molecules in strong laser fields is a fundamental quantum process. In attosecond science tunneling of an electron trough the barrier formed by the superposition of the electric field and the atomic potential is assumed to act as a trigger for all the subsequent dynamics, such as above threshold ionization (ATI), nonsequential double ionization, high harmonic generation (HHG) and attosecond pulse generation. Therefore, understanding the timing of single and multiple ionization is of particular importance. Nevertheless, there are still open questions: At what time during the pulse was an electron ionized? How good are the commonly used tunneling formulas? Are there electron-electron correlation mechanisms that are not induced by recollision? Is there a tunneling delay?

Recent experiments [1] challenge the validity of the independent-electron approximation in sequential double ionization. The measured release times of the second electron in double ionization disagrees with the augmented quantum tunneling (AQT) formula.

To investigate the multi-electron dynamics in the ionization process elliptically polarized laser light is a useful tool. In contrast to linear polarization, for elliptically polarized many-cycle pulses, the final ion momentum distribution provides complete information on the ionization field strength as well as the ionization time [2].

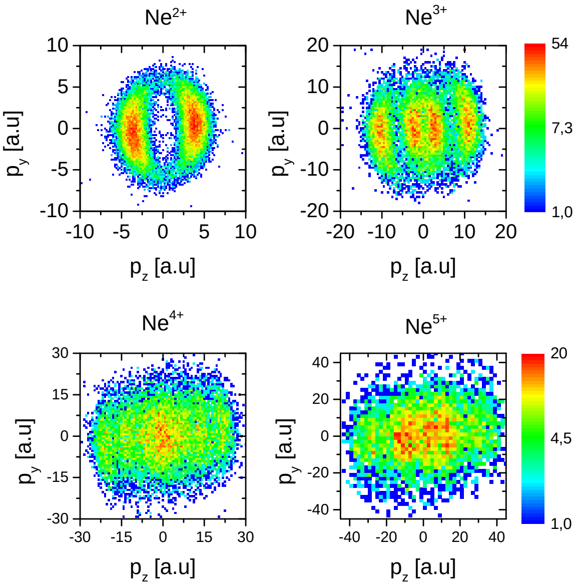

Figure 1: Measured ion momentum distributions in the polarization plane for single, double, triple and quadruple ionization of Ne^{+}-ions. The major polarization axis is y axis ($\varepsilon = 0.74$). The peak intensity of the laser pulse was 4±2 $\cdot 10^{16}$ W/cm^2. Note that the peak intensity is only the upper limit of the intensity and not the intensity where ionization occurs. Most of the ionization occurs before the peak of the laser pulse. The different final charge states of the ions are created in different areas of the focal volume.

Typically, the Keldysh parameter, i.e. $\gamma = \sqrt{\frac{I_p}{2U_p}}$ where I$_p$ is the atomic ionization energy and U$_p$ is the ponderomitive potential in the laser field, is used to separate the ionization process into two limiting cases [3]. Multi-photon ionization occurs at low-intensity and short wavelength i.e. $\gamma \gg 1$,while for long wavelength, high intensity fields ($\gamma \ll 1$), the ionization is understood to be quasi-static tunneling of the electron through the potential barrier, which is formed by the superposition of the laser field and the binding potential of the molecular or atomic target. Here, we will present results covering a range of Keldysh parameters from $\gamma \approx 0.2$ to $\gamma \approx 1$.

EXPERIMENTAL SETUP

The imaging technique used here provides complete information about the 3D momentum of each ionized particle [4]. A beam of Ne$^+$ ions is produced in a hollow-cathode discharge duoplasmatron ion source and accelerated to an energy of 8 keV. The interaction of ion and laser beam takes place in the weak longitudinal electrostatic field of a spectrometer, which allows the direct separation of different final charge states in the time-of-flight (TOF) spectrum. Additionally, an electro-static field perpendicular to the ion beam after the interaction region separates the different charge states in space.The detector is a position- and time-sensitive microchannel plate (MCP) delay-line detector (DLD). The 3D momentum gained by the nucleus from the ionization(s) is then reconstructed from the time and position information recorded for each event. A Ti:Sapphire chirped-pulse amplification (CPA) system is used to produce 800 nm, 36±3 fs, 10±0.2 mJ, pulses at 1 kHz, which are then focused with a f=150 mm, 90° off-axis parabolic mirror to a peak intensity of $(4\pm2)\cdot 10^{16}$ W/cm^2. The ellipticity, ε, is adjusted using a quarter-wave plate.

RESULTS AND DISCUSSION

The ion momentum distributions for single, double, triple and quadruple ionization of single charged Neon ions for an ellipticity ε=0.74 are shown in Fig. 1 . For the case of single ionization the radial size of the distributions gives the vectorpotential and hence the time during the intensity envelope when the ionization occurred. For double ionization the distribution is a convolution of the two independent ionization steps, where the momentum of the ion is the sum of the momenta of the first and the second electron. Therefore, it is possible to deconvolute the four peak structure to determine the first and the second ionization time (see Fig. 2). The two outer peaks of the four peak structure corresponds to the case, where the two electrons are emitted in the same direction, the two inner peaks to the case, where the two electrons are emitted to opposite directions. Consequently, for triple- and quadruple-ionization a splitting into eight peaks and sixteen peaks is observed.

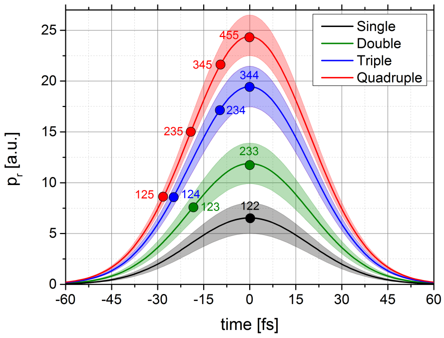

Figure 2: The radial momentum $p_r = \sqrt{(\varepsilon^2+1)^2((p_z/\varepsilon)^2+p_y^2)}$ resulting from an elliptically polarized Gaussian laser pulse for all ionization steps up to quadruple ionization steps are retrieved from the deconvolution of the measurement shown in Fig. 1. For example, the step '123' means the ionization step from Ne^+ to Ne^{2+} from all ions ending in the final charge state of Ne^{3+}.

CONCLUSION

In conclusion, sequential multiple ionization up to quadruple ionization of Ne$^+$-ions by elliptically polarized pulses is investigated. We have developed a method to deconvolute the momentum distribution of multiple ionized ions and extract the information about all ionization times during the laser pulse for each ionization step in multiple sequential ionization.

---

[1] A. N. Pfeiffer, C. Cirelli, M. Smolarski, R. Dörner, U. Keller, *Nature Physics* **7**, 428 (2011).

[2] X. Wang, J. H. Eberly, *Physical Review A* **86**, 013421 (2012).

[3] L. Keldysh, *Sov. Phys. JETP* **20**, 1307 (1965).

[4] I. Ben-Itzhak, *et al.*, *Physical Review Letters* **95** (2005).

Extreme Ultraviolet Surface High Order Harmonic Radiation from JETI-40 – Recent Experiments and Plans for the Future

Mark Yeung[1,*], Matt Zepf[1], Christian Rödel[1,2], Jana Bierbach[1,2], Arpa Galestian Pour[1,2], Martin Wünsche[1,2], Silvio Fuchs[1,2], Stephan Kuschel[1,2], Erich Eckner[1,2], Gerhard Paulus[1,2], Thomas Hahn[3], Dirk Hemmers[3], Christian Stelzmann[3], Georg Pretzler[3], B. Dromey[4]

[1]*Helmholtz-Institut Jena, Fröbelstieg 3, 07743 Jena, Germany*

[2]*Institut für Optik und Quantenelektronik, Friedrich-Schiller-Universität Jena,*
Max-Wien-Platz 1, 07743 Jena, Germany

[3]*Institut für Laser- und Plasmaphysik, Heinrich-Heine-Universität Düsseldorf,*
Universitätsstraße 1, 40225 Düsseldorf, Germany

[4]*Department of Physics and Astronomy, Queen's University Belfast,*
University Road, Belfast, BT7 1NN, UK

[*]Corresponding Author: *m.yeung@gsi.de*

Abstract

Surface high harmonic generation is a promising route to high brightness XUV sources. The main mechanism behind this phenomenon is discussed and the current state of experiments on the JETI-40 laser are presented.

INTRODUCTION

When Einstein proposed his special theory of relativity [1], one of its predictions described the frequency upshifting of a light pulse that is reflected from a perfect mirror moving towards the source at relativistic velocities. This was simply a consequence of the well known relativistic Doppler effect. Whilst the velocities required to observe such an effect make this phenomenon seem far removed from our domain of experience, remarkably, such mirrors are routinely generated in high intensity laser labs around the world. Furthermore, laser pulses are bounced off these relativistic mirrors and their frequencies are upshifted into the extreme ultraviolet (XUV – approx. 10 to 120nm) or even the soft X-ray (<10nm) regimes.

The JETI-40 laser, housed at the Friedrich-Schiller-Universität in Jena, is one of these systems. Here we will briefly cover the background theory of high order harmonic generation (HOHG) followed by a discussion of some of the recent experiments that have been performed at JETI-40 and what our plans for the future are.

HARMONIC GENERATION MECHANISMS

When a high intensity laser is incident on a flat solid target surface, the material is ionised on the rising edge of the pulse forming a dense plasma. The population of newly liberated free electrons allow the plasma to act like a conductor and, for typical solid densities, means the plasma is almost completely reflective for the laser pulse.

When the peak of the laser pulse impinges, the huge fields there are able to drive the plasma surface very fast. If the intensity is high enough ($>10^{18}$Wcm^{-2}) then the fields are so strong that the surface can be made to oscillate with peak velocities close to the speed of light. As this plasma surface is driven towards the laser pulse, it is able to reflect and upshift the optical or infrared wavelength light into the XUV range and, because this happens with the periodicity of the laser pulse, this high frequency radiation appears in a train of attosecond scale pulses which are seen spectrally as harmonics of the laser frequency. Although this is a relatively simple description (known as the relativistically oscillating mirror ROM model [2]) of this complex laser-plasma interaction, it has been quite successful at describing many of the main properties of this radiation such as the power scaling laws of the XUV spectrum [3], the divergence of the harmonic radiation [4] and the maximum harmonic order generated for different intensities [5]. An excellent in-depth review of this subject can be found in [6].

RECENT AND FUTURE EXPERIMENTS

The JETI-40 laser produces laser pulses with a central wavelength of 800nm and contains an energy of 1J concentrated within just 30fs (1fs=10^{-15}s) thus the peak power of these pulses are enormous (approx. 30TW). By focusing this power to micron scale spots they can generate the relativistic intensities required for the ROM mechanism.

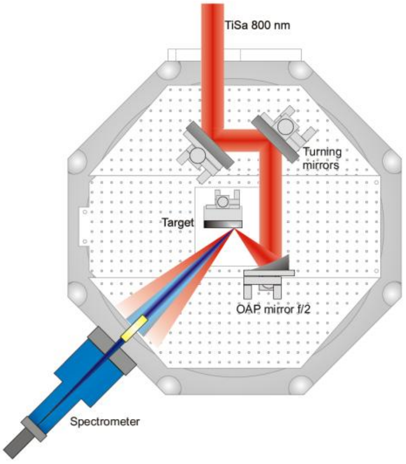

Figure 1: Typical experimental setup for HOHG on JETI-40

The setup for a typical HOHG experiment is shown in figure 1. The laser is focused onto the surface of a polished glass surface and the specular reflection is sent into a energy calibrated XUV spectrometer. An example of a typical HOHG spectrum is shown in figure 2.

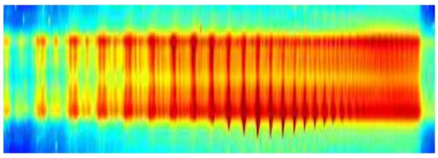

Figure 2: Recorded raw harmonic spectrum. The sharp cutoff on the right is due the spectral cutoff of an aluminium filter

Successful experiments that have been performed on JETI-40 include characterization of the efficiency of the harmonic emission [7], demonstration of HOHG operation at 10Hz [8] and controlling the angular distribution of the harmonics by the use of blazed grating targets [9].

At shallow angles of incidence, it is known that the harmonic efficiency is suppressed when using elliptically polarized light. Future experiments will hope to exploit this to effect by forming a pulse which is elliptically polarized with the exception of a brief linear gate in the centre – a technique known as polarization gating. In this manner, the usual train of attosecond pulses can be reduced to just a couple or even one.

ROM is not the only mechanism that can lead to HOHG in this interaction. Dense bunches of electrons can be generated and driven on synchrotron like trajectories by the laser pulse. This leads to coherent synchrotron emission (CSE) in the XUV wavelength range. To date, this has only been observed in transmission of thin foils [10] and it is hoped that this can also be observed in JETI-40.

In conclusion, JETI-40 is a state-of-the-art laser system, ideally suited for studying HOHG. It is hoped that future experiments on this system will help further understanding of this phenomenon.

[1] A. Einstein, Ann. Phys. Lpz. **17,** 891 (1905)

[2] R. Lichters, J. Meyer-ter-Vehn and A. Pukhov, Phys. Plasmas E **3**, 3425 (1996)

[3] T. Baeva, S. Gordienko and A. Pukhov, Phys. Rev. E **74**, 046404 (2006)

[4] M. Yeung *et al.* Phys. Rev. Lett. **110**, 165002 (2013)

[5] B. Dromey *et al.* Phys. Rev. Lett. **99**, 085001 (2007)

[6] C. Thaury and F. Quéré, J. Phys. B, **43**, 213001 (2010)

[7] C. Rödel *et al.* Phys. Rev. Lett. **109,** 125002 (2012)

[8] J. Bierbach *et al.* New J. Phys. **14,** 065005 (2012)

[9] M. Yeung *et al.* New J. Phys. **15,** 025043 (2013)

[10] B. Dromey *et al.* Nature Phys. **8,** 804 (2012)

Design and Simulation of the Hyperchromatic Confocal System in Metrology

Minyi Zhong[1], Herbert Gross[*1]

[1]*Institute of Applied Physics*
Friedrich Schiller University Jena
Albert-Einstein-Str. 15, 07745 Jena, Germany

[*]Corresponding Author: *herbert.gross@uni-jena.de*

Abstract

An optical design of three spherical lenses is proposed for hyperchromatic confocal system in metrology. An axial-chromatic measuring range of 1 mm without spherical aberration was achieved. The Zernike coefficients of the wavefront in the fiber (pinhole) plane were derived in Zemax by double-pass ray trace. A simulation of the confocal signal including diffraction effect was realized in Matlab. The FWHM of the confocal signal Δλ was estimated to be 5.5 nm in the central wavelength 550 nm, with deviation of 14% compared to the Wilson's Formula in theory.

INTRODUCTION

Glass materials have refractive indices varied by wavelengths. In lens systems, the focal power is a function of refractive index. Therefore there is change of focal length for different wavelengths due to dispersion, called axial chromatic aberration. In a hyperchromatic confocal design, chromatic aberration is exploited as an advantage to give varied focal lengths as a moving sample plane, to offer depth selection of the sample. An optical fiber with finite diameter works as an illumination source, also as a confocal pinhole in the double pass to capture the confocal signal of certain wavelengths after reflected by the sample plane.

Here an optical design of a hyperchromatic confocal system with three spherical lenses is proposed, with a white light LED as the illumination source through a step-index optical fiber with diameter 26 μm. Zernike coefficients were derived directly from Zemax to evaluate the overall aberrations of the system to reconstruct the real point spread function of the confocal signal in the fiber plane. Under double-pass propagation with diffraction and the residual aberrations, the confocal signal information was simulated in Matlab.

THEORY

Effective Focal Length. The effective focal length f of a thin lens is a function dependent on wavelength due to the dispersion effect of refractive glasses [1]

$$\frac{1}{f} = K = (n(\lambda) - 1)\left[\frac{1}{R_1} - \frac{1}{R_2}\right]$$

in which K is the lens power, R_1 and R_2 are the radii of the lens bending at the front and rear surface respectively.

Chromatic Aberration. If a system is composed of two lenses with refractive indices n_1 and n_2 for the wavelength λ, when the wavelength is shifted to $\lambda+\delta\lambda$, the indices become $n+\delta n_1$ and $n+\delta n_2$, then the change of the effective lens power is [1]

$$\delta K = \frac{\delta n_1}{n_1 - 1} K_1 + \frac{\delta n_2}{n_2 - 1} K_2$$

By having a proper combination of refractive indices chromatic aberration can be enhanced significantly. On the other hand, combination of refractive indices also influences the spherical aberration [2], which is the primary aberration that should be avoided to guarantee the image quality in design. Therefore selecting glasses of proper refractive indices and Abbe numbers is the major approach in the optimization.

Zernike Polynomials. Zernike polynomials [3] are applied to evaluate the aberrations in the wavefront reconstruction simulation.

$$\mathrm{W}(\rho,\theta) = \sum_{n}^{\infty} \sum_{m=0}^{n} \left[\frac{[2(n-1)]}{1+\delta_{m0}}\right]^{1/2} R_n^m(\rho) \cdot (c_{nm} cos m\theta + s_{nm} sin m\theta)$$

$$R_n^m(\rho) = \sum_{s=0}^{(n-m)/2} \frac{(-1)^s (n-s)!}{s!\left(\frac{n+m}{2}-s\right)!\left(\frac{n-m}{2}-s\right)!}\rho^{n-2s}$$

where c_{nm} and s_{nm} are the expansion or the aberration coefficients, δ_{ij} is a Kronecker delta. The index n represents the radial degree or the order of the polynomial.

Wilson's Formula. The FWHM estimation of the confocal signal was proposed by T Wilson [4]

$$\mathrm{FWHM}_{axial} = 0.45\frac{\lambda}{n-\sqrt{n^2-NA_{MR}^2}}\sqrt[3]{1+1.47\left(\frac{D_{PH}\cdot NA_{PH}}{1.22\lambda}\right)^3}\cdot\frac{1}{CHS}$$

where the NA_{MR} is the numerical aperture in the sample measuring range, NA_{PH} is the pinhole numerical aperture, D_{PH} is the pinhole diameter. CHS is the chromatic shift of focus in the measuring range, $CHS = \frac{ds\prime}{d\lambda}$. Aberration effect is neglected in this formula.

OPTICAL DESIGN

The chromatic aberration was optimized to be 1 mm among the wavelength range 450 - 675 nm, while spherical aberration was eliminated to be minimum. The spot size was almost diffraction limited.

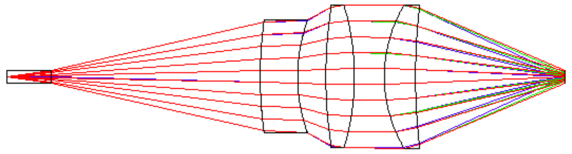

Figure 1. The lens design of a hyperchromatic confocal system. The first component on the left is the additional top layer (3 mm BK7) of the optical fiber. Three spherical lenses are used to generate axial chromatic measuring range 1 mm among the wavelength range 450 - 675 nm while the spherochromatism corrected.

SIMULATION RESULTS

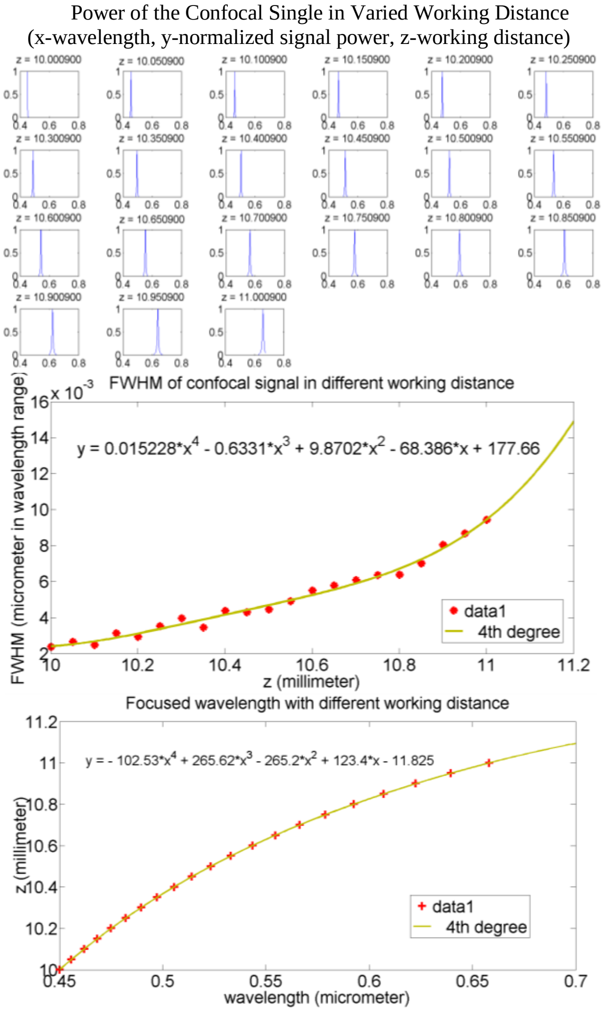

Figure 2. The simulation results of the confocal signal in varied sample distance of a step change 0.05 mm.

The simulated FWHM Δλ of the confocal signal in 550 nm is 5.5 nm, 14% deviated compared to the Wilson's formula in theory. This deviation can be understood as the difference between the chromatic confocal systems and the fluorescence confocal systems. Wilson's formula was corrected for one wavelength, self-luminous object (fluorescence molecule), spherical-aberration free systems.

---

[1] W. T. Welford, Aberrations of Optical Systems, Taylor & Francis Group LLC, 1986.
[2] E. Delano, "A General Contribution Formula for Tangential Rays," Journal of the Optical Society of America, vol. 42, September 1952.
[3] V. N. Mahajan, "Zernike Circle Polynomials and Optical Aberrations of Systems with Circular Pupils," Applied Optics, 1 December 1994.
[4] T. Wilson, "Resolution and optical sectioning in the confocal microscope," Journal of Microscopy, vol. 244, p. 113–121, 2011.

On the evolution of primary constituents of ultrashort pulse-induced nanogratings

Felix Zimmermann[*1], Anton Plech[2], Sören Richter[1] and Stefan Nolte[1]

[1]*Institute of Applied Physics, Abbe Center of Photonics, Friedrich-Schiller-Universität Jena, Max-Wien-Platz 1, 07743 Jena, Germany*

[2]*Institute for Synchrotron Radiation, Karlsruhe Institute of Technology, PO box 3640, 76021 Karlsruhe, Germany*

[*]Corresponding Author: *Felix.Zimmermann@uni-jena.de*

By tightly focusing femtosecond laser pulses into a glass substrate, self-organized periodic nanostructures, so-called nanogratings, are generated in a certain parameter regime. They consist of nanopores and cracks embedded within the otherwise isotropic host material. In order to map their evolution, we employed focused ion beam (FIB) milling and small angle X-ray scattering (SAXS). Our results show that nanopores with dimensions of (284x24)nm and (29x24)nm are formed. While the dimensions remain constant with prolonged laser exposure, the pore shape changes from cuboid cracks to ellipsoidal structures.

INTRODUCTION

Since the first demonstration in 1996 that focused femtosecond laser pulses can induce a refractive index increase inside glass [1], such laser material interactions have gained particular interest in order to explore the possible modifications. In this regard it has been found that self-assembled grating like structures with periods smaller than the laser wavelength evolve within an intermediate regime of laser pulse energies [2]. These so called “nanogratings” emerge after several laser pulses and arrange perpendicular to the laser polarization. Since their structural properties (period) can be tuned by adjusting the laser parameters [3] the strong form-birefringence can be controlled enabling the fabrication of numerous interesting devices for applications [4,5]. Nevertheless the formation process is up to now not fully understood. One major issue concerns the underlying structure which is hard to explore. Due to their small feature size conventional imaging methods (e.g. optical microscopy, SEM) cannot be used or require sample preparation techniques leading to bluring and distorting of essential structure details. First experiments based on nonintrusive techniques as small angle x-ray scattering (SAXS) and focused ion beam milling (FIB) explored the porous structure of the nanogratings [6]. However, based on the SAXS setup used in these experiments, only dimensions in the range of several tens of nanometers were directly accessible. Additionally, the sample was probed in only one direction, thus important particle features were excluded (e.g. size and shape). To overcome these limitations we performed an extensive study of the evolution of the induced nanopores and cracks in terms as nanograting constituents by using SAXS, FIB and scanning electron microscopy (SEM).

METHODOLOGY

Nanogratings are inscribed using the frequency doubled (515 nm) light of a mode locked laser oscillator (Amplitude t-pulse 500). This laser provides pulses with durations of about 450 fs, pulse energies up to 200 nJ at repetition rates up to 10 MHz. The repetition rate was reduced to 500 kHz by an external acusto-optical modulator in order to avoid heat accumulation effects. For focusing we used an aspheric lens (New Focus 5722) with a numerical aperture of 0.55.

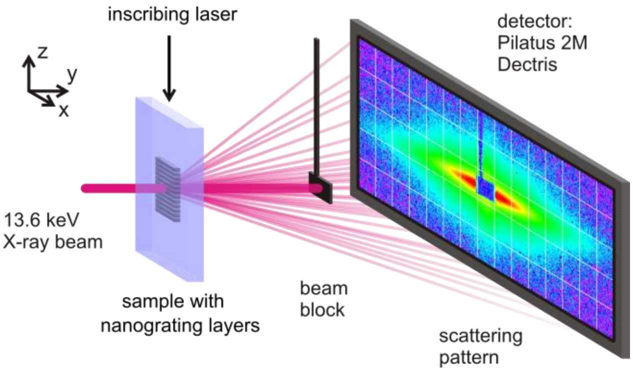

Fig.1 Scheme of the SAXS measurement.

In order to analyze nanograting features in longitudinal direction we inscribed several layers with a layer distance of 2 µm. For the SAXS measurements the sample was laterally polished down to a thickness of about 300 µm to avoid significant absorption of the x-ray beam when probing the sample from the side (fig. 1). The SAXS patterns nondestructively reveal density inhomogeneities of particle ensembles. In this regard the samples were illuminated with a probe beam (photon energy 11.2 keV, cSAXS beamline at the Swiss Light Source (Villigen, CH)) that is scattered and the pattern is recorded with a large direct converting pixel converter. In addition FIB has been used whereby a volume containing nanogratings was dissected in 12 nm slices and analyzed per SEM imaging.

RESULTS

The evaluation of the x-ray scattering intensity along the inscribing direction (z) shows a broad distribution whereby two distinct populations with different diameters can be distinguished. As figure 2 (a) shows, these are independent of the applied pulse energy and number of pulse. This indicates that once the structure is formed no further growth takes place.

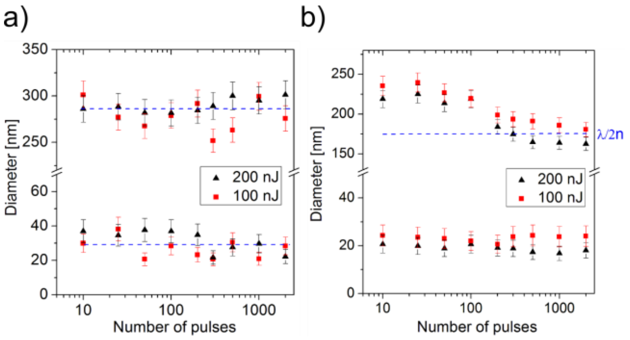

Fig. 2 Results of the SAXS measurements. Analyzing along z (a) and x (b) reveal two distinct feature sizes.

By analyzing the SAXS data along x (fig. 2 (b)) a constant feature size of about 24 nm can be observed. Additionally, a large population is visible and shows a decreasing diameter that corresponds well to the smaller nanograting period with prolonged laser exposure [3]. In accordance with the SAXS measurements the SEM micrograph in fig. 3 (a) illustrates the pore dimension of (284 x 24) nm and (29 nm x 24 nm), respectively.

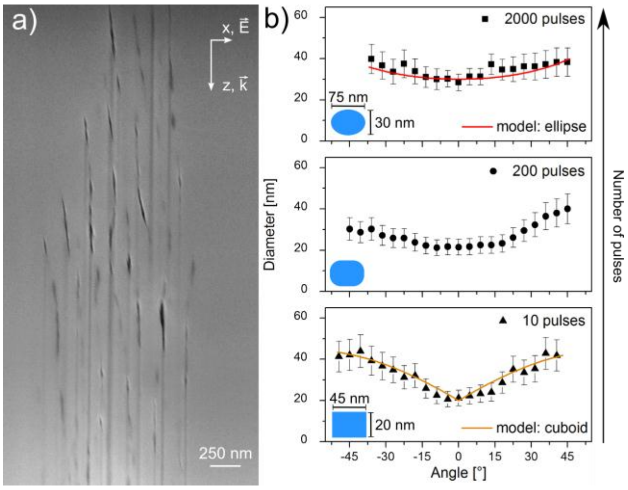

Fig. 3 SEM micrograph of a FIB-slice in the z-x-plane (a) and angle dependence of the diameter of the small population along x (b).

Figure 3 (b) shows the results along x of the SAXS measurements by rotating the sample around z. The decreasing angle dependence with prolonged laser exposure indicates that the shape of the structures induced changes from cuboid cracks to ellipsoidal shaped pores.

ACKNOWLEDGEMENTS

We thank Swiss Light Source (cSAXS beamline at Paul Scherrer Institut Villigen, CH) for the beamtime. Furthermore the authors gratefully acknowledge financial support from Deutsche Forschungsgemeinschaft DFG (priority program 1327). Sören Richter was supported by the Hans L. Merkle Stiftung.

---

[1] K.M. Davis, K. Miura, N. Sugimoto, K. Hirao, Opt. Lett. 21, 1729 (1996)
[2] Y. Shimotsuma, P.G. Kazansky, J. Qiu and K. Hirao, Phys. Rev. Lett. 91, 247405 (2003)
[3] Richter S., Heinrich M., Döring S., Tünnermann A., Appl. Phys. A 104, 503-507 (2011).
[4] Ramirez L.P.R., Heinrich M. Richter S., et al., Appl. Phys. A 100, 1-6 (2010).
[5] Beresna M., Gecevičius M., Kazansky P.G., and Gertus T., Appl. Phys. Lett. 98 (2011).
[6] S. Richter, A. Plech, et al., Laser Phot. Rev., 6, 787 (2012).

Spectral measurements on noble metal nanoparticles using imaging Fourier transform spectroscopy

David Zopf*, Ondrej Stranik, Jacqueline Jatschka, Norbert Jahr, André Dathe and Wolfgang Fritzsche

Institute of Photonic Technology, Albert-Einstein-Straße 9,
07745 Jena, Germany

*Corresponding Author: *david.zopf@ipht-jena.de*

Abstract

The parallel read-out of the scattering spectra of single noble metal nanoparticles (MNP's) was realized by an imaging Fourier transform spectroscopy setup.

INTRODUCTION

Due to their nanoscale dimension and special optical behavior noble MNP's provide a multiplicity of possible applications. The special optical properties are caused by collective excitation of the conductive electrons of the metal. The spectral position of localized surface plasmon resonance (LSPR) is strongly dependent on the size, material, shape and the local dielectric environment of the nanoparticle [1]. The dependence of the LSPR peak position on the surrounding medium can be utilized to investigate biomolecular interactions taking place on the surface of nanoparticles for instance DNA-DNA binding events [2].

The observation of these events can be performed by spectroscopic measurements at the single particle level. There are different methods to obtain the spectrum of a single nanoparticle, micro-spectroscopy and imaging spectroscopy. In micro-spectroscopy a spectrum of a defined area can be measured, so that every single nanoparticle has to be appointed individually. Whereas in imaging spectroscopy the spectral information of a whole image section with all nanoparticles can be obtained. One approach is to collect the scattering intensity of plasmonic nanostructures at individual wavelengths [3, 4]. Another approach is imaging Fourier transform spectroscopy where the spectral information is contained in an interferogram which by applying Fourier transformation (FT) leads to the spectrum. Here, we present an imaging Fourier transform spectrometer based on a Michelson interferometer (MI) for the parallel readout of plasmonic MNP.

THEORY

In a MI (see Fig. 1) a beam of radiation is divided into two paths and recombined after an optical path difference (*OPD*) has been introduced.

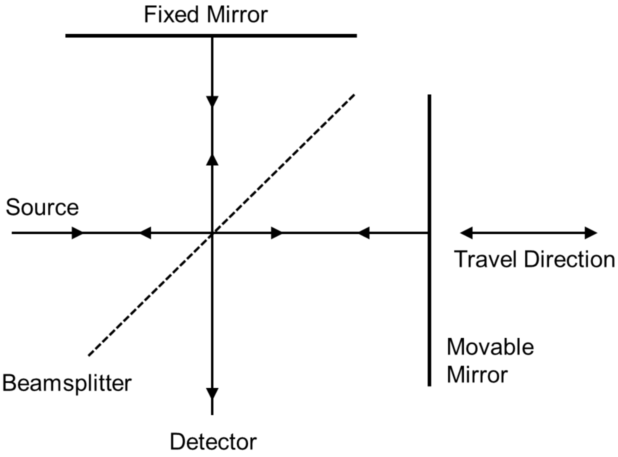

Figure 1: Scheme of a Michelson Interferometer

The measured intensity as a function of the *OPD* is called interferogram. The intensity of monochromatic light with wavenumber $\tilde{\nu}_0$ measured at the detector is given by

$$I_{\tilde{\nu}_0}(OPD) = \frac{I_0}{2}(1+\cos(2\pi\tilde{\nu}_0 OPD)) \qquad (1)$$

where I_0 is the intensity entering the interferometer from the source. For light with an intensity distribution $S(\tilde{\nu})$ the measured interferogram is given by

$$I(OPD) = \int_0^\infty S(\tilde{\nu}) I_{\tilde{\nu}}(OPD) \mathrm{d}\tilde{\nu}. \qquad (2)$$

Calculating the FT of $I(OPD)$ leads to the intensity as a function of the wavenumbers $S(\tilde{\nu})$.

EXPERIMENTAL RESULTS

A dark-field microscopy setup was used to collect the scattered light of the sample. The *OPD* of the MI is varied in steps using a piezo motor moving one mirror. An image is captured by a CCD camera at every *OPD*. The intensity values of each pixel were read out and they generate the interferogram.

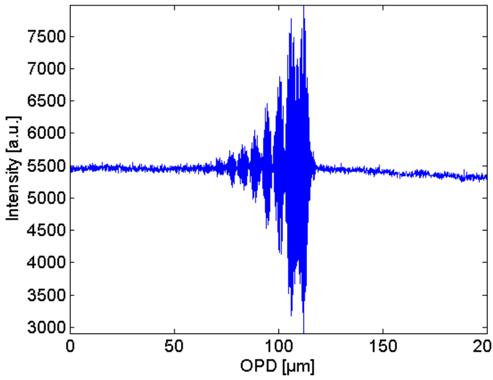

Figure 2: The interferogram of the scattered light of a spherical 100 nm gold nanoparticle is shown.

The imaging spectrometer was calibrated by measuring three laser lines with known wavelengths (488 nm, 532 nm and 633 nm). The peak positions were compared to the simulated peak positions.
The performance of the device was checked by comparison with micro-spectroscopy. Gold and silver nanoparticles were immobilized on glass substrates and their spectra, measured by imaging spectroscopy and micro-spectroscopy, was compared (see Figure 3).

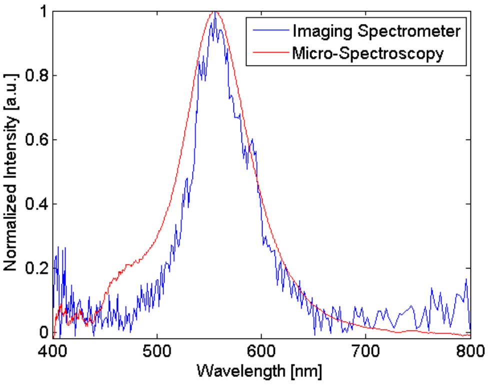

Figure 3: The nanoparticle spectrum calculated applying FT to the interferogram shown in Figure 2 (blue). The red curve shows the spectrum measured with the micro-spectroscopy setup.

As a biological model, few nm thick polymer layers were subsequentially adsorbed on the nanoparticles by layer-by-layer deposition technique. The refractive index change of the surrounding medium leads to a LSPR shift which was measured at single particle level.

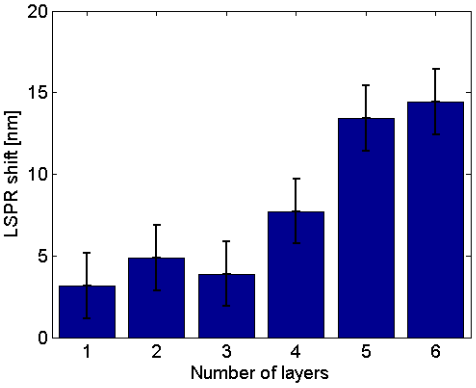

Figure 4: Measured LSPR shift for polymer-layers on a single 80 nm gold nanoparticle

The obtained measurements show promising results for further bioanalytical applications.

---

[1] K. L. Kelly, E. Coronado, L. L. Zhao, G. C. Schatz, *The Journal of Physical Chemistry B* **107**, 668 (2003).

[2] T. Schneider, *et al.*, *Journal of Nanoparticle Research* **15**, 1 (2013).

[3] G. Liu, J. Doll, L. Lee, *Opt. Express* **13**, 8520 (2005).

[4] J. M. Bingham, K. A. Willets, N. C. Shah, D. Q. Andrews, R. P. Van Duyne, *The Journal of Physical Chemistry C* **113**, 16839 (2009).

List of Contributors

ALAEE, RASOUL

Complete light absorption in deep-subwavelength graphene plasmonic structures (poster)

Institute of Condensed Matter Theory and Solid State Optics, Friedrich-Schiller-Universität, Jena, Germany

BECKER, NILS

Airy pulses and pulses with arbitrary temporal trajectories (talk)

Institute of Applied Physics, Friedrich-Schiller-Universität, Jena, Germany

BRÜNING, ROBERT

Numerical Mode Analysis of Laser Beams (talk)

Institute of Applied Optics, Friedrich-Schiller-Universität, Jena, Germany

BRÜNING, ROBERT

Vortex Beam Analysis Using Holographic Correlation Filters (talk)

Institute of Applied Optics, Friedrich-Schiller-Universität, Jena, Germany

CHEMNITZ, MARIO

Supercontinuum generation in an all-normal dispersion fiber for broadband MHz absorption spectroscopy (talk)

Department of Chemical Engineering and Biotechnology, University of Cambridge, Cambridge, United Kingdom

DA SILVA, RICARDO E.

Effect of the silica bridge thickness of suspended core fiber on the acousto-optic modulation of fiber Bragg gratings (poster)

Institute of Photonic Technology, Friedrich-Schiller-Universität, Jena, Germany

ECKNER, ERICH

Relativistic Frequency Synthesis of Light Fields (poster)

Institute of Optics and Quantum Electronics, Friedrich-Schiller-Universität, Jena, Germany

EICHELKRAUT, TONI

Diffusion and ballistic transport in non-Hermitian systems (talk)

Institute of Applied Physics, Friedrich-Schiller-Universität, Jena, Germany

EILENBERGER, FALK

Black Holes and Revelations: on the Extraction of Optical Pulses from Cavities (talk)

Institute of Applied Physics, Friedrich-Schiller-Universität, Jena, Germany

Emsia, Ali

DPSK-based reach extension for N×Gbit/s NG-PON (talk)
Institute of Microwave Engineering and Photonics, Technische Universität Darmstadt, Darmstadt, Germany

Falkner, Matthias

Advanced experimental characterization techniques for plasmonic nanostructures (talk)
Institute of Applied Physics, Friedrich-Schiller-Universität, Jena, Germany

Fasold, Stefan

Plasmonic Moire Magnifier (talk)
Institute of Applied Physics, Friedrich-Schiller-Universität, Jena, Germany

Filter, Robert

Towards Strong Coupling of Nanoantennas and Quantum Systems (talk)
Institute of Condensed Matter Theory and Solid State Optics, Friedrich-Schiller-Universität, Jena, Germany

Fruhnert, Martin

Tunable magnetic dipole response of core-shell clusters (talk)
Institute of Condensed Matter Theory and Solid State Optics, Friedrich-Schiller-Universität, Jena, Germany

Fuchs, Silvio

Towards extreme ultra violet coherence tomography with high harmonic generation light sources (talk)
Institute of Optics and Quantum Electronics, Friedrich-Schiller-Universität, Jena, Germany

Geiss, Reinhard

Fabrication of Freestanding Photonic Crystals in Lithium Niobate by Combining Focused Ion-Beam Writing and Ion-Beam Enhanced Etching (talk)
Institute of Applied Physics, Friedrich-Schiller-Universität, Jena, Germany

Heisel, Christian

Comparison of Electric Field Induced Second Harmonic (EFISH) in reflection and transmission from an oxidized silicon membrane (poster)
Institute of Photonic Technology, Friedrich-Schiller-Universität, Jena, Germany

Hidi, Izabella J.

Drug detection using LOC-SERS technology (poster)
Institute of Physical Chemistry, Friedrich-Schiller-Universität, Jena, Germany

Hou, Jiamin

Entanglement generation in the vicinity of nano-structure (poster)
Institute of Condensed Matter Theory and Solid State Optics, Friedrich-Schiller-Universität, Jena, Germany

Jahn, Martin

Lipophilic sensor layers for detecting Sudan dyes using surface enhanced Raman scattering (talk)
Institute of Photonic Technology, Friedrich-Schiller-Universität, Jena, Germany

Jost, Aurelie

Blind reconstruction of Structured Illumination Microscopy (SIM) data (poster)
Institute of Photonic Technology, Friedrich-Schiller-Universität, Jena, Germany

Kaiser, Thomas

Effective photonic parameters from an eigenmode perspective (talk)
Institute of Applied Physics, Friedrich-Schiller-Universität, Jena, Germany

Kämmer, Helena

Laser induced damage threshold (LIDT) with fs-laser pulses (talk)
Institute of Applied Physics, Friedrich-Schiller-Universität, Jena, Germany

Knipper, Richard

Field amplifying perfect absorber in the THz range (poster)
Institute of Photonic Technology, Friedrich-Schiller-Universität, Jena, Germany

Kopielski, Andreas

One-pot annealing of DNA-nanoparticle structures (talk)
Institute of Photonic Technology, Friedrich-Schiller-Universität, Jena, Germany

Krämer, Ria G.

High power 1.2 kW monolithic fiber laser with a femtosecond inscribed fiber Bragg grating (talk)
Institute of Applied Physics, Friedrich-Schiller-Universität, Jena, Germany

Liu, Weici

High Power Dual-Wavelength Self-Similar Parabolic Pulse Yb3+ Doped Fiber Laser (poster)
Institute of Condensed Matter Theory and Solid State Optics, Friedrich-Schiller-Universität, Jena, Germany

Lopaeva, Elizaveta D.

Experimental realization of quantum illumination (talk)
Department of Applied Science and Technology, Politecnico di Torino, Torino, Italy

Lorenz, Adrian

Microstructured Optical Fibers from Preforms by Free Form Silica Laser Drilling (poster)
Institute of Photonic Technology, Friedrich-Schiller-Universität, Jena, Germany

MALEKIZANDI, MOHAMMADREZA

Power budget extension for OFDM-TDM-WDM PON (talk)
Institute of Microwave Engineering and Photonics, Technische Universität Darmstadt, Darmstadt, Germany

MEYER, FRANK

Generation of 2-Cycle Laser Pulses around 1.8μm for the Investigation of Strong Field Phenomena (poster)
Institute of Optics and Quantum Electronics, Friedrich-Schiller-Universität, Jena, Germany

PAHLOW, SUSANNE

Chip-based Isolation of Microorganisms with Subsequent Raman Spectroscopic (poster)
Institute of Physical Chemistry, Friedrich-Schiller-Universität, Jena, Germany

QI, JING

Highly resonant and directional nanoantenna (talk)
Institute of Condensed Matter Theory and Solid State Optics, Friedrich-Schiller-Universität, Jena, Germany

RADU, ANDREEA-IOANA

Determination of vitamins by surface enhanced Raman spectroscopy (SERS) (poster)
Institute of Physical Chemistry, Friedrich-Schiller-Universität, Jena, Germany

RICHTER, DANIEL

Influence of Gouy phase on the spectral behaviour of a volume Bragg grating (talk)
Institute of Applied Physics, Friedrich-Schiller-Universität, Jena, Germany

RUTCKAIA, VIKTORIIA V.

Luminescence of Si/Ge-quantum dots resonators around 1550nm wavelength and enhancement with photonic crystal microcavities (talk)
Centre for Innovation Competence SiLi-nano, Martin-Luther-Universität, Halle, Germany

SCHULZE, CHRISTIAN

Beam quality measurements with a spatial light modulator (talk)
Institute of Applied Optics, Friedrich-Schiller-Universität, Jena, Germany

SCHULZE, CHRISTIAN

Measuring the modal bend loss in multimode optical fibers (talk)
Institute of Applied Optics, Friedrich-Schiller-Universität, Jena, Germany

SHUKLA, SAPNA

Optical Sectioning in a Single Exposure Using Polarisation-Coded Structured Illumination Microscopy (picoSIM) and Nanogratings (poster)
Institute of Photonic Technology, Friedrich-Schiller-Universität, Jena, Germany

SOJKA, FALKO

Compensating geometric distortions, not only in CCD images, for enhanced quantitative analysis - shown by the example of LEED images (talk)
Institute for Solid State Physics, Friedrich-Schiller-Universität, Jena, Germany

SPITTEL, RON

Band gap analysis of metal-filled photonic crystal fibers (talk)
Institute of Photonic Technology, Friedrich-Schiller-Universität, Jena, Germany

STÜTZER, SIMON

Hybrid Bloch-Anderson (talk)

Institute of Applied Physics, Friedrich-Schiller-Universität, Jena, Germany

TALKENBERG, FLORIAN

Novel Hetero-Junction Solar Cell Concept based on Silicon Nanowires (poster)
Institute of Photonic Technology, Friedrich-Schiller-Universität, Jena, Germany

TIEGEL, MIRKO

Development of new laserglasses for high-energy systems – opportunities and challenges of alumino silicate glasses (poster)
Otto Schott Institute of Materials Research , Friedrich-Schiller-Universität, Jena, Germany

VETTER, CHRISTIAN

Generation of Optical Solenoid Beams for Particle Manipulation (talk)

Institute of Applied Physics, Friedrich-Schiller-Universität, Jena, Germany

VON GRAFENSTEIN, LORENZ

Ultra-long enhancement cavities as a promising approach to raise femtosecond lasers to a new level of output parameters (talk)
Institute of Applied Physics, Friedrich-Schiller-Universität, Jena, Germany

WALTHER, BENNY

Blessings and curse of silver in plasmonic nanostructures (talk)

Institute of Applied Physics, Friedrich-Schiller-Universität, Jena, Germany

WÜRZLER, DANIEL

Velocity Map Imaging of Trajectory Controlled Above-Threshold Ionization Spectra of Xenon Using the Two-Color Field Technique (talk)
Institute of Optics and Quantum Electronics, Friedrich-Schiller-Universität, Jena, Germany

WUSTELT, PHILIPP

Ionization of atomic Ions under elliptical Polarization (talk)
Institute of Optics and Quantum Electronics, Friedrich-Schiller-Universität, Jena, Germany

YEUNG, MARK K.

Extreme Ultraviolet Surface High Order Harmonic Radiation from JETI-40 – Recent Experiments and Plans for the Future (talk)
Helmholtz Institute Jena, Friedrich-Schiller-Universität, Jena, Germany

ZHONG, MINYI

Design and Simulation of the Hyperchromatic Confocal System in Metrology (talk)
Institute of Applied Physics, Friedrich-Schiller-Universität, Jena, Germany

ZIMMERMANN, FELIX

On the evolution of primary constituents of ultrashort pulse-induced nanogratings (talk)
Institute of Applied Physics, Friedrich-Schiller-Universität, Jena, Germany

ZOPF, DAVID

Spectral measurements on noble metal nanoparticles using imaging Fourier transform spectroscopy (talk)
Institute of Photonic Technology, Friedrich-Schiller-Universität, Jena, Germany

Accomodation

The Ringberg Hotel Suhl is located high atop the surrounding area in midst the Thuringian forest. At 750 m above sea level one has an excellent view over the city Suhl, the Rhön Mountains and the Thuringian-Franconian Highlands. The exposed location within the heart of Germany and the easy access by the A71 and A73 autobahn makes the Ringberg Hotel an ideal place for events from all over Germany. The Hotel offers a large conference room which is complemented by various additional seminar rooms and a generously sized lobby to ensure the optimal working atmosphere.

Besides the professional affairs, the Ringberg Hotel is known for its extensive variety of sports and leisure facilities as well as an outstanding cuisine. In 2012 the Hotel won the Thuringian tourism price. For contributers and guests of **DoK**DoK we are offering accommodation in comfortable double rooms including full board. Oral presentations and keynote talks will take place in one of the larger seminar rooms. For the poster session, the conference room foyer will provide the required space for stimulated discussions.

Frequently Asked Questions

- Where will the sessions take place?

  All talks will be given in the room ”‘Sachsen”’ in the conference area (1st basement floor). The poster session will take place in the conference area foyer.

- Where will the welcome reception take place?

  The welcome reception is going to be in the conference area foyer (1st basement floor). Drinks are included up to a certain limit.

- Where do we get breakfast, lunch and dinner?

  All meals are served in the restaurant area (ground floor). Drinks from the beverage dispenser are free during that time.

- Where will the conference dinner take place?

  Our special conference dinner will take place in the room ”‘Karin Roth”’ (ground floor).

- What kinds of leisure activities are available?

  The hotel offers many sports and wellness activities. For participants of **DoK**DoK , the swimming pool and the sauna (once during the conference) is free of charge. For further offers, please get the information at the info desk.

- Where will the bus for the social day leave?

  The bus will leave from the hotel parking area. All participants meet at 12:30 in front of the hotel.

- In which cases are drinks for free and in which not?

  During all meals, the drinks from the beverage dispenser are for free. During the sessions and coffee breaks, beverages are also available cost-free. For the welcome reception, the poster session and the conference dinner, drinks are included. At any other time, drinks have to be bought at the hotel bar.

Autumn School

This year the Abbe School of Photonic's Autumn School follows up **DoK**DoK on the 10th and 11th October 2013 in the Ringberg Hotel in Suhl. Two additional skills seminars are offered to you:

- Time and Self-Management
- Leadership Skills

Course descriptions

Time and Self-Management

October 10th, 1 pm, 0.5 days, max. 12 participants
When it comes to organizing their work, students face the same problems as, for example, people working in management. In this module they are provided with an introduction to different approaches to time and self-management. This includes analyzing one's personal effectiveness by identifying time wasters and learning how to keep an activity log. Students are taught how to set work priorities by classifying their goals and arranging them in 4 categories resulting from different combinations of urgency and importance (Eisenhower principle). They learn how to set up action plans and prioritized to-do-lists, and are introduced to the rules for effective scheduling. The students are shown how to tackle the time wasters they have identified in the beginning and are given a quick introduction to Speed Reading.
Instructor: Kerstin Kathy Meyer-Ross

Leadership Skills

October 11th, 9 am, 1 day, max. 12 participants
This course is providing basic theoretical and practical knowledge concerning leadership in projects and teams. Interactive exercises will help you to understand more about yourself being in a "leading" or "led" position. You will learn more about the driving forces (motivation), decision making and negotiating as valuable skills for any leader.
In discussions and exercises you will look at different leadership types and also learn about your own talents and behaviors regarding leadershop. You will practice various communication skills as active listening, paraphrasing, reflecting, constructive feedback and dealing with conflicts.
Instructor: Peter Wagner, Kleist-Wagner Projekt

Board of Organizers

Institute of Applied Physics, Friedrich-Schiller-Universität Jena:

- Matthias Falkner (General Conference Chair)
- Ria Krämer (General Conference Co-Chair)
- Daniel Richter (Technical Program Chair)
- Christian Vetter (Accomodation)
- Stefan Fasold (Accomodation, Social Day)
- Jessica Richter (Social Day, Accomodation)
- Felix Zimmermann (Communication, Web)

Institute of Optics and Quantum Electronics, Friedrich-Schiller-Universität Jena / Helmholtz Institute Jena:

- Jana Bierbach (Design, Communication)
- Max Möller (Fundraising, Finance)

Institute of Physical Chemistry, Friedrich-Schiller-Universität Jena:

- Martin Jahn (Fundraising, Finance)
- Sophie Zierbock (Communication)

Stefan, Jessica, Matthias, Martin, Ria, Max Planck, Christian, Felix, Daniel, Jana.
Not in the picture: Max, Sophie.

Notes

"... denn was man schwarz auf weiß besitzt, kann man getrost nach Hause tragen!"
Goethe, Faust I

We gratefully acknowledge our supporters:

ZEISS

Fraunhofer
IOF

INSTITUTE of
PHOTONIC
TECHNOLOGY
ipht jena

HELMHOLTZ
GEMEINSCHAFT
Helmholtz-Institut Jena

LAYERTEC®
OPTICAL COATINGS · OPTICS

LOT
QuantumDesign

activefiber
systems

AHF ANALYSENTECHNIK

asphericon

jenaoptronik

OSA®

THORLABS

LIMO
Lissotschenko Mikrooptik

JENOPTIK

eagleyard
PHOTONICS
We focus on power.

DAAD
Deutscher Akademischer Austausch Dienst
German Academic Exchange Service

Abbe School of Photonics | JENA
Friedrich-Schiller-Universität

SPONSORED BY THE
Federal Ministry
of Education
and Research